UNIVERSITÉ DU QUEBEC À CHICOUTIMI

MÉMOIRE PRÉSENTÉ À
L'UNIVERSITÉ DU QUÉBEC À CHICOUTIMI
COMME EXIGENCE PARTIELLE
DE LA MAÎTRISE EN INGÉNIERIE

PAR
GHOLAMALI FARHADI CHESHMEH MORVARI

LES EFFETS DES ELEMENTS DE TRACE SUR LES CARACTERISTIQUES DES ALLIAGES DE TYPE 6XXX POUR LES APPLICATIONS AUTOMOBILES

OCTOBRE 1999

Bibliothèque
Paul-Émile-Boulet

UQAC
Université du Québec
à Chicoutimi

Mise en garde/Advice

Afin de rendre accessible au plus grand nombre le résultat des travaux de recherche menés par ses étudiants gradués et dans l'esprit des règles qui régissent le dépôt et la diffusion des mémoires et thèses produits dans cette Institution, **l'Université du Québec à Chicoutimi (UQAC)** est fière de rendre accessible une version complète et gratuite de cette œuvre.

Motivated by a desire to make the results of its graduate students' research accessible to all, and in accordance with the rules governing the acceptation and diffusion of dissertations and theses in this Institution, the **Université du Québec à Chicoutimi (UQAC)** is proud to make a complete version of this work available at no cost to the reader.

L'auteur conserve néanmoins la propriété du droit d'auteur qui protège ce mémoire ou cette thèse. Ni le mémoire ou la thèse ni des extraits substantiels de ceux-ci ne peuvent être imprimés ou autrement reproduits sans son autorisation.

The author retains ownership of the copyright of this dissertation or thesis. Neither the dissertation or thesis, nor substantial extracts from it, may be printed or otherwise reproduced without the author's permission.

To those who have filled my life with love

my wife, Flora;

my son, Khashayar; my daughter, Sarina.

In loving memory of my father, Hassan Gholi.

RÉSUMÉ

Les alliages d'aluminium corroyés sont employés aujourd'hui, plus intensivement, comme matières pour la structure et la carrosserie des véhicules, les fabricants de voitures s'efforcent de diminuer le poids des automobiles pour augmenter les économies d'essence. Dans ces alliages, α-Al_8Fe_2Si et β-AlFeSi sont les deux intermétalliques de fer prédominants combinés qui surviennent dans la structure solidifiée. La phase α, apparaissant comme une écriture chinoise a une morphologie plus compacte, en comparaison avec les plaquettes apparaissant de la phase β. Le type d'intermétallique présent a un important effet sur le temps d'homogénéisation, les caractéristiques de laminage et le temps de vieillissement d'une partie du produit de ces alliages.

Le travail actuel était exécuté pour étudier la formation des intermétalliques de fer dans les alliages d'aluminium de type 6XXX. Les alliages 6063 expérimental et commercial étudiés, contenant des concentrations de fer dans le domaine 0.17 - 0.39 % poids, de silicium dans le domaine de concentration 0.4 - 4.5 % et du magnésium dans le domaine 0.6 - 0.7 % poids de. Les effets de taux de refroidissement durant la solidification et l'addition d'éléments en trace tels que le silicium, le manganése et le bérylium dans la phase β-AlFeSi caractérisés dans les deux alliages non-modifié et modifié au Sr étaient étudiés. L'effet de la présence des intermétalliques et de la prédeformation sur les propriétés de traction a aussi été étudié. Les barreaux d'essai de ces alliages étaient traités à 520 °C pendant 8h, désaltérés dans de l'eau chaude, et vieilli, par la suite, à 175 °C jusqu'à 100h. Les phases rapportées dans cette étude étaient identifiées en utilisant un microscope optique et un microscope à balayage. La quantification des intermétalliques était faite en utilisant l'analyseur d'image.

Les résultats révèlent que dans les alliages de Sr-modifiés, les particules de Mg_2Si diminuent en taille et atteignent une forme plus globulaire après le traitement thermique. Pour un rapport de $Si^*/Fe > 1.5$ (où Si^* réfère à la présence de silicium libre dans l'alliage et non en combinaison avec Mg), la longue et épaisse précipitation de la phase plaquette de β-AlFeSi est observé. Pour les mêmes valeurs du rapport Si^*/Fe, la modification avec le strontium réduit seulement la taille des particules de β-AlFeSi. Les alliages démontrent de pauvres propriétés de formage mais de très hautes propriétés de traction. Pour un rapport de $Si^*/Fe < 1.5\%$, et en fonction de l'addition effectuée, la présence d'intermétallique peut être l'une ou l'autre des phases α-fer, β-fer ou un mélange des deux, et les propriétés mécaniques varient en conséquence conformément (maniable pour matière dure). La tendance de précipitation de la phase α-fer écriture chinoise augmente avec la modification au strontium et le taux de refroidissement.

L'addition de Mn à ces alliages implique une précipitation de la phase $\alpha–Al_{15}(Fe,Mn)_3Si_2$ écriture chinoise, et diminue les propriétés de formage et les propriétés de traction en comparaison avec l'absence de Mn. Les taux plus hauts de refroidissement et les modifications au strontium accroissent les propriétés de traction légèrement, mais réduisent sévèrement la ductilité et la formabilité. La formabilité des alliages est de beaucoup améliorée par l'addition de ~200 ppm Sr ou 0.02% Be. Un combiné de Be+Sr implique la précipitation de très fine et globulaire particules de écriture chinoises α-Al_8Fe_2SiBe, avec un alliage démontrant de très bonne propriétés de traction.

Il a été aussi démontré dans le travail actuel que la prédéformation (de 4%) diminue dramatiquement le temps de vieillissement requis pour atteindre le même niveau de propriétés de traction des alliages.

ABSTRACT

Aluminum wrought alloys are being used more extensively nowadays as structural and closure sheet materials for vehicle bodies, as automobile manufacturers strive for improved fuel economy by reducing vehicle weight. In these alloys, α-Al_8Fe_2Si and β-AlFeSi are the two predominant iron intermetallic compounds that occur in the solidified structure. The α-phase, appearing as Chinese script has a more compact morphology compared to the brittle plate-like β-phase. The type of intermetallic present has an important bearing on the homogenization time, workability and aging time of the parts produced from these alloys.

The present work was carried out to investigate the formation of iron intermetallics in 6XXX type aluminum alloys. Experimental and commercial 6063 alloys were studied, containing iron concentrations in the range of 0.17- 0.39 wt %, silicon in the range of 0.4 - 4.5 wt % and 0.6 - 0.7 wt % magnesium. The effects of cooling rate during solidification and the addition of trace elements such as Si, Mn and Be on the β-AlFeSi phase characteristics in both unmodified and Sr-modified alloys were studied. The effect of the intermetallics present on alloy tensile properties and prestraining were also studied. Test bars cast from these alloys were solution heat treated at 520 °C for 8h, quenched in hot water, and aged thereafter at 175 °C for times up to 100h. The phases reported in this study were identified using optical microscopy and electron microprobe analysis. Quantification of the intermetallics was done using image analysis.

The results reveal that in the Sr-modified alloys, the Mg_2Si particles decrease in size and attain a more globular shape after heat treatment. At Si^*/Fe ratios >1.5 (where Si^* refers to the free silicon present in the alloy and not in combination with Mg), precipitation of long, thick platelets of the β-AlFeSi phase is observed. At such Si^*/Fe ratios, modification with strontium only reduces the β-AlFeSi particle size. The alloys exhibit poor formability but very high tensile strain. At Si^*/Fe ratios <1.5%, and depending upon the addition made, the intermetallic present can be either α-iron, β-iron or a mixture of both, and the mechanical properties are seen to vary accordingly (ductile to hard material). Tendency for the α-iron Chinese script phase precipitation increases with strontium modification and higher cooling rates in such cases.

Addition of Mn to these alloys results in the precipitation of the α-$Al_{15}(Fe,Mn)_3Si_2$ Chinese script phase, and lower formability and tensile properties compared to those in absence of Mn. Higher cooling rates and Sr-modification are found to increase the tensile strain slightly, but severely reduce the ductility and formability. Alloy formability is greatly improved by the addition of ~200 ppm Sr or 0.02% Be. A combined Be+Sr addition results in the precipitation of very fine and globular α-Al_8Fe_2SiBe Chinese script particles, with the alloy exhibiting very good tensile properties.

It has also been demonstrated in the present work that prestraining (in the amount of 4%) dramatically decreases the aging time needed to reach the same level of alloy tensile properties.

ACKNOWLEDGEMENTS

It is with great pleasure that I have taken up the task of acknowledging all those who were involved directly or indirectly in making this work a success. Knowing fully well the limitations language has imposed upon me, I take it as a pleasure to convey my sincere thanks to my supervisor Prof. F. H. Samuel for his invaluable guidance. Each stage of my thesis was closely monitored by him. I would like to acknowledge Dr. Agnes Samuel for her help and guidance, particularly during the writing stages of my work.

Financial assistance received in the form of scholarships from UQAC (PAIR), the Fondation de l'Université du Québec à Chicoutimi (FUQAC), and the Natural Sciences and Engineering Research Council of Canada (NSERC) are gratefully acknowledged.

Financial support provided by NSERC and Timminco Metals, (ON), for the duration of this work and the provision of alloys by Alcan Beauharnois (QC), master alloys by KB Alloys, Inc. (USA), analytical services (chemical analyses) by General Motors Powertrain (USA), fractographic and radiographic analyses by Alcan Kingston R & D Centre (Kingston, ON), and beryllium analyses by Cercast (Montreal, QC) are duly acknowledged. I also wish to express my sincere thanks to Mme Hélène Dufour of Alcan Arvida R & D

Centre (Jonquière, QC) for her kind help with the scanning electron microscopy and EDX work.

I would like to express my appreciation to several colleagues, particularly Mr. Andre Bouchard, for their selfless help and for creating an enjoyable working atmosphere. Many thanks to Shahriar Varkiani and Mahin Derakhshanian who motivated me to join UQAC and who have been a constant source of encouragement, as also to Prof. Masoud Farzaneh who has been very helpful and supportive.

Finally, I would like to record my deep gratitude to the members of our family for their encouragement and support. Last, but by no means least, my heartfelt thanks go to my dear wife Flora, for her support, patience and love.

TABLE OF CONTENTS

RÉSUMÉ ..... **I**

ABSTRACT ..... **III**

ACKNOWLEDGEMENTS ..... **V**

TABLE OF CONTENTS ..... **VII**

LIST OF FIGURES ..... **X**

LIST OF TABLES ..... **XVII**

CHAPTER 1

DEFINITION OF THE PROBLEM **1**

1.1 INTRODUCTION 1
1.2 OBJECTIVES OF THE PRESENT STUDY 3

CHAPTER 2

LITERATURE REVIEW **4**

2.1 INTRODUCTION 4
2.2 ALUMINUM ALLOY SERIES DESIGNATION SYSTEM 6
2.3 TEMPER DESIGNATION SYSTEM 8
2.4 STRENGTHENING MECHANISMS 9
2.4.1. Heat-Treatable Alloys 9
2.4.2. Non-Heat Treatable Alloys 11
2.5 THERMAL TREATMENT 12
2.5.1 Annealing 12
2.5.2 Stabilizing 12
2.5.3 Homogenizing 12

2.6 ALLOYING ELEMENTS 13
2.7 IRON INTERMETALLICS IN ALUMINUM ALLOYS 14
2.7.1 Chemical Composition 14
2.7.2 Morphology and Crystal Structure 15
2.7.3 Effect of Iron and Silicon 17
2.8 MODIFICATION OF IRON INTERMETALLICS 21
2.8.1 Rapid Solidification 21
2.8.2 Addition of Neutralizing Elements 22
2.8.2.1 Manganese 22
2.8.2.2 Other Trace Elements 25
2.8.3 Grain Refining 29
2.8.4 Strontium Modification 32
2.8.5 Melt Superheating 40
2.8.6 Non-Equilibrium Heat Treatment 41
2.9 FORMABILITY 44

CHAPTER 3

IRON INTERMETALLIC CHARACTERISTICS 47

3.1 INTRODUCTION 47
3.2 EXPERIMENTAL PROCEDURE 49
3.2.1 Alloy Preparation 49
3.2.2 Casting and Sample Preparation 52
3.2.3 Quantitative Metallographic Measurements 53
3.2.3.1 Dendrite Arm Spacing (DAS) 54
3.2.3.2 Maximum Average β-needle Length 54
3.2.3.3 Presence of α-AlFeSi Phase 54
3.3 RESULTS AND DISCUSSION 55
3.3.1 Dendrite Arm Spacing 55
3.3.2 β and α Phase Characteristics 56
3.3.2.1 Experimental Alloys 56
3.3.2.2 Industrial Alloys 58
3.3.3 Microstructural Analysis 63
3.3.3.1 Effect of Si, Si+Sr Additions 63
3.3.3.1.1 Experimental Alloys 63
3.3.3.1.2 Industrial Alloys 72
3.3.3.2 Effect of Mn, Mn+Sr Addition 75
3.3.3.3 Effect of Be, Be+Sr Addition 78
3.3.4 Mechanism of α and β Phase Precipitation 82

CHAPTER 4

FORMABILITY **86**
4.1 INTRODUCTION 86
4.2 EXPERIMENTAL PROCEDURE 88
4.2.1 Alloy Preparation 88
4.2.2 Casting and Sample Preparation 88
4.2.3 Cold Working and Recrystallization Treatment 88
4.3 RESULTS AND DISCUSSION 89
4.3.1 Cold Rolling 89
4.3.2 Microstructural Analysis 97

CHAPTER 5

TENSILE PROPERTIES AND AGING RESPONSE **103**
5.1 INTRODUCTION 103
5.2 EXPERIMENTAL PROCEDURE 106
5.2.1 Alloy Preparation 106
5.2.2 Casting and Sample Preparation 107
5.2.3. Tensile Testing 108
5.2.4. Fractography 109
5.3 RESULTS AND DISCUSSION 110
5.3.1. Radiography 110
5.3.2 Microstructure 114
5.3.3 Tensile Properties 119
5.3.3.1 Effect of Strontium Addition and Aging Time 119
5.3.3.2 Effect of Trace Elements and Strontium Addition 124
5.3.3.3 Prestraining Prior to Aging 136
5.3.4 Fractography 140

CONCLUSIONS **155**

SUGGESTIONS FOR FURTHER WORK: **159**

REFERENCES **160**

ANNEX **169**

LIST OF FIGURES

CHAPTER 2

Figure 2.1. Partial equilibrium diagram for aluminum-copper alloys. 10

Figure 2.2. Principal aluminum alloys. 14

Figure 2.3. Transmission electron micrograph of: (a) α-AlFeSi phase and (b) β-AlFeSi phase 15

Figure 2.4. Microstructure of alloy 319 showing (a) α-phase, (b) β-phase. 16

Figure 2.5. Microstructure of an experimental 6XXX alloy showing (a) α-phase, (b) β-phase (present work). 16

Figure 2.6. Dependence of the percentage of β-phase *vs.* iron content 18

Figure 2.7. Dependence of the percentage of β-phase *vs.* silicon content 18

Figure 2.8. Simplified phase diagrams of the Al-Fe-Si system at constant manganese (Mn) levels of (a) 0% , (b) 0.1% , (c) 0.2% and (d) 0.3%. 23

Figure 2.9. Effect of manganese on tensile properties of wrought 99.95% aluminum. 25

Figure 2.10. Variation of average grain size in casting with titanium concentration and as a function of the parameter. 30

Figure 2.11. Variation of yield strength of A356 alloy with artificial aging time. Samples were solution treated at 540 °C and aged at 155 °C. 33

Figure 2.12. Schematic characterisation of the three stages of spheroidization and coarsening of the silicon phase. 34

Figure 2.13. Effect of strontium and homogenisation time on the surface roughness of 6061 alloys. 36

Figure 2.14. Aluminum-rich corner of Al-Fe-Si phase diagram 37

Figure 2.15. Peritectic reaction mechanism 39

Figure 2.16. Silicon-rich layer surrounding α-AlFeSi phase in the presence of strontium. 39

Figure 2.17. Microstructure of as-cast commercial 6061 extrusion alloy: (a) 300 ppm strontium, (b) no strontium 39

Figure 2.18. Effects of superheating temperature and iron content on crystallized structure of iron compounds in: (a) Al-6% Si-Fe, (b)Al-11% Si-Fe alloys 40

Figure 2.19. Effect of magnesium content on crystallized structure of iron compounds in Al-6% Si-Mg-0.4% Fe alloy castings. 41

Figure 2.20. Aging response of 6111 alloy at 177 °C after different degrees of prestrain 46

CHAPTER 3

Figure 3.1. Schematic diagram showing cross-sections of gauge sample, and graphite and metallic molds used in the present study. Specimens for microstructural observation were cut and polished along the A-A plane as shown..... 55

Figure 3.2. Effect of cooling rate (different casting molds) on the dendrite arm spacing. 55

Figure 3.3. Effect of Si, Fe concentration on: a) the average maximum β-needle length, b) the percentage of α-script phase present in unmodified and Sr-modified A, B, C and D alloys. 55

Figure 3.4. Effect of cooling rate and solution heat treatment (8h at 520 °C) on: a) the average maximum β-needle length, b) the percentage of α-script phase present in unmodified and Sr-modified B alloys. 60

Figure 3.5. Effect of cooling rate and solution heat treatment (8h at 520 °C) on: a) the average maximum β-needle length, b) the percentage of α-script phase present in unmodified and Sr-modified A alloys.....61

Figure 3.6. Effect of cooling rate and solution heat treatment (8h at 520 °C) on: a) the average maximum β-needle length, b) the percentage of α-script phase present in unmodified and Sr-modified D alloys.....62

Figure 3.7. Microstructures observed in A alloy samples obtained from graphite and metallic molds: a) unmodified alloy A, graphite mold; b) Sr-modified alloy A1, graphite mold; c) unmodified alloy A, metallic mold; d) Sr-modified alloy A2, metallic mold. 64

Figure 3.8. Effect of Sr-modification combined with solution heat treatment (SHT-8h at 520 °C) on A alloy samples: a) A-SHT, b) A2-SHT, c) A4-SHT, d) M-A4 65

Figure 3.9. Fragmentation of β-phase needles in: a) unmodified and b)-d) Sr-modified B alloy samples obtained from the graphite mold: a)E-B; b), c) and d) E-B2 66

Figure 3.10. Backscattered image obtained from B alloy showing the formation of α-Al_8Mg_3FeSi.....68

Figure 3.11. EDX spectrum showing Al, Mg, Fe and Si reflections corresponding to the α-Al_8Mg_3FeSi phase shown in Figure 3.10.....69

Figure 3.12. Backscattered image obtained from B alloy showing the platelet-like morphology of the β-AlFeSi phase. 69

Figure 3.13. EDX spectrum showing Al, Si & Fe reflections from β-needles shown in Figure 3.12. 69

Figure 3.14. Effect of Sr-modification and solution heat treatment on β-needles in B alloy samples: a) non-modified, b) 163 ppm Sr-modified, c) solution-treated alloy (8h at 520 °C), d) solution treated and 163 ppm Sr-modified alloy 70

Figure 3.15. Microstructure observed in B alloy samples obtained from test bar gauge section and graphite mold samples: a) G-B, b) G-B1, c) E-C, d) E-C2 71

Figure 3.16. Microstructure observed in industrial alloy samples obtained from graphite and metallic molds. a) E-D, b) E-D2, c) M-D, d) M-D2 73

Figure 3.17. Microstructure showing effect of Si*/Fe ratio and Sr-modification in industrial alloys solutionized 8h at 520 °C a) D-SHT, b) D2-SHT, c) 6I-SHT, d) 6IS-SHT. 74

Figure 3.18. Effect of Mn and Mn+Sr addition on iron intermetallics precipitation in graphite (E) and metallic (M) mold samples: a) E-M6, b)E-M6S, c) M-M6, d) M-M6S 76

Figure 3.19. Effect of Mn and Mn+Sr on iron intermetallic precipitations in solution heat treated (SHT) samples of: a) M6-SHT, b) M6S-SHT, c) M6S-SHT alloys 77

Figure 3.20. Effect of Be addition on the size and distribution of α-phase in: a) E-1B6, b) E-2B6, c) E-5B6, d) E-1B6 alloys 79

Figure 3.21. Effect of Be and Be+Sr addition on the size and distribution of α-phase in:. a) E-B6, b) E-B6, c) E-B6S alloys 80

Figure 3.22. Effect of Be and Be+Sr additions on the size and distribution of α-phase in: a) M-B6, b) B6-SHT, c) B6-SHT, c) B6S-SHT alloys 81

Figure 3.23. Schematic representation of iron intermetallic formation during solidification process. 84

Figure 3.24. Aluminum-rich corner of Al-Fe-Si phase diagram showing effect of Sr and cooling rate in expanding the α-phase region 85

CHAPTER 4

Figure 4.1. Effect of cold rolling on Brinell hardness (BHN) in non-modified alloys: (a) after homogenization for 10h at 520 °C, (b) after recrystallization for 8h at 520 °C, (c) total deformation. 91

Figure 4.2. Effect of cold rolling on Brinell hardness (BHN) in Sr-modified alloys: (a) after homogenization for 10h at 520 °C, (b) after recrystallization for 8h at 520 °C, (c) total deformation 94

Figure 4.3. Microstructures showing the effect of cold working on S6 alloys: a) homogenized, b) cold rolled after homogenizing, c), and d), cold rolled after annealing 99

Figure 4.4. Microstructures showing the effect of cold working on M6 alloys: a)homogenized, and b) cold rolled after annealing 100

Figure 4.5. Effect of cold working on 2B6S alloy samples: a) after homogenization, b) cold rolled after homogenization, c) cold rolled after annealing. 101

Figure 4.6. Effect of cold working on 6I alloys-Non-modified alloys: a) homogenized, b) cold rolled after annealing; Sr-modified alloys: c) homogenized, d) cold rolled after homogenizing 102

CHAPTER 5

Figure 5.1. Diffusion coefficients for various elements in aluminum. 105

Figure 5.2. Schematic diagram of a Stahl mold casting 108

Figure 5.3. Showing temperature versus time for T6 (and T8) condition. 109

Figure 5.4. Radiographs of selected tensile test bars: (A) S6, (B) S6S, (C) M6, (D) M6S, (E) B6, (F) B6S, (G) 5B6, (H) 5B6S 112

Figure 5.5. Radiographs showing hot tear cracks on gates and test bars of selected alloys: (1) S6, (2) S6S, (3) M6, (4) M6S, (5) 5B6, (6) 5B6S 113

Figure 5.6. Equilibrium solubility of Mg and Si in solid aluminum when both Mg_2Si and Si are present 114

Figure 5.7. Effect of solution heat treatment (8h at 520 °C) and Sr-modification on the dissolution of Mg_2Si in: a) S6 as-cast, b) S6S as-cast, c) S6-SHT, c) S6S-SHT alloys 116

Figure 5.8. Effect of solution heat treatment (8h at 520 °C) and Sr-modification on the dissolution of Mg_2Si in: a) G-6 as-cast, b) G-6S as-cast, c) 6 SHT, c) 6S SHT alloys 118

Figure 5.9. Tensile properties of A alloy series solution heat treated at 520 °C for times up to 100h: a) YS, b) UTS, c) %EL 123

Figure 5.10. Effect of aging time on the tensile properties of non-modified and Sr-modified 6 alloys. 128

Figure 5.11. Effect of aging time on the tensile properties of non-modified and Sr-modified S6 alloys. 129

Figure 5.12. Effect of aging time on the tensile properties of non-modified and Sr-modified M6 alloys. 130

Figure 5.13. Effect of aging time on the tensile properties of non-modified and Sr-modified 2B6 alloys. 133

Figure 5.14. Effect of aging time on the tensile properties of non-modified and Sr-modified 5B6 alloys. 134

Figure 5.15. Effect of aging time on the tensile properties of non-modified and Sr-modified B6 alloys. 135

Figure 5.16. Tensile properties of 2B6S and 6IS alloys solution heat treated at 520 °C for times up to 24h. a) YS, b) UTS, c) %EL 139

Figure 5.17. Fractographs obtained from 2B6S alloy in the as-cast condition: (a) SE, at low magnification, (b) SE, at high magnification, (c) BSE image of (b) 144

Figure 5.18. Fractographs obtained from 2B6S alloy in the T6 condition: (a) SE, at low magnification, (b) SE, at high magnification, (c) BSE image of (b) 146

Figure 5.19. Fractographs obtained from 2B6S alloy in the prestrained/aged condition: (a) SE, at low magnification, (b) SE, at high magnification, (c) BSE image of (b) 148

Figure 5.20. Fractographs obtained from 6IS alloy in the as-cast condition: (a) SE, at low magnification, (b) SE, at high magnification, (c) BSE image of (b) 144

Figure 5.21. Fractographs obtained from 6IS alloy in the T6 condition: (a) SE, at low magnification, (b) SE, at high magnification, (c) BSE image of (b), (d) a high magnification micrograph of (c) showing the size a distribution of the precipitated particles..... 152

Figure 5.22. Fractographs obtained from 6IS alloy in the prestrained/aged condition:. (a) SE, at low magnification, (b) SE, at high magnification, (c) BSE image of (b) 154

LIST OF TABLES

CHAPTER 2

Table 2.1. Data pertaining to metals. 26

CHAPTER 3

Table 3.1. Chemical compositions of alloys used in the present study (wt%) 51

CHAPTER 5

Table 5.1. Summary of microstructural observations reported in Chapter 3 105

Table 5.2. Radiographic analysis of selected alloy test bars. 111

Table 5.3. Summary of microstructural observations on Mg_2Si dissolution and intermetallics obtained in alloy S6 with solution heat treatment.. 115

Table 5.4. Tensile properties of 6063 industrial alloys. 120

Table 5.5. Effect of strontium and trace elements on tensile properties in the as-cast condition. 124

ANNEX

Table A.1. Quantitative metallographic measurements of iron intermetallics 170

Table A.2. Tensile test data for experimental alloys. 171

CHAPTER 1

DEFINITION OF THE PROBLEM

1.1 INTRODUCTION

The word "wrought" indicates that certain aluminum alloys are available primarily in the form of worked products such as sheet, foil, plate, and extruded rods, bars and wires. Working operations and heat treatments transform the cast ingot structure into a rod structure that may range from fully recrystallized to fibrous, depending upon the alloy and product. The structure influences strength, corrosion resistance, and other properties [1].

Wrought aluminum alloys are classified into two main categories: non-heat treatable and heat-treatable alloys. Non-heat treatable alloys include alloys that are strengthened by solid solution hardening, such as the 1XXX, 3XXX, and 5XXX series alloys. Heat-treatable alloys contain elements that are soluble in aluminum to a significant extent at elevated temperatures (*e.g.*, Si, Mg, and Cu), such as 2XXX and 6XXX series alloys. Artificial aging of these alloys following quenching from elevated temperatures leads to precipitation of fine particles of Mg_2Si and $CuAl_2$, which render the alloy its strength.

One of the major problems associated with the production of aluminum alloys is the presence of iron-based intermetallics, which contribute to the alloy brittleness and, hence, premature failure. The two main iron intermetallics are (i) β-AlFeSi, which occurs in the

form of platelets and causes surface pick-up problems, and (ii) α-Al_8Fe_2Si, which occurs in the form of Chinese script. The occurrence of these phases depends primarily on the Fe/Si ratio in the base alloy, the presence of neutralizers such as Mn and Cr, and the cooling rate. It should be mentioned here that the ß-phase is heat-treatable (soluble in the aluminum matrix at high temperature), whereas the α-iron phase is non-heat treatable. Also, the volume fraction of the α-phase is relatively greater than that of the ß-phase.

In 1975, Morris and Miners [2] proposed the addition of small amounts of strontium to 6XXX alloys as a modifying agent, where the main role of strontium was to transform the ß-phase into the α-phase. While other studies have been carried out along the same lines in recent years, no accompanying mechanical properties have been reported, however, to emphasize the industrial importance of this transformation. Also, the role of other trace elements that are always present in commercial alloys has not been considered.

Thus, the present work was undertaken to investigate the formation of these intermetallics, taking into consideration all of the above factors. The microstructural studies reported in this thesis have been substantiated by extensive tensile testing to arrive at concrete conclusions and possible recommendations.

1.2 OBJECTIVES OF THE PRESENT STUDY

In the present work, the 6XXX alloy series was chosen for study due to its ability to form into complex shapes. Also, due to the good aging response, most current automotive builders use 6XXX series alloy for the outer skin sheet. The aim of the present work is to understand the relation between microstructure and mechanical properties. The main goals of the present study are:

1. Understanding the mechanism of intermetallic formation, dissolution, and transformation in dilute alloys (in the absence of other microstructural constituents such as eutectic Si, $CuAl_2$, *etc.*)

2. Applicability of the addition of minor elements with respect to the formability of wrought alloys designed for cold and hot rolling, with the possibility of reducing alloy production costs.

3. The effect of these additions on the alloy aging response, in particular, in the presence of Sr in small amounts.

CHAPTER 2

LITERATURE REVIEW

2.1 INTRODUCTION

The unique combinations of properties provided by aluminum and its alloys, make aluminum one of the most versatile, economical and attractive metallic materials for a broad range of uses from soft, highly ductile wrapping foil to the most demanding engineering applications. As is well known, the properties of an aluminum alloy are greatly influenced by its internal structure such as the grain size and type, and the presence of various intermetallic phases and their shape, size and distribution. The composition of aluminum alloys is based on the solubility of the alloying elements in aluminum. These elements can be categorised as principal alloying components, additional alloying components, and impurities.

Aluminum alloys are divided into two major categories: aluminum casting alloys and aluminum wrought alloys. Aluminum casting alloys are the most versatile of all common foundry alloys and generally have the highest castability ratings. Aluminum casting alloys have the following favorable characteristics: excellent castability, low melting temperature,

low gas solubility, high strength to weight ratio, good machinability and high thermal and electrical conductivity. Casting alloys are described by the following designation system (the major alloying elements being indicated in parentheses): 1XX.X (pure aluminum), 2XX.X (copper), 3XX.X (silicon, copper, magnesium), 4XX.X (silicon), 5XX.X (magnesium), 7XX.X (zinc), and 8XX.X (tin). Aluminum wrought alloys are those that have been subjected to plastic deformation by a hot or cold working process (such as rolling, extruding, drawing), to transform the cast aluminum ingot into the desired product form. Wrought alloys are commonly grouped into alloy series designated as: 1XXX (pure aluminum), 2XXX (copper), 3XXX (manganese), 4XXX (silicon), 5XXX (magnesium), 6XXX (magnesium and silicon), 7XXX (zinc), and 8XXX (other elements).

A further differentiation for each category is based on the primary mechanism of property development, *i.e.*, heat treatable and non-heat treatable alloys. The initial strength of heat-treatable alloys is enhanced by the addition of alloying elements such as copper, magnesium, zinc, lithium, and silicon. As these elements show increasing solid solubility in aluminum with increasing temperature, it is possible to subject these alloys to thermal treatments that impart pronounced strengthening. The initial strength of non-heat-treatable alloys depends on the hardening effect of elements such as manganese, silicon, iron and magnesium. Because these alloys are work hardenable, further strength is made possible by various degrees of cold working [3].

Iron is the most deleterious impurity element in aluminum alloys because it forms large needles of an iron-aluminum-silicon intermetallic that cause inferior mechanical

properties. By the use of neutralization methods, it is possible to reduce the harmful effects of this iron intermetallic.

2.2 ALUMINUM ALLOY SERIES DESIGNATION SYSTEM

Aluminum alloys are commonly grouped into alloy series. A three-digit designation system is used for casting alloys and a four-digit designation system for wrought alloys. The first digit indicates the alloying group [4].

Aluminum casting alloy series designations:

1xx.x Series. Controlled unalloyed compositions (pure aluminum).

2xx.x Series. Aluminum alloys containing copper as the major alloying element.

3xx.x Series. Aluminum-silicon alloys also containing magnesium and/or copper.

4xx.x Series. Binary aluminum-silicon alloys.

5xx.x Series. Aluminum alloys containing magnesium as the major element.

7xx.x Series. Aluminum alloys containing zinc as the major element.

8xx.x Series. Aluminum alloys containing tin as the major element.

Aluminum wrought alloy series designations:

1XXX Series. Aluminum of 99.00% or higher purity. This group of aluminum alloys are characterized by their excellent corrosion resistance, high thermal and electrical conductivites, low mechanical properties and excellent workability. These alloys are non-heat-treatable.

2XXX Series. Copper is the principal alloying element in this group, often with magnesium as a secondary addition. These alloys require solution heat treatment to obtain optimum properties.

3XXX Series. Manganese is the major alloying element in this group. These alloys are generally non-heat treatable.

4XXX Series. The major alloying element of this group is silicon. Most alloys in this group are non-heat treatable.

5XXX Series. The major alloying element in this group is magnesium. These alloys are non-heat-treatable and possess a wide range of strength, good formability, welding characteristics, and high resistance to general corrosion.

6XXX Series. Alloys in this group contain silicon and magnesium approximately in the proportions required for formation of magnesium silicide (Mg_2Si), thus making them heat treatable. These alloys have good formability, weldability, machinability and corrosion resistance, with medium strength.

7XXX Series. Zinc is the major alloying element in this group. These are heat-treatable alloys and are used for high-strength aircraft and medium-strength general-purpose components.

2.3 TEMPER DESIGNATION SYSTEM

The temper designation system is used for all forms of wrought and cast (heat treatable and non-heat treatable) aluminum alloys except ingots. The basic temper designations are as follows [4]:

F as fabricated. Applies to products of shaping processes in which no special control over thermal conditions or strain hardening is employed. For wrought products, there are no mechanical property limits.

0 annealed (wrought products only). Applies to wrought products, which are fully annealed to obtain the lowest strength condition.

H strain hardened (wrought products only). Applies to products which have their strength increased by strain hardening with or without thermal treatments to produce some reduction in strength. Two or more digits in non-heat treatable alloys always follow the H.

W solution heat treated. An unstable temper applicable only to alloys which spontaneously age at room temperature for a long period of time after solution heat.

T thermally treated to produce stable tempers other than F, 0, or H. Applies to products which are thermally treated with or without strain hardening, to produce stable tempers. In heat treatable alloys one or more digits always follow T:

T4 solution heat-treated and naturally aged to a substantially stable condition. Applies to products that are not cold worked after solution heat- treatment.

T6 solution heat-treated and then artificially aged. Applies to products which are not cold worked after solution heat-treatment.

2.4 STRENGTHENING MECHANISMS

The main objective in the design of aluminum alloys is to increase strength, hardness, and resistance to wear, creep or fatigue. Effects on these properties are specific to different combinations of alloying elements, thermomechanical history, heat treatment or cold working process [5].

2.4.1. Heat-Treatable Alloys

Solution-Heat Treating. The heat treatable aluminum alloys contain alloying elements that are more soluble at elevated temperatures than at room temperature. Thus, holding of these alloys at an elevated temperature (slightly below the eutectic temperature) allows the alloying elements to go back into solid solution. If the alloy is rapidly quenched thereafter, a supersaturated condition is obtained. The driving force for this increases with degree of supersaturation, decreasing temperature, increasing solute atom percentage and atomic mobility.

The strength of the alloy is developed as the alloying elements precipitate out of solution with the passage of time. This effect is referred to as precipitation or age hardening.

Precipitation Hardening (Age Hardening). The mechanism of strengthening by age hardening involves the formation of coherent clusters of solute atoms (that is, the solute atoms have collected into a cluster but still have the same crystal structure as the solvent

phase). This causes a great deal of strain because of mismatch in size between the solvent and solute atoms. The cluster stabilizes dislocations, because dislocations tend to reduce the strain, similar to the reduction in strain energy of a single solute atom by a dislocation. When dislocations are anchored or trapped by coherent solute clusters, the alloy is considerably strengthened and hardened. By precipitation hardening, alloys can reach the higher strengths of which they are capable.

Varying degrees of age hardening occur at room temperature, but artificial aging (or precipitation heat treatment at high temperature) is usually employed to develop maximum strengths as quickly as possible. Figure 2.1 shows the temperature range of solution heat treating for aluminum-copper alloys. Solution of the relatively large microconstituents present in casting alloys requires longer soaking times than wrought alloys.

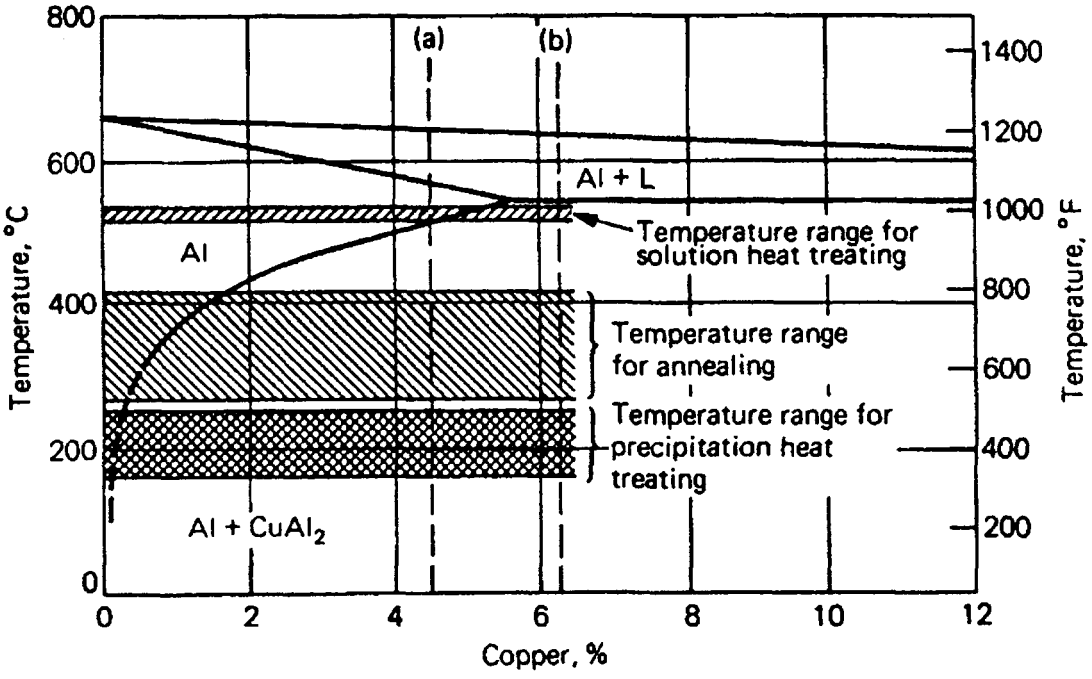

Figure 2.1. Partial equilibrium diagram for aluminum-copper alloys [1].

2.4.2. Non-Heat Treatable Alloys

Solid-Solution Hardening. Solid solution hardening of alloys is made by dissolving other metals in aluminum to form solid solutions. Some atoms of the alloying metals replace certain aluminum atoms in the matrix; this is called substitutional solid solution. Other atoms of alloying elements may occupy spaces between the base metal atoms in the matrix; this is called interstitial solid solution. In both cases, the metallurgical structure is usually distorted by the new atoms in the structure, thus increasing the strength. Strengthening tends to increase with increasing difference in the atom radii of the solvent (aluminum) and solute (alloying element) atoms. Strain hardening by cold rolling, drawing or stretching is a highly effective means of increasing the strength of non-heat treatable aluminum wrought alloys.

The rapid precipitation in cast alloys has been attributed to the presence of excess silicon in solid solution. Thus, at any given temperature, a greater degree of supersaturation is achieved in alloys containing excess silicon and, hence, a finer dispersion of precipitates is obtained. The precipitation behaviour in cast aluminum alloys is extremely complex and is influenced by several process parameters including alloy composition, natural aging time, and preaging and artificial aging conditions. Because of the presence of about 1.4% excess silicon in solid solution, precipitation of Mg_2Si occurs much faster in cast alloys than in wrought alloys [6].

2.5 THERMAL TREATMENT

2.5.1. Annealing

Aluminum and all of its alloys may be annealed to remove the hardening or strengthening effects of cold working or heat-treatment. Annealing is accomplished by heating the metal above its recrystallization temperature (345-425 °C), and maintaining the required level until recrystallization is complete. Figure 2.1 shows the annealing temperature range for aluminum-copper alloys.

2.5.2. Stabilizing

Certain non-heat treatable, work hardening alloys containing magnesium, such as 5052, have ductility but lose strength upon room temperature aging. Such age softening alloys often are stabilized by heating to 110-180 °C to accelerate the softening to its ultimate limit.

2.5.3. Homogenizing

Controlled heating and cooling of the as-cast metal can improve the workability of aluminum ingots. Heat treatable alloy ingots usually have large crystals of intermetallic components distributed in the as-cast structure. Fabrication qualities are improved when a more uniform distribution of these hardening components is achieved by heating the alloy ingot to near its solution heat treatment temperature, holding it at that level for several hours, then cooling at a controlled rate.

2.6 ALLOYING ELEMENTS

Alloying components present in aluminum alloys are categorised as principal alloying components, additional alloying components and impurities. Principal alloying components are usually added to increase the strength and other properties of the aluminum casting alloys. The principal alloying components for commercial aluminum alloys are zinc, magnesium, copper, manganese and silicon. Figure 2.2 shows the principal aluminum alloys based on these elements.

Additional alloying components such as Sr, Na, Sb, Ce, Nb, Be, Pb, Bi, Sn are added due to their useful effect in aluminum alloys. Transition metals such as manganese, chromium and zirconium are added for their ability to precipitate as fine intermetallic particles which do not dissolve during hot working or annealing.

All components that are not classified as alloying components are termed impurities, and they have a negative effect on the castability, mechanical properties and heat treatment of aluminum alloys.

The most important impurity in aluminum alloys is iron. In general, during the solidification process, the impurities and alloying components partly go into solid solution in the matrix and partly form intermetallic particles [1].

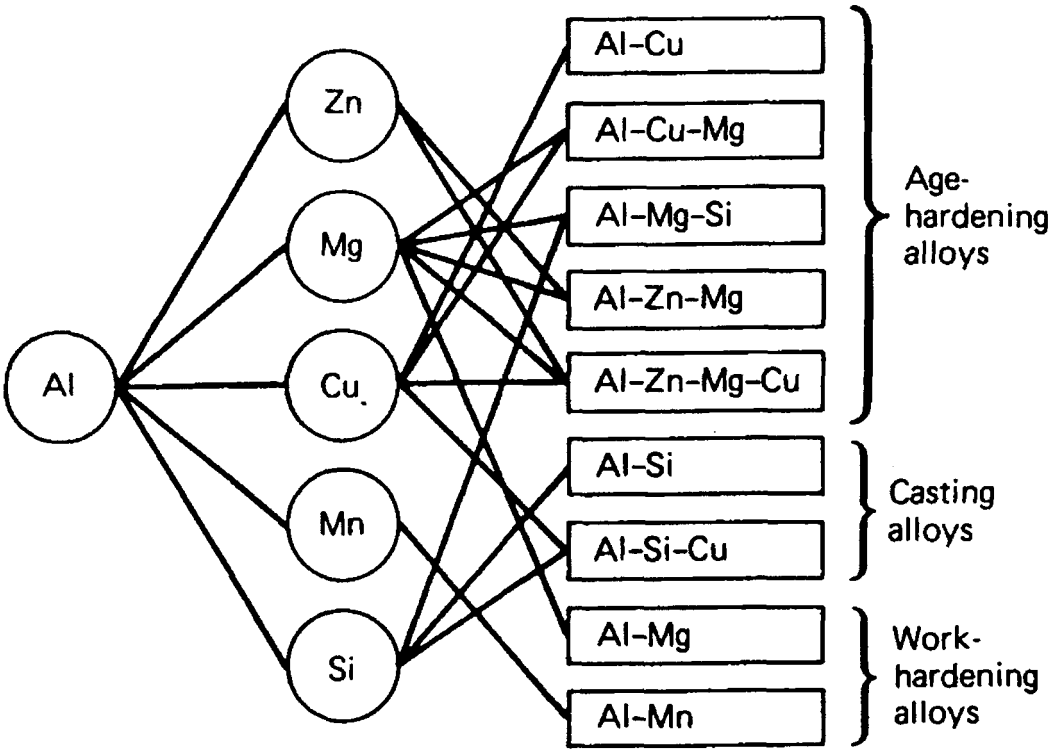

Figure 2.2. Principal aluminum alloys [4].

2.7 IRON INTERMETALLICS IN ALUMINUM ALLOYS

2.7.1. Chemical Composition

The most important iron intermetallic phases in aluminum alloys are the α-AlFeSi and β-AlFeSi phases. The α-AlFeSi phase has the composition Al_8Fe_2Si (32-36%Fe, 6-9.5%Si), while the composition of the β-AlFeSi phase is Al_5FeSi (27-28%Fe, 14-16%Si [7].

2.7.2. Morphology and Crystal Structure

The reported α-phase is hexagonal with parameters a=12.3Å, c=26.3Å, density 3.58g/cm^3, and appears in the form of Chinese script particles. The β-phase has monoclinic structure with parameters a=b=6.12 Å, c=41.5 Å, A=91°, density 3.30-3.35g/cm^3, and appears in the form of platelets. The α-phase and β-phase have different growth modes. Mulazimoglu *et al.* [8] studied the iron intermetallics in 6201 alloys by using high resolution transmission electron microscopy. The authors showed that the α-AlFeSi(Al_8Fe_2Si) particle, Figure 2.3(a), has a nonfaceted interface with the aluminum matrix, exhibits no growth twinning, allowing better bonding with the aluminum matrix. However, the β-AlFeSi particle, Figure 2.3(b), is very sharp, highly faceted, poorly bonded to the matrix and contains multiple (001) growth twins parallel to the growth direction.

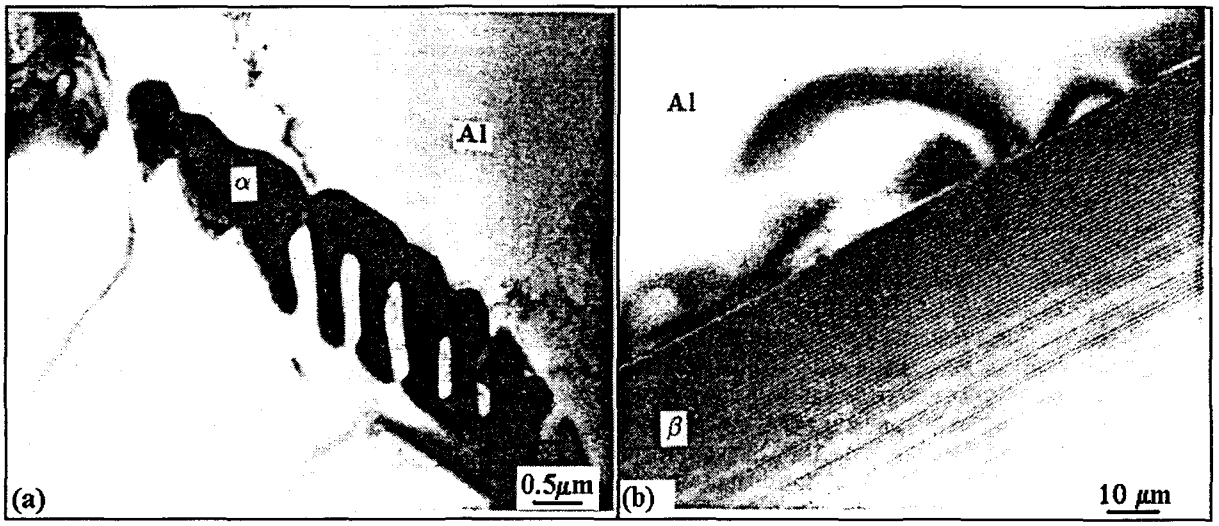

Figure 2.3. Transmission electron micrographs of: (a) α-AlFeSi phase and (b) β-AlFeSi phase [8].

Iron intermetallics present in casting alloys are bigger and longer than those observed in wrought alloys. Examples of the α-AlFeSi(Al_8Fe_2Si) and β-AlFeSi phases obtained in casting and wrought alloys are shown in Figure 2.4 and Figure 2.5, respectively.

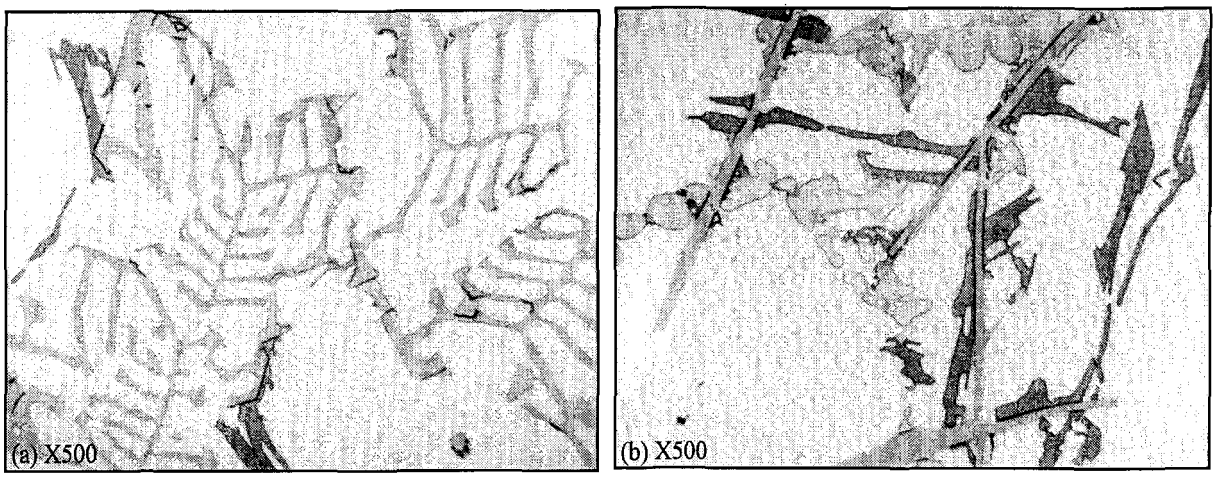

Figure 2.4. Microstructure of alloy 319 showing (a) α-phase, (b) β-phase [9].

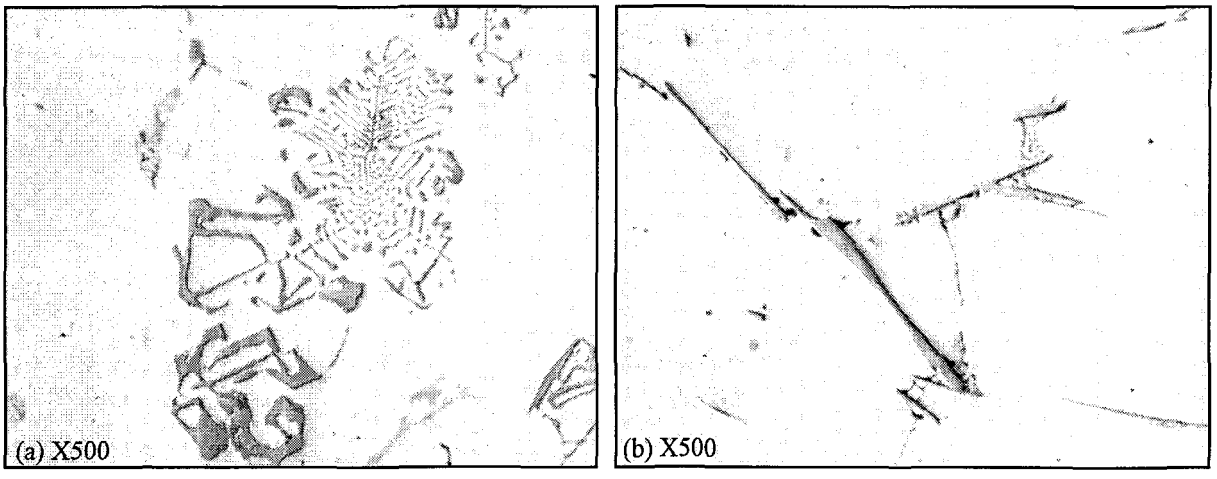

Figure 2.5. Microstructure of an experimental 6XXX alloy showing (a) α-phase, (b) β-phase (present work).

2.7.3. Effect of Iron and Silicon

Iron and silicon are the most common impurities found in aluminum alloys [10] because of their low solubility during solidification. Iron forms complex intermetallic compounds with aluminum, silicon, manganese and chromium. During the casting of aluminum alloys, a large number of intermetallic phases can precipitate, depending on the solidification conditions and alloy chemistry [11]. In alloys containing high levels of silicon the β-AlFeSi phase is the main iron intermetallic observed.

Casting alloys: The presence of iron, even in small amounts, decreases the alloy ductility considerably, due to precipitation of the β-AlFeSi phase in the form of intercepted platelets [12]. These platelets, which appear as needles in the microstructure, are very fragile and possess a relatively weak coherence with the aluminum matrix. Progressive increase in the iron concentration produces a corresponding increase in the platelet length, particularly for iron contents higher than 0.7%. The precipitation of these platelets occurs mostly in the liquid-solid zone *i.e.*, in a pre-eutectic reaction [9].

The observations made by Mascré [13] confirm that pre-eutectic β-phase platelets deteriorate the alloy mechanical properties. In contrast, the β-platelets that precipitate during co-eutectic and post-eutectic reactions may improve the mechanical properties of a given alloy. The presence of iron in quantities higher than 0.5% normally increases the alloy strength, but at the cost of a reduction in ductility [14,15]. Increasing the iron content from 0.5 to 1.2% in an Al-13 %Si casting alloy dramatically reduces the mechanical

properties, particularly the elongation because of β-phase platelet phase formation [16]. The β-phase platelets act as stress raisers, which contributes to the brittleness of the material.

Yaneva *et al.* [17] have studied the appearance of iron intermetallic phases in Al-Si cast alloys at different Fe and Mn concentrations. They show that for a given concentration of Mn, the percentage of the β-phase rapidly increases with increasing iron concentration, as shown in Figure 2.6. At 0.9 % Fe, nearly all iron-containing precipitates are plate-like causing a decrease in the alloy fatigue strength. Figure 2.7 shows how the β-phase decreases with lower Si-content in Al-Si alloys.

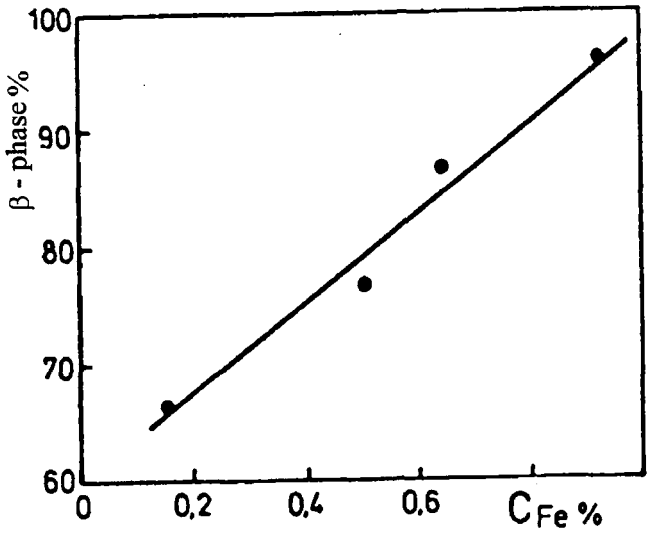

Figure 2.6. Dependence of the percentage of β-phase *vs.* iron content [17].

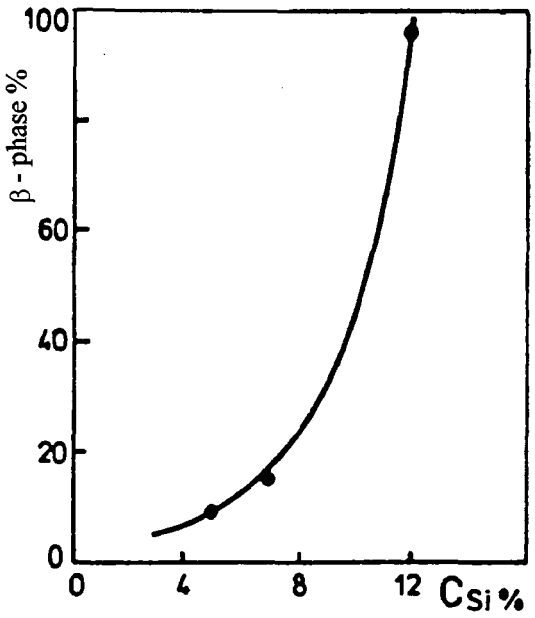

Figure 2.7. Dependence of the percentage of β-phase *vs.* silicon content [17].

Narayanan *et al.* [18,19] also studied the effect of iron in Al-6% Si-3.5% Cu-0.3% Mg alloys and found that increasing the iron content from 0.15 to 1% in permanent mold castings markedly reduced the alloy tensile properties. Similarly, Murali *et al.* [20] have also shown that iron deteriorates the alloy properties (Al-7% Si-0.3% Mg alloy) due to formation of β-AlFeSi phase, particularly at high iron contents and low cooling rates.

Villeneuve *et al.* [21] have also reported that increasing the iron content results in the precipitation of long, thick needles of the β-AlFeSi phase. They also observed that these needles are often branched into several needles, and large shrinkage cavities can be formed within the casting due to the inability of the liquid metal to feed into the spaces between these branches.

Wrought alloys: Most of the iron and silicon form coarse constituent particles during casting. The iron may produce various intermetallic compounds, while the silicon is present mainly as Mg_2Si. Flood *et al.* [22] studied the effect of iron and silicon on AA5182 alloy. This results show that in 5182 type alloys, a low Fe:Si ratio favours the formation of α-AlFeMnSi. Increasing the iron and silicon levels cause a deterioration in the mechanical properties, due to the increased number of intermetallic particles formed. Decreasing the Fe:Si ratio causes cubic α-AlFeMnSi to be produced in the cast state instead of $Al_{13}(Fe,Mn)_4$. The volume fraction of Mg_2Si is proportional to the silicon content of the alloy. Marshall *et al.* [23] investigated the effect of iron and silicon on the microstructure and

properties of 5182 alloys and showed that the iron intermetallic particle size increases with addition of iron and silicon.

It has been reported [24] that addition of 0.1% silicon to a base Al-0.5% Fe alloy increase the stability of the $Al_{13}Fe_2$ phase. It has also been found that, by increasing iron in 6XXX alloys, the yield strength increases while the elongation decreases [25]. According to Chen [26], in low-silicon 1XXX alloys, the common intermetallic phases are Al_3Fe, Al_mFe, and Al_6Fe; with increased silicon content the α-AlFeSi phase becomes one of the major phases in the ingot structure. An increase in the Fe:Si ratio from 2 to 4 has the effect of eliminating the cubic α phase in favour of Al_6Fe outside the Fir Tree Zone, FTZ [27]. The observations made by Mulazimoglu *et al.* [28] also confirm that in 1XXX alloys, by increasing the Fe/Si ratio (Fe+Si=0.75%), the microstructure will contain only the α-AlFeSi phase.

2.8 MODIFICATION OF IRON INTERMETALLICS

The α-AlFeSi phase is considered less detrimental to the mechanical properties compared to the β-AlFeSi phase [16]. In order to reduce the harmful effects of iron intermetallics in Al-Si alloys, various methods have been developed. These are:

- Rapid solidification
- Addition of neutralizing elements
- Grain refining
- Strontium addition
- Melt superheating
- Non-equilibrium heat treatment

2.8.1. Rapid Solidification

The rapid solidification method consists of solidifying the melt at a very high cooling rate which affects almost all the microstructural parameters. With rapid solidification, iron is retained in solid solution [19]. Iglessis *et al.* [29] found that the conversion from β-AlFeSi to α-AlFeSi phase is possible only at low levels of iron and silicon, and at low cooling rates.

Awano and Shimizu [30] showed that the α-AlFeSi Chinese script phase is independent of the cooling rate, but increasing the cooling rate decreases the volume fraction of the β-AlFeSi intermetallic phase. At high cooling rates, the intermetallic particles are quite small and interspersed more uniformly. However the rapid solidification method is not practically feasible because it is impossible to achieve uniform solidification rates when complicated shapes with different section thicknesses are involved.

2.8.2. Addition of Neutralizing Elements

Manganese, chromium and beryllium are the elements commonly added as "neutralizers" to reduce the precipitation of the β-AlFeSi phase and promote formation of the α-AlFeSi phase, instead.

2.8.2.1. Manganese

Cast alloys: Manganese is the common alloying element that is used to neutralize the effect of iron and modify the morphology and type of intermetallic components [31]. It is also found that manganese is considered more effective when compared to Cr, Ni, Co and Mo. Iglessis *et al.* [29] showed the effectiveness of manganese addition in contributing to the precipitation of iron intermetallics in the form of the α-Chinese script $Al_{15}(Fe,Mn)_3Si_2$ phase or sludge particles in the presence of Cr.

The simplified phase diagrams of the Al-Si-Fe system at constant manganese levels are shown in Figure 2.8, where it can be seen that increasing the manganese content expands the α-AlFeMnSi phase region. As a result, the crystallization of α-AlFeMnSi phase is possible even at high levels of iron. The morphology and chemical composition of this phase is very similar to the α-AlFeSi phase obtained in alloys without manganese, except for some solution of manganese observed in the former case. This phase can dissolve a fairly good amount of copper, chromium, nickel, *etc.*, if these are present as alloying elements. The latter replace part of the iron and, thus, the overall chemical composition of the phase remains almost the same [9].

According to the ASTM specifications, if the iron content exeeds 0.45%, the manganese content should not be less than half of the iron. Manganese in an Mn:Fe ratio of 1:2 breaks down the long needles of the β-AlFeSi phase and thus helps improve both the mechanical properties and castability. Komiyama *et al.* [32] showed that the manganese content has a strong effect on the alloy tensile strength only at iron contents higher than one percent. However, when the Mn:Fe ratio exceeds a certain limit, then Mg addition has a harmful effect. Narayanan *et al.* [33] found that at low cooling rates, the morphology of the iron intermetallics changed to script type with Mn addition, whereas at high cooling rates, both α and β phases crystallized.

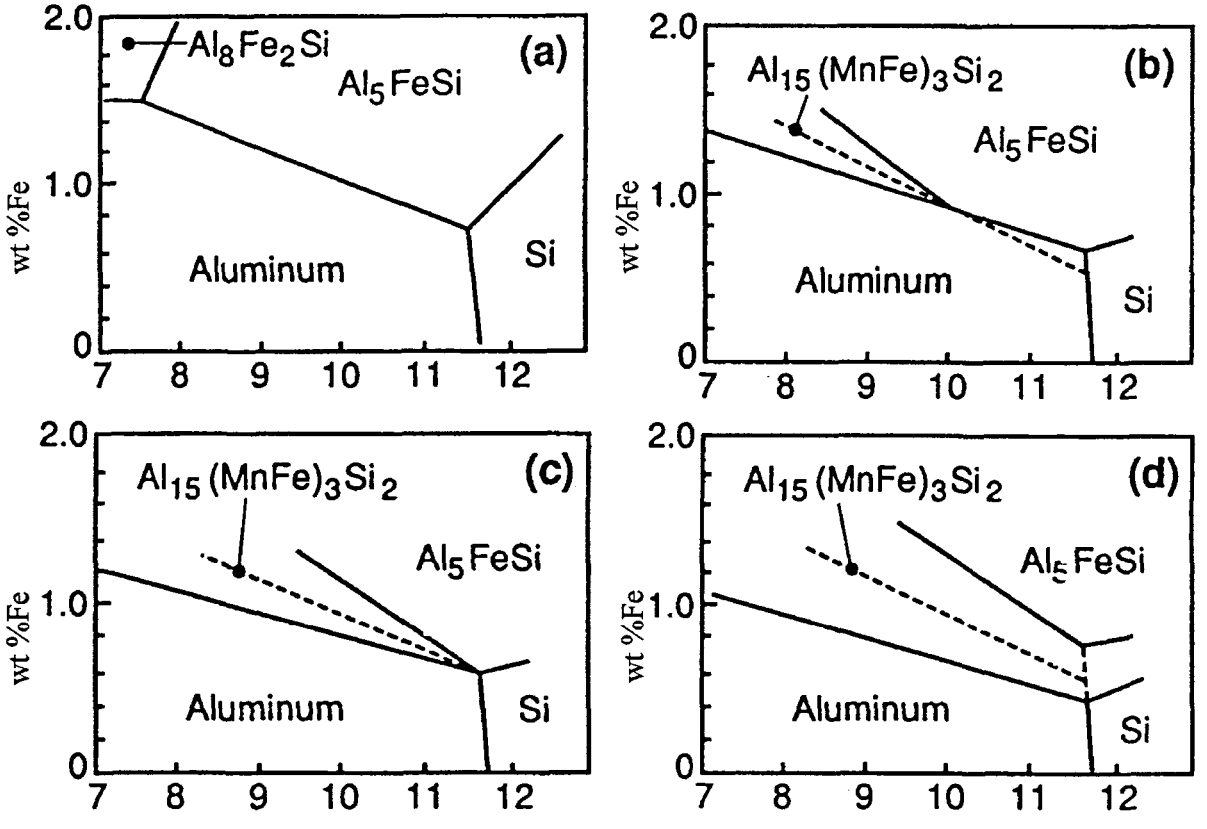

Figure 2.8. Simplified phase diagrams of the Al-Fe-Si system at constant manganese (Mn) levels of (a) 0%, (b) 0.1%, (c) 0.2%, and (d) 0.3% [9].

Wrought alloys: Manganese is a common element addition to 6XXX alloys. As in the case of casting alloys, manganese is added to accelerate the precipitation of α-AlFeMnSi phase. Manganese ensures both a quick and consistently high level of β-AlFeSi to α-AlFeMnSi transformation. In these alloys, silicon is added in excess of the level required to form Mg_2Si, as this leads to the best strength/extrudability combination according to Musulin and Celliers [34]. These authors also found that with manganese levels close to 0.5%, the alloy is significantly more quench sensitive. It has been reported that addition of a small amount of manganese accelerated the precipitation of small and more rounded particles of α-AlFeMnSi phase instead of the platelet β-AlFeSi phase during homogenisation of 6063 alloy [35].

Addition of up to 0.75% manganese to aluminum-magnesium alloys increases their hardness, decreases their ductility, increases their strength in the work-hardened condition and resistance to corrosion, and improves their welding characteristics. Increased amounts of either magnesium or manganese, however, intensify the difficulty of fabrication and increase the tendency toward cracking during hot rolling. The two main advantages of manganese additions are that the precipitation of the magnesium phase is more general throughout the structure, and that for a given increase in strength, Figure 2.9, manganese allows for a lower magnesium content and ensures a greater degree of stability to the alloy [4].

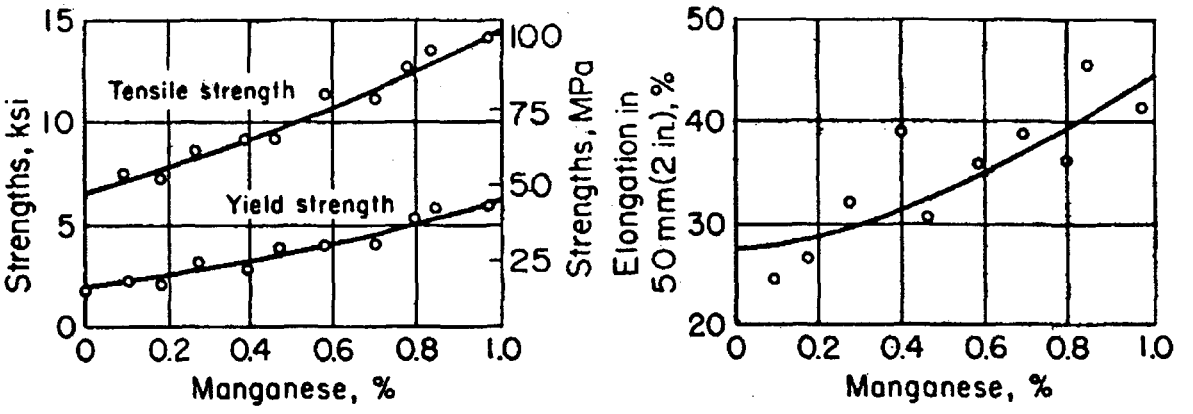

Figure 2.9. Effect of manganese on tensile properties of wrought 99.95% aluminum [4].

2.8.2.2. Other Trace Elements

The morphology of the β-AlFeSi phase in aluminum casting alloys is also affected by the addition of other trace elements such as Cr, Mo, Co, Be and Ca. These are discussed briefly below.

Chromium behaves in the same way as manganese. It can modify the morphology and type of intermetallic phases in cast aluminum alloys. Gustafsson *et al.* [31] observed that chromium addition to Al-7% Si-0.3% Mg alloy containing 0.52% Fe altered the morphology of the β-AlFeSi phase into Chinese script. Granger [36] has reported similar observations. The complex intermetallic that is formed with aluminum, silicon, iron, manganese and chromium is called "sludge". Sludge particles have a high melting point and high specific gravity. To avoid sludge formation, an experimental formula called "sludge factor" is suggested as a guide for these alloys [36,37].

$$\text{Sludge Factor (S F)} = \%Fe + 2(\%Mn) + 3(\%Cr)$$

With the casting temperature for die casting alloys around 650 °C, a sludge factor of 1.8 is considered normal.

Beryllium, due to its unique physicochemical characteristics, is used in aluminum casting alloys to reduce oxidation of the molten metal. This allows for an increase in the magnesium content and hence acceleration of the hardening process when the alloy is heat treated in the T6 condition. Table 2.1 shows the physical properties of Be, Mg and Al. Note that beryllium has the smallest atomic diameter, the highest melting point, and a high boiling point. The diffusion of the small beryllium ions into the oxide film causes a contraction of the oxide which establishes a denser, more protective film on the melt surface that prevents attack from O_2 and N_2 present in the atmosphere[38].

Table 2.1. Data pertaining to metals [38].

Metal	Atomic Wt.	Atomic Dia. KX Units	Density g/cc	Atomic Volume cm^3/g atom	Melting Point	Boiling Point
Be	9.01	2.26	1.85	4.9	1284C (2343F)	2400C (4352F)
Mg	24.3	3.20	1.74	14.0	650C (1202F)	1202C (2196F)
Al	27.0	2.86	2.70	10.0	660C (1220F)	2450C (2442F)

Addition of beryllium causes the precipitation of the iron intermetallic compound "$Al_5BeFeSi$" to occur in a smaller, more globular form rather than in the form of large, brittle platelets of Al_5FeSi. The small, globular forms of the beryllium-containing compound eliminate the embrittling and weakening effect of the platelets. Beryllium additions also inhibit the oxidation of the magnesium-alloying constituent and maintain a cleaner alloy. It is generally recognized by aluminum mills that a 0.005% beryllium content in wrought alloys make aluminum alloy mill shapes work more easily with improved surface quality and consistently high mechanical properties. Welding is also improved by the small beryllium addition. In addition, beryllium improves the fluidity and castability, especially in the case of automotive casting alloys [39].

Beryllium has a marked effect on the strength and the mechanical properties of 356 variant-T6 aluminum alloys. Both in sand castings and in chilled castings, at any aging temperature or time used experimentally, ultimate strength and yield strength increased. Elongation was not affected by beryllium additions. Part of the alloy strength, as tested in bending, was increased by the increase in beryllium content [39]. The beryllium addition also modifies β-AlFeSi phase into Chinese script but the amount of beryllium used is smaller than other trace elements [38].

Murali *et al.* [40,41] showed that addition of small amounts of beryllium to Al-7% Si-0.3% Mg-0.6% Fe alloy results in the formation of a new Be-Fe phase (Al_8Fe_2SiBe) with Chinese script morphology and polygon shapes grows along with the primary α-Al dendrites. This nucleation mechanism is quite different from that of the β-AlFeSi phase in

unmodified alloy and leads to superior mechanical properties. The presence of Be also results in some grain refinement. Compared to other neutralizing elements beryllium is used in very low concentrations due to its toxicity.

Magnesium is used to improve the alloy mechanical properties through the precipitation of Mg_2Si. Samuel *et al.*[42] have shown that addition of 0.35% Mg to commercial 319 aluminum alloy changes the β-Al_5FeSi phase to $Al_5Mg_3FeSi_6$ phase. Increasing the magnesium content increases the volume fraction of this phase. Magnesium up to 0.5% contributes to both strength parameters and to alloy ductility [43]. Increasing the magnesium content beyond this limit has a negligible effect on the mechanical properties of the 319 aluminum alloy, either in the as-cast or in the T5 condition [44].

Sukumaran *et al.* [45] reported that in the as-cast condition the ultimate tensile strength, proof strength, elongation to fracture and hardness decreased with the increase in magnesium content in Al-7% Si-0.3% Mg alloy. The microstructure revealed an increase in the porosity levels with the increase in magnesium content and precipitation of Mg_2Si and Mg_5Al_8 phases in 1.8 and 2.6% magnesium-containing alloys. Solution treatment substantially improved the alloy tensile parameters as well as hardness, while the microstructure showed spheroidization of Si and Mg_2Si.

In Al-7% Si and Al-13% Si synthetic alloys, a low concentration of magnesium changes the silicon phase morphology. At high levels (~1%), however, magnesium only slightly refines the silicon phase. The magnesium in Al-13% Si eutectic alloy modifies the eutectic silicon morphology from sharp-acicular flakes to rough faceted lamellae.

Furthermore, magnesium has a negative effect on strontium modification. This effect is most likely due to the formation of a complex $Mg_2SrAl_4Si_3$ intermetallic compound, which probably is formed prior to the eutectic reaction [46].

2.8.3. Grain Refining

It is well known that the properties of a cast component are greatly influenced by its internal structure such as grain size and precipitate structure morphology. Depending on the constitutional and heat flow conditions in a solidifying aluminum alloy, two different grain morphologies are possible, namely, equiaxed and columnar. The formation of a fine equiaxed grain structure is always desired due to its inherent uniform mechanical properties, reduced ingot cracking, improved feeding, enhanced fluidity and fabricability, improved machinability, and better surface finishing [47].

Aluminum alloys are grain refined with titanium or Al-Ti-B master alloys to control the casting grain structure. The grain refiner provides nucleating sites for the formation of primary aluminum dendrites and facilitates the production of a casting with a large number of small uniform and equiaxed grains. Typical grain size data for 319 alloy castings are plotted in Figure 2.10 as a function of titanium concentration. It can be seen that a minimum titanium content of 0.15 to 0.2% is necessary to obtain substantial grain refinement [48].

Kearns and Cooper [49] studied the effects of solutes on the grain refinement of wrought aluminum alloys. Their results show that silicon is the best, followed by

chromium, iron, magnesium, zinc and copper, while manganese and zirconium encourage grain coarsening. Boone *et al.* [50], using aluminum master alloys containing aluminum-titanium-boron (Al-Ti-B) and aluminum-strontium (Al-Sr), reported that grain refinement improves the mass feeding characteristics during casting and solidification. Also, a fine grain size creates a smaller and more uniform distribution of secondary intermetallic phases and pores that form due to the evolution of dissolved gas in the melt.

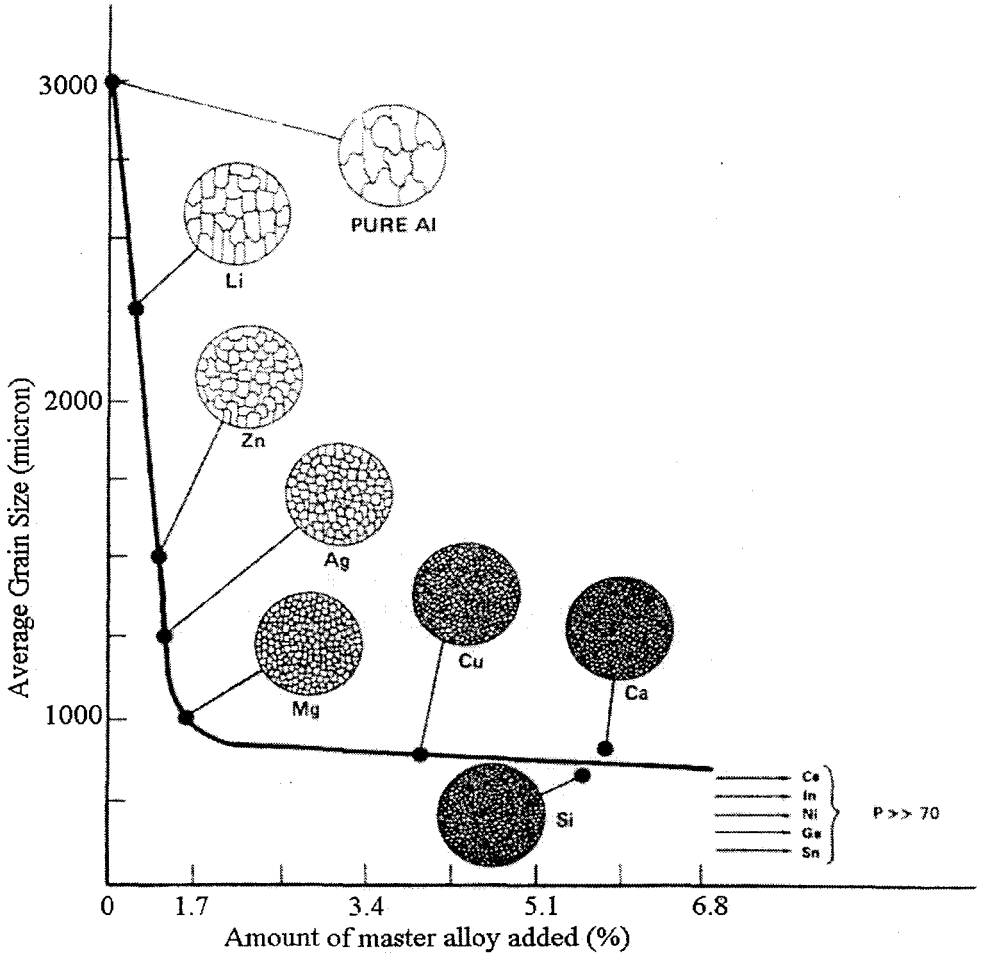

Figure 2.10. Variation of average grain size in casting with titanium concentration and as a function of the parameter [48].

Fisher and Campbell [51] found that by repeated recycling, all grain refiners lose some effectiveness, and borides are more efficient nuclei than carbides. Meredith *et al.* [52] studied the effect of Al-Ti-B grain refining on intermetallics in dilute aluminum alloys, and found that the addition of a grain refiner to a dilute Al-Fe alloy slightly increased the presence of $Al_{13}Fe_4$ with respect to Al_6Fe, where the classic rod-like appearance of Al_6Fe was replaced by curved, plate-like intermetallics. The grain refiner addition also increased the temperature interval between the dendrite and eutectic growth fronts in binary alloys.

The influence of cooling rate and grain refining on particle size in as-cast 3004 alloy have been studied by Anyalebechi *et al.* [53]. They showed that at cooling rates of less than 1 °C/s, the average particle size in a non-grain-refined casting is significantly larger than that in a grain-refined casting. Particle size distribution becomes bimodal at cooling rates above 1 °C/s and 14.7 °C/s in the nongrain-refined and grain-refined castings, respectively. Particle size in both castings increases linearly with an increase in the dendrite arm spacing, which is controlled primarily by growth conditions during solidification of the melt.

2.8.4. Strontium Modification

Strontium, a surface-active element, is widely applied in aluminum-silicon casting alloys. It is commonly employed to modify the shape of the eutectic silicon and is also found to refine the detrimental intermetallic compounds.

Casting alloys: Strontium increases the spheroidization rate and lowers the coarsening rate of eutectic silicon particles [54]. Samuel *et al.* [12] have studied the effect of strontium on the formation of β-phase in 319 type alloys. According to them, the addition of 300 ppm strontium accelerates the fragmentation and dissolution of the β-AlFeSi phases and formation of the blocky Al_2Cu intermetallic phase during solidification. Also in Sr-modified alloys, fragmentation of the β-AlFeSi phase is associated with an increase in yield strength.

Paray and Gruzleski [55] studied strontium modification of 356 permanent mold castings. The yield strength was not affected by modification in the as-cast and T4 conditions, while it decreased in the T6 condition. The shorter the solution heat-treatment, the higher the difference existing between the unmodified and modified alloys, Figure 2.11.

The observed effects of strontium on heat treatment may be attributed to two reasons [56]; a) it is possible that strontium retards precipitation of Mg_2Si during the aging process, b) in the case when less magnesium and silicon are present in solid solution, strontium may stabilize the Mg_2Si phase which forms during solidification, making it more difficult to dissolve. The microhardness is consistently lower in the strontium-containing alloys. By increasing the holding time, dissolution will be complete and the microhardness

become similar [57]. It is also found that in 413 alloy addition of strontium leads to fragmentation of the β-Al_5FeSi platelets and an increase in the amount of α-AlFeSi [56].

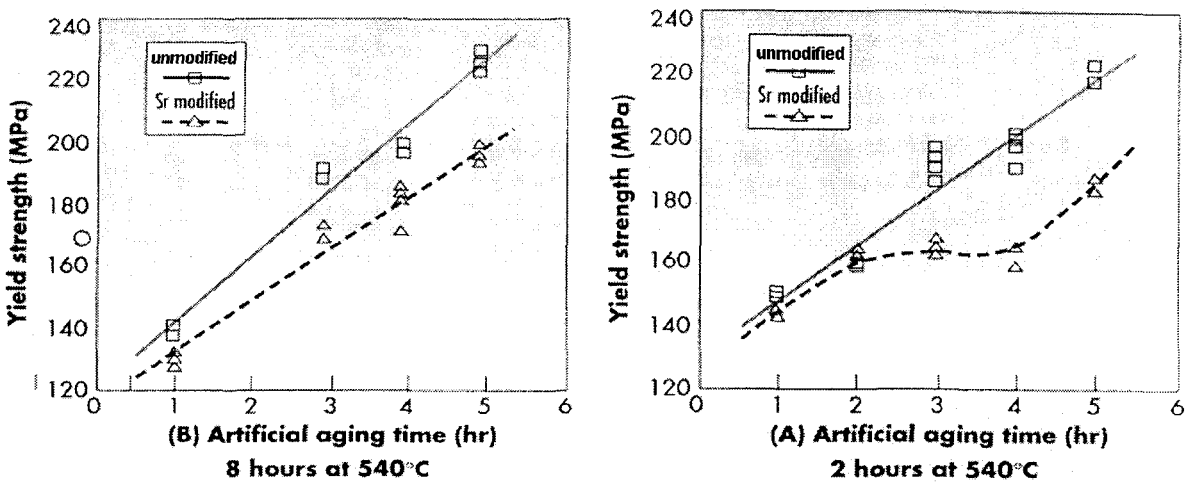

Figure 2.11. Variation of yield strength of A356 alloy with artificial aging time. Samples were solution treated at 540 °C and aged at 155 °C [56].

The changes in the size and morphology of discontinuous silicon phase have a significant influence on the alloy mechanical properties. It has been proposed that the granulation or spheroidization process of the silicon particles through heat treatment takes place in two stages: fragmentation or dissolution of the eutectic silicon branches and spheroidization of the separated branches [58]. During solution treatment, the particles undergo changes in size and in shape. In the initial stages of solution heat treatment, the unmodified silicon particles undergo necking and separate into segments, which retain their original morphology, Figure 2.12(a). Due to the separation, the average particle size decreases and the fragmented segments are eventually spheroidized. The spheroidization and the coarsening of the eutectic Si can occur concurrently during the second stage. Modification facilitates fragmentation as it promotes eutectic silicon branching. The rate of

spheroidization of the eutectic silicon phase is faster in the modified alloys than in the unmodified alloys, as it depends on the size of the fragmented segments, Figure 2.12(b). This effect is due to the increased driving force provided by the finer as-cast structure of the modified eutectic silicon phase.

Kulunk and Zuliani [59] have also studied the effect of strontium on 380 high-pressure die-casting alloy. They showed that reduction in the size and number of iron intermetallic phase particles by the addition of strontium would lead to an increase in the tolerance of these alloys to higher iron concentrations without altering the mechanical properties. It has been found that the addition of (0.04-0.06)% of strontium to A413, 413P, and 413 alloys modifies the size of intermetallic phase particles and enhances the transformation of the β-AlFeSi phase into α-Al_8Fe_2Si phase [60]. Fat-Halla [61] has also reported that the addition of 0.02% strontium to Al-13%Si type alloys increases the %elongation and the ultimate tensile strength values without significantly changing the yield strength.

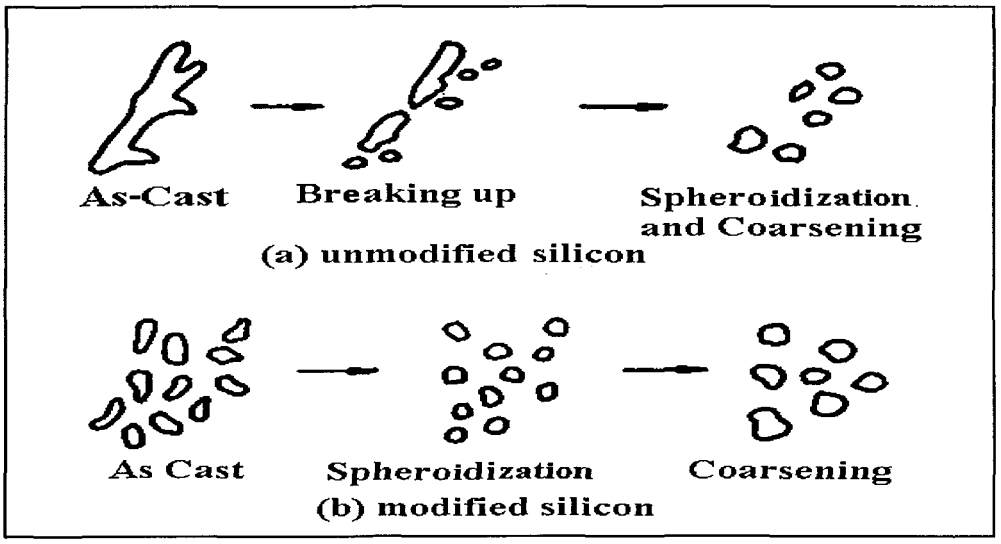

Figure 2.12. Schematic characterization of the three stages of spheroidization and coarsening of the silicon phase [58].

Wrought alloys: Morris and Miners [2] have found that the addition of strontium and/or calcium in a total amount of 0.01-0.5% to a homogenized Al-Mg-Si extrusion alloy (6069) ingot containing β-Al_5FeSi transforms a major proportion of the β-Al_5FeSi phase into the α-Al_8Fe_2Si phase, thereby reducing the formation of pick-up upon extrusion of the ingot.

The results of Vernam and Lifka [62] show that the addition of 0.01-0.1% strontium to Al-Cu-Mg-Zn wrought alloys refines the intermetallic phases including Mg_2Si, Al-Cu-Fe and Al-Cu-Mg. As a result, the strontium-modified alloys have enhanced toughness, shorter homogenizing times and finer grain sizes compared to the non-modified alloys. Dimayuga *et al.* [63] studied the effect of strontium in wrought 6201 and 6063 alloys. They reported that addition of 0.015% strontium promotes the transformation of iron intermetallic particles found in these alloys from the plate-like β-Al_5FeSi phase to the more desirable Chinese-script α-Al_8Fe_2Si phase. The same authors also mentioned that the addition of strontium to Al-Mg-Si alloy leads to superior surface quality.

Modification with strontium results in ultra fine α-AlFeSi dendrite arm spacings in Al-Si-Fe direct chilled (DC) alloys [64]. Strontium modifies many other complex intermetallic compounds in various wrought alloy systems. In 7000 series alloys, strontium refines the intermetallic phases, whereas a strontium and zinc addition reduces the number of intermetallic particles in 5000 series alloys.

Paray *et al.* [65] studied the effect of strontium on 6061 alloys. The addition of 150-300 ppm strontium to 6061 series alloys resulted in the preferred α-Al_8Fe_2Si phase forming during billet solidification rather than the β-AlFeSi phase. They also showed that the

presence of 180 ppm strontium improved the surface finishing of these alloys. Figure 2.13 reveals the effect of strontium addition and homogenisation time on the surface roughness of the extruded alloys.

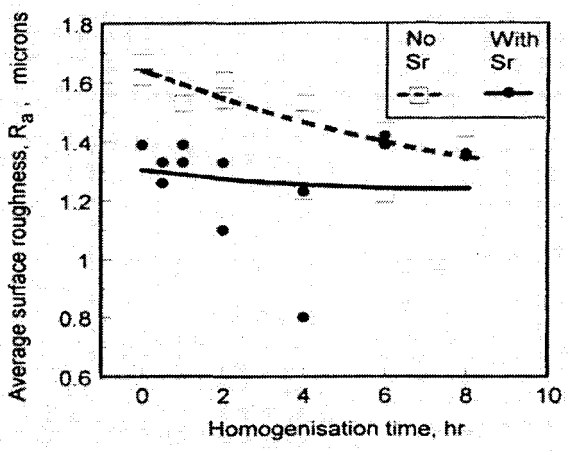

Figure 2.13. Effect of strontium and homogenisation time on the surface roughness of 6061 alloys [65].

Closset *et al.* [66] showed that the formation of a less compact α-Al_8Fe_2Si phase is promoted by the presence of strontium, and that strontium has a positive effect on the tensile strength and electrical resistivity of commercial 6201 aluminum electrical conductor alloy containing 0.6% magnesium and 0.6% silicon. Mulazimoglu *et al.* [28] reported on the effect of strontium modification on the intermetallic phases in 1XXX, 6061, 5182 alloy series. Their findings indicate that strontium alters the plate-like β-Al_5FeSi phase to the Chinese script α-Al_8Fe_2Si phase in synthetic 1XXX and 6061 alloys, and in DC cast commercial 6061 alloys.

Mulazimoglu *et al.* [67] also carried out studies on 6201 aluminum alloys, by using transmission electron microscopy (TEM). They established that strontium stabilizes the more desirable α-Al_8Fe_2Si phase in the 6201 series. From the aluminum-rich corner of the

Al-Fe-Si phase diagram [67], Figure 2.14, the formation mechanism of AlFeSi intermetallic phases in 6XXX series alloys may take place through the following series of reactions:

655 °C	$L \longrightarrow$ Al dendritic network	(1)
618 to 615 °C	$L \longrightarrow Al + Al_8Fe_2Si$	(2)
612 °C	$L + Al_8Fe_2Si \longrightarrow L + Al + Al_5FeSi$	(3)
585 °C	$L \longrightarrow Al + AlFeSi + Si + Mg_2Si$	(4)

The key reaction is the peritectic reaction (reaction 3 at 612 °C) and it is different from that expected on the basis of the equilibrium phase diagram in which there is an invariant peritectic between the primary Al_3Fe and liquid to form Al_8Fe_2Si. The α-Al_8Fe_2Si phase will form directly from the liquid at 618 to 615 °C (reaction 2). The intermetallic particles then grow freely in the liquid, which gradually becomes enriched with silicon and iron due to solute rejection from the growing Al-dendrites. The α-Al_8Fe_2Si can only grow for a short period of time before the peritectic temperature of 612 °C is reached.

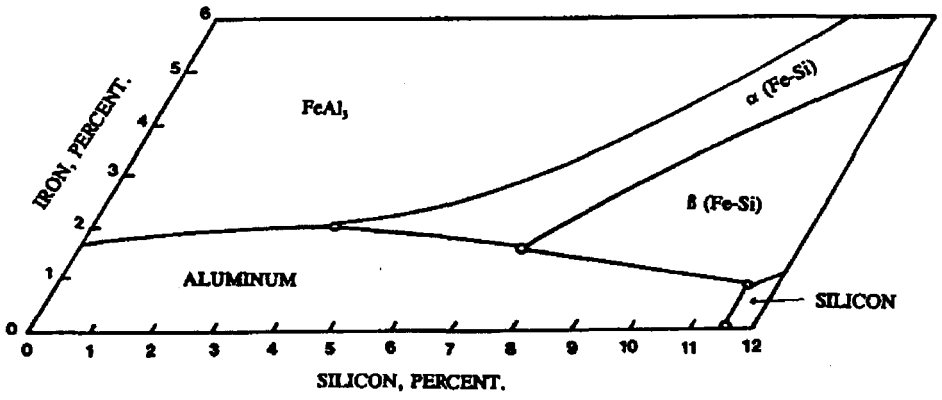

Figure 2.14. Aluminum-rich corner of Al-Fe-Si phase diagram [67].

With completion, or near completion, of reaction (3), further segregation of the alloy components occurs until reaction (4) at 585 °C. These phases may be completely replaced by Al_5FeSi. It has been suggested that strontium stabilizes the Al_8Fe_2Si phase by extending its equilibrium region shown in the phase diagram of Figure 2.14. The cast microstructure will be completed through the formation of eutectic Si, Al_5FeSi, and Mg_2Si, at 585 °C. Therefore, the microstructure will consist of peritectic β-Al_5FeSi with small amounts of residual α-Al_8Fe_2Si, eutectic Si, Al_5FeSi, and Mg_2Si. Fredriksson and Nylen [68] proposed a different model, shown in Figure 2.15, in which the nucleated β phase grew laterally on the α phase which dissolved by solute transport through the liquid.

Regarding the effect of strontium in stabilizing the α-Al_8Fe_2Si phase, Mulazimoglu *et al.* [67] have suggested that the absorption of strontium by the α-Al_8Fe_2Si particle surfaces act as a barrier to solute transport of silicon into these particles. Under these conditions, the transport of silicon into the α-Al_8Fe_2Si particles to form the β-AlFeSi phase will most likely be retarded. Figure 2.16 is a TEM micrograph of an α-Al_8Fe_2Si particle surrounded by a layer that was found to be rich in silicon, which supports this mechanism. This phenomenon is likely to occur in view of the well known surface-related effect of strontium in modifying the growth morphology of eutectic Si in Al-Si alloys.

Kulunk and Zuliani [59] have reported the stabilizing effect of strontium addition on the α-Al_8Fe_2Si phase in 6061 alloys, which has an important bearing on the hot workability of these alloys and on productivity through a reduction in billet homogenization times.

Figure 2.17 shows the microstructures of unmodified and Sr-modified 6061 alloy in the as-cast condition.

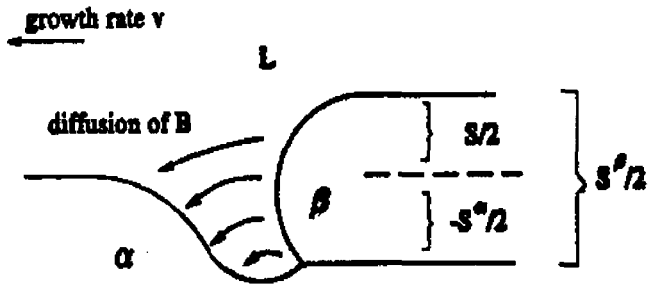

Figure 2.15. Peritectic reaction mechanism [68].

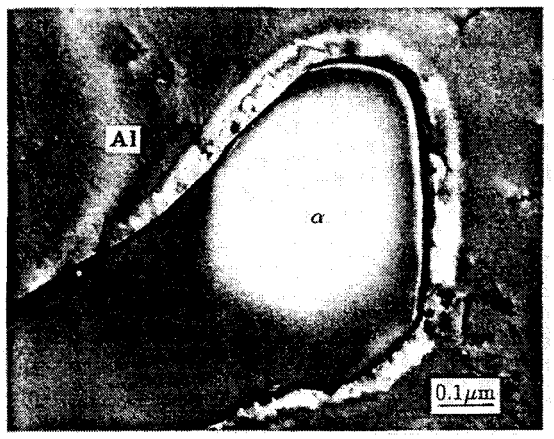

Figure 2.16. Silicon-rich layer surrounding α-AlFeSi phase in the presence of strontium [67].

In their work, Gruzleski *et al.* [56] also studied the effect of strontium on the mechanical properties of the 6061 extrusion alloy, and found that addition of 0.03% Sr was sufficient to stabilize the α-Al_8Fe_2Si phase in the as-cast billet (Figure 2.17). They proposed the same formation mechanism of the AlFeSi intermetallic phases as reported by Mulazimoglu [67].

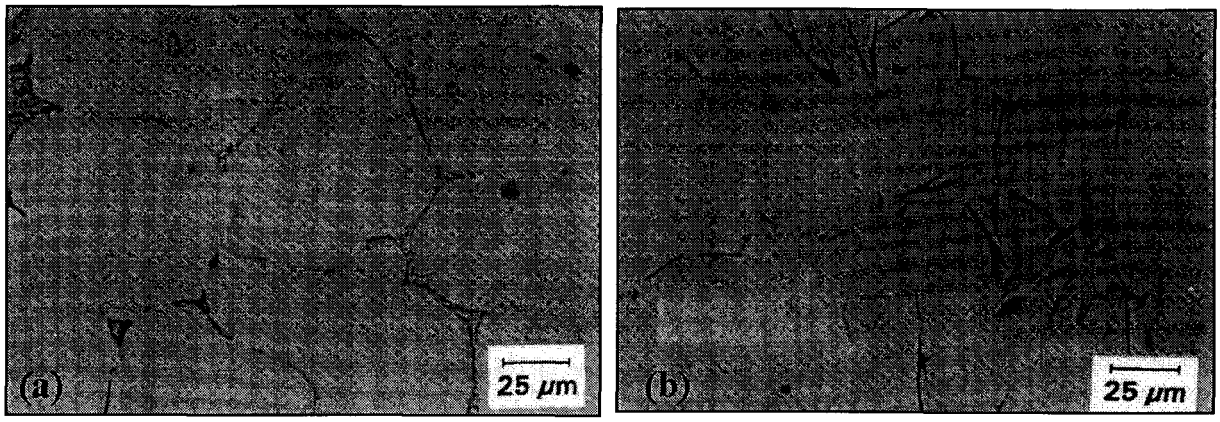

Figure 2.17. Microstructure of as-cast commercial 6061 extrusion alloy: [56] containing (a) 300 ppm strontium, (b) no strontium

2.8.5. Melt Superheating

It has been reported that melt superheating is expected to change the morphology of the iron intermetallic from plate-like to Chinese script [69]. Awano and Shimizu [30] indicated that even in the absence of iron neutralizers, the morphology of the iron phase may also be altered by superheating the melt appropriately. Also if the melt is once superheated to the temperature at which the iron intermetallic crystallizes in Chinese script form, the change in its shape is not affected by the thermal history of the melt.

The relations between melt superheating temperature and shape of the iron compound upon crystallization, as well as the effects of iron, silicon and magnesium content and solidification time were also investigated by them. The influence of these parameters on the microstructure is plotted in Figures 2.18 and 2.19. Their results highlight the importance of low iron, silicon and magnesium contents, as well as a high cooling rate in order to achieve complete crystallization of the iron compounds in the α-AlFeSi form.

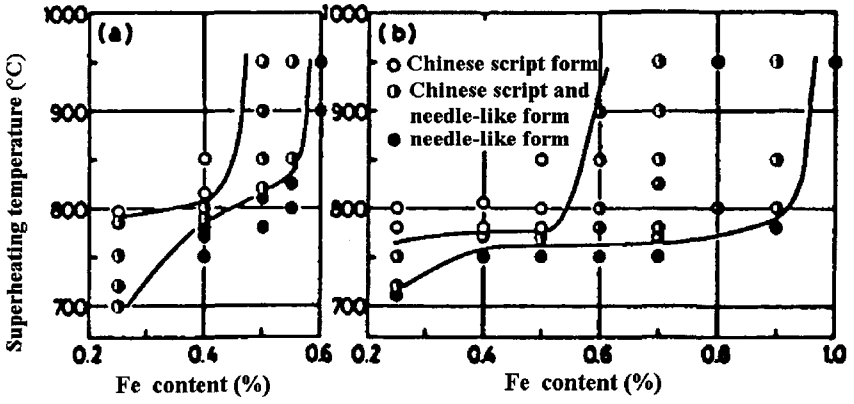

Figure 2.18. Effects of superheating temperature and iron content on crystallized structure of iron compounds in: (a) Al-6% Si-Fe, (b)Al-11% Si-Fe alloys [30].

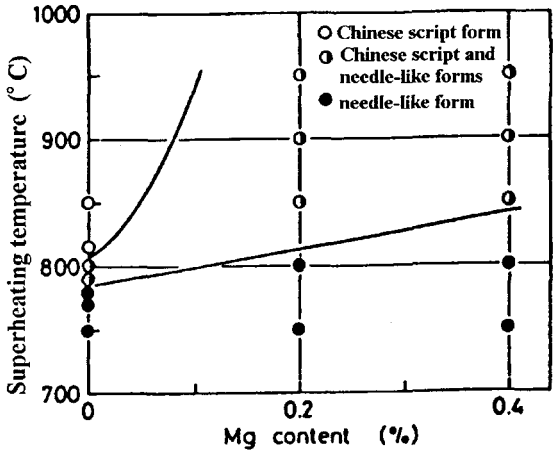

Figure 2.19 Effect of magnesium content on crystallized structure of iron compounds in Al-6% Si-Mg-0.4% Fe alloy castings [30].

Xiufang *et al.* [69] studied the effect of melt superheat on the iron intermetallic morphology in an Al-12.15% Si-0.52% Cu-0.33% Mg-0.3% Mn-1.8% Fe alloy, and found that the β-iron intermetallic that forms in the alloy changes into a spheroidal form as a result of heating the metal to a high temperature (980 °C), followed by pouring into a permanent mould. By this technique, the iron intermetallics can be spheroidized completely.

2.8.6. Non-Equilibrium Heat Treatment

Non-equilibrium heat treatment can result in partial dissolution of the harmful β-iron intermetallic in the Al-Si alloy matrix. During solution treatment, the silicon fibres develop periodic variations in thickness, which leads to their breakdown into particles. The dissolution of the iron intermetallic improves with increasing solution temperature. Non-

equilibrium heat treatment increases the strength of high iron alloys until a critical solution temperature is exceeded. Above this temperature, a large amount of liquid phase is formed due to interdendritic and grain boundary melting. It has also been reported that non-equilibrium heat treatment improves the mechanical properties of 319 alloys [18].

Awano and Shimizu [30] studied the non-equilibrium heat treatment of Al-7% Si-3% Cu aluminum alloy. They found that under equilibrium heat treatment conditions, it is not possible to put all of the copper intermetallics into solid solution. Even at long solution treatment times, a large proportion of the copper-rich phases may remain undissolved.

Using a non-equilibrium heat treatment, however, the copper intermetallic phases can be readily dissolved, even up to 100%. Griger *et al.* [70] observed that the metastable α-AlFeSi phase which forms in 1XXX alloys transforms to Al_3Fe phase during heat treatment between 450-575 °C for prolonged times. A study of the impact strength as a function of different solution temperatures ranging from 485 to 535 °C, showed that impact properties increase with increasing solution temperature, reaching a maximum at 520-525 °C. Above this temperature range, the properties decrease due to grain and interdendritic boundary melting.

Narayanan *et al.* [18] studied the influence of solution temperature and time on the dissolution behaviour of iron intermetallics in Al-6% Si-3.5% Cu-0.3% Mg-1% Fe alloy, and found that with increasing solution temperature, the β-AlFeSi phase platelets dissolved, whereas the α-AlFeSi phase did not undergo any dissolution. Also, the solution temperature was much important than solution time, and addition of manganese would

hinder the dissolution kinetics of the iron intermetallics. They showed that the optimum solutionizing temperature for low iron alloys lies between 515 and 520 °C, in which temperature range a maximum amount of the iron intermetallic dissolves in the aluminum matrix.

Villeneuve *et al.* [21] reported that solution heat treatment of iron-containing Al-Si cast alloys accelerates the dissolution of β-Al_5FeSi phase. The minimal β-Al_5FeSi needle length is achieved after 30 h for unmodified alloys and 10 h for Sr-modified alloys. The dissolution of the β-Al_5FeSi phase occurs by decomposition of the β-phase into Al_6Fe and Si. The mechanism of β-Al_5FeSi phase dissolution comprises the rejection of Fe and Si from the β-Al_5FeSi phase needles at their ends (rather than along their sides), which explains the noticeable decrease in the needle length rather than in the needle thickness.

In AA-8011 aluminum wrought alloy with 0.58%Fe and 0.53%Si, the β-AlFeSi phase (that forms in cast alloys with higher silicon contents), would decompose into the α-AlFeSi phase and Si during annealing heat treatment. This solid state reaction is controlled by diffusion processes and favored by higher temperatures. Increasing the silicon concentration in solid solution will increase the alloy strength [71].

2.9 FORMABILITY

The formability of any material is the extent to which it can be deformed in a particular process before the onset of failure. Aluminum sheets or aluminum shapes usually fail by localized necking or by ductile fracture. In dilute alloys, the extent of necking or limit strain is reduced by cold work, age hardening, large grain size, and the presence of alloying elements in solid solution. Lloyd [25] studied the ductility and bendability in 6000 aluminum alloy series, and found that the tensile elongation is controlled by the work hardening rate. However, the bendability is fracture controlled and can be understood in different alloys in terms of their fracture strains.

The effect of precipitated phases on the recrystallization and formability of AA 3003 aluminum alloy has been studied by Li *et al.* [72]. The precipitated structure and the degree of solute supersaturation are greatly affected by intermediate annealing during continuous strip casting. The degree of solute supersaturation drops during annealing and depends on the temperature and time used. The lower the intermediate annealing temperature, the finer the precipitates obtained during the final annealing.

Hove and Andersson [73] studied the mechanism of initiation and growth of edge cracking during hot rolling of AA5182 alloy. The edge cracks result from the combination of a brittle surface zone and high tensile stresses at the edge. The high magnesium-alloyed material makes the propagation of the cracks easier. Lloyd [74] investigated the formability in 6000 series alloys. He showed that increasing the iron level decreases the tensile

elongation, and that a high iron content results in a higher volume fraction of constituent particles.

Bryant [75] has studied the effects of pre-aging on formability and paint bake response in AA6111 alloys. Pre-aging of these alloys has been shown to be a successful method to modify their mechanical properties in the as-preaged condition. Pre-aging increases the activation energy for cluster dissolution and subsequent β" precipitation, and induces the precipitation of an additional metastable phase.

SS → Si rich clusters → GP-1 zones → GP-2 zones(β") → β' → β

where SS represents the supersaturated solution, β is the stable Mg_2Si phase precipitate, β' is a metastable rod aligned with the [100] direction of the aluminum matrix, and GP-2 (β") is a fine needle-shaped phase also aligned with the [100] direction of the aluminum matrix.

The cluster dissolution is associated with an increase in the matrix concentration of both elements (Mg and Si). The transient increase in the matrix vacancy concentration results in the formation of an intermediate metastable phase and an enhancement of the aging kinetics of β". The enhancement in the precipitation kinetics and the refinement of the precipitate structure leads to higher yield strengths during short aging cycles, typical of automotive paint bake cycles [76]. It is believed that nearer the edges, the solute supersaturation of the matrix could be quite significant and therefore both solid solution effects and precipitation of small dispersoids could be much more pronounced, leading to slower recrystallization kinetics and coarsening of the recrystallized grain structure [77].

The combined effect of deformation and homogenization processes produces significant changes in the morphology and distribution of the intermetallic particles initially present in the alloy. The colonies of dendrite-like particles are observed to disappear after the homogenization, together with the coarsening and enrichment of the resulting particles, and a partial depletion of the as-cast matrix in the main alloying elements. The annealing response of the material depends upon the amount of prior cold working applied to the alloy [78].

Prestraining is one of the methods used to increase strength at short aging times in wrought alloys. Normally, cold work is introduced by prestraining. Lloyd *et al.* [79] have studied the effect of prestraining on the alloy aging response in 6XXX series alloys. Figure 2.20 shows the aging response of 6111 alloy. Ding and Morris [80] have shown that in AA3004 can stock alloys, the best combination of mechanical strength and ductility in the alloy sheet is achieved by using a prestrain processing procedure.

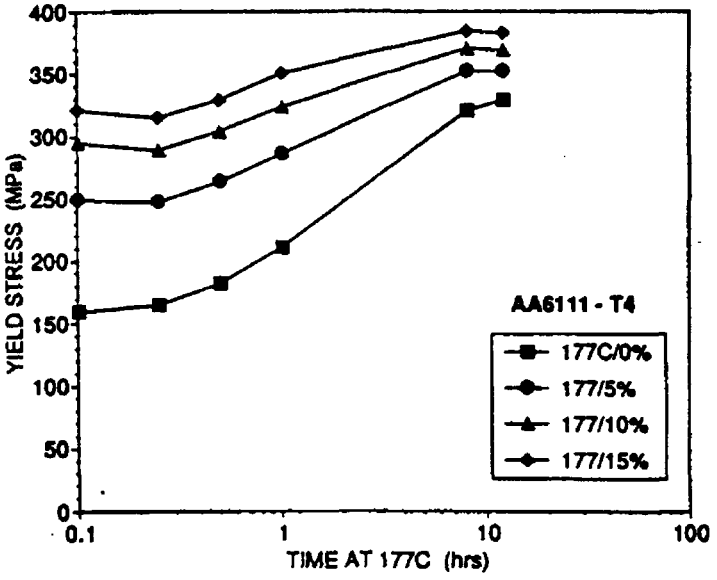

Figure 2.20. Aging response of 6111 alloy at 177 °C after different degrees of prestrain [79].

CHAPTER 3

IRON INTERMETALLIC CHARACTERISTICS

3.1 INTRODUCTION

The formation of a wide variety of intermetallic phases is possible during ingot or billet solidification. In silicon-containing aluminum alloys the most common phases are the α-Al_8Fe_2Si and β-Al_5FeSi phases. Depending upon the alloy composition and solidification rate, one or both phases can be present in the microstructure. The β-Al_5FeSi phase has a needle/plate-like morphology and is considered detrimental to the ductility of the alloy. The α-Al_8Fe_2Si phase is believed to be less harmful than the β-phase form as it has a more desirable compacted Chinese script morphology.

By increasing the iron and silicon content, the iron intermetallic particle size and volume fraction are expected to increase. It is well known that at higher cooling rates, neutralization by the addition of trace elements such as Mn, Be, Sr can change the crystallization of the iron intermetallic to the Chinese script α-phase form which improves the mechanical properties.

The key reaction in the formation mechanism of AlFeSi intermetallic phases in 6XXX series alloys is:

$$L + Al_8Fe_2Si \longrightarrow L + Al + Al_5FeSi$$

This reaction takes place at 612 °C [8]. The α-Al_8Fe_2Si phase forms directly from liquid. The liquid gradually becomes enriched with the rejected iron and silicon from the growing Al-dendrites. At the peritectic temperature, the α-AlFeSi phase transforms to the β-AlFeSi phase.

The effect of strontium in stabilizing the α-AlFeSi phase is suggested to take place as follows: strontium is absorbed to the α-particle surface in the form of a thin layer. Rejected silicon can not diffuse through this layer and is stacked up ahead of the α-particles. This process results in the reduction of the β-platelet phase in the microstructure. Addition of a small amount of beryllium produces a new Be-Fe phase (Al_8Fe_2SiBe) having a Chinese script morphology or polygon shapes, that is different from the β-phase in the unmodified alloy [8,56].

The iron intermetallics obtained in 6XXX series of aluminum alloys at various Fe/Si ratios and at three different cooling rates were studied, where the role of trace elements such as Si, Sr, Mn, and Be in modifying the iron intermetallics formed was examined in detail. Both experimental and industrial alloys were used. The results are presented in this chapter. It should be mentioned here that all alloy compositions and additions are given in weight percentages throughout the text.

3.2 EXPERIMENTAL PROCEDURE

3.2.1. Alloy Preparation

In order to study the effects of silicon, magnesium, iron, manganese, strontium and beryllium on the morphology of iron intermetallics, the respective additions were made using pure silicon, pure magnesium, and Al-25%Fe, Al-25%Mn, Al-10%Sr and Al-5%Be master alloys to the melt in the amounts required. For grain refining purposes, Al-5%Ti-1%B master alloy was added (in terms of a 0.01-0.02 %Ti addition) to all the melts.

For preparing the alloy melts, gates and runners obtained from previous castings (see Chapter 5), were cut into smaller pieces, cleaned, dried, and melted in a 2-kg capacity SiC crucible using a small electrical resistance furnace. The melt was heated up to 720 ± 5 °C, then poured into the different molds. Prior to each pouring, the melt was held for ~10 min, stirred for ~5 min, and the melt surface was thoroughly skimmed. Samplings for chemical analysis were also taken simultaneously for each pouring.

The chemical compositions of the alloys used in the present work are shown in Table 3.1. The experimental 6XXX alloys were coded A and 6 for the base alloy, B and S6 for the 1.01% Si-containing base alloys, C for 4.52% Si-containing A base alloy, M6 for the 0.2% Mn containing 6 base alloy, and B6 for Be-containing 6 base alloys. The two lots of as-received 6063 industrial alloys were coded D and 6I, respectively. An S or a digit suffix was used to denote the corresponding Sr-modified alloy in each case.

Table 3.1. Chemical compositions of alloys used in the present study (wt%).

Alloy	Si	Fe	Cu	Mn	Mg	Cr	Ni	Zn	B	Sn	Sr	V	Ti	Al
A	0,60	0,29	0,002	0,004	0,645	0,001	0,016	0,007	0,002	0,002	0,0002	0,004	0,001	98,430
A1	0,61	0,29	0,002	0,005	0,663	<.0005	0,017	0,007	0,002	0,001	0,0231	0,004	0,001	98,370
A2	0,65	0,31	0,002	0,005	0,652	<.0005	0,016	0,007	0,002	0,002	0,0477	0,004	0,001	98,300
A3	0,67	0,30	0,002	0,004	0,647	<.0005	0,016	0,008	0,002	0,002	0,0746	0,004	0,002	98,260
A4	0,68	0,29	0,002	0,005	0,647	<.0005	0,016	0,008	0,002	0,002	0,0951	0,004	0,002	98,250
B	1,05	0,30	0,002	0,004	0,584	<.0005	<.005	<.005	0,002	<.001	0,0001	0,005	0,002	97,980
B1	1,05	0,34	0,002	0,004	0,659	0,002	<.005	0,013	0,003	0,000	0,0163	0,004	0,009	97,920
B2	1,05	0,33	0,002	0,004	0,571	0,004	<.005	0,013	0,002	<.001	0,0410	0,004	0,003	97,920
B4	1,05	0,34	0,003	0,005	0,564	0,005	<.005	<.005	0,002	<.001	0,0748	0,005	0,002	97,900
C	4,52	0,30	0,002	0,004	0,584	<.0005	<.005	<.005	0,002	<.001	0,0001	0,005	0,002	94,570
C2	4,66	0,33	0,002	0,004	0,579	0,004	<.005	0,013	0,002	<.001	0,0354	0,005	0,002	94,370
C4	4,49	0,34	0,003	0,005	0,564	0,005	<.005	<.005	0,002	<.001	0,0623	0,005	0,002	94,520
D	0,65	0,17	0,013	0,033	0,696	0,003	0,015	0,017	0,002	0,002	0,0002	0,007	0,008	98,390
DS	0,70	0,17	0,013	0,034	0,713	0,003	0,016	0,016	0,002	0,002	0,0415	0,007	0,008	98,270

Alloy	Si	Fe	Cu	Mn	Mg	Cr	Ni	Zn	B	Be	Sr	V	Ti	Al
6	0,61	0,38	0,003	0,004	0,644	0,003	<.005	0,013	0,003	0	0,0009	0,004	0,008	98,320
6S	0,63	0,38	0,003	0,004	0,653	0,003	<.005	0,013	0,003	0	0,0144	0,004	0,007	98,270
S6	1,01	0,35	0,003	0,006	0,682	0,002	<.005	0,013	0,003	0	0,0014	0,004	0,008	97,910
S6S	1,01	0,34	0,002	0,004	0,659	0,002	<.005	0,013	0,003	0	0,0163	0,004	0,009	97,920
M6	0,62	0,34	0,002	0,196	0,606	0,003	<.005	0,013	0,003	0	0,0002	0,004	0,007	98,210
M6S	0,66	0,34	0,002	0,217	0,636	0,004	0,005	0,013	0,003	0	0,0206	0,005	0,010	98,090
B6	0,64	0,35	0,005	0,006	0,617	0,006	0,006	0,014	0,003	0,130	0,0038	0,007	0,006	98,340
B6S	0,64	0,34	0,003	0,005	0,606	0,004	<.00526	0,014	0,003	0,130	0,0147	0,007	0,009	98,350
5B6	0,66	0,39	0,002	0,004	0,663	0,001	<.005	0,013	0,004	0,040	0,0005	0,006	0,010	98,240
5B6S	0,67	0,39	0,003	0,005	0,597	0,009	0,009	0,013	0,003	0,040	0,0162	0,005	0,007	98,270
2B6	0,68	0,39	0,004	0,003	0,639	0,002	<.005	0,013	0,003	0,022	0,0019	0,004	0,009	98,260
2B6S	0,68	0,39	0,004	0,003	0,639	0,002	<.005	0,013	0,003	0,022	0,0171	0,004	0,009	98,260
1B6	0,68	0,39	0,009	0,004	0,605	0,006	0,006	0,015	0,003	0,010	0,0016	0,004	0,010	98,260
6I	0,43	0,18	0,059	0,037	0,519	0,003	<.0005	0,015	0,003	<.001	0,0000	0,006	0,018	98,720
6IS	0,40	0,19	0,011	0,036	0,548	0,003	<.0005	0,015	0,003	<.001	0,0265	0,006	0,020	98,740

3.2.2. Casting and Sample Preparation

In order to achieve different cooling rates, a preheated graphite mold, a cold metallic mold and a Stahl permanent mold (type ASTM B-108) were used. The cylindrical graphite mold (inner dimensions: 10 cm length, 6 cm diameter), was preheated at 600 °C, to obtain close to equilibrium cooling conditions. The cold metallic mold provided a higher cooling rate, whereas the Stahl permanent mold was used to prepare castings from which test bars were obtained for tensile testing purposes. Each Stahl mold casting provided two test bars.

A schematic diagram of the three molds used is shown in Figure 3.1. The castings (and the metallographic samples sectioned from them) were coded E (for equilibrium cooling condition, graphite mold), M (for metallic mold), and G (for gauge specimen-Stahl mold), respectively.

The metallographic samples were sectioned and polished along the A-A plane in each case, as shown in Figure 3.1: 2.5 x 2.5 cm samples from the graphite mold casting, and 2.5 cm wide round samples from the metallic mold casting. For the gauge sample obtained from the Stahl mold casting, the sample was taken directly from the tensile tested bar from the round section of the gauge length, cut normal to the tensile axis and away from the fracture surface, as shown.

For solution heat treatment studies, some test bars were solution treated at 520 °C for 8h, followed by quenching in warm water. Samples obtained from these test bars were coded SHT. All samples were mounted in bakelite and polished for metallographic examination.

3.2.3. Quantitative Metallographic Measurements

Microstructures of the polished sample surfaces were examined using an Olympus optical microscope. The dendrite arm spacing (DAS) and maximum average β-platelet (or β-needle) length were measured and quantified using a LECO-2001 image analyser in conjunction with the optical microscope. In each case, the measurements were made over a selected number of fields ("field" representing the field of observation of the optical microscope, and covering an area of 2.2608 x 10^4 μm^2 at 500 magnification), such that the sample surface was traversed in a regular, systematic manner. The presence (or absence) of the α-AlFeSi phase in each field was also noted.

In addition to optical microscopy, the phases reported in the present study were also identified using scanning electron microscopy (Jeol SEM operating at 20 kV) coupled with energy dispersion spectroscopy (EDS).

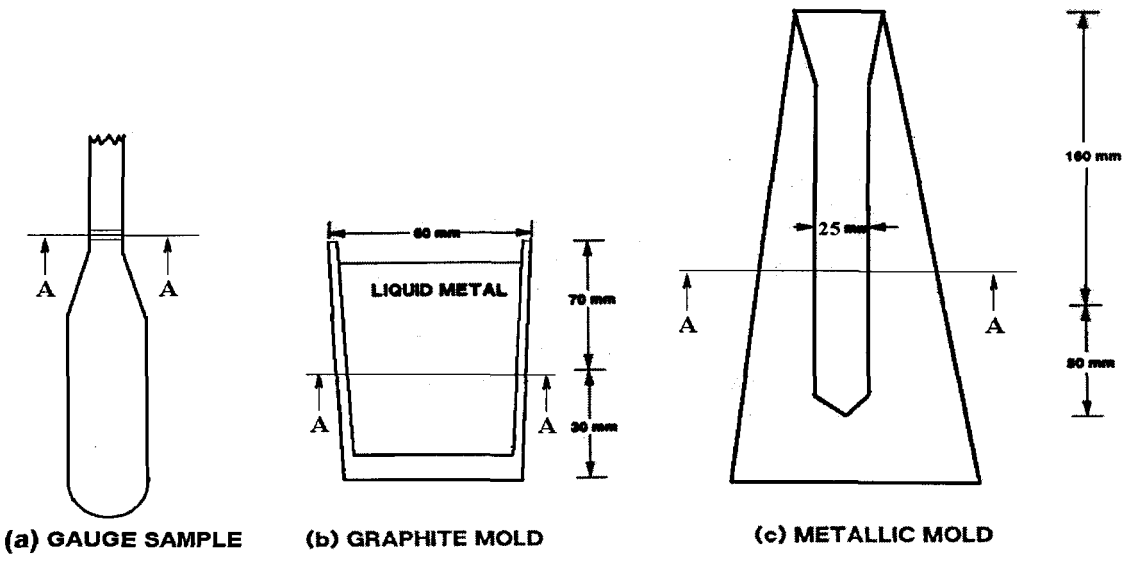

Figure 3.1. Schematic diagram showing cross-sections of gauge sample, graphite and metallic molds used in the present study. Specimens for microstructural observation were cut and polished along the A-A plane, as shown.

3.2.3.1. Dendrite Arm Spacing (DAS)

A total of 30 fields for the graphite mold samples, and 50 fields each for the metallic mold and gauge samples were analyzed. Dendrite arm spacings were measured (3-5 measurements per field). The measurements were carried out manually in the direct measurements mode, at 50X and 100X magnifications, depending upon the sample structure.

3.2.3.2. Maximum Average β-needle Length

A total of 30 fields for the graphite mold samples, and 70 fields for the metallic mold and gauge samples were examined, where three to five of the longest β-needle lengths were measured in each field. The measurements were carried out manually, in the direct measurements mode, at 200X magnification for the graphite mold samples, and at 500X magnification for the metallic mold and gauge samples. As the largest β-needle lengths were measured in each field, the average obtained was considered as the average maximum β-needle length for the sample in question.

3.2.3.3. Presence of α-AlFeSi Phase

For each sample (graphite mold, metallic mold and gauge) a total of 100 fields were examined. The presence or absence of the α-AlFeSi phase in each of the examined fields (*i.e.*, yes/no) was noted. The measurements were carried out manually, at 200X, 500X and 500X magnifications for graphite mold, metallic mold and gauge samples, respectively.

3.3 RESULTS AND DISCUSSION

3.3.1. Dendrite Arm Spacing

The effect of cooling rate on the average dendrite arm spacing (DAS) is shown in Figure 3.2. The standard deviations is also plotted in each case. The average DAS for graphite, metallic and test bar gauge samples are 91, 44, 23 μm respectively.

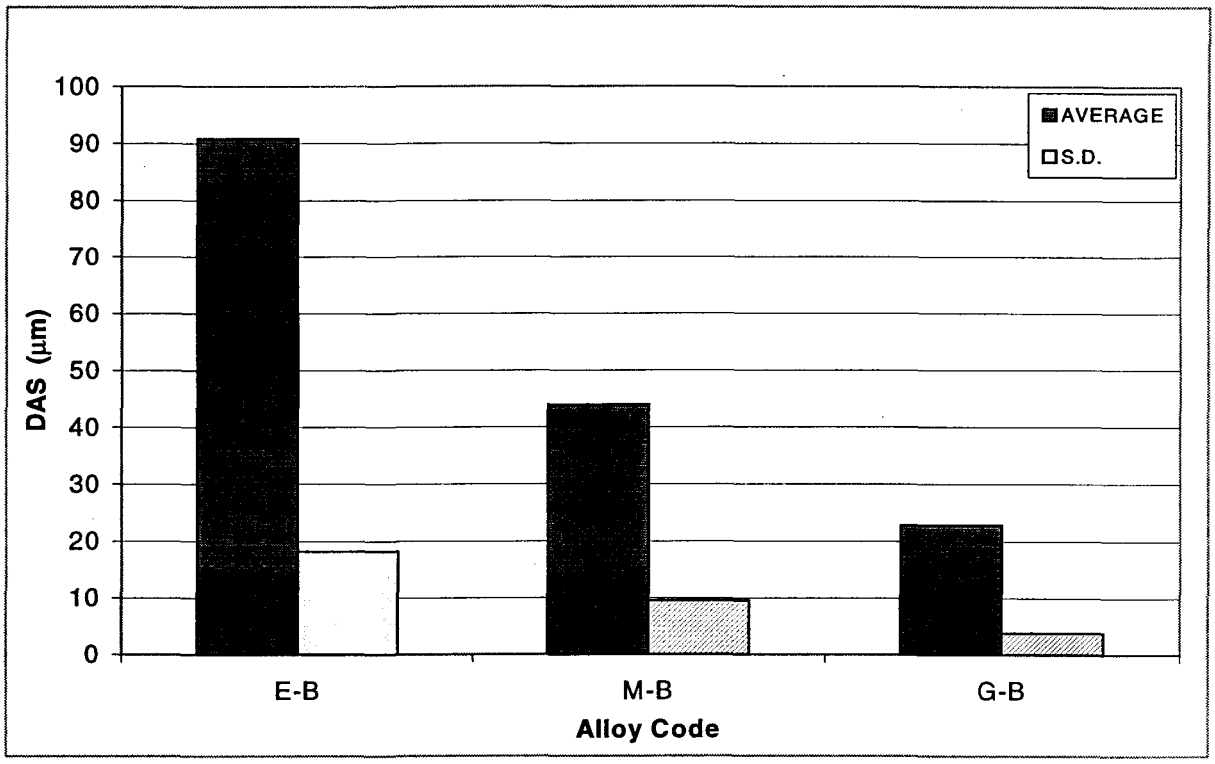

Figure 3.2. Effect of cooling rate (different casting molds) on the dendrite arm spacing.

3.3.2. β and α Phase Characteristics

3.3.2.1. Experimental Alloys

Figures 3.3(a) and 3.3(b) demonstrate the effect of increasing silicon, iron, and strontium contents on the average maximum β-needle lengths and the presence of the α-iron phase in A, B, C, D and 6I alloys, in the non-modified and Sr-modified conditions, at two levels of Fe (0.17 and 0.3 %), and three levels of Si (0.6, 1 and 4.5 %). As can be seen, increasing the Fe content at the same level of Si increases the average maximum β-needle length from 86 μm to 100 μm, while the amount of α-phase present is not changed. The addition of Sr (415 ppm Sr in DS and 477 ppm in A2 alloy) does not affect the β-needle length. The amount of α-phase present, however, increases from 5% to 31%, due to the lower Si*/Fe ratio (E-A samples), Si* representing free Si or that above the Si needed for Mg_2Si formation. As can be seen from Table 3.1, D alloy has 0.7 % Mg and A alloy has 0.65 % Mg. Thus any remaining Si (free Si) above that needed for Mg_2Si reaction will be consumed to form the α-iron intermetallic.

At constant levels of Fe and Mg, increasing the Si content increases the average maximum β-needle length from 100 μm to 157 μm, with practically no α-phase being observed. Modification with Sr in each case is seen to decrease the average maximum β-needle length but at Sr levels greater than 400 ppm, overmodification of the β-needles is observed. Presence of the α-phase in the Sr-modified samples increases from 5% to 31% in E-A2 alloy. At 1% Si levels or above, strontium is not effective, since the higher Si content

would enhance its diffusion through the protective film around the α-particles, making the second peritectic reaction possible, and leading to the formation of the β-phase.

The average maximum β-needle length and the presence of the α-phase in non-modified and Sr-modified Al-1% Si-0.3% Fe-0.65% Mg alloy samples obtained from the graphite mold, metallic mold and test bar castings are presented in Figures 3.4(a) and 3.4(b), respectively. As can be seen from Figure 3.4(a), the β-needle length reduces from 123 μm (graphite mold, DAS ~91μm) to 40 μm (gauge sample, DAS ~23μm). The amount of α-phase is found to increase from 0% to 8%. The combined effect of modification and high cooling rate results in smaller β-platelets and a higher percentage of α-phase precipitation.

Reduction in the β-needle length due to the cooling rate is ~47.8% (graphite *vs* metallic mold samples) and 67.5% (graphite mold *vs* gauge samples), whereas maximum reduction due to Sr-modification is ~16% for graphite mold samples. This result shows that cooling rate is more effective in reducing the β-needle length than Sr-modification. The amount of α-phase increases slightly due to Sr-modification (from 0% to 8%), but is practically unaffected by the cooling rate.

From Figures 3.5(a) and 3.5(b), we also observe that in A alloy samples (containing Al-0.6 % Si-0.3 % Fe-0.65 % Mg), obtained from graphite mold, metallic mold and solution heat treated samples, the β-needle length is decreased by ~48%. The presence of α is not affected by cooling rate. Modification with Sr results in reducing the β-needle length by 35% for the graphite mold, 65% for the metallic mold, and 89% for the solution heat

treated samples. Modified alloys exhibit up to 24% α-phase in the graphite mold samples, and up to 86% in the metallic mold samples.

3.3.2.2. Industrial Alloys

Figure 3.6(a) shows the diminution in the average maximum β-needle length as a function of cooling rate and solution heat treatment in D alloy. The β-needle length decreases from 86 μm (graphite mold) to 62 μm (metallic mold), *i.e.* by 28%. From Figure 3.6(b), the presence of the α-phase is not affected much by an increase in the cooling rate. Modification with 415 ppm Sr leads to a decrease in the β-needle length from 86 μm to 76 μm (*i.e.*, 11.6%) in the graphite mold samples, and from 62 μm to 57 μm (*i.e.*, 8%) in the metallic mold samples. Strontium modification combined with solution heat treatment (8h at 520 °C) reduces the β-needle length to 44 μm. Neither Sr-modification nor solution heat treatment significantly affect the presence of the α-phase.

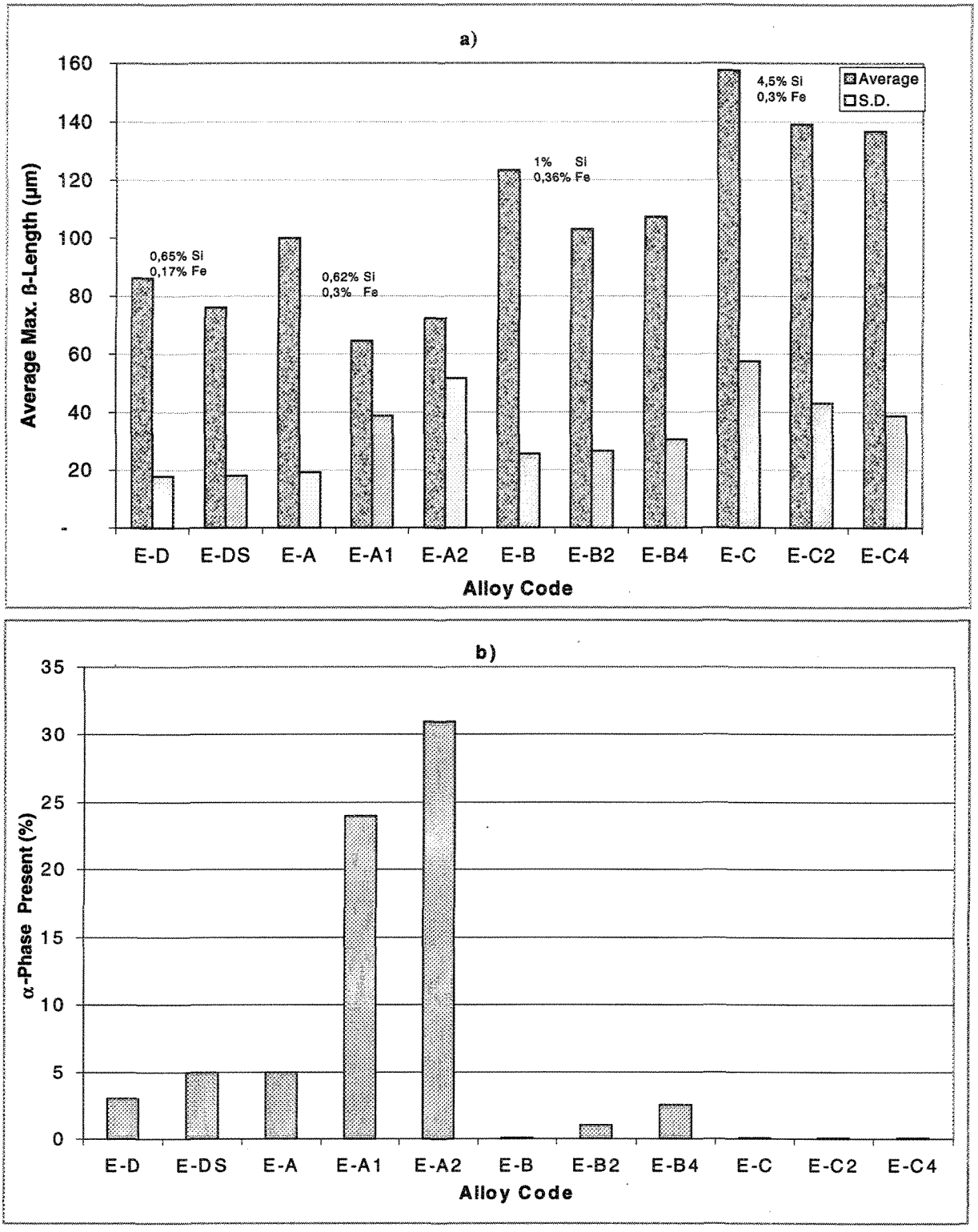

Figure 3.3. Effect of Si, Fe concentration on: a) the average maximum β-needle length, b) the percentage of α-script phase present in unmodified and Sr-modified A, B, C and D alloys.

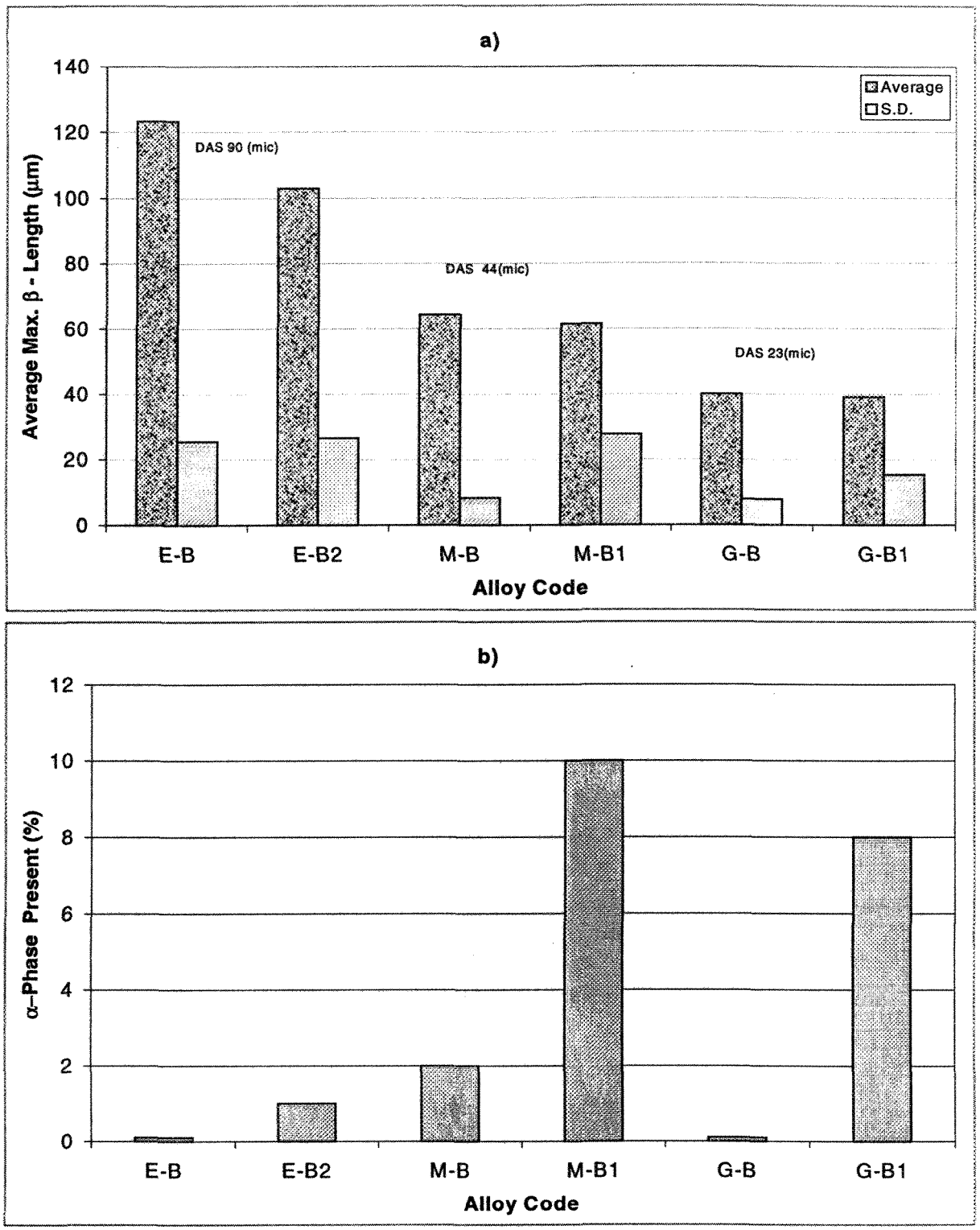

Figure 3.4. Effect of cooling rate and solution heat treatment (8h at 520 °C) on: a) the average maximum β-needle length, b) the percentage of α-script phase present in unmodified and Sr-modified B alloys.

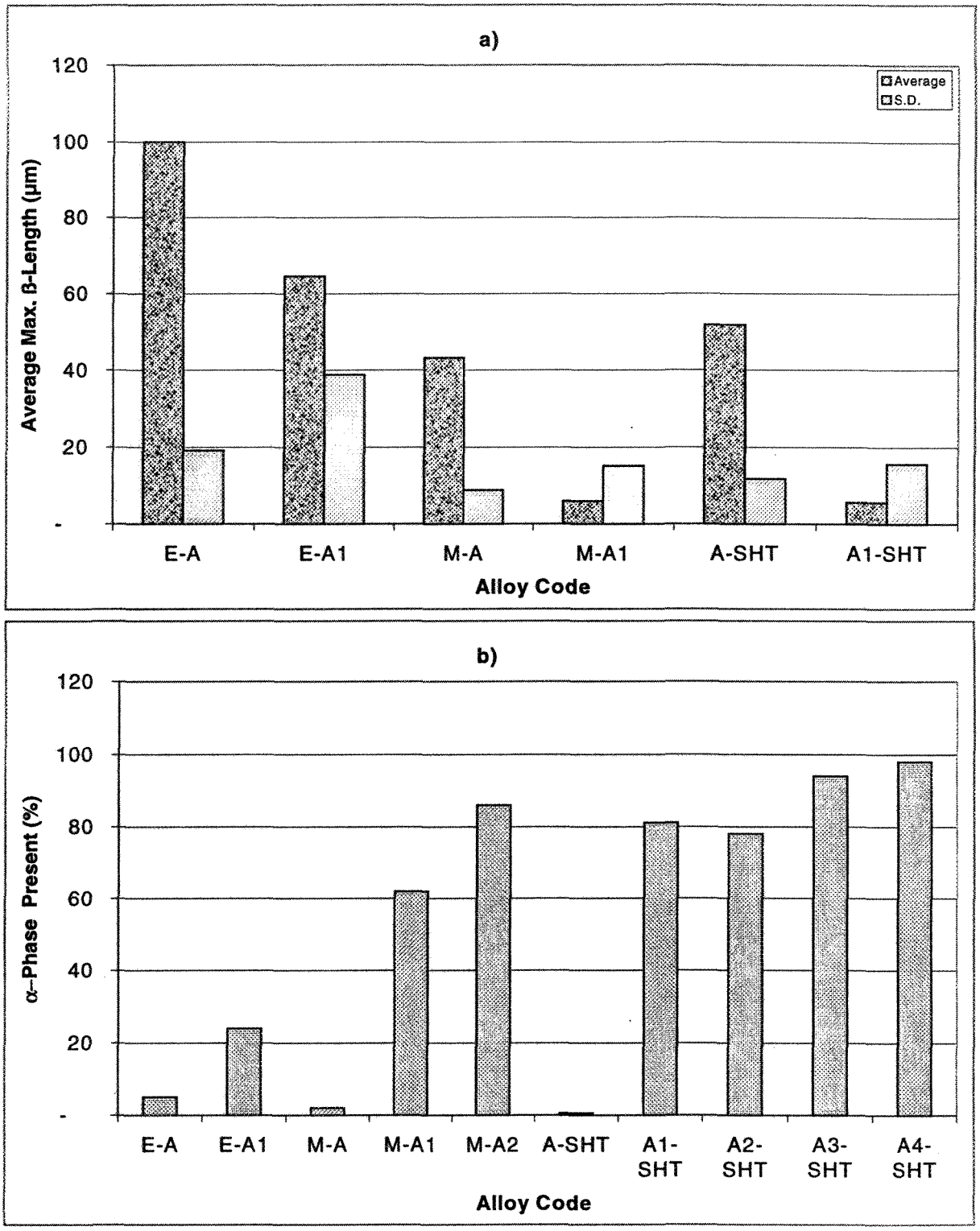

Figure 3.5. Effect of cooling rate and solution heat treatment (8h at 520 °C) on: a) the average maximum β-needle length, b) the percentage of α-script phase present in unmodified and Sr-modified A alloys.

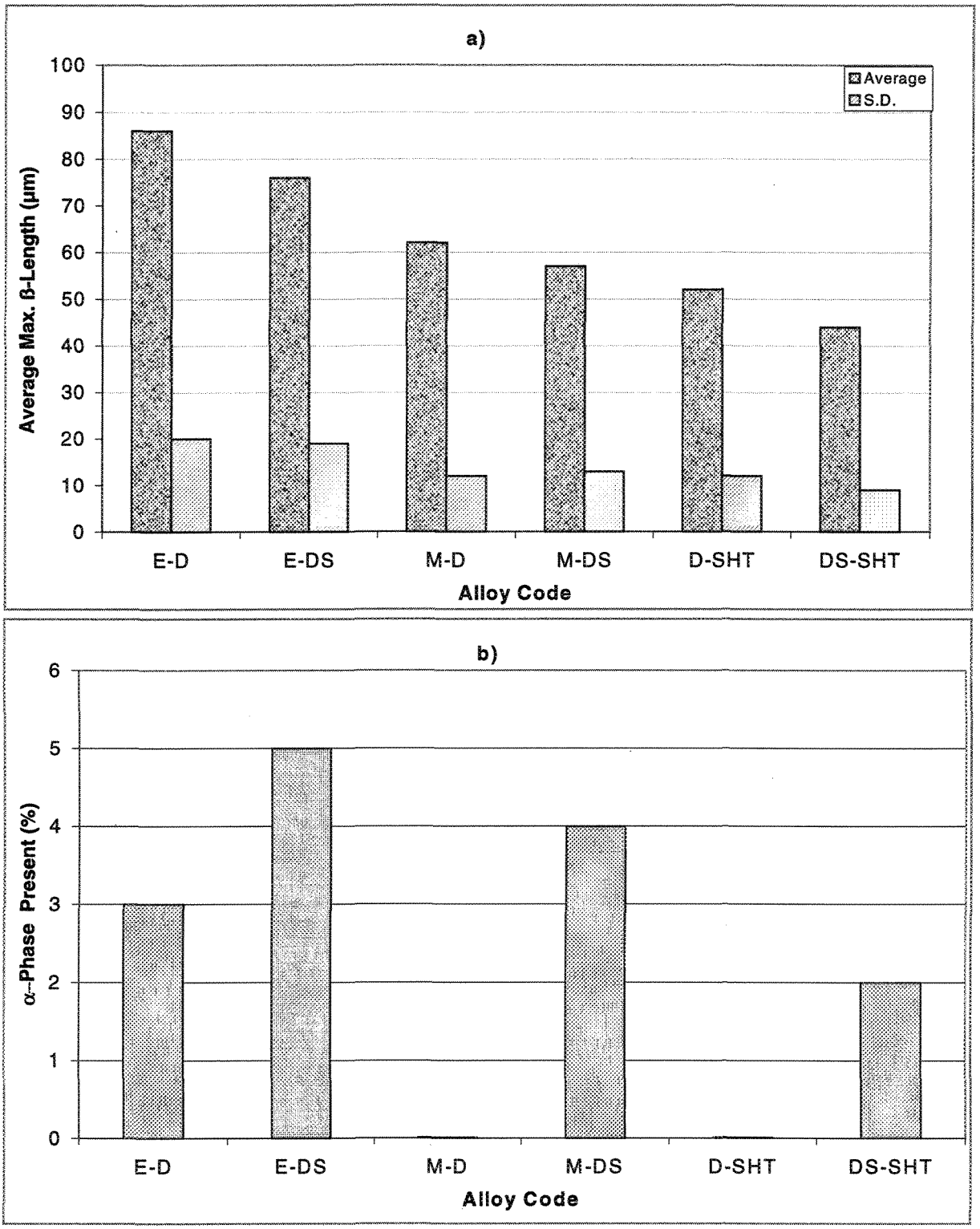

Figure 3.6. Effect of cooling rate and solution heat treatment (8h at 520 °C) on: a) the average maximum β-needle length, b) the percentage of α-script phase present in unmodified and Sr-modified D alloys.

3.3.3. Microstructural Analysis

3.3.3.1. Effect of Si, Si+Sr Additions

3.3.3.1.1. Experimental Alloys

Figures 3.7(a) and 3.7(b) show the microstructures obtained from graphite mold samples of unmodified and 231 ppm Sr-modified A alloy (Al-0.62% Si-0.3% Fe-0.65% Mg). As can be seen from Figures 3.7(a), the unmodified alloy shows mainly the β-needle phase. Modification with Sr changes the phase to the α-script phase. At higher cooling rates, Figures 3.7(c), the β-needles are much smaller. When the alloy is modified with Sr, coarse α-script particles are observed, together with Mg_2Si, Figure 3.7(d).

The microstructure of the alloy in the solution heat treated condition is displayed in Figures 3.8(a) through 3.8(c). As can be seen, solutionizing for 8h at 520 °C results in spheroidization of the Mg_2Si particles and some of the β-needles. Increasing the Sr content increases the α-script particles *i.e.*, 477 ppm Sr addition leads to the formation of larger α-script phase particles together with spheroidization of the Mg_2Si phase, Figure 3.8(d), compared to that observed in the metallic mold sample.

Figures 3.9(a) through 3.9(d) represent the microstructures observed in graphite mold samples of B alloy (Al-1% Si-0.3% Fe-0.65% Mg) in the unmodified and Sr-modified (410 ppm) cases. In the unmodified sample, the microstructure shows mainly β-needles, Figure 3.9(a). Modification breaks down the β-needles into smaller particles, Figure 3.9(b). As can be seen, the β-needles are longer and thicker than those shown in Figure 3.7, due to the higher Si^*/Fe ratio of the alloy.

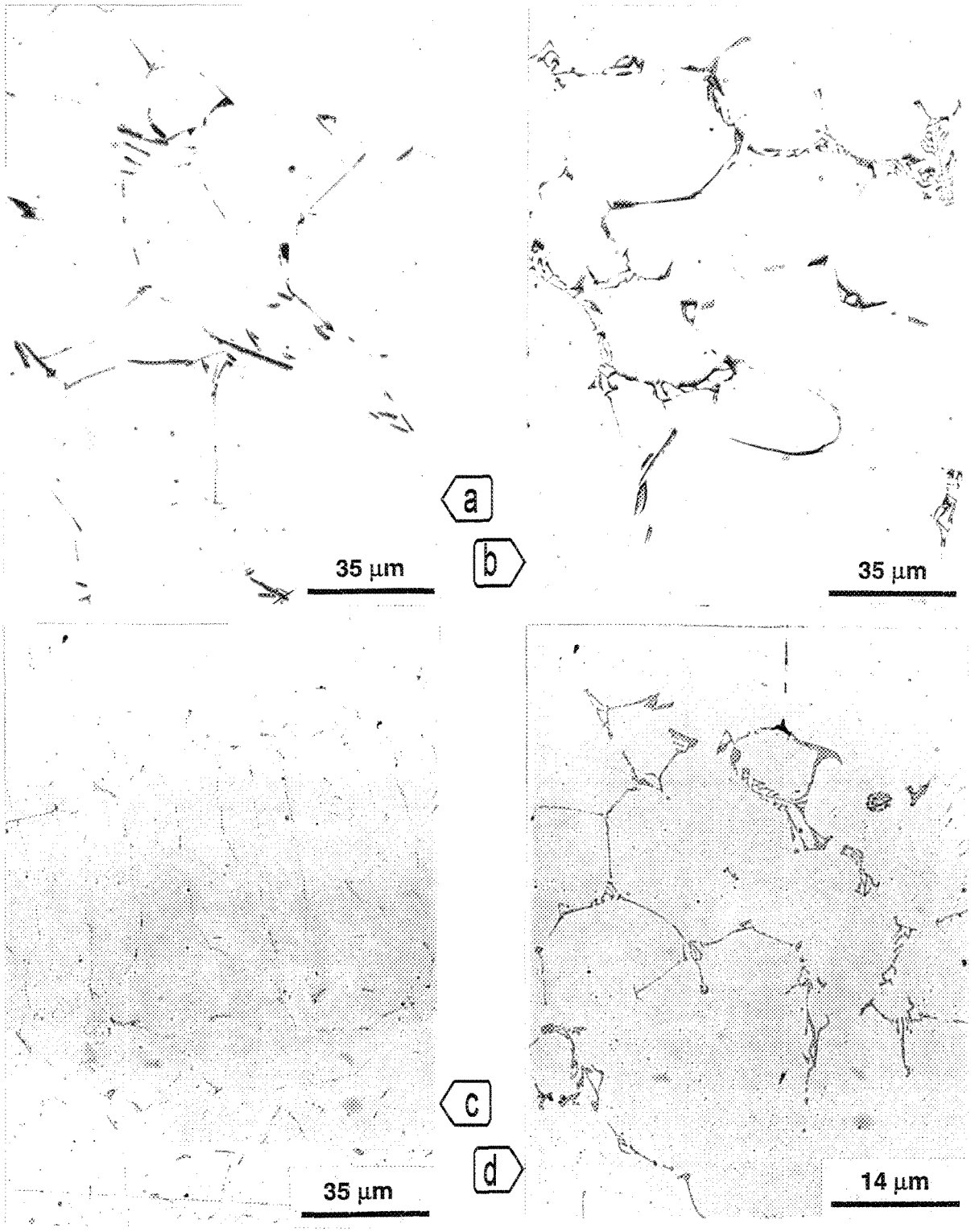

Figure 3.7. Microstructures observed in A alloy samples obtained from graphite and metallic molds: a) unmodified alloy A, graphite mold; b) Sr-modified alloy A1, graphite mold; c) unmodified alloy A, metallic mold; d) Sr-modified alloy A2, metallic mold.

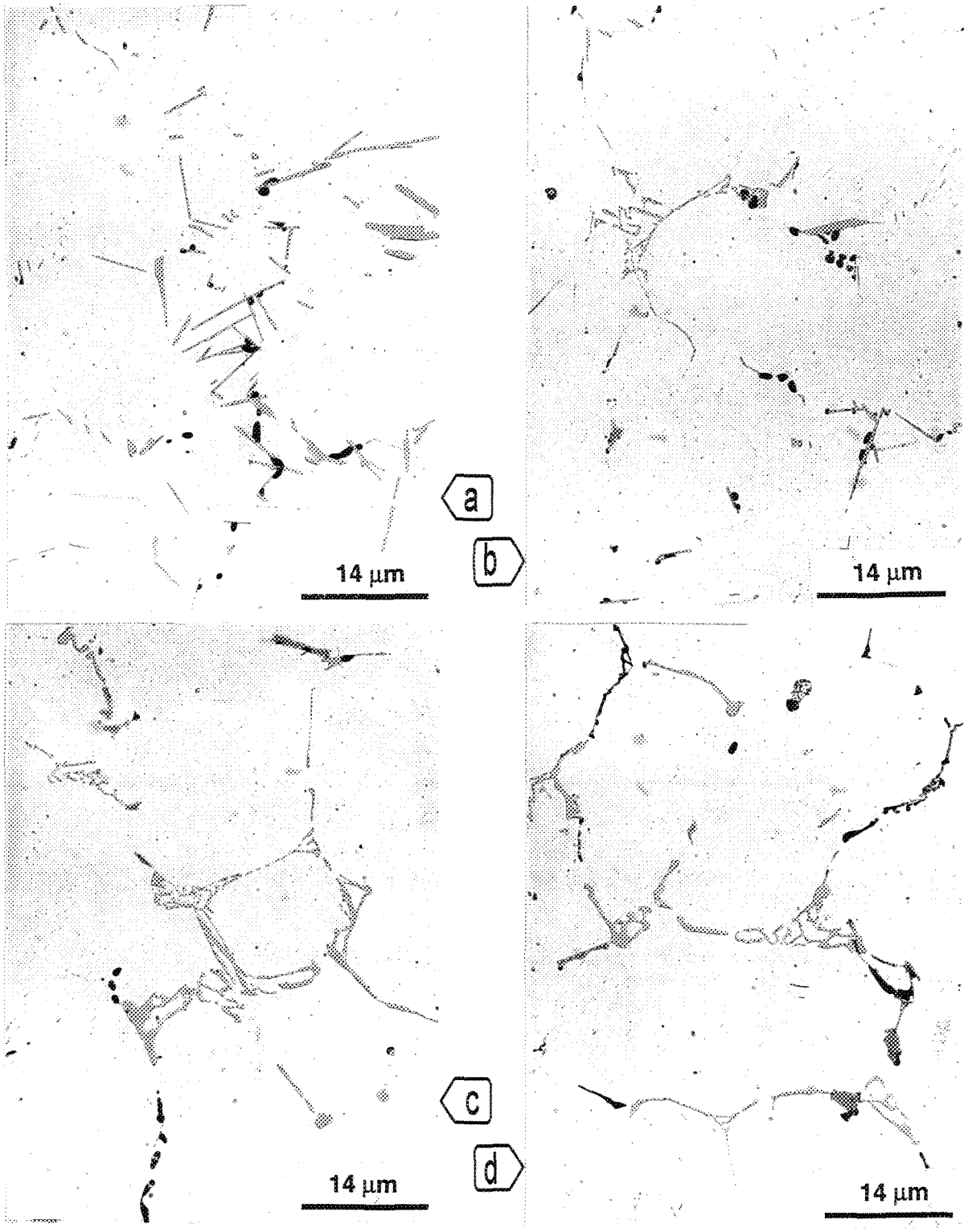

Figure 3.8. Effect of Sr-modification combined with solution heat treatment (SHT)(8h at 520 °C) on A alloy samples: a) A-SHT, b) A2-SHT, c) A4-SHT, d) M-A4

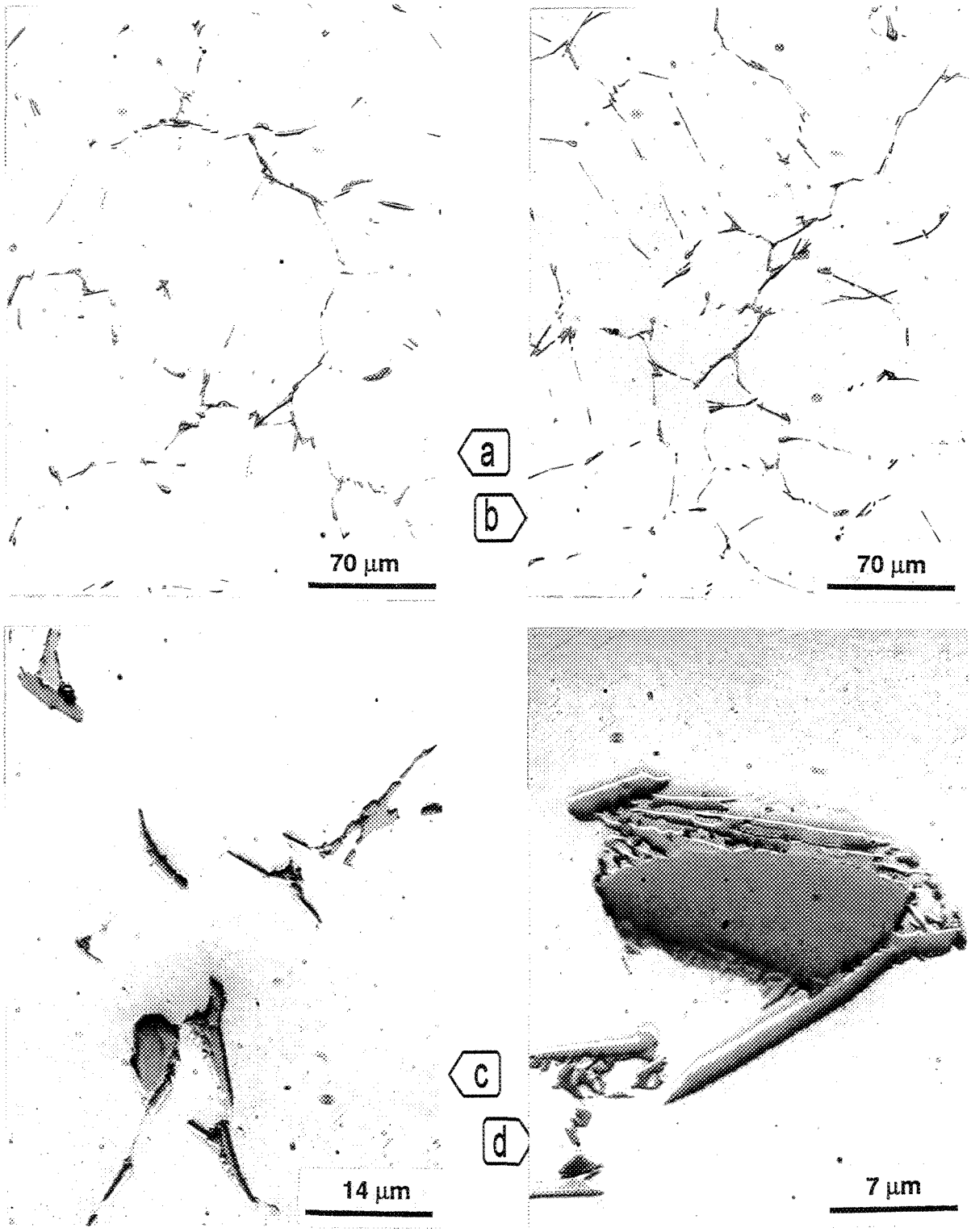

Figure 3.9. Fragmentation of β-phase needles in: a) unmodified and b)-d) Sr-modified B alloy samples obtained from the graphite mold: a) E-B; b), c), and d) E-B2

A higher magnification micrograph, Figure 3.9(c), shows how Sr leads to the splitting of the β-needles into smaller needles along their lengths. Figure 3.9(d) shows an example of the platelet-like morphology of the β-phase. The β-needles on either side have a nonfaceted interface with the aluminum matrix. The formation of the script-like α-$Al_8Mg_3FeSi_6$ phase between the β-platelet and the β-needles results from the transformation reaction:

$$Al_5FeSi + Mg \longrightarrow Al_8Mg_3FeSi_6$$

The backscattered image shown in Figure 3.10 confirms the transformation of the β-phase into the α-$Al_8Mg_3FeSi_6$ phase observed along the edges of the β-needles in the examined sample. The corresponding X-ray spectrum (EDX) obtained from this phase, Figure 3.11, confirms that this phase is approximately $Al_8Mg_3FeSi_6$. The backscattered image of Figure 3.12 clearly reveals the plate-like nature of the β-Al_5FeSi phase in the B alloy samples. The corresponding X-ray spectrum (EDX), Figure 3.13, gives the chemical composition of the β-phase.

Figures 3.14(a) through 3.14(d) display the microstructures observed in B alloy (Al-1% Si-0.6% Fe-0.6% Mg) samples obtained from metallic mold castings, depicting the features observed in the unmodified alloy (a), 163 ppm Sr-modified alloy (b), after solution heat treatment (c), and after solution heat treatment of the modified alloy (d). Compared to the graphite mold sample of Figure 3.9(a), the β-needles in this case are smaller. Increasing the cooling rate (gauge sample) is very effective in reducing both the length and thickness of the β-needles, as seen from Figures 3.15(a) and 3.15(b). Again, from these microstructures it is clear that the β-needles are not affected by the presence of Sr.

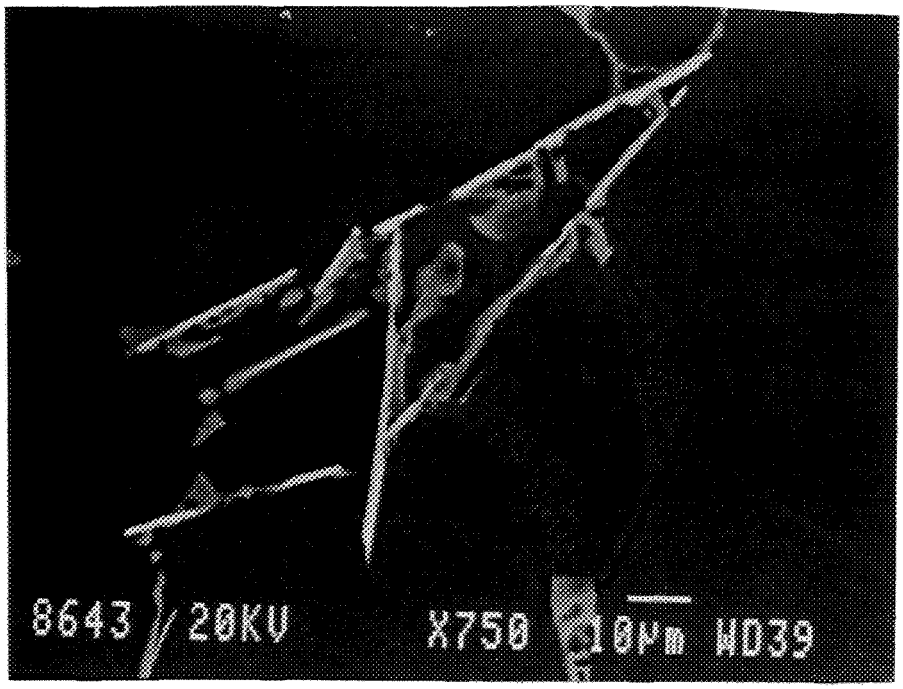

Figure 3.10. Backscattered image obtained from B alloy showing the formation of α-Al_8Mg_3FeSi.

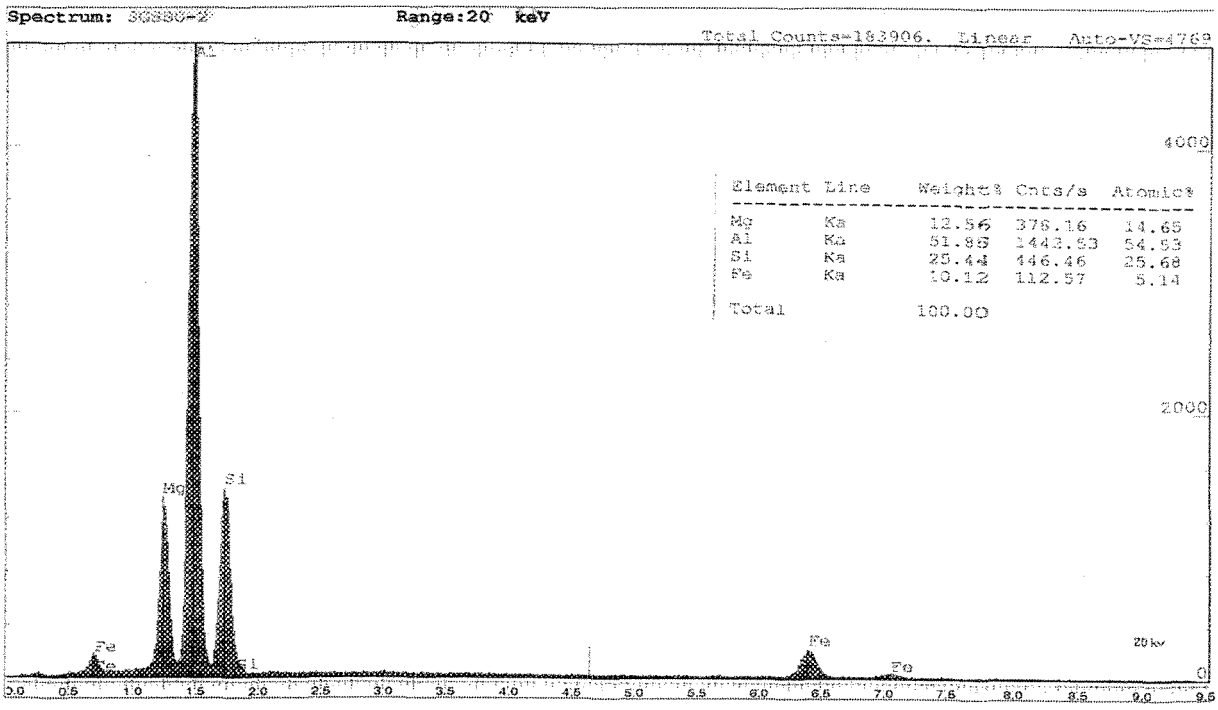

Figure 3.11. EDX spectrum showing Al, Mg, Fe and Si reflections corresponding to the α-Al_8Mg_3FeSi phase shown in Figure 3.10.

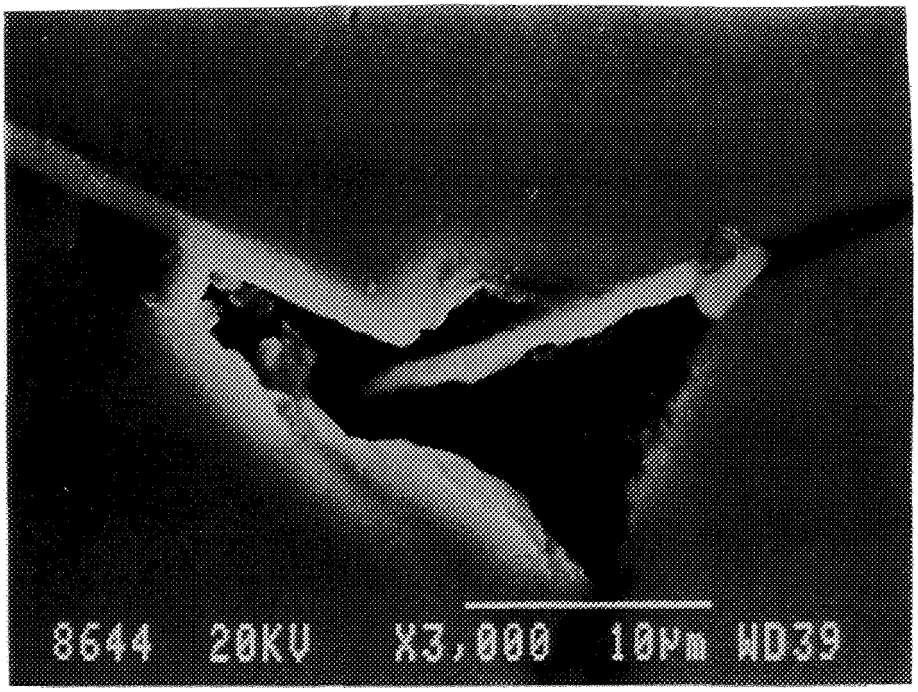

Figure 3.12. Backscattered image obtained from B alloy showing the platelet-like morphology of the β-AlFeSi phase.

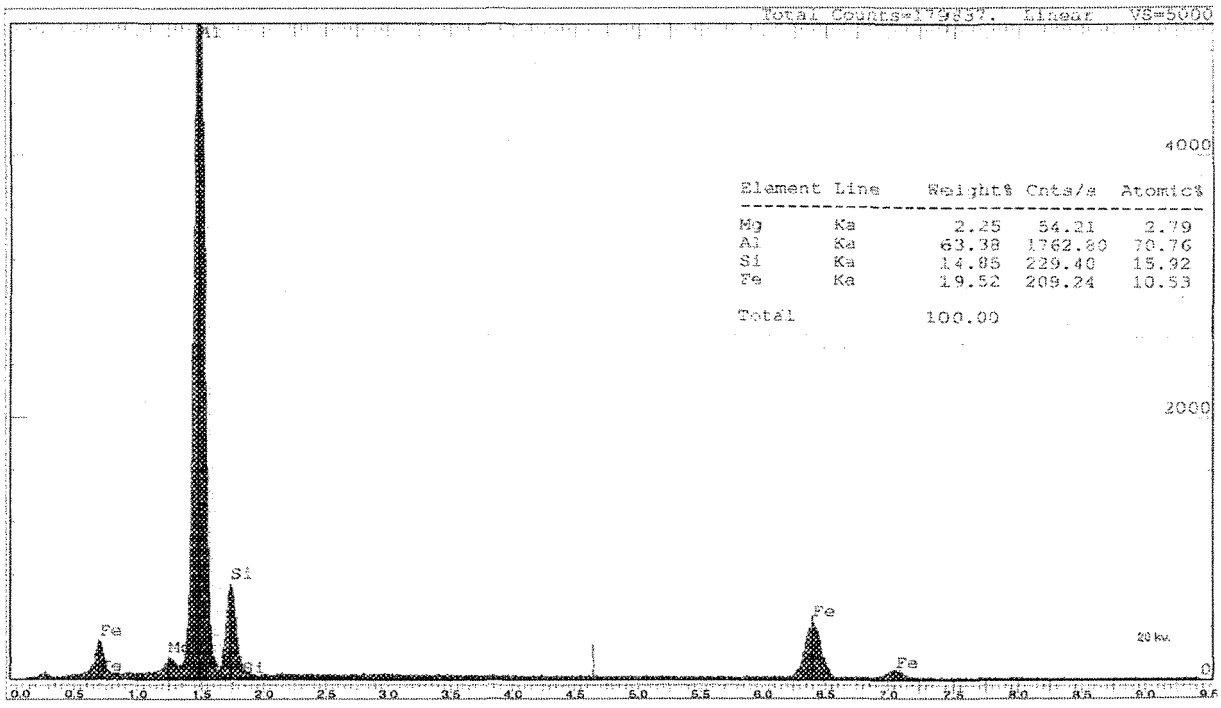

Figure 3.13. EDX spectrum showing Al, Si & Fe reflections from β-needles shown in Figure 3.12.

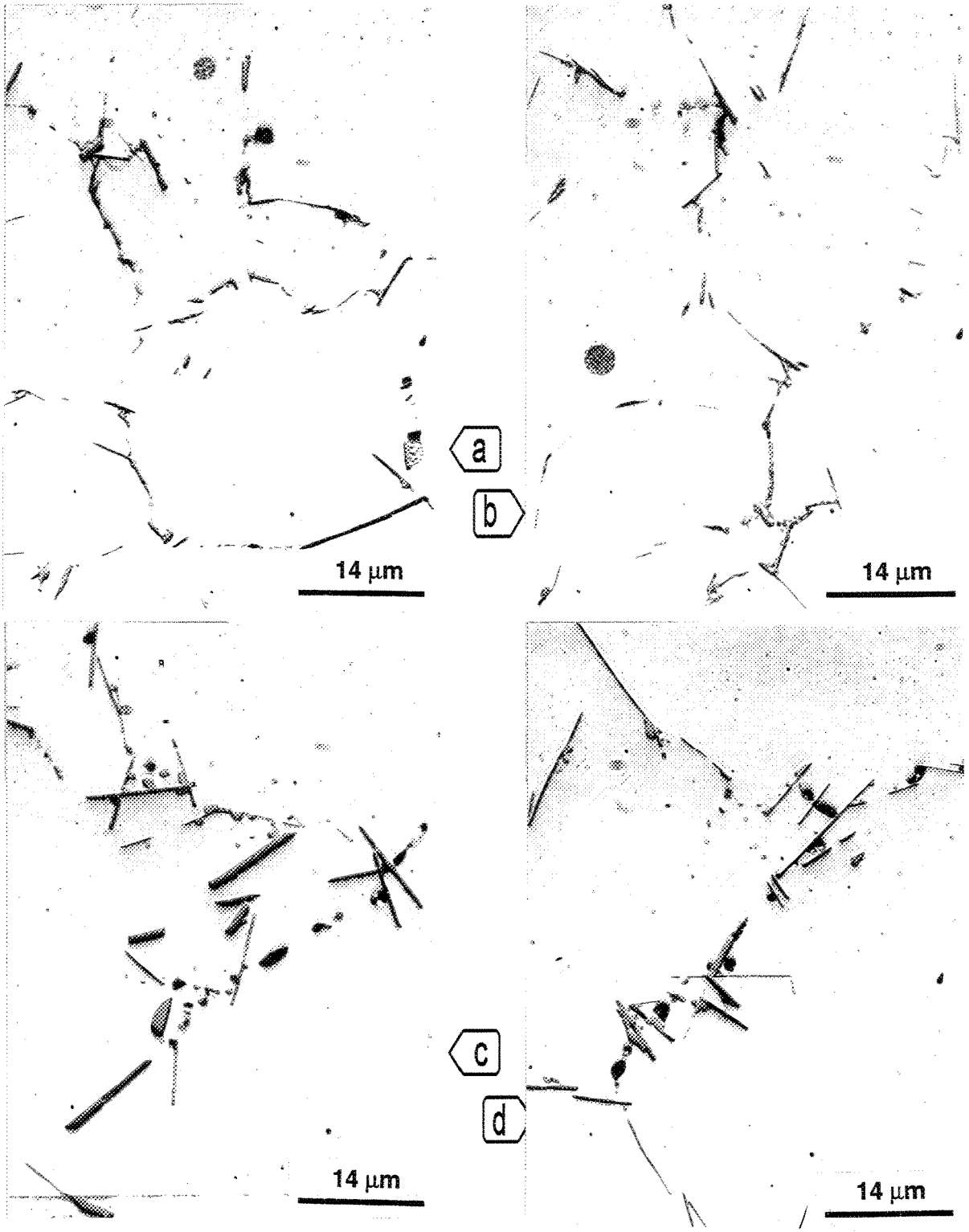

Figure 3.14. Effect of Sr-modification and solution heat treatment on β-needles in B alloy samples: a) non-modified, b) 163 ppm Sr-modified, c) solution-treated alloy (8h at 520 °C), d) solution treated and 163 ppm Sr-modified alloy.

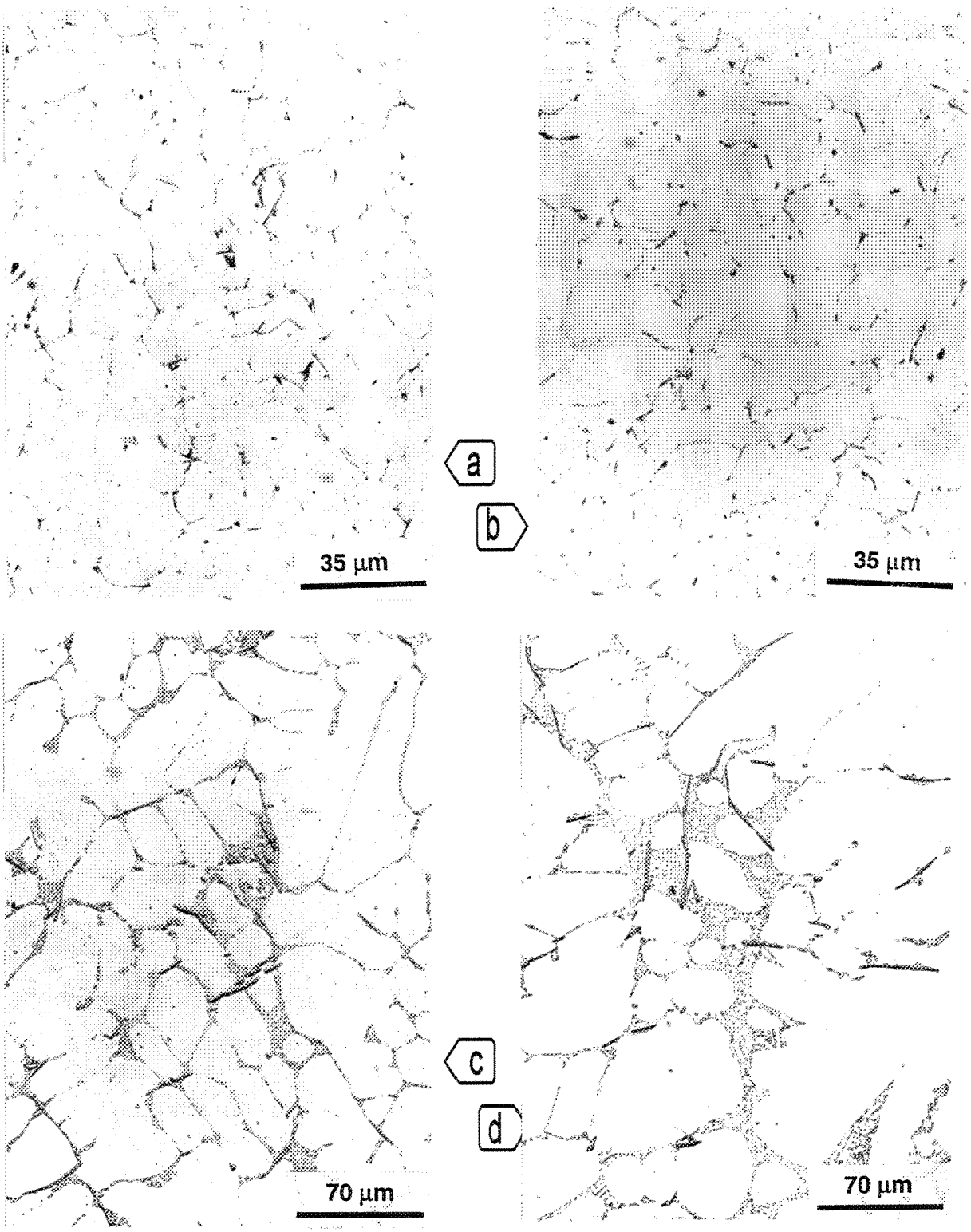

Figure 3.15. Microstructures observed in B alloy samples obtained from test bar gauge section and graphite mold samples: a) G-B, b) G-B1, c) E-C, d) E-C2

The microstructures of non-modified and 354 ppm Sr-modified C alloy (Al-4.5% Si-0.3% Fe-0.6% Mg) samples obtained from the graphite mold casting are presented in Figures 3.15(c) and 3.15(d), respectively. As can be seen, increasing the silicon content promotes the formation of long, thick β-needles and eutectic Si. When the alloy is modified with Sr, the β-needles are not considerably changed, while the eutectic Si regions are well modified *i.e.*, the silicon particles are very fine.

3.3.3.1.2. Industrial Alloys

Non-modified and 415 ppm Sr-modified D alloy (Al-0.7% Si-0.17% Fe-0.7% Mg) samples obtained from graphite and metallic mold castings, are presented in Figure 3.16. As can be seen from the Figure, Sr-modification or an increased cooling rate or a combination of both, results in fragmentation of the β-needles into smaller segments. Solutionizing for 8h at 520 °C causes dissolution of the β-needles and spheroidization of Mg_2Si particles. Solution heat treatment combined with Sr-modification assists in further reduction and fragmentation of the β-needles, Figure 3.17(a) and (b).

Compared to the experimental alloys (shown in Figures 3.7 and 3.9), the β-needles are smaller in this case, due to the comparatively lesser Fe content of the alloy. Figures 3.17(c) and 3.17(d) show the microstructures observed in 6I alloy samples (Al-0.4% Si-0.17% Fe-0.52% Mg) containing 0 and 265 ppm strontium, respectively, and solutionized for 8h at 520 °C. As shown in the case of the experimental alloys, decreasing the Si*/Fe ratio leads to the precipitation of the α-script phase. Modification with 265 ppm strontium produces a structure containing very fine α-script phase particles.

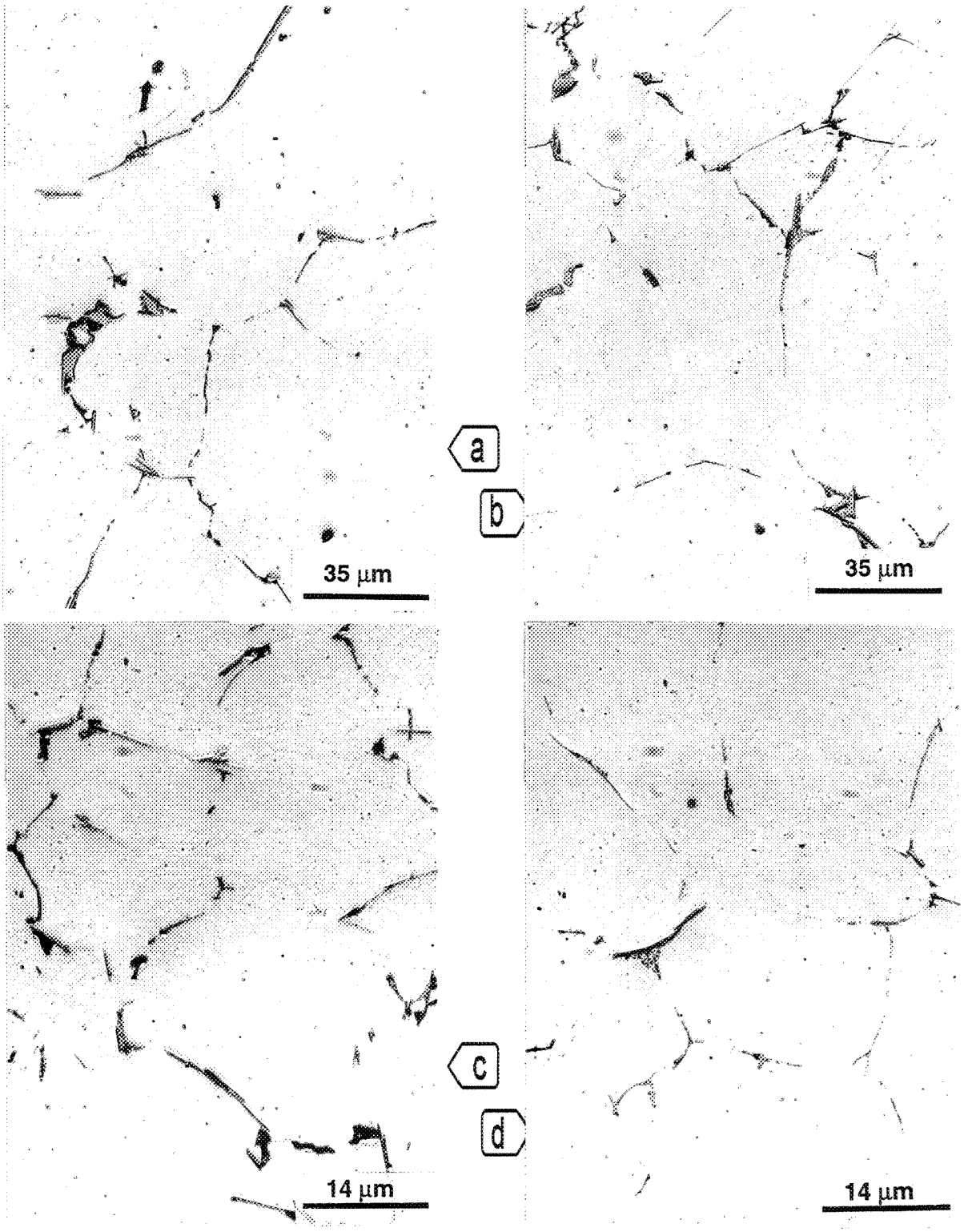

Figure 3.16. Microstructures observed in industrial alloy samples obtained from graphite and metallic molds: a) E-D, b) E-D2, c) M-D, d) M-D2

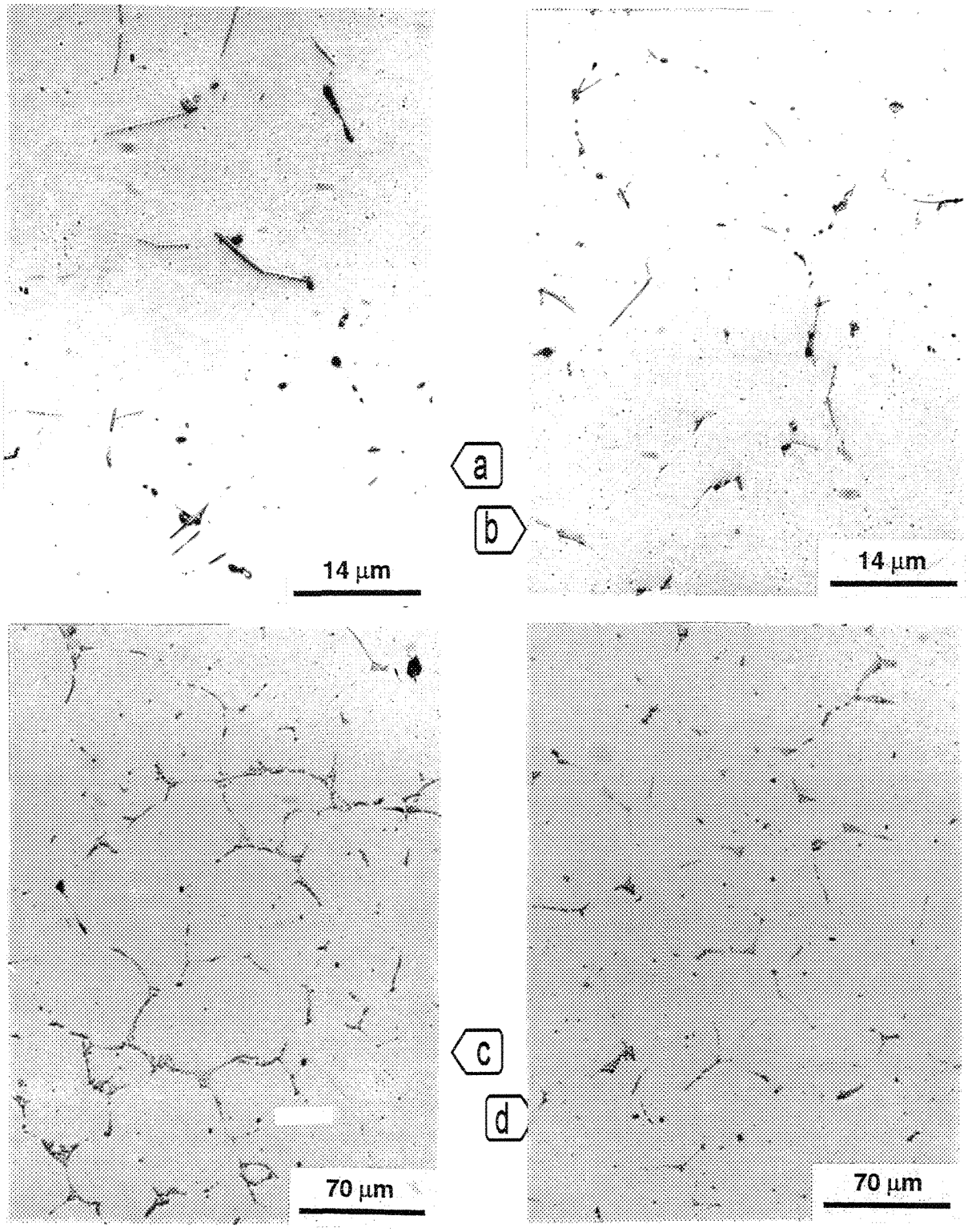

Figure 3.17. Microstructures showing the effect of Si*/Fe ratio and Sr-modification in industrial alloys solutionized for 8h at 520 °C: a) D-SHT, b) D2-SHT, c) 6I-SHT, d) 6IS-SHT

3.3.3.2. Effect of Mn, Mn+Sr Addition

In Figure 3.7, showing the microstructure obtained from the graphite mold sample of A alloy (Al-0.62% Si-0.3% Fe-0.65% Mg) in the absence of Mn, the microstructure was seen to consist of β-phase platelets. With the addition of 0.2 % Mn (Mn/Fe ratio ≈ 0.7) to this alloy (A alloy), the iron intermetallics are seen to precipitate in the α-AlFeMnSi form as $Al_{15}(Fe,Mn)_3Si_2$ phase particles, with Chinese script morphology. The shape and size of these α-particles are shown in Figure 3.18(a). Addition of 206 ppm Sr does not appear to cause significant changes in the iron intermetallic morphology, Figure 3.18(b).

However, with increasing cooling rate, the microstructural constituents become smaller, Figures 3.18(c) and (d). Again, addition of Sr does not appear to cause any significant changes in the microstructure. Solution heat treatment (8h at 520 °C) also does not seem to produce any noticeable changes in the iron intermetallic morphology, Figures 3.19(a) and (b). The higher magnification micrograph of Figure 3.19(c) clearly shows the precipitated α-$Al_{15}(Fe, Mn)_3 Si_2$ intermetallic.

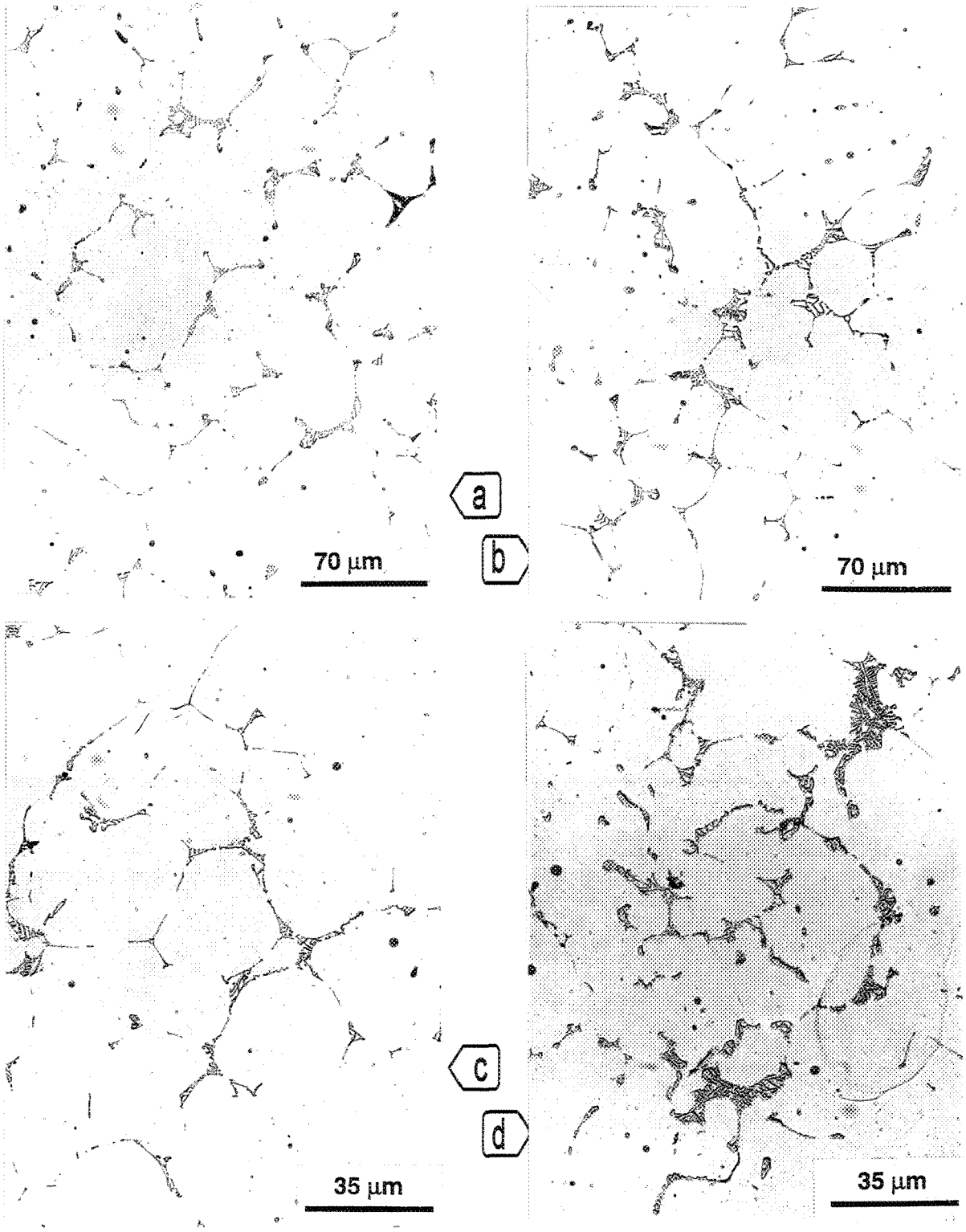

Figure 3.18. Effect of Mn and Mn+Sr additions on iron intermetallic precipitation in graphite (E) & metallic (M) mold samples: a) E-M6, b) E-M6S, c) M-M6, d) M-M6S

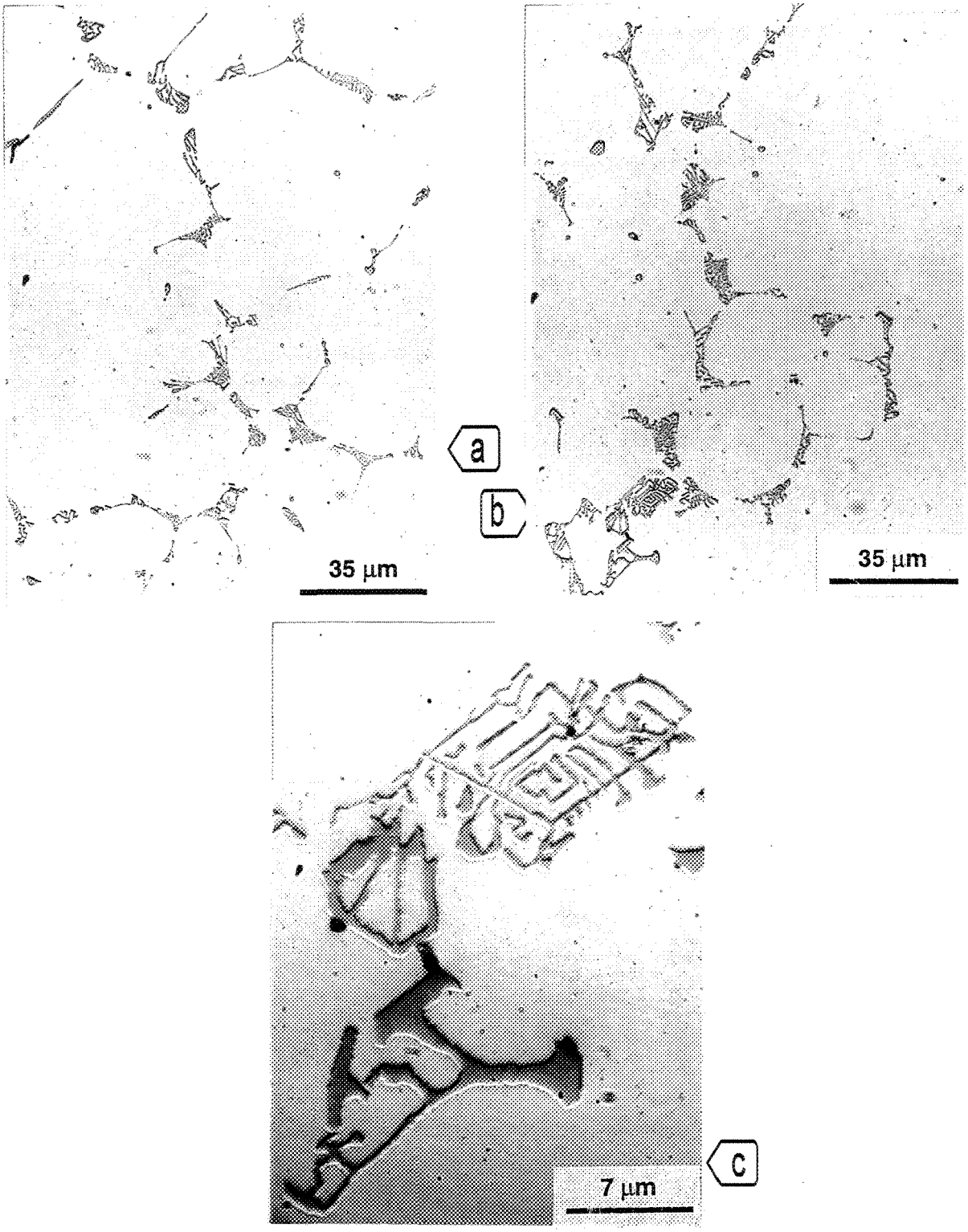

Figure 3.19. Effect of Mn and Mn+Sr on iron intermetallic precipitation in solution heat treated (SHT) samples of: a) M6-SHT, b) M6S-SHT, c) M6S-SHT alloys.

3.3.3.3. Effect of Be, Be+Sr Addition

As mentioned before, in the absence of Be the iron intermetallics in A alloy crystallize only in the β-needle-like morphology. With the addition of 0.01% (1B6), 0.02 % (2B6), and 0.04% (5B6) Be, the iron intermetallics crystallize in the α-AlFeBeSi (Al_8Fe_2BeSi) Chinese script form in the graphite mold samples obtained from these alloys, Figures 3.20(a) through 3.20(c). From these microstructures, it can be seen that increasing the Be content decreases the Chinese script particle size. Figure 3.20(d) is a micrograph taken at 500X magnification, and reveals an α-Al_8Fe_2BeSi particle with Chinese script morphology precipitated in the interdendritic region.

By increasing the amount of Be to 0.13 % (B6 alloy), the interdendritic α-Chinese script phase is replaced by small particles having globular shapes, Figure 3.21(a). Modification with 147 ppm Sr causes significant fragmentation of the α-particles into very small globular particles, as shown in Figures 3.21(b) and 3.21(c).

Figures 3.22(a) through 3.22(d) show the microstructures of metallic mold samples obtained from the unmodified, solution heat treated, and Sr-modified + solution heat treated alloys. As can be seen, increasing the cooling rate leads to precipitation of very fine broken α-Chinese script, Figure 3.22(a), compared to those shown previously in Figure 3.21(a). Again, solutionizing for 8h at 520 °C decomposes the α-Chinese script into very fine particles. The higher magnification micrographs of Figures 3.22(c) and (d) display the decomposed α-Chinese script, where the effectiveness of Be as a α fragmentation agent is markedly increased in the presence of Sr, Figure 3.22(d).

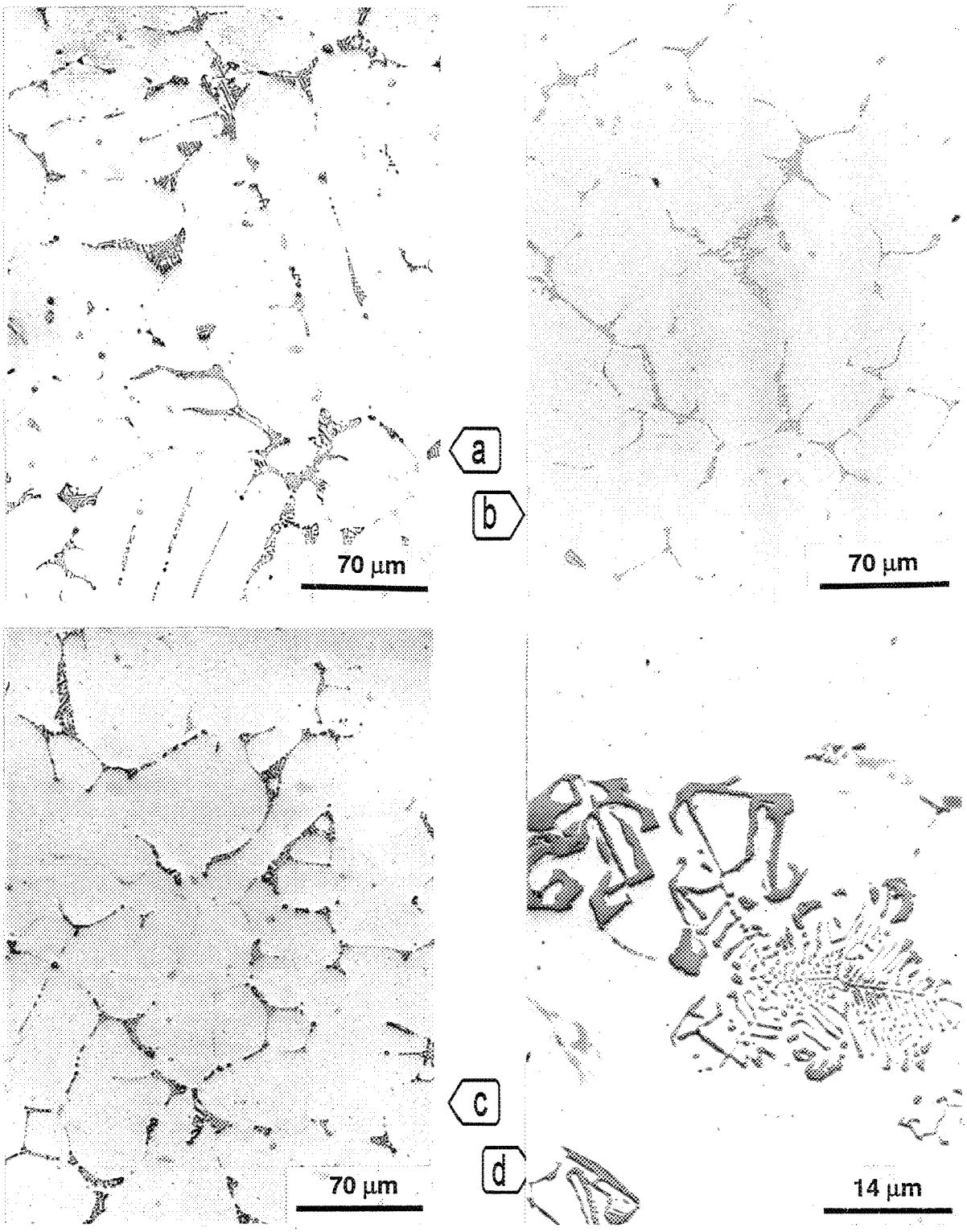

Figure 3.20. Effect of Be addition on the size and distribution of α-phase in: a) E-1B6, b) E-2B6, c) E-5B6, d) E-1B6 alloys.

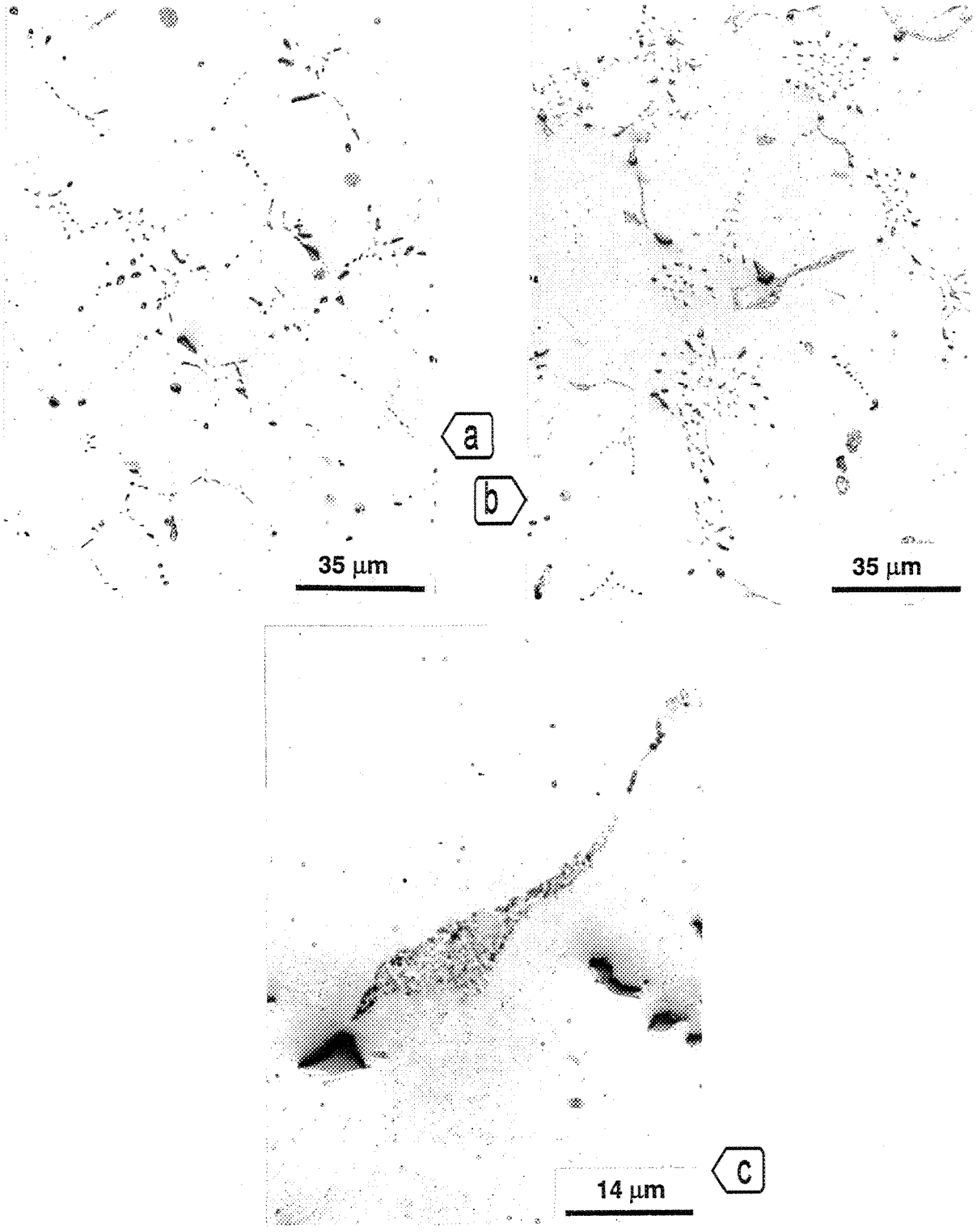

Figure 3.21. Effect of Be and Be+Sr addition on the size and distribution of α-phase in: a) E-B6, b) E-B6, c) E-B6S alloys.

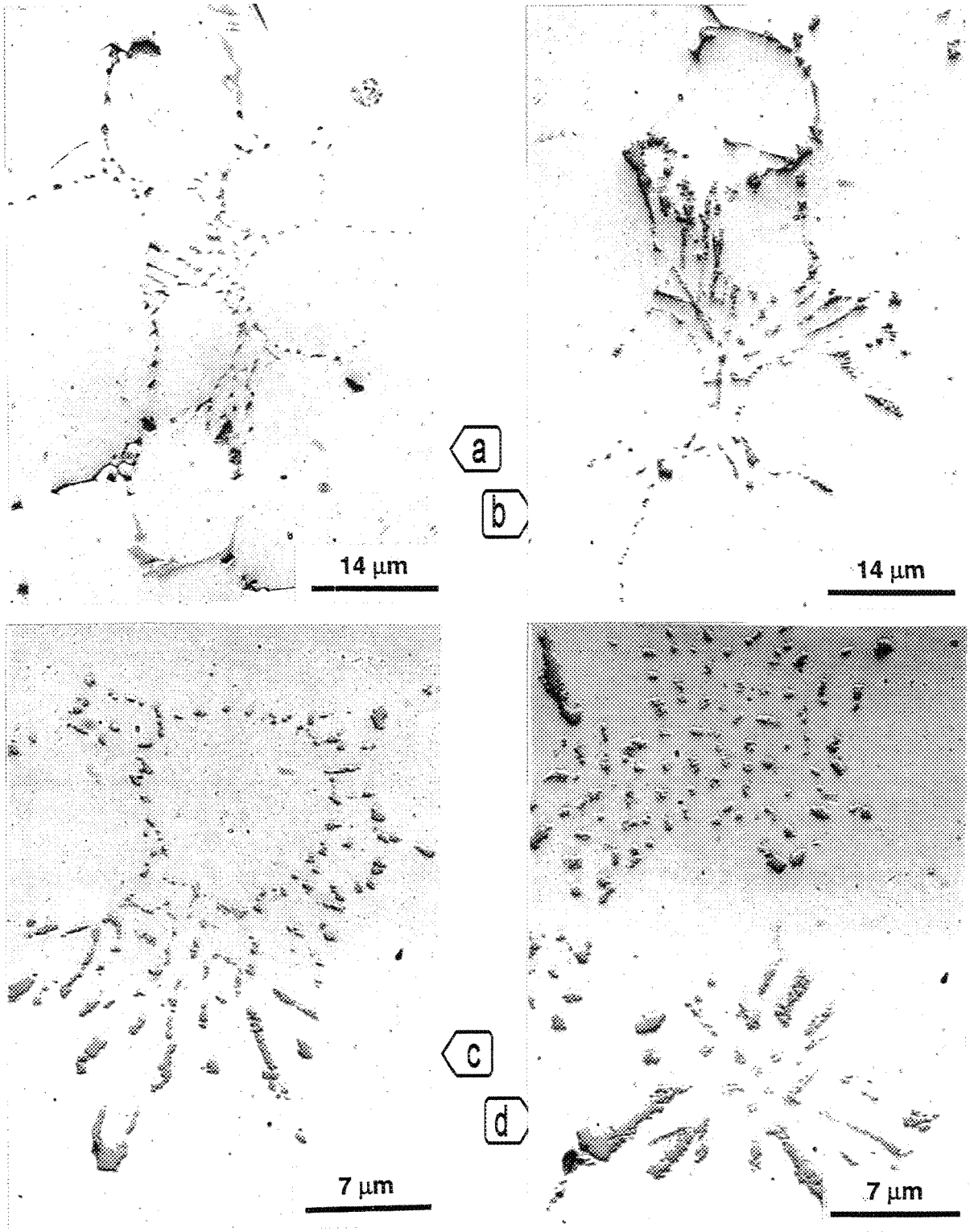

Figure 3.22. Effect of Be and Be+Sr additions on the size and distribution of α-phase in: a) M-B6, b) B6-SHT, c) B6-SHT, d) B6S-SHT alloys.

3.3.4. Mechanism of α and β Phase Precipitation

The present work confirms that the α-Al_8Fe_2Si phase precipitates directly in the liquid state. During solidification, iron is rejected from the Al-dendrites due to its low solubility (0.05%). Depending upon the actual iron and silicon concentrations, the Al_3Fe phase may precipitate first from the liquid aluminum, as shown in Figure 3.23(a), followed by the precipitation of the α-Al_8Fe_2Si phase, Figure 3.23(b). As solidification progresses, the α-Al_8Fe_2Si phase absorbs the silicon from the surrounding liquid and transforms into the β-Al_5FeSi phase, Figure 3.23(c), according to the following peritectic reaction:

$$L\ (Si) + Al_8Fe_2Si + Si \longrightarrow Al_5FeSi$$

The proportion of α and β phases that precipitate will depend on the amount of Sr added to the melt and the Fe:Si ratio.

Figure 3.24 depicts the aluminum-rich corner of the Al-Fe-Si phase diagram, where the effect of Sr and cooling rate in expanding the α-phase region are depicted. In the unmodified alloy, and under equilibrium conditions (*i.e.*, slow cooling rate), the iron and silicon concentrations are at their critical values (black spot in Figure 3.24(a)) for the formation of the β-phase at the α - β border.

Under these conditions, increasing the Sr concentration or the cooling rate or both shifts the α - β border towards higher silicon concentrations. Thus, the black spot falls within the α-phase region instead of in the β-phase region. This explains the stabilization of the α-phase in the Sr-modified alloy samples obtained from the metallic mold.

Increasing the silicon content at the same level of iron shifts the black spot further into the β-phase region, and away from the α - β boundary. Thus, only the β-phase is observed in the microstructure, even in the presence of strontium. In such cases, only a high cooling rate can affect the proportion of α-phase observed in the final microstructure, due to its effect in shifting the α - β boundary to the right.

Mulazimoglu *et al.* [67] proposed that Sr is "adsorbed" at the α-phase particle interface with the Al-matrix and prevents the diffusion of the silicon atoms from the matrix into the α-phase, as shown in Figure 2.16. This results in the stabilization of the α-phase in the microstructure. Thus, increasing the silicon concentration above that of iron (*i.e.*, Fe:Si* <1) would increase the possibility for silicon diffusion through the Sr barrier, and converting the α to β according to the peritectic reaction mentioned previously.

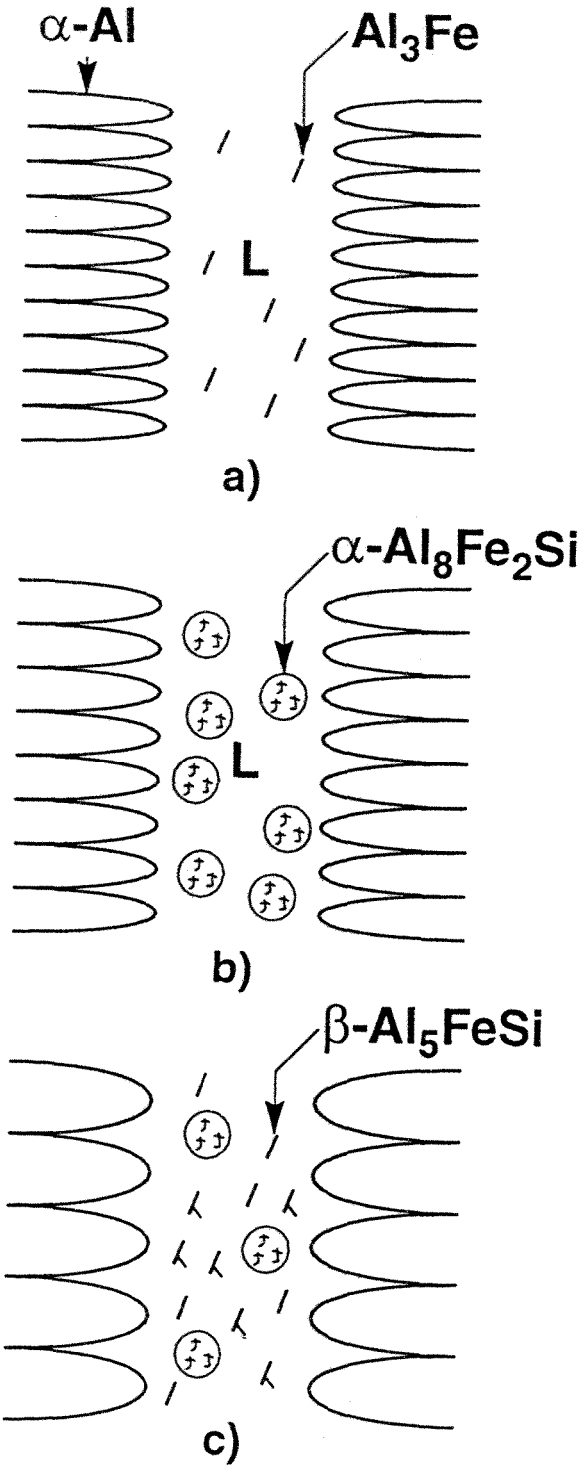

Figure 3.23. Schematic representation of iron intermetallic formation during the solidification process.

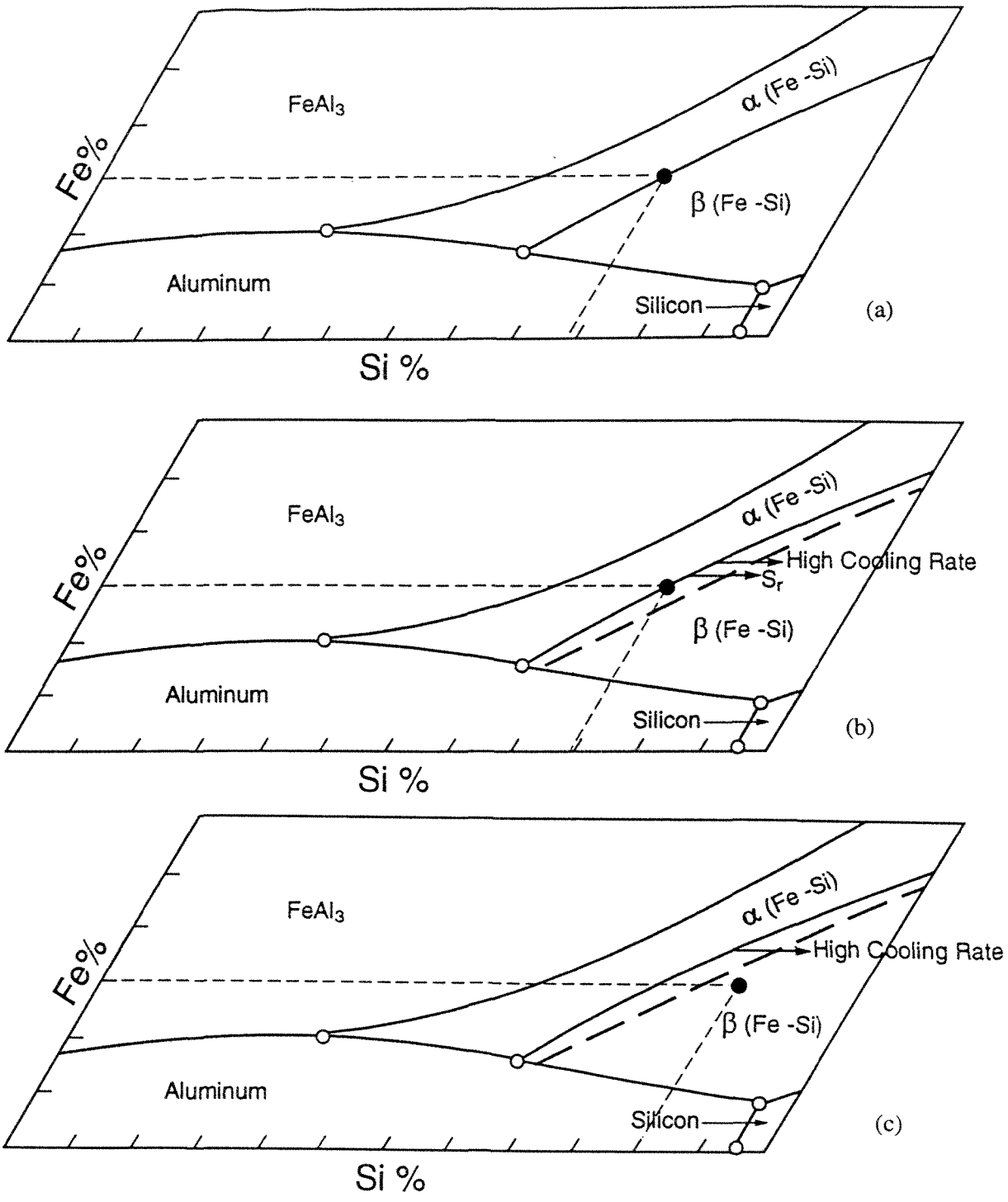

Figure 3.24. Aluminum-rich corner of the Al-Fe-Si phase diagram showing the effects of Sr and cooling rate in expanding the α-phase region.

CHAPTER 4

FORMABILITY

4.1 INTRODUCTION

Formability is defined as the relative ease and success with which a metal can be shaped through plastic deformation. Aluminum is among the most workable common metals. Aluminum shapes usually fail by localized necking or by ductile fracture. Necking is governed largely by material properties such as cold working and strain-rate hardening, and it depends critically on the strain path followed by the forming process. In dilute alloys the extent of necking or limit strain is reduced by cold work, age hardening, gross defects, large grain size, and the presence of alloying elements in solid solution. Ductile fraction occurs as a result of the nucleation and linking of microscopic voids at particles and the concentration of strain in narrow shear bands.

During plastic deformation, 'slip' takes place within the grains along certain crystallographic planes. The slip planes are blocked so that further deformation of the aluminum requires ever increasing forces so that, finally, no additional deformation is possible. The result is a change in grain shape, depending on the character and intensity of the stress. When the working is carried out below the recrystallization temperature, it is called "cold working", and the deformation changes are permanent, resulting in an increase

in strength and a reduction in ductility. A part of the energy used in cold deformation is stored in the form of lattice distortions (atoms with high-energy state). In order to remove these, it is necessary that the atoms migrate to their regular positions (low-energy state). When the cold-worked metal is heated above the recrystallization temperature (annealing), the deformed grains recrystallize into new grains, substantially equiaxed in character. Working of metal above the annealing temperature is known as "hot working". While hot working distorts the grains, they are at a temperature where recrystallization can occur; the result is a normal structure with little change in hardness.

The principal alloys that are strengthened by alloying elements in solid solution are those belonging to the aluminum-magnesium (5XXX and 6XXX) series. These alloys could contain small additions of trace elements and grain refiners used to control the grain or subgrain structure. Iron and silicon impurities and manganese are usually present in the form of intermetallic particles and have little influence on either strain hardening or strain-rate hardening. Thus, they have a relatively minor influence on the necking behaviour. Different types of foreign atoms affect the lattice to differing degrees. Depending on their distribution, they impede the movement of the dislocations and, thereby, the progress of plastic deformation to widely varying degrees.

In this chapter, the effect of trace elements such as Si, Mn, Be, Si+Sr, Mn+Sr and Be+Sr on the formability of the alloys studied will be presented, with the aim of understanding the role of these elements on the structures obtained in the as-cast condition, and after homogenization, cold rolling, recrystallization, and the final deformation. The phases obtained were identified and analyzed using optical microscopy.

4.2 EXPERIMENTAL PROCEDURE

4.2.1. Alloy Preparation

The alloys used and the alloy preparation procedures are the same as those described in Chapter 3 (section 3.2.1). The chemical composition are listed in Table 3.1.

4.2.2. Casting and Sample Preparation

The melt was poured into a rectangular metallic mold with inner dimensions of 15 X 15 X 7 cm. The approximate dimensions of the mold are indicated in Figure 3.1. From each casting, two slabs (7 x 11 x 1.5 cm each) were machined. The slabs were then homogenized for 10 h at 520 °C, followed by air cooling.

4.2.3. Cold Working and Recrystallization Treatment

Cold working of the homogenized slabs was carried out using a Stanat™ rolling machine with two rolls (of 7.5 cm diameter and 12 cm length each). For each pass, 0.5 % deformation was applied, till cracks about 3 mm long were seen to appear on either side of the slabs. The slab edges were machined (5 mm off of each edge) to remove the cracks. Following this, the slabs were annealed for 8h at 520 °C (recrystallization treatment), then air-cooled. The annealed samples were deformed in the same way, to the smallest thickness possible. It is necessary to mention that the deformation of the samples (after annealing) was stopped when the crack length was about 3 mm long on either side. After each 5% deformation, the hardness was measured, using a Brinell Hardness tester, employing a 500 kg load and a 10 mm steel ball indenter.

4.3 RESULTS AND DISCUSSION

4.3.1. Cold Rolling

During the first passes in the rolling process, the thickness reduction per pass is small compared to the thickness. The deformation is then concentrated in the two rolling faces. There will be two nearly independent deformation fields and the friction at each face will result in a concave edge profile, because of which there will be a high tensile stress at the edges near the rolling face. This situation leads to easy initiation of cracks. Normally, the cracks are formed in one of the bulges and do not penetrate the whole thickness.

The effect of increasing the amount of cold rolling on the Brinell hardness (BHN) and starting point of edge cracks is shown in Figures 4.1(a) through 4.1(c) for non-modified alloys, and in Figures 4.2(a) through 4.2(c) for Sr-modified alloys. The effect of alloying elements on the initiation of cracks in the homogenized (10h at 520 °C), cold rolled samples is shown in Figures 4.1(a) and 4.2(a). The arrows in each case indicate the crack initiation points for the respective alloys.

As can be seen, for the base alloy (alloy 6) containing Al-0.61% Si-0.38% Fe-0.644% Mg, the cracks start to appear at 39% deformation. After recrystallization for 8h at 500 °C, further reduction is possible till 36% reduction, giving a total deformation of 80.5% (55 BHN hardness). In the 144 ppm Sr-modified alloy (6S alloy), the cracks start appearing at 40% deformation. After annealing another 34% reduction is possible, giving a total reduction of 78% for the modified alloy (and a hardness of 65 BHN).

With addition of silicon to this alloy (S6 alloy with 1.01% Si), the cracks start to appear at 21% deformation, further deformation of 16% is obtained after annealing, giving

a total deformation of 43% (42 BHN hardness). Modification with Sr (163 ppm) results in the appearance of cracks at 20% deformation, a further 15% deformation after annealing, and a total deformation of 45% (36 BHN hardness). These alloys were found to have the lowest formability in the present study.

Normally, Mn increases the strain hardening and decreases ductility. Addition of Mn (M6 alloy, with 0.196% Mn) to the base alloy (6 alloy) lowers the starting point of cracks to 31% deformation. Further deformation of 60% is obtained after annealing, giving a total deformation of 77% (49 BHN hardness). Modification with 206 ppm Sr is not so effective, as the cracks start to appear at 21.5% deformation. Further deformation of 26% is possible after annealing, giving a total deformation of 67% (55 BHN hardness) for this alloy.

With the addition of 0.022% Be to the non-modified base alloy (alloy 6), the cracks start appearing at 42% deformation. Another 24% deformation is possible after annealing, giving a total deformation of 69% (57 BHN hardness). The combined effect of Be with 171 ppm Sr changes the crack initiation point to 50% deformation, and 94% deformation is possible after annealing. The total deformation is 97% (53 BHN hardness). This was the maximum reduction that was possible for the experimental alloys.

In the 6I industrial alloy (Al-0.43% Si-0.18% Fe-0.519% Mg), the cracks start appearing at 36% deformation, further deformation after annealing is 60.5%, and the total deformation is 97% (42 BHN hardness). Modification with 265 ppm Sr allows for a 48% deformation before the cracks begin to form, a further reduction of 94% after annealing, and a total deformation of 97% (53 BHN hardness).

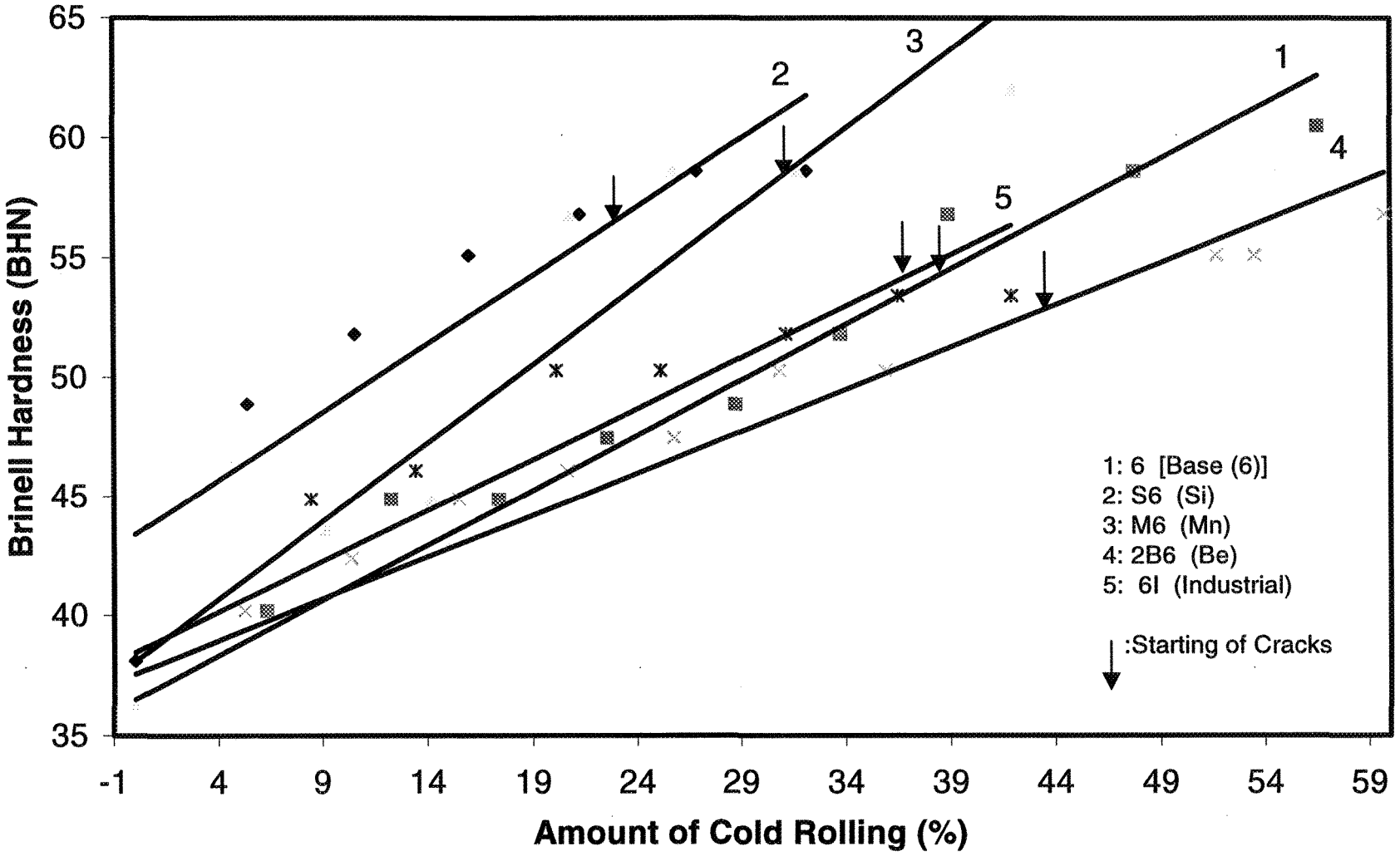
Brinell Hardness (BHN)
65
60
55
50
45
40
35
-1
4
9
14
19
24
29
34
39
44
49
54
59
Amount of Cold Rolling (%)
1
2
3
4
5
1: 6 [Base (6)]
2: S6 (Si)
3: M6 (Mn)
4: 2B6 (Be)
5: 6I (Industrial)
:Starting of Cracks

Figure 4.1(a)

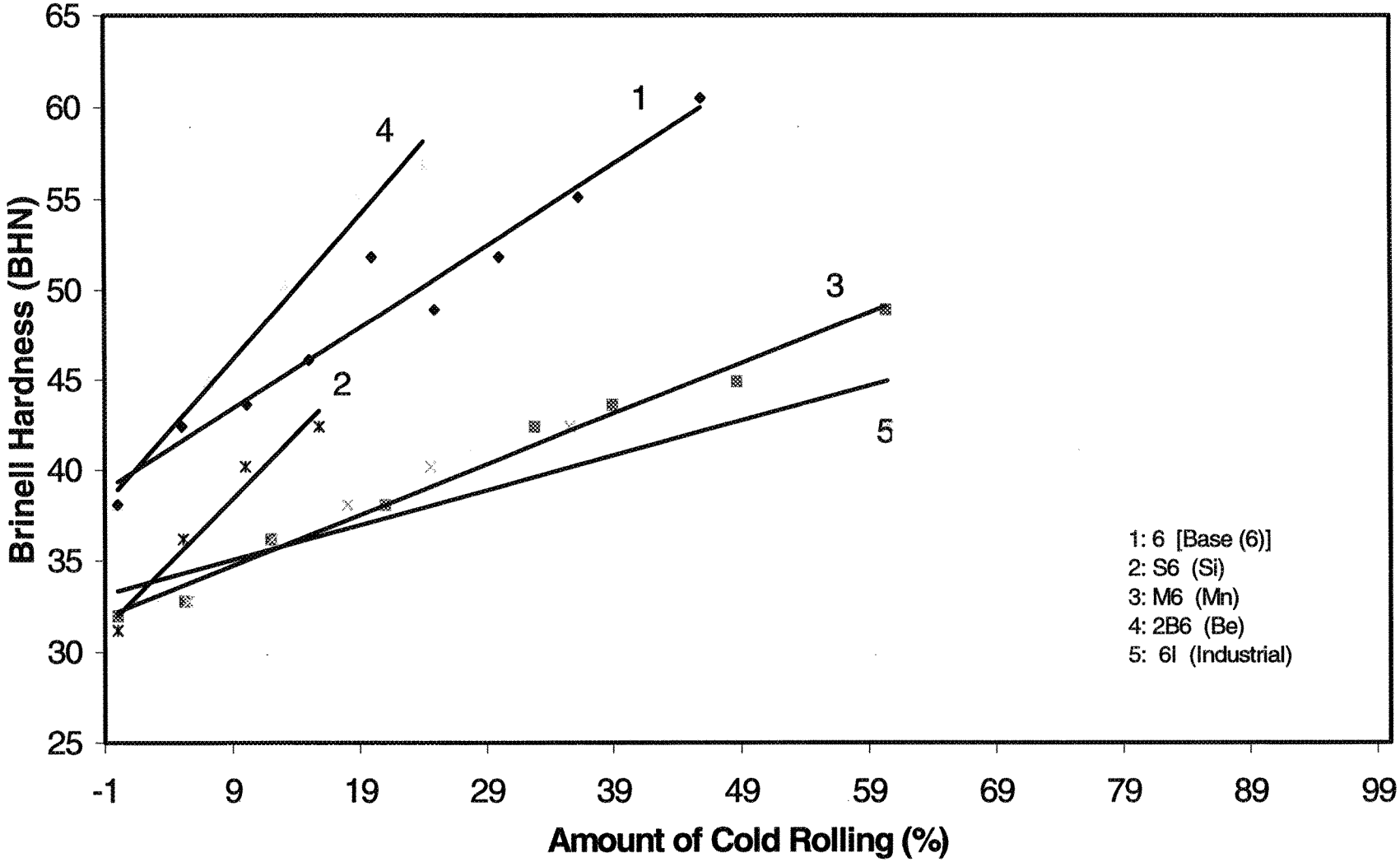
Brinell Hardness (BHN)
65
60
55
50
45
40
35
30
25
-1
9
19
29
39
49
59
69
79
89
99
Amount of Cold Rolling (%)
1
2
3
4
5
1: 6 [Base (6)]
2: S6 (Si)
3: M6 (Mn)
4: 2B6 (Be)
5: 6I (Industrial)

Figure 4.1(b)

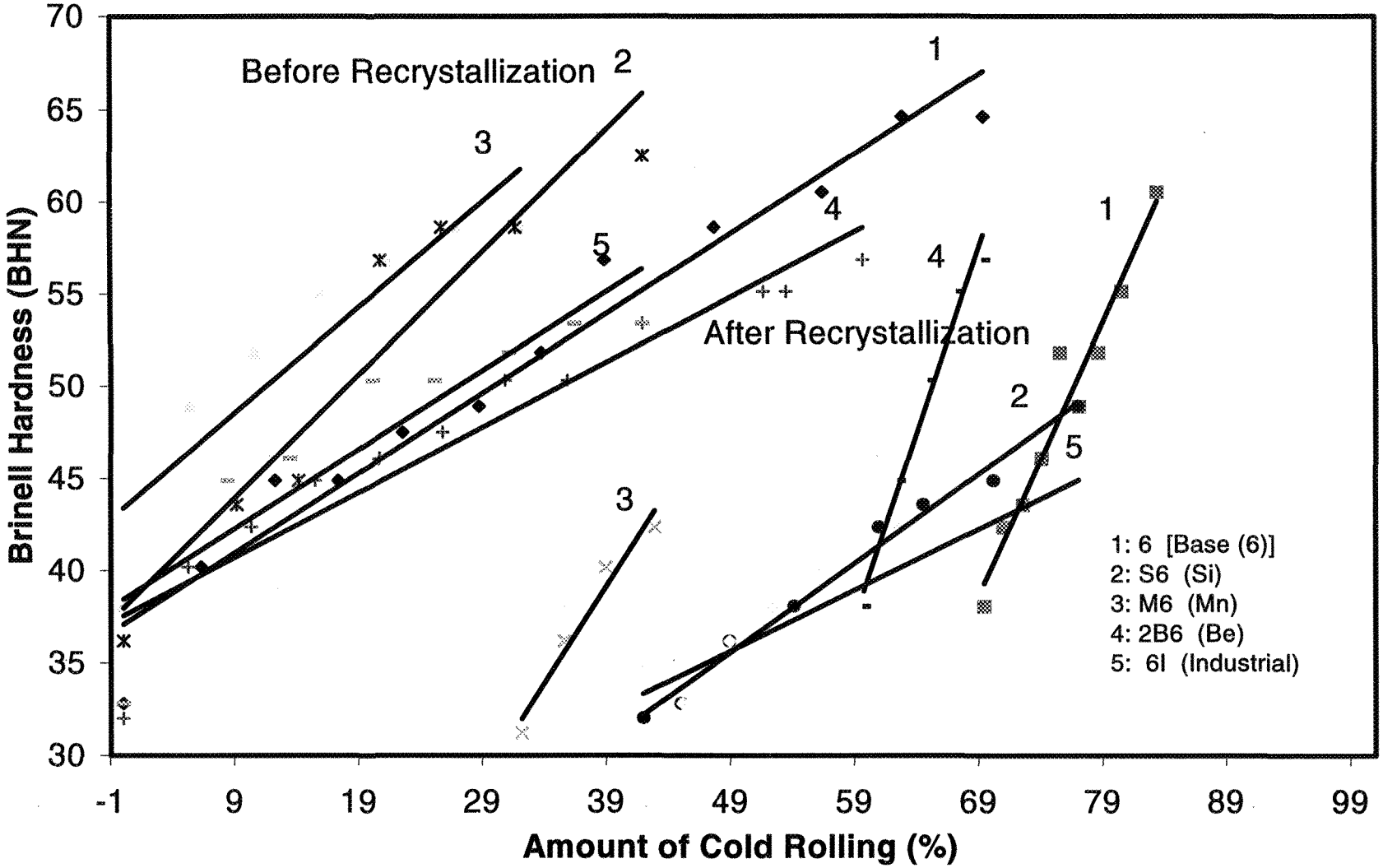

Figure 4.1(c)

Figure 4.1. Effect of cold rolling deformation before edge cracking on Brinell hardness (BHN) in non-modified alloys: (a) before recrystallization for 8h at 520 °C, (b) after recrystallization, (c) total deformation

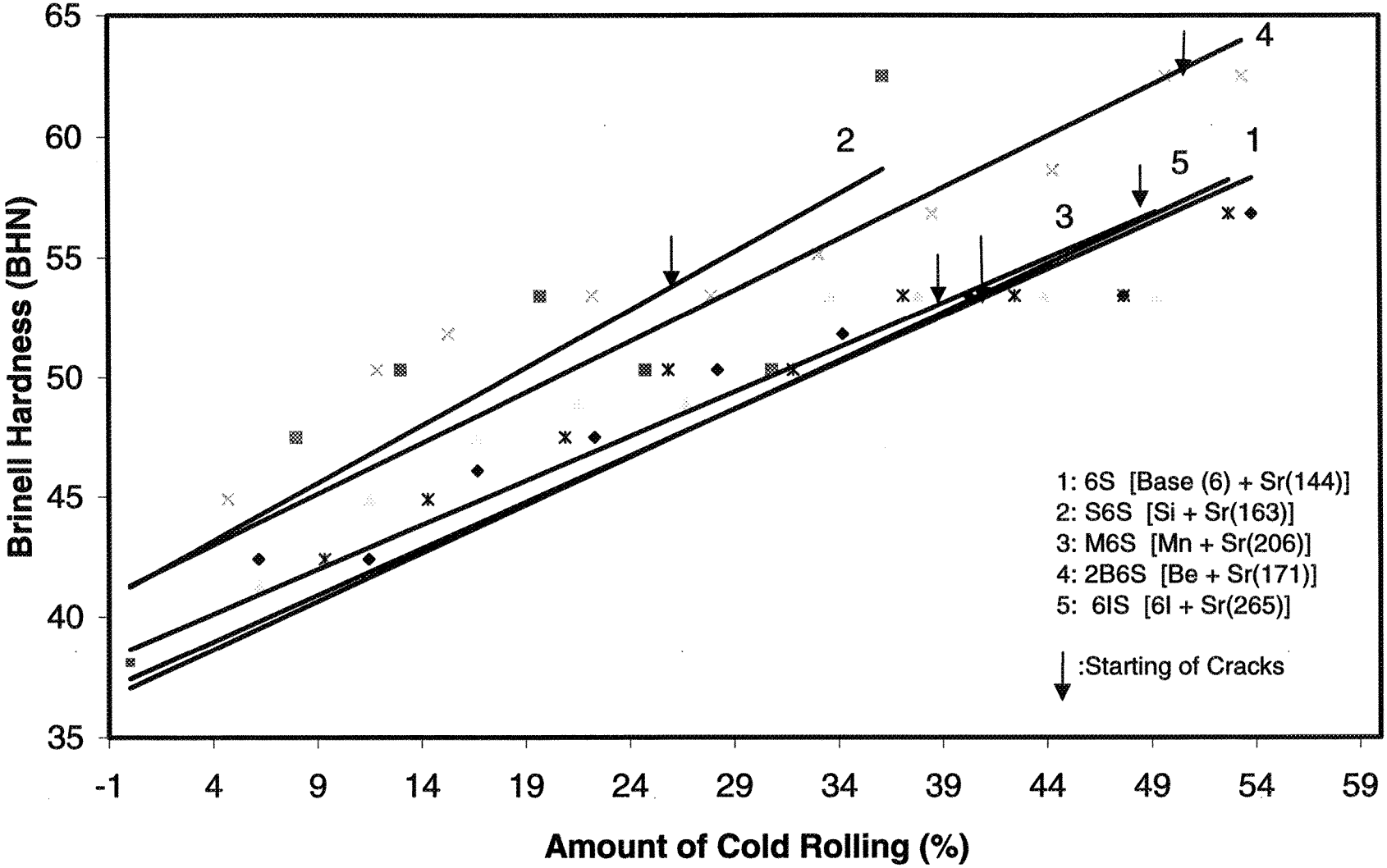
Brinell Hardness (BHN)
65
60
55
50
45
40
35
-1
4
9
14
19
24
29
34
39
44
49
54
59
Amount of Cold Rolling (%)
1
2
3
4
5
1: 6S [Base (6) + Sr(144)]
2: S6S [Si + Sr(163)]
3: M6S [Mn + Sr(206)]
4: 2B6S [Be + Sr(171)]
5: 6IS [6I + Sr(265)]
:Starting of Cracks

Figure 4.2(a)

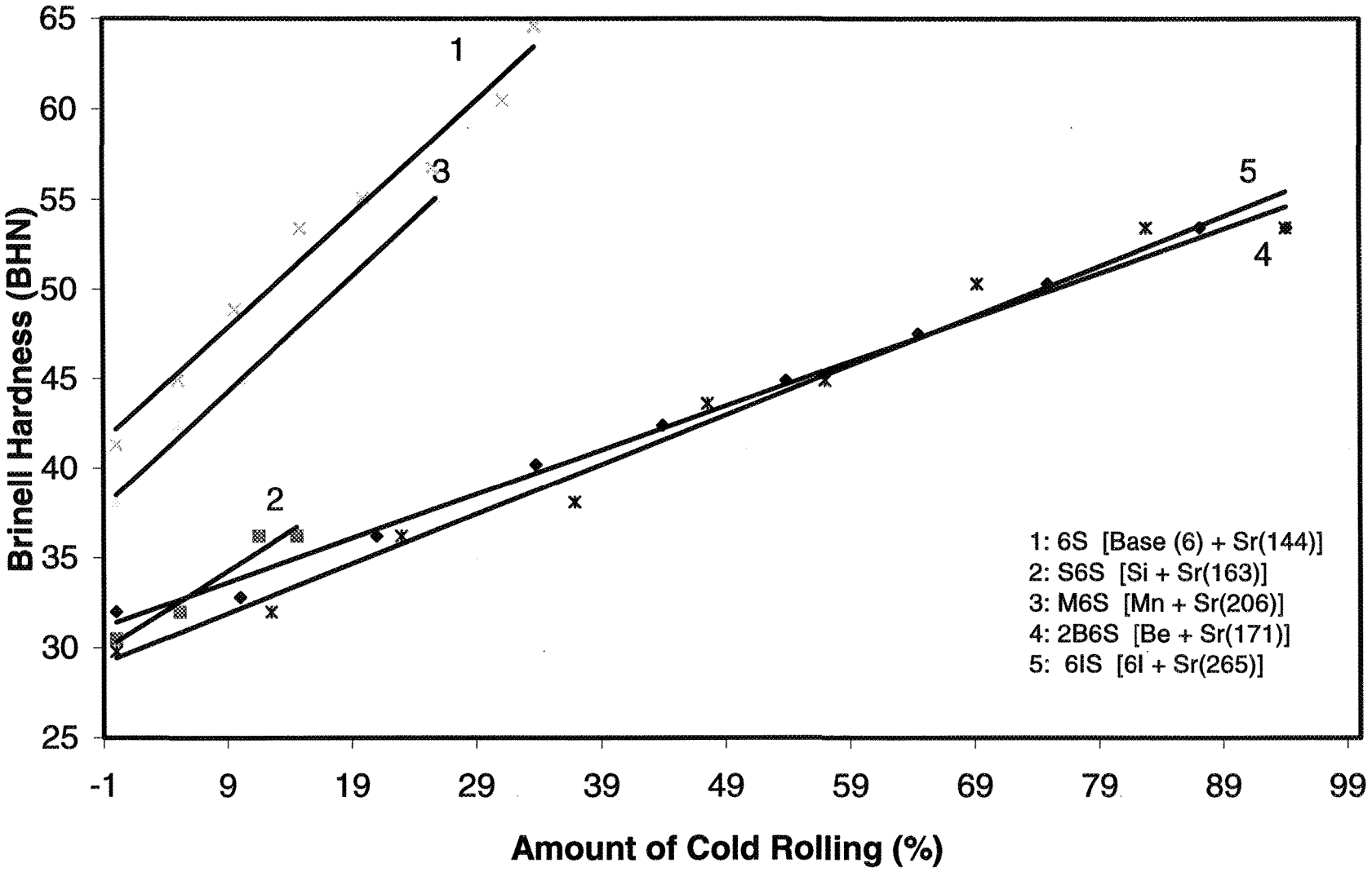
Brinell Hardness (BHN)
65
60
55
50
45
40
35
30
25
-1
9
19
29
39
49
59
69
79
89
99
Amount of Cold Rolling (%)
1
2
3
4
5
1: 6S [Base (6) + Sr(144)]
2: S6S [Si + Sr(163)]
3: M6S [Mn + Sr(206)]
4: 2B6S [Be + Sr(171)]
5: 6IS [6I + Sr(265)]

Figure 4.2(b)

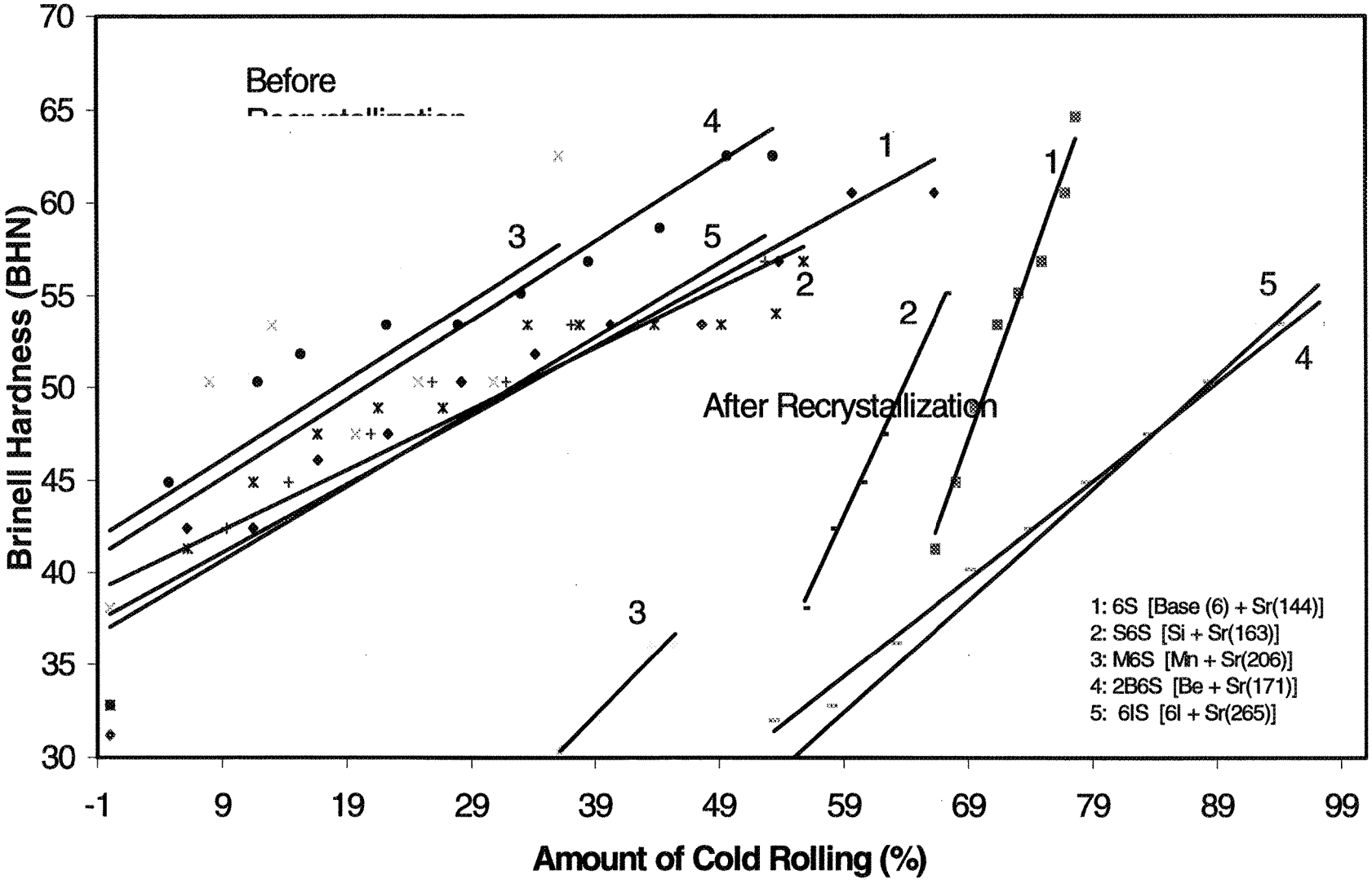

Figure 4.2(c)

Figure 4. 2. Effect of cold rolling deformation before edge cracking on Brinell hardness (BHN) in Sr-modified alloys: (a) before recrystallization for 8h at 520 °C, (b) after recrystallization, (c) total deformation

4.3.2. Microstructural Analysis

As shown previously in Figure 3.8(a), the structure of 6 alloy (A alloy) consisted of β-phase platelets, where modification with 144 ppm strontium did not change their morphology. The β-needles in both cases had a slightly nonfaceted interface with the aluminum matrix. With addition of Si (S6 alloy), and after homogenizing, the β-needles become more thick and stable, Figure 4.3(a). The cold rolled structure of this alloy until cracks start to appear is demonstrated in Figure 4.3(b). The structure is seen to contain elongated grains with broken β-needles situated along their lengths. The cold rolled structure after annealing reveals that the β-needles are broken into smaller pieces but still retain their needle shapes and non-faceted interface with the aluminum matrix, Figure 4.3(c). These interfaces are very weak, and as a result, cracks start to appear at these interfaces as the cold working is continued, Figure 4.3(d).

As mentioned in Chapter 3 (Section 3.3.3.2), with the addition of Mn, the iron intermetallics precipitate in the α-$Al_{15}(Fe,Mn)_3Si_2$ Chinese script form, as shown in Figure 4.4(a). The cold worked structure after annealing is shown in Figure 4.4(b). As can be seen, the particles have broken into smaller fragments, with high concentrations in some regions along the grain boundaries. Such regions with a high density of particles hinder the plastic flow, and further deformation results in the appearance of cracks in these areas.

In the previous section, a combined addition of Be and Sr was seen to result in the highest work hardening rate. Figure 4.5(a) illustrates the structure of the corresponding alloy (2B6S alloy) after homogenization. As shown earlier, the structure consists of very

fine α-Al_8Fe_2SiBe Chinese script particles. The structure obtained after cold working until the appearance of the first cracks is shown in Figure 4.5(b), and consists of very fine and globular shaped particles elongated along the rolling direction. Figure 4.5(c) illustrates the microstructure of this alloy after cold rolling and annealing, where fragments of very fine globular α-particles may be observed in the structure.

The microstructures of non-modified and 265 ppm Sr-modified industrial alloy (Al-0.43% Si-0.18% Fe-0.52% Mg alloy) are presented in Figures 4.6(a) through 4.6(d). In the homogenized condition, the structure of the non-modified alloy contains α-Chinese script particles. The structure of the cold rolled alloy after annealing is very fine, again with a high density of particles present in some grain boundaries. Modification with 265 ppm Sr can lead to the precipitation of very fine α-Chinese script particles. After homogenization, the cold rolled alloy structure exhibits very fine script particles along the grain boundaries.

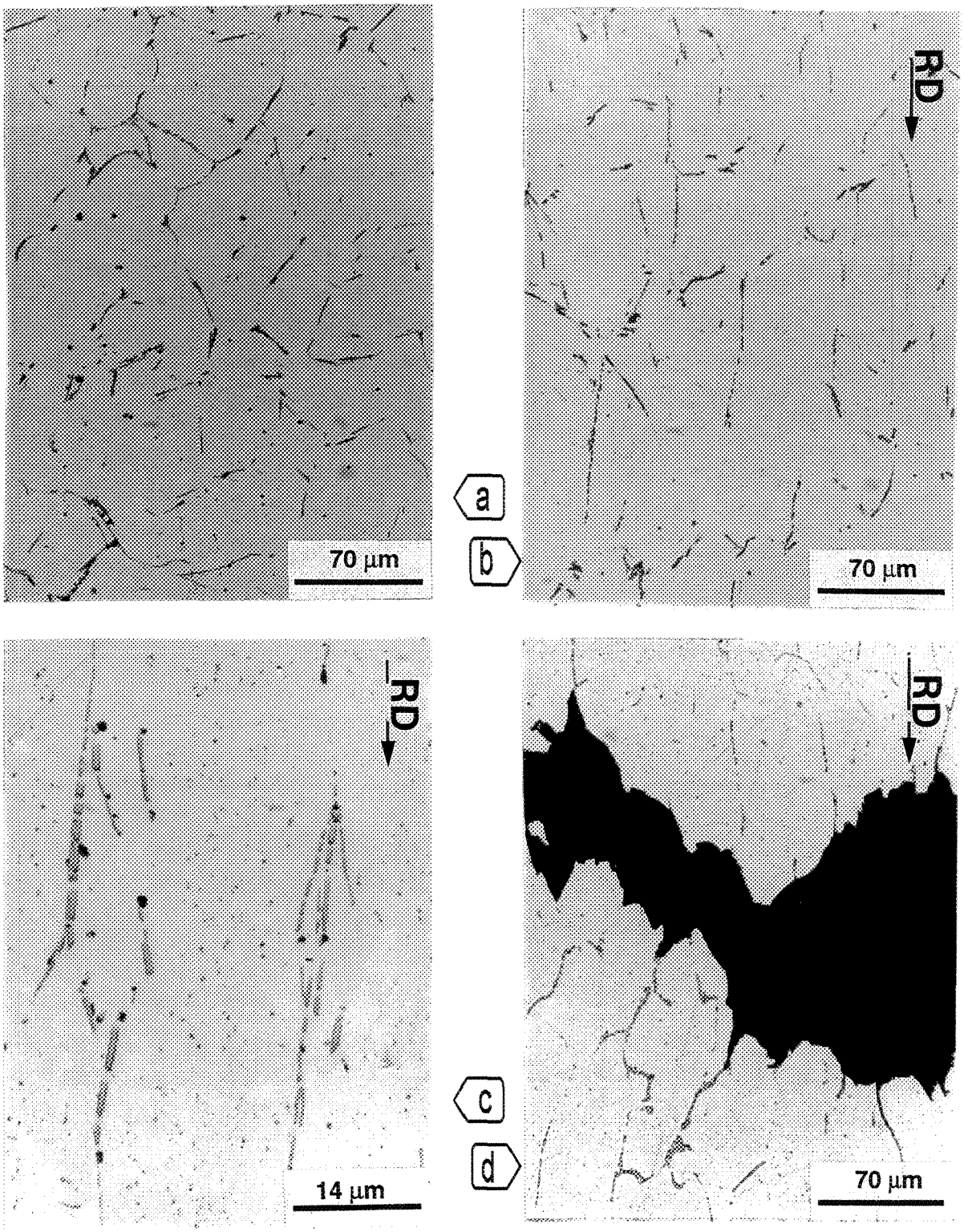

Figure 4.3. Microstructures showing the effect of cold working on S6 alloys: a) homogenized; b) cold rolled after homogenizing; c) and d) cold rolled after annealing

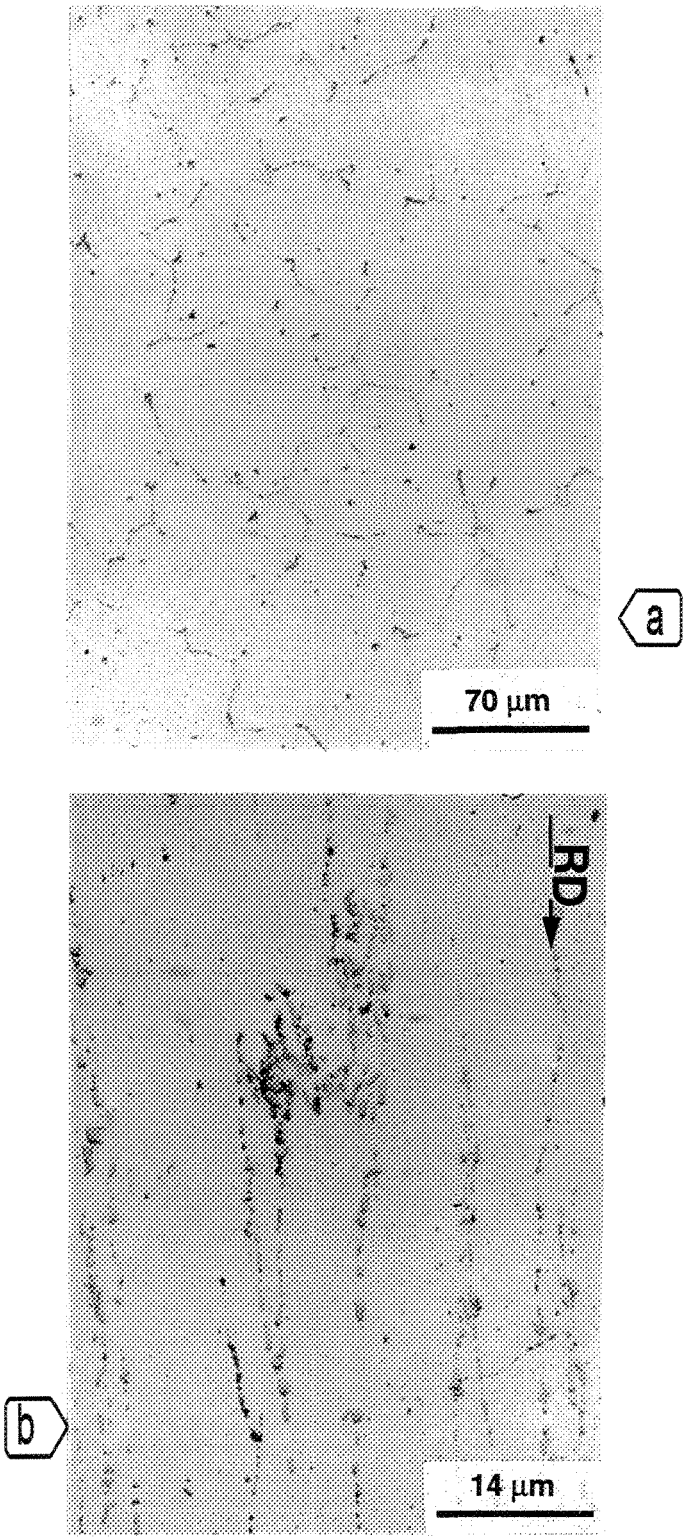

Figure 4.4. Microstructures showing the effect of cold working on M6 alloys: a) homogenized, b) cold rolled after annealing

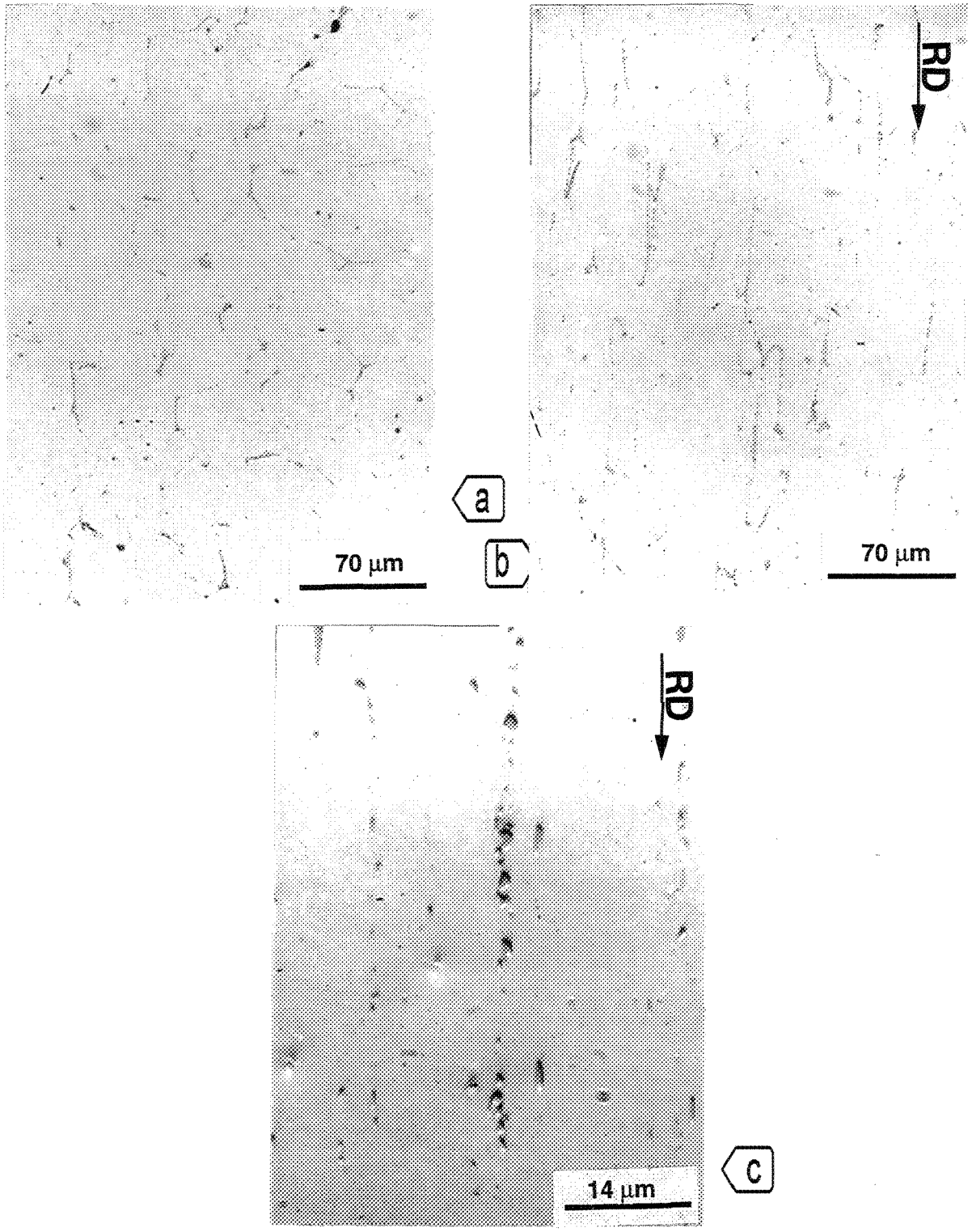

Figure 4.5. Effect of cold working on 2B6S alloy samples: a) after homogenization, b) cold rolled after homogenization, c) cold rolled after annealing

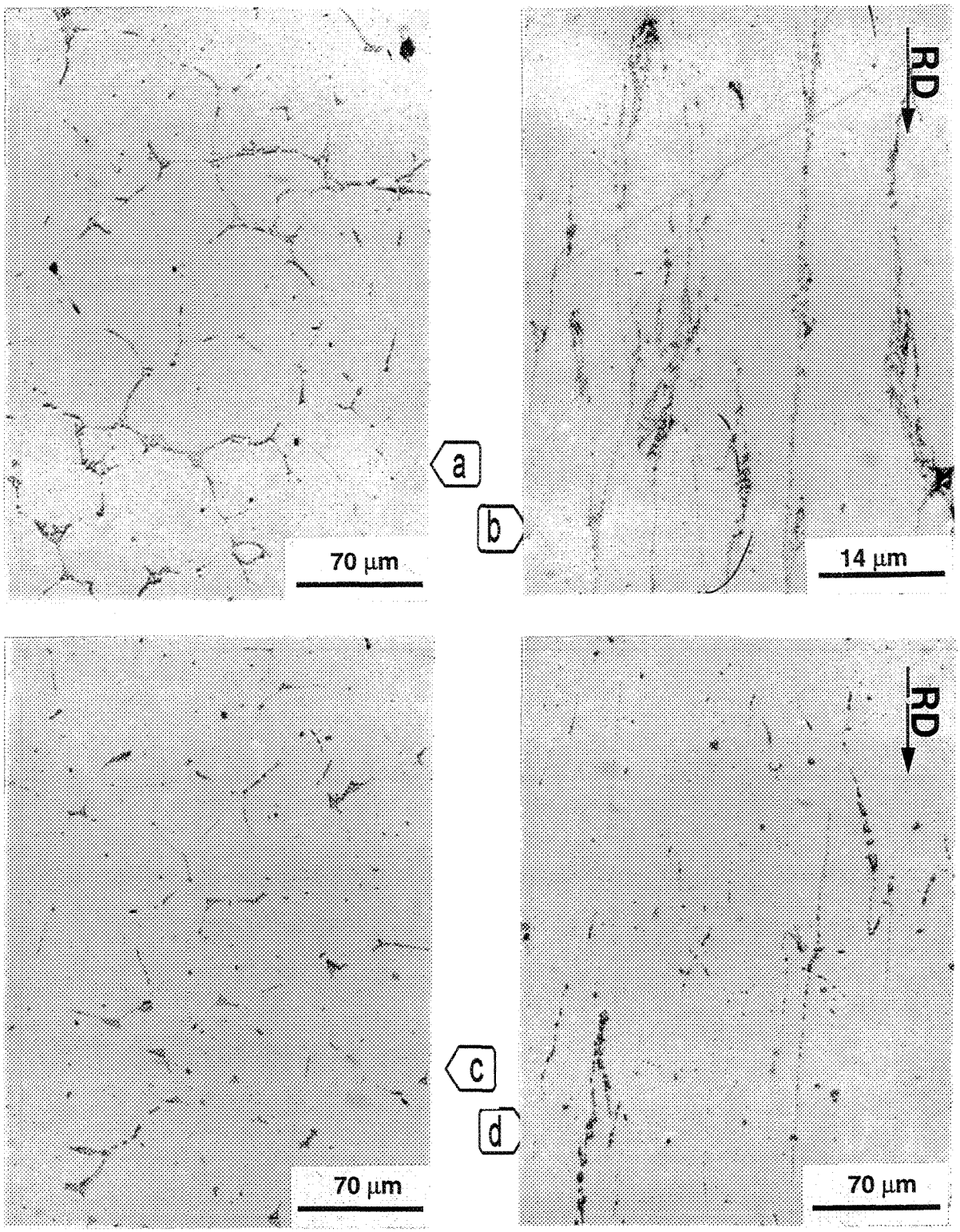

Figure 4.6. Effect of cold working on 6I alloys-Non-modified alloys: a) homogenized, b) cold rolled after annealing; Sr-modified alloys: c) homogenized, d) cold rolled after homogenizing

CHAPTER 5

TENSILE PROPERTIES AND AGING RESPONSE

5.1 INTRODUCTION

The main objective in the design of aluminum alloys is to increase strength, hardness, and resistance to wear, and creep or fatigue. Effects on these properties are specific to different combinations of alloying elements, thermomechanical history, heat treatment or cold working process. The heat-treatable alloys contain alloying elements that are more soluble at elevated temperatures than at room temperature.

Traditionally, aluminum alloy is either direct chill cast as ingot or continuous cast in the form of a thick strip material, and then hot rolled to a preliminary thickness. In a separate operation, the strip is then cold rolled to the final thickness and wound into coil. The coil then undergo solution heat treatment, which involves heating the metal to a suitably high temperature (*e.g.*, 480-580 °C) to bring back all of the soluble alloying elements into solid solution, and then rapid quenching to ambient temperature to create a solid supersaturated solution. The metal is then precipitation hardened by holding it at room temperature (or a higher temperature to accelerate the effect) for a period of time, to cause the formation of the precipitates.

It is highly desirable that the alloy sheet, when delivered to the manufacturer, be relatively easily deformable so that it can be stamped or formed into the required shapes without difficulty and without excessive springback. However, it is also desirable that the sheets, once formed and subjected to the normal painting and baking procedure, be relatively hard so that thin sheets can be employed and still provide good dent resistance.

Gupta and Wheeler [81] have patented a process for producing solution heat treated aluminum alloy sheet material. The method comprises subjecting the hot or cold rolled aluminum alloy sheet to solution heat treatment, followed by quenching before substantial age hardening has taken place. Subjecting the alloy sheet material to one or more subsequent heat treatments involves heating the material to a peak temperature in the range of 130-270 °C, holding the material at the peak temperature for a period of time, and cooling the alloy from the peak temperature to a temperature of 85 °C or less. The sheet material treated in this way has a good paint bake response.

The relative rates at which solution and precipitation occur with different solutes depend on their respective diffusion rates, in addition to their solubilities and alloying contents. Bulk diffusion coefficients for several commercially important alloying elements in aluminum are shown in Figure 5.1. As can be seen, magnesium and silicon, which are the principal solutes involved in precipitation hardening reactions, have relatively high rates of diffusion in aluminum.

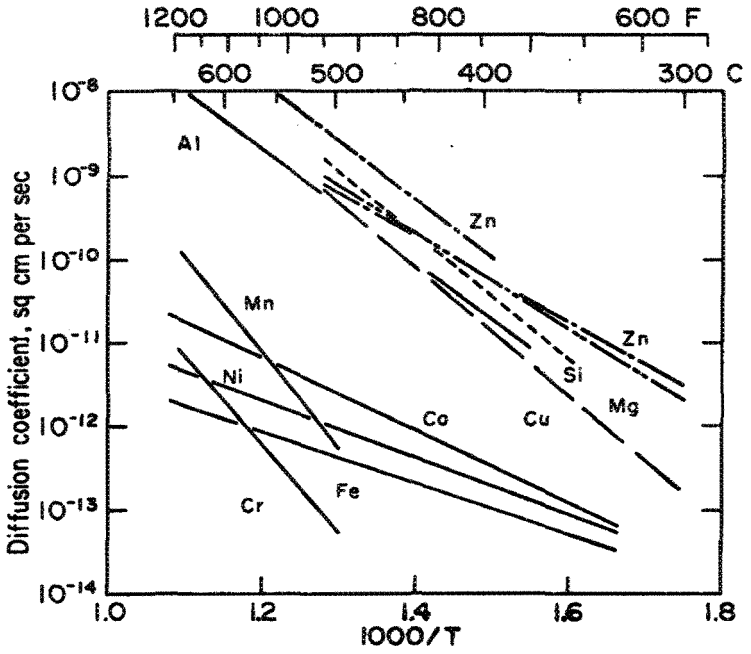

Figure 5.1. Diffusion coefficients for various elements in aluminum [1].

In Chapter 3 of the present study, we reported on the microstructure of the alloys studied, and a summary of these observations is provided in Table 5.1. In this chapter, the effect of trace elements on the tensile properties of these alloys in the non-modified and Sr-modified conditions is described and discussed. The effect of aging time and prestraining on the precipitation of Mg_2Si, and their impact on the alloy tensile properties is also examined.

Table 5.1. Summary of microstructural observations reported in Chapter 3.

Alloy code	6	6S	S6	S6S	M6	M6S	Be Alloys *	6I	6IS
Intermetallic type	β	β+α (80% α)	β	β	α-Mn	α-Mn	α-Be	α	α

* 5B6, 5B6S, B5, B6S, 2B6, 2B6S, 1B6 alloys
α: Al_8Fe_2Si α-Mn: $Al_5(Fe, Mn)_3Si_2$
β: Al_5FeSi α-Be: Al_8Fe_2BeSi

5.2 EXPERIMENTAL PROCEDURE

5.2.1. Alloy Preparation

The industrial 6063 alloy was received in two batches from two different sources in the form of as-cast and cylindrical ingots that were cut into smaller pieces. The chemical compositions of the as-received 6063 alloys (coded D and 6I) are given in Table 3.1. For the experimental alloys, pure aluminum ingots (99.95% pure, in 12.5 kg ingots) were used, cut into two halves. Alloy melts were prepared using the procedure described below for both industrial and experimental alloys.

The cut pieces in each case were cleaned, dried, and melted in a silicon carbide crucible of 40-kg capacity, using an electrical resistance furnace. The melting temperature was held at 735 °C ± 5 °C. At this temperature, the required melt treatment was given: measured amounts of Mg, Si, Mn, Be and Sr (in the form of pure Mg metal, pure Si, and Al-25% Mn, Al-5% Be and Al-10% Sr master alloys) were added with the help of a perforated graphite bell. In the case of the experimental alloys, small amounts of iron as Al-25% Fe master alloy were added to the molten aluminum. Strontium was added in amounts of 0, 250, 500, 750 and 1000 ppm, to cover the unmodified, modified and over-modified conditions. Prior to casting each melt was grain refined using Al-5%Ti-1%B master alloy (based on a 0.01-0.02 % Ti addition).

The molten metal was degassed for ~30 min using pure argon (injected into the molten metal using a graphite impeller rotating at ~150 r.p.m), then the melt surface was thoroughly skimmed before pouring. In all cases, the hydrogen level was less than 0.1

ml/100 g Al (as measured by an AlScan^{TM} apparatus). Samples for chemical composition were also taken for each pouring.

5.2.2. Casting and Sample Preparation

The prepared molten metal was poured into a Stahl permanent mold (type ASTM B-108) heated at 420 °C. Figure 5.2 shows the schematic diagram of a Stahl mold casting, where the dimensions of the test bars obtained from the casting (two per casting) are indicated as well. The mold walls were coated with a thick layer of vermiculite. This type of coating reduces the heat transfer rate which in turn allows hot metal with proper fluidity to enter into the casting (test bar) cavities. The gauge length part of the mold, however, was coated with a thin layer of graphite (~50 μm) to enhance the cooling rate and, hence, decrease the gas porosity obtained [82]. The two coatings were thus expected to improve the quality of the test bars produced. Test bars were prepared for tensile testing in the following conditions:

* As-cast condition (coded As)
* Solution heat treated condition (coded T0), where the solution treatment was carried out for 8h at 520 °C in a forced-air furnace followed by quenching in hot water (60 °C). The quenched test bars were kept at -20 °C to prevent any natural aging.
* Artificially aged condition, where the test bars were aged at 175 °C for 1, 3, 8, 24 and 100h times (coded T1, T3, T8, T24 and T100) in a forced-air furnace, followed by air-cooling. The schematic diagram of Figure 5.2 shows the temperature-time details for the solution heat and aging treatments.

* Prestrained condition (coded P), where the solution heat treated test bars were pulled to 4% under tension, followed by aging at 175 °C for 1, 3, 8 and 24h times, then air-cooled (coded P1, P3, P8 and P24). Thereafter, the test bars were pulled to final fracture at room temperature.

In order to study the presence of porosities and cavities, selected test bars were also analyzed using X-ray radiography.

5.2.3. Tensile Testing

The test bars (five test bars per treatment/condition) were pulled to fracture at room temperature in an Instron Universal testing machine at a strain rate of $4x10^{-4}$/s. A strain gauge extensometer (2-in or 5 cm range) was attached to the gauge section of the test bars for measuring the alloy ductility. The data was analyzed using special software designed for this work. Mechanical properties, namely, yield strength (YS) at 0.2% offset strain, ultimate tensile strength (UTS), and fracture elongation (EL%), were derived from the data acquisition system.

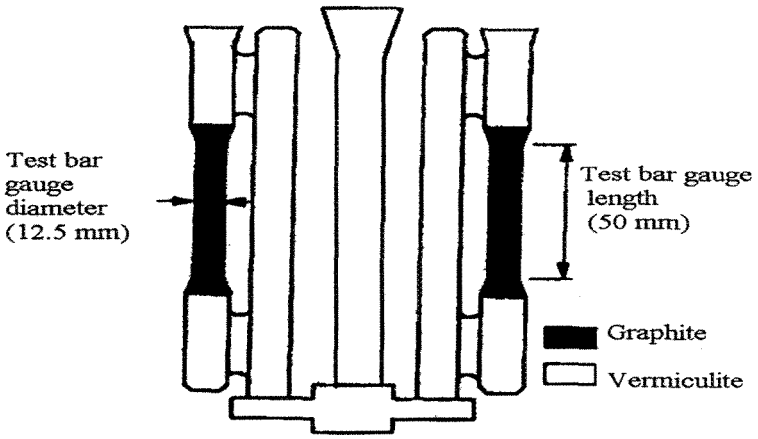

Figure 5.2. Schematic diagram of a Stahl mold casting.

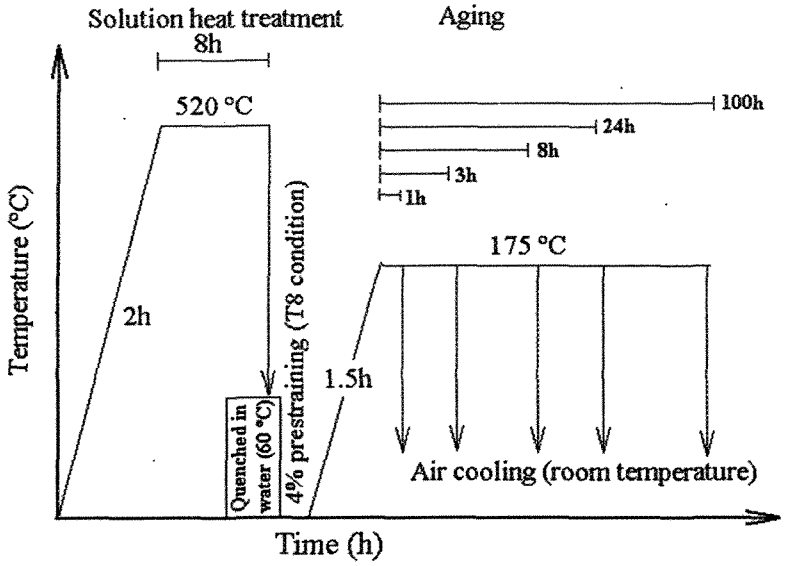

Figure 5.3. Showing temperature versus time for T6 (and T8) condition.

5.2.4. Fractography

The fractured surfaces of selected tensile tested bars were also examined to determine the rupture mode. The samples were examined in a Jeol GSM 5800 scanning electron microscope operating at 10 kV.

5.3 RESULTS AND DISCUSSION

5.3.1. Radiography

To determine the quality and soundness of the test bars produced, sixteen tensile test bars and six others (with gates attached, and used for hot tearing studies) were selected at random (two bars per chemical composition) for radiographic analysis. The results are given in Table 5.2, while the corresponding radiographs are presented in Figures 5.4 and 5.5. Those shown in Figure 5.4 give a good idea about the porosities and cavities present in the respective alloy test bars, where the porosities appear as white spots. Beryllium appears to increase the presence of sponge shrinkage. The test bars with higher Be levels are seen to contain the heaviest concentrations of sponge shrinkage. Strontium appears to reduce the quantity of sponge shrinkage.

An analysis of the cracks due to hot tearing observed in the radiographs of Figure 5.5 reveals that:

1-Manganese additions appear to promote hot cracking along with associated heavy sponge shrinkage in the test bar.

2-Strontium additions only slightly reduce the amount of shrinkage present in the bar.

3-Beryllium additions appear to greatly reduce the possibility of hot cracking in the casting and to change the appearance of the shrinkage.

4-Even the samples without Mn and Be show hot cracking in the gate sections.

Table 5.2. Radiographic analysis of selected alloy test bars.

Alloy code	Shrinkage porosity	Shrinkage cavity	Gas cavity	Hot tear cracks
S6	-	-	-	2-3 (gate *)
S6S	-	-	-	2 (gate *)
M6	-	-	-	4-5 (bar)
M6S	-	-	-	4 (bar)
B6	4	-	-	N/A
B6S	3	-	-	N/A
5B6	2	-	-	3 (bar)
5B6S	1	-	-	2 (bar)

Legend	Remarks
(1) ASTM Designation E-155 1,2 - slight 3,4 - moderate 5,6 - heavy 7,8 - excessive (2) Universal terminology (3) Shape includes undercut, suck back, *etc.*	1) Hot tear samples S6 and S6S contain a more dispersed type of sponge shrinkage. 2) Sponge shrinkage is associated with the hot cracks in hot tear samples M6 and M6S. 3) Shrinkage is more localized in hot tear samples 5B6 and 5B6S. Hot tearing may be starting in sample 5B6. 4) Very good test bars in groups S6, S6S, M6 and M6S. 5) Varying degrees of sponge shrinkage in groups B6, B6S, 5B6 and 5B6S. * at thin/thick junction

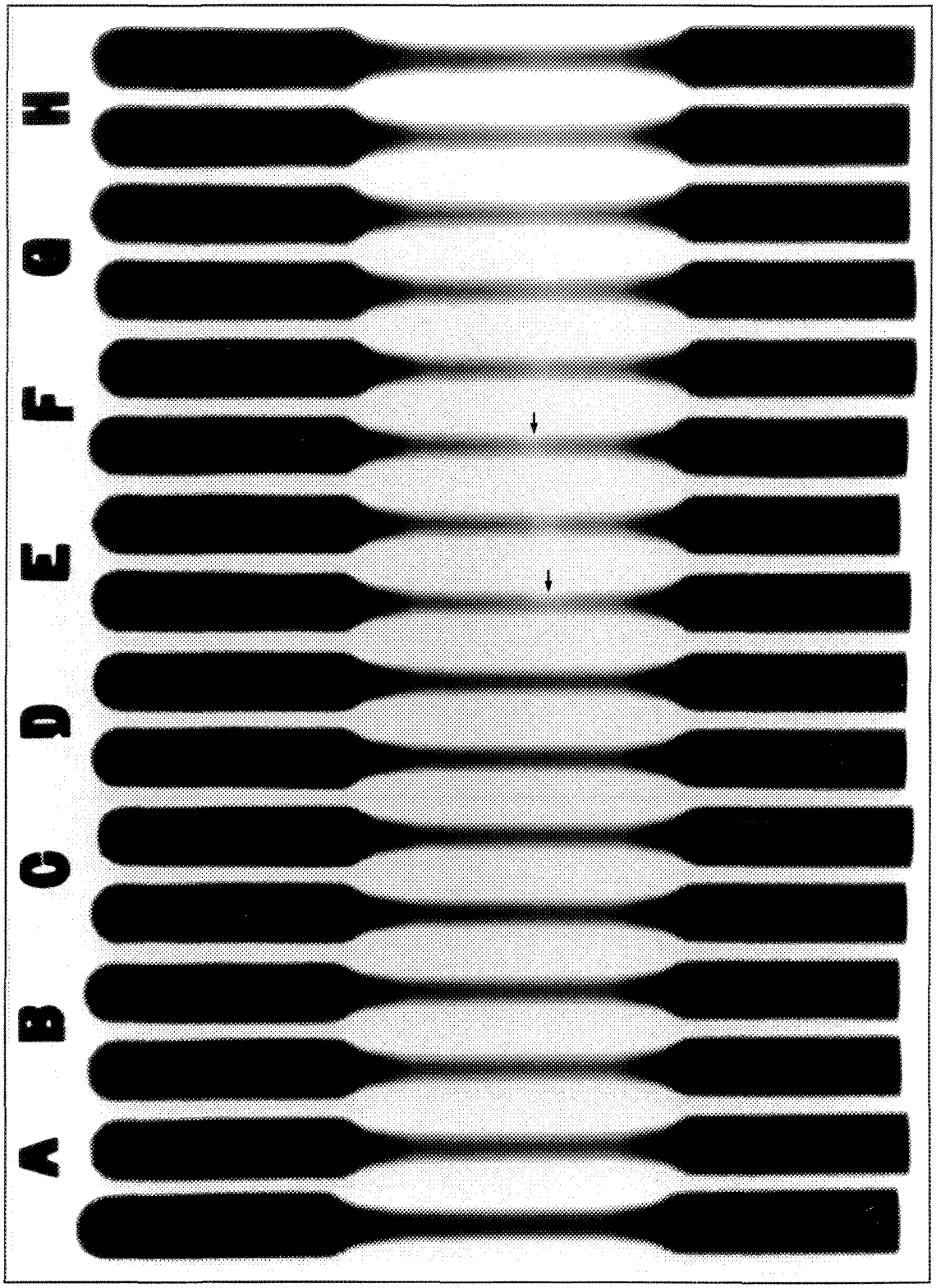

Figure 5.4. Radiographs of selected tensile test bars: (A) S6, (B) S6S, (C) M6, (D) M6S, (E) B6, (F) B6S, (G) 5B6, (H) 5B6S

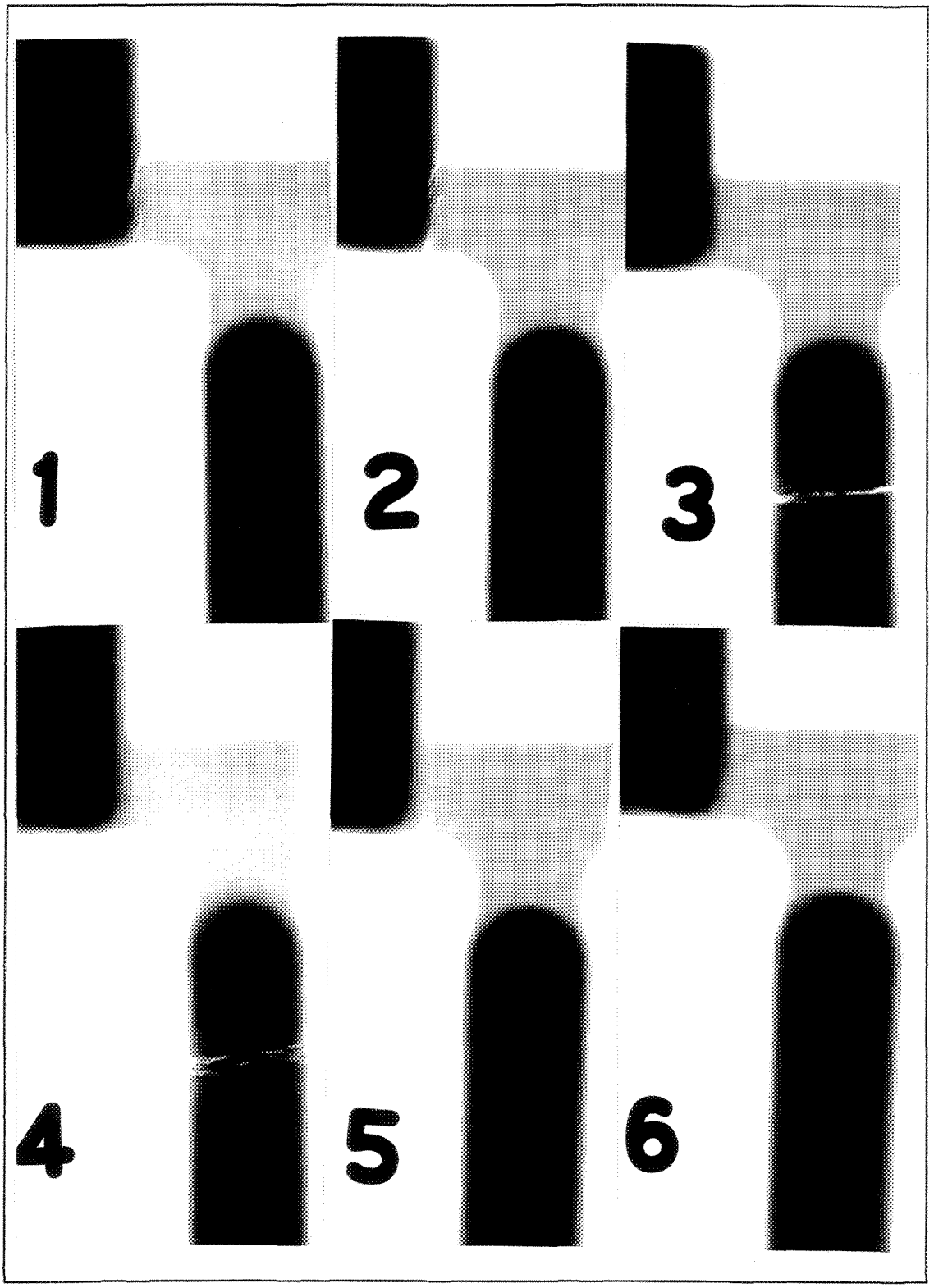

Figure 5.5. Radiographs showing hot tear cracks on gates and test bars of selected alloys: (1) S6, (2) S6S, (3) M6, (4) M6S, (5) 5B6, (6) 5B6S

5.3.2. Microstructure

Aluminum 6XXX series alloys display appreciable solid solubility of the precipitating Mg_2Si phase at the solidus temperature. Under equilibrium conditions, solubility decreases with temperature and the second phase precipitates out as coarse particles. Solubility of Mg and Si in the Al-rich phase decreases with temperature, as can be seen from Figure 5.6. In order to obtain a maximum concentration of Mg and Si particles in solid solution, the solution temperature should be as close as possible to the eutectic temperature [83].

Figure 5.7(a) shows the as-cast microstructure of S6 alloy (Al-1.01% Si-0.3% Fe-0.6% Mg) comprising an aluminum dendrite network, the β-iron intermetallic phase and Mg_2Si particles segregated into the interdendritic regions. Modification with 163 ppm Sr results in smaller β-phase and Mg_2Si particles, where the Mg_2Si particles precipitate in globular form, Figure 5.7(b).

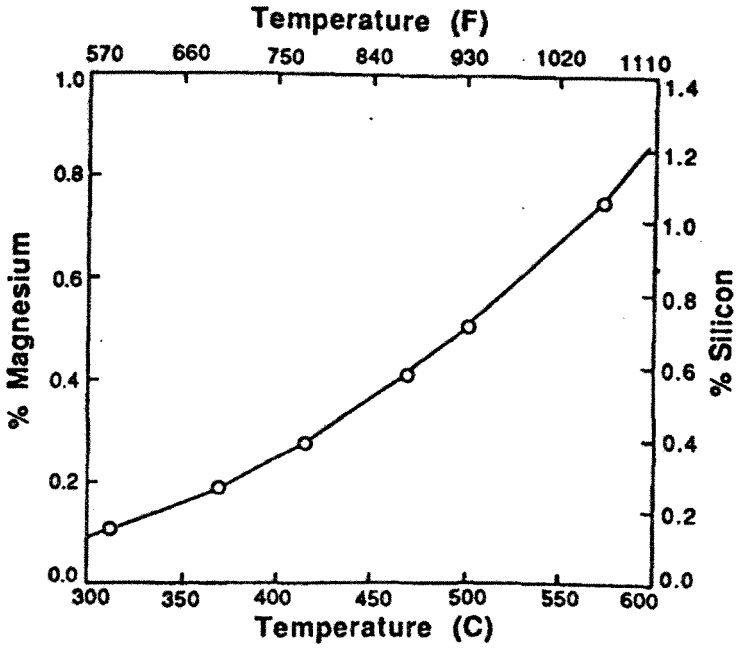

Figure 5.6. Equilibrium solubility of Mg and Si in solid aluminum when both Mg_2Si and Si are present [83].

When S6 alloy is solution heat-treated for 8h at 520 °C, Fig 5.7(c), the amount of Mg_2Si present in the microstructure is seen to decrease, and the particles precipitate as very small globules. The combined effect of modification (163 ppm Sr) and solution heat treatment, shown in Figure 5.7(d), also results in very small β-needles and globular Mg_2Si particles.

Table 5.3 summarizes the main microstructural characteristics observed with respect to solution heat treatment. These observations are not similar to those reported by Paray *et al.* [84], in that homogenization treatment does not cause any transformation of β to α-phase, regardless of the temperature or time of the treatment. In the present case, by using a lower solution temperature (520 °C instead of 575 °C), and also from Figure 5.6, it is found that at this temperature, a maximum of 0.85% Si and 0.6% Mg will be in solid solution. Therefore there is enough free Si (minimum 0.25%) to react with the iron present in the alloy to form the β-phase. Strontium modification cannot change the morphology of the β-phase due to the higher Si*/Fe (1.9%) ratio in the alloy.

Table 5.3. Summary of microstructural observations on Mg_2Si dissolution and intermetallics obtained in alloy S6 with solution heat treatment.

Alloy condition	Solution time at 520 °C (hr)	Dissolution of Mg_2Si	Intermetallic type
Non-modified	0 (as-cast)	none	β
	8	almost	β
163 ppm Sr-modified	0 (as-cast)	none	β
	8	almost	β

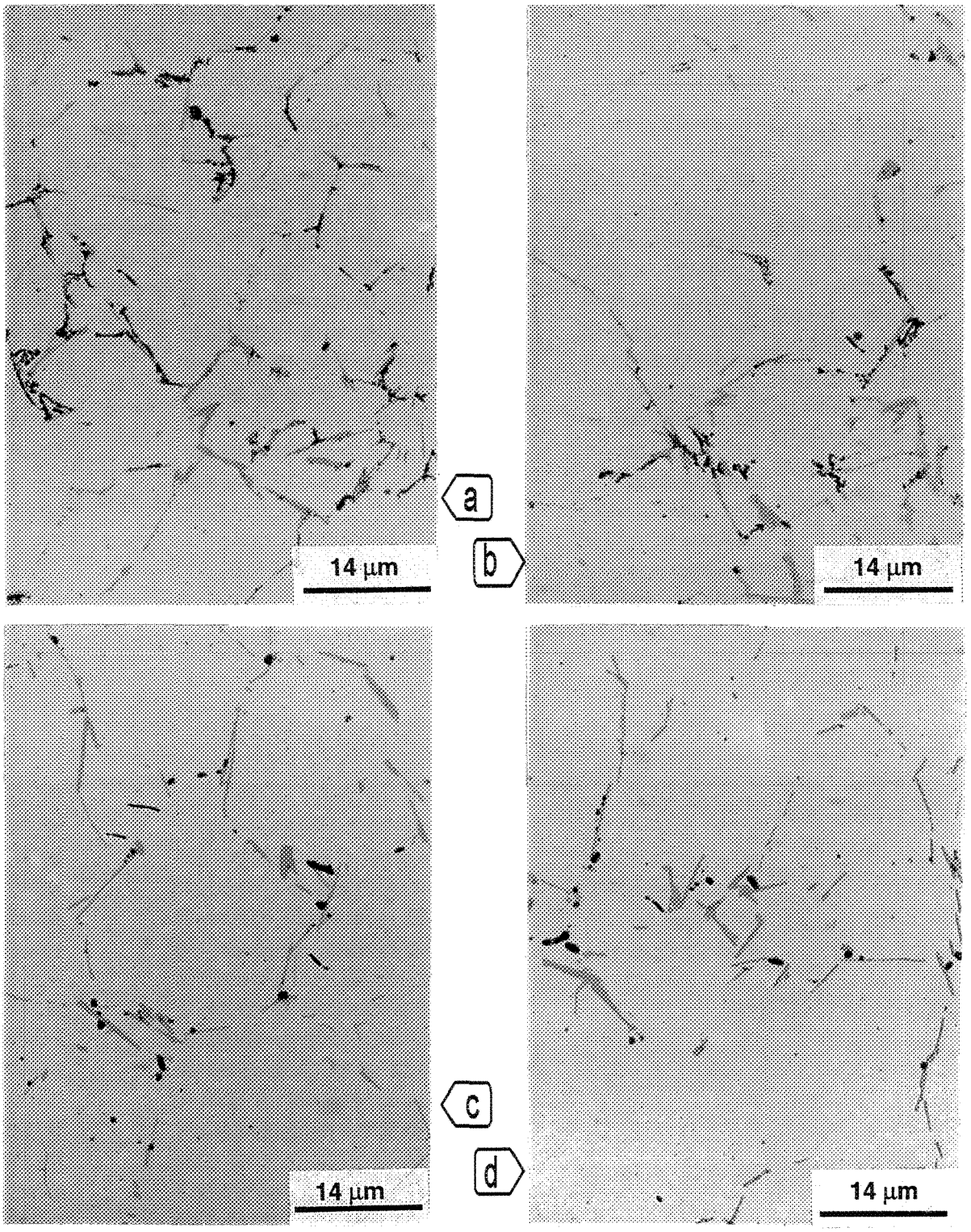

Figure 5.7. Effect of solution heat treatment (8h at 520 °C) and Sr-modification on the dissolution of Mg_2Si in: a) S6 as-cast, b) S6S as-cast, c) S6-SHT, d) S6S-SHT alloys.

Figure 5.8(a) shows the microstructure of a 6 alloy test bar sample in the as-cast condition. All samples for microstructural examination were sectioned from an area away from the fracture surface *i.e.*, away from the plastic deformation zone. From Figure 5.8(a), it is seen that the microstructure displays the β-AlFeSi phase as the main iron intermetallic, together with undissolved Mg_2Si. A few α-Al_8Fe_2Si script particles were also observed. This is expected because of the high cooling rate when Si*/Fe ~1, as explained previously. As the amount of free silicon (Si* or silicon available to react with iron to form intermetallics above that required to form Mg_2Si) is equal to the amount of iron, the addition of 250 ppm strontium results in changing the type of iron intermetallic precipitated from β to α-Al_8Fe_2Si in the 6S alloy, Figure 5.8(b), under as-cast conditions.

Solution treatment of the 6 alloy (8h at 520 °C) results in dissolution of most of the Mg_2Si and in partial fragmentation of the β-phase, without change in its morphology, Figure 5.8(c). When the 6S alloy is solution treated similarly, the α-iron phase is seen to persist, *i.e.*, it does not undergo dissolution or fragmentation, indicating its high stability, even at 520 °C solution temperature, Figure 5.8(d).

Thus, solution heat treatment does not alter the intermetallics that are present in the as-cast structure. It may cause fragmentation and dissolution of the β-phase and dissolution of the Mg_2Si, but does not change the β-AlFeSi to the α-AlFeSi phase.

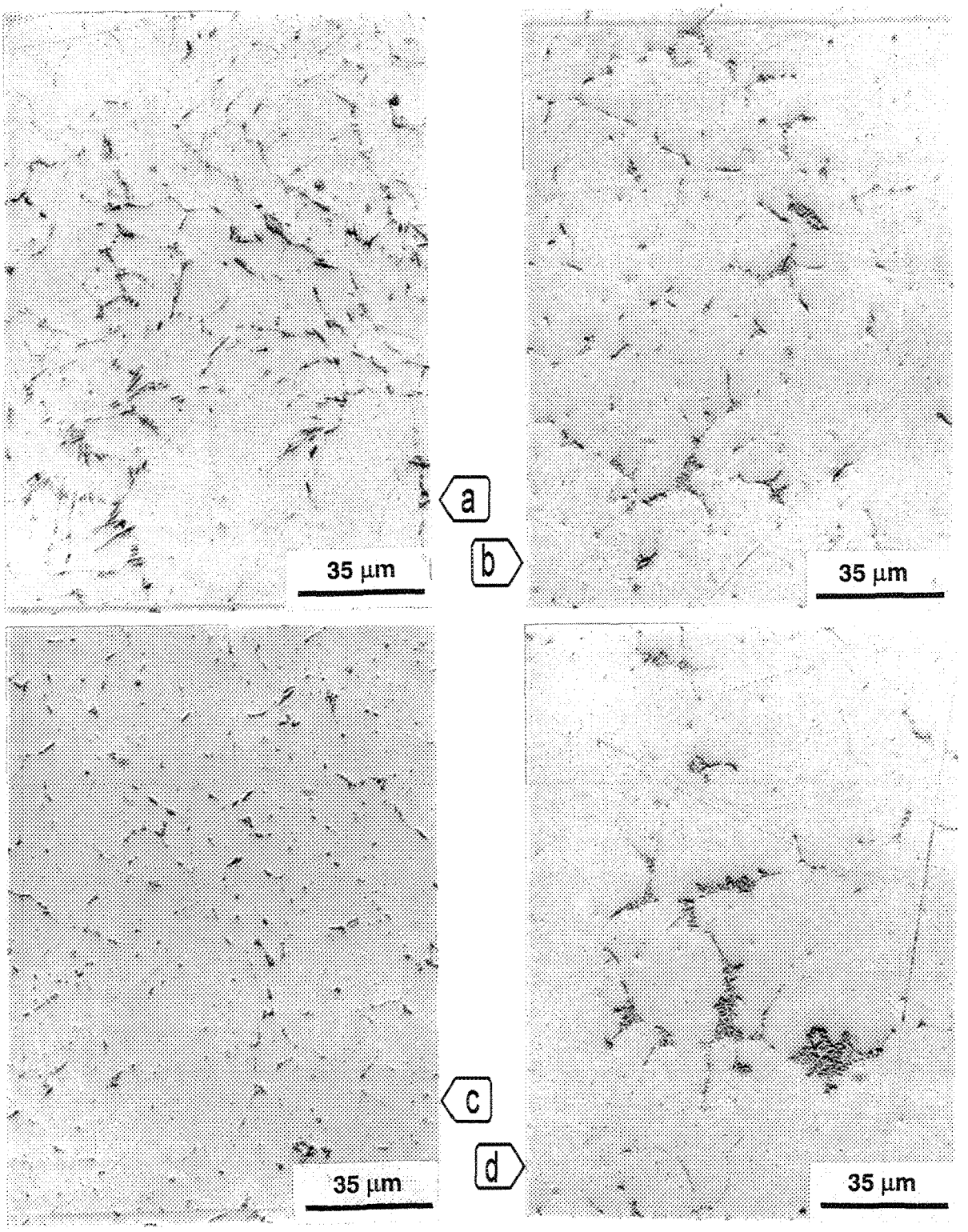

Figure 5.8. Effect of solution heat treatment (8h at 520 °C) and Sr-modification on the dissolution of Mg_2Si in: a) G-6 as-cast, b)G-6S as-cast, c) 6-SHT, d) 6S-SHT alloys.

5.3.3. Tensile Properties

5.3.3.1. Effect of Strontium Addition and Aging Time

Experimental Alloys

The effect of increasing the strontium content on the tensile properties of (Al-0.6% Si-0.3% Fe-0.64% Mg) alloy (A alloy) in the as-cast (coded AS), solution heat-treated (8h at 520 °C, coded T0), and artificially aged conditions (3, 8, 24 and 100h at 175 °C - coded T3, T8, T24 and T100, respectively) are shown in Figures 5.9(a) through 5.9(c). Strontium does not seem to provide any significant improvement to the alloy properties. On the contrary, the properties decrease, particularly the ductility, which shows a clear drop with increasing strontium content, as seen in Figure 5.9(c).

Figures 5.9(a) and 5.9(b) show that 235 ppm strontium is enough to produce well-modified alloys that give optimum strength values. Addition of more than 235 ppm strontium does not essentially produce further changes. These figures also indicate that an aging time of 24h is recommended for achieving appreciable solid solution of Mg in the Al matrix.

Industrial Alloys

The effect of strontium on the mechanical properties of the industrial 6063 (D) alloy (Al-0.65% Si-0.17% Fe-0.69% Mg), in the as-cast condition (coded AS), and after artificial aging at 175 °C for 8h (coded T8) is summarized in Table 5.4. There is a slight increase in YS and UTS, with a slight decrease in the ductility. It seems that, same as in the case of the

experimental alloys, a strontium addition of less than 415 ppm is good enough to modify the structure without producing any changes in the three tensile parameters. The same trend is observed in 6I (Al-0.42% Si-0.18% Fe-0.52% Mg) alloy. However, the properties of D alloy are higher, due to its higher Si content.

Table 5.4. Tensile properties of 6063 industrial alloys.

Alloy Batch	Alloy code	Strontium addition (ppm)	Temper	YS (MPa)	UTS (MPa)	EL (%)
D	D	0	as-cast	89 ± 3.7	176 ± 6.3	10 ± 1.3
	DS	415	as-cast	83 ± 3.8	179 ± 8.9	11 ± 2.7
	D2	812	as-cast	92 ± 6.0	168 ± 8.2	7 ± 0.4
	D	0	T8	282 ± 4.1	320 ± 2.4	8 ± 0.6
	DS	415	T8	293 ± 3.9	322 ± 1.6	4 ± 0.7
	D2	812	T8	291 ± 0.8	305 ± 4.5	2 ± 0.3
6I	6I	0	as-cast	59 ± 3.0	123 ± 6.2	16 ± 1.0
	6IS	265	as-cast	55 ± 0.1	116 ± 2.1	16 ± 1.0
	6I	0	T8	218 ± 0.7	246 ± 2.5	8 ± 1.2
	6IS	265	T8	189 ± 9.2	217 ± 1.8	6 ± 1.9

It was shown in Chapter 4 (Section 4.3.1) that strontium-containing alloys were easier to roll, due to the formation of the more ductile α-Al_8Fe_2Si phase rather than the brittle β-AlFeSi phase. This is especially so for the 6I alloys, where the amount of iron intermetallics are very low. This is in good agreement with the observations made by Paray *et al.* [84].

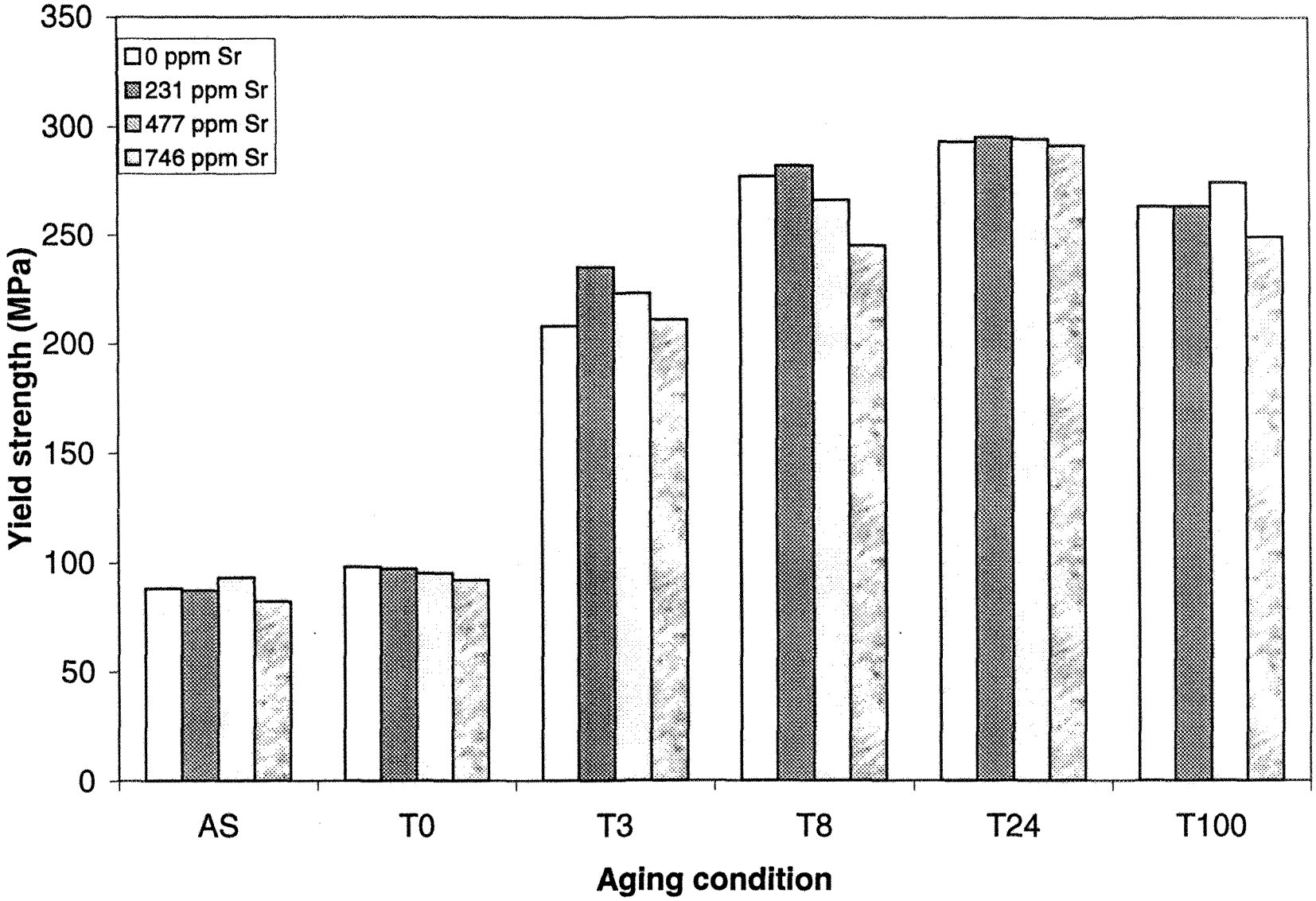
0 ppm Sr
231 ppm Sr
477 ppm Sr
746 ppm Sr
Yield strength (MPa)
350
300
250
200
150
100
50
0
AS
T0
T3
T8
T24
T100
Aging condition

Figure 5.9(a)

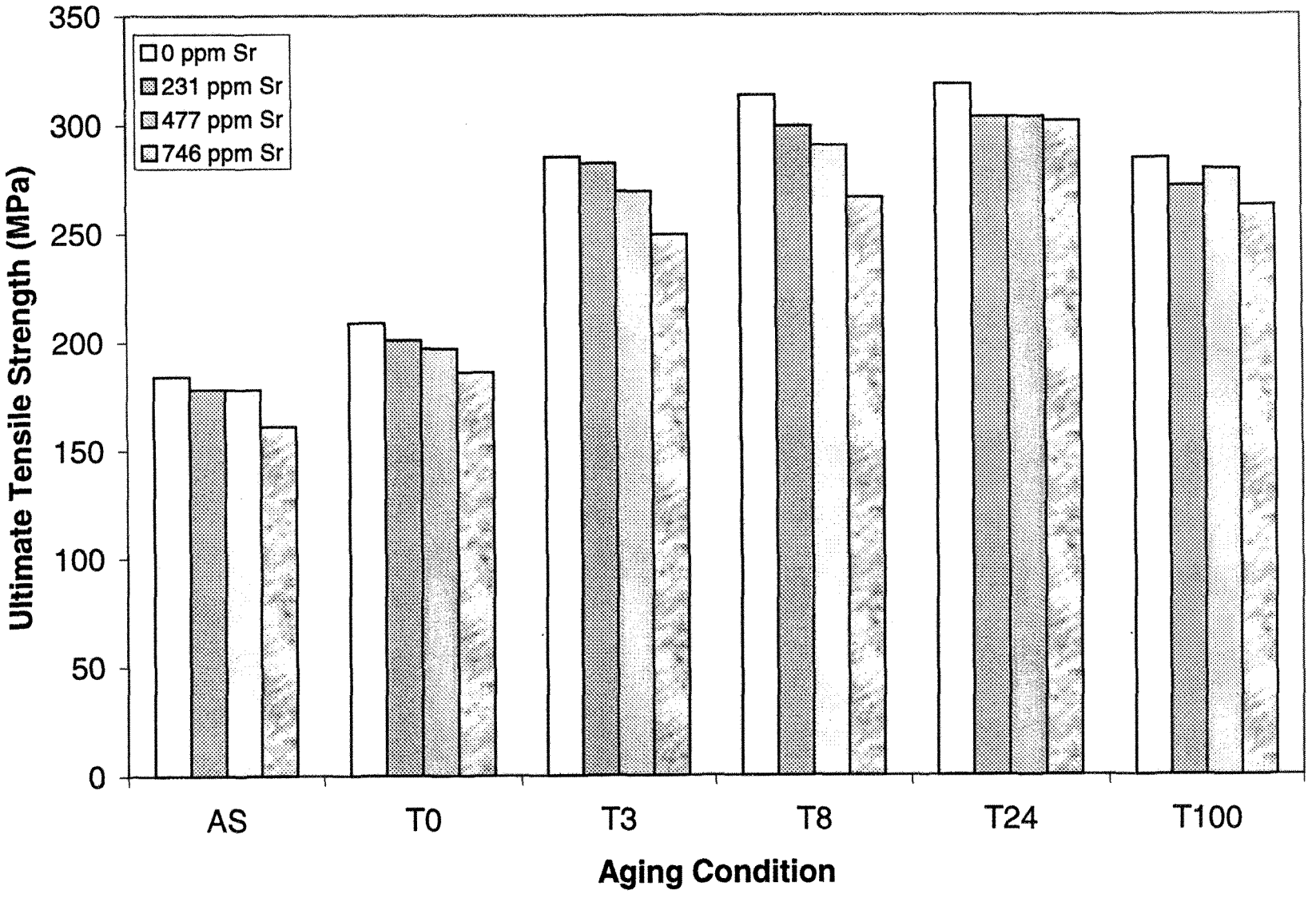
0 ppm Sr
231 ppm Sr
477 ppm Sr
746 ppm Sr
Ultimate Tensile Strength (MPa)
350
300
250
200
150
100
50
0
AS
T0
T3
T8
T24
T100
Aging Condition

Figure 5.9(b)

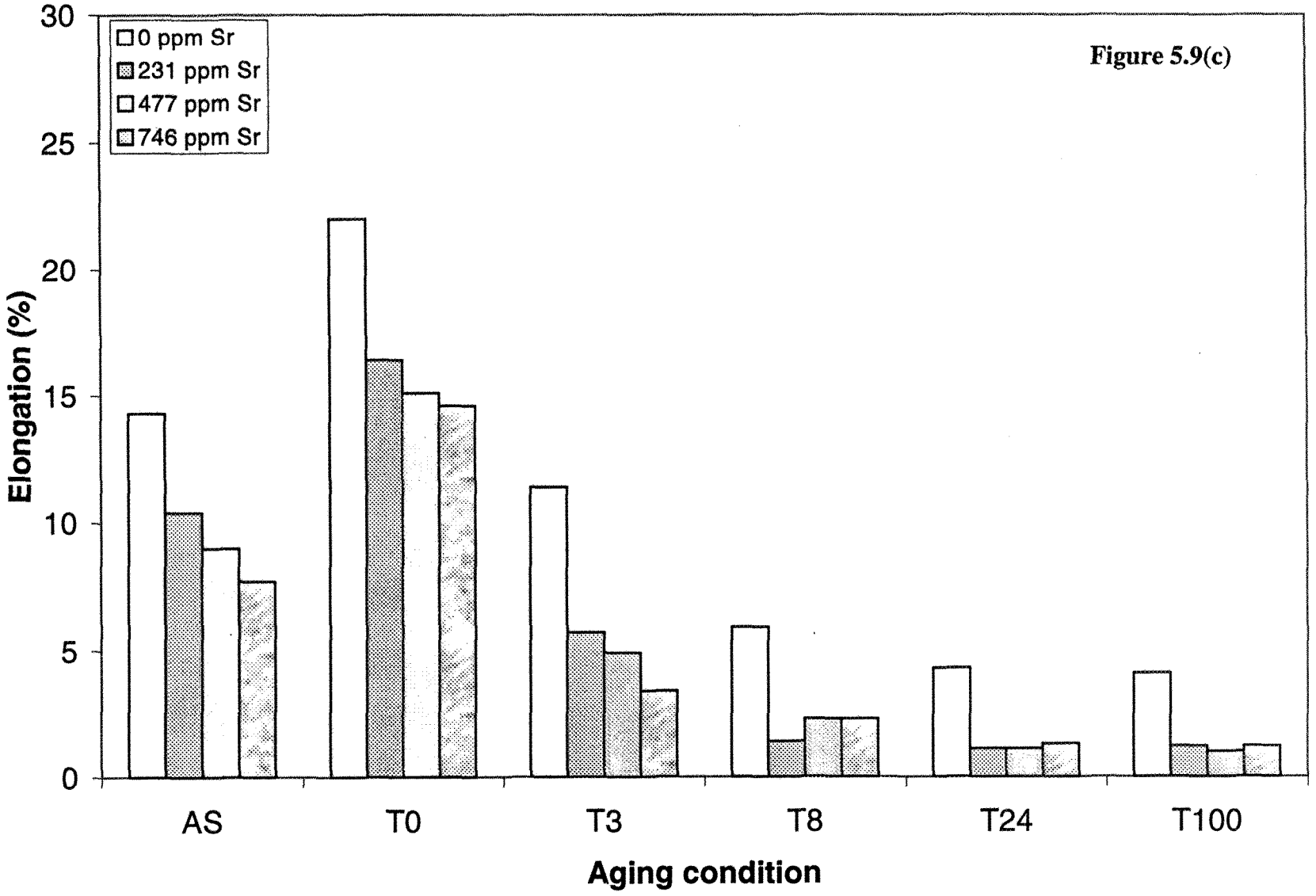

Figure 5.9 Tensile properties of A alloy series solution heat treated at 520 °C for times up to 100h: a) YS, b) UTS, c) %EL

5.3.3.2. Effect of Trace Elements and Strontium Addition

Table 5.5 demonstrates the effect of trace elements and strontium addition on the alloy tensile properties in the as-cast condition. As can be seen, the tensile properties obtained with the respective trace element additions are not essentially affected by further addition of strontium.

Table 5.5. Effect of strontium and trace elements on tensile properties in the as-cast condition.

Alloy code	Strontium addition (ppm)	YS (MPa)	UTS (MPa)	EL (%)
6	0	84 ± 4.0	175 ± 7.7	14 ± 2.2
6S	144	83 ± 4.6	172 ± 3.6	10 ± 1.3
M6	0	86 ± 2.6	183 ± 1.9	18 ± 2.4
M6S	206	85 ± 4.5	171 ± 1.8	10 ± 1.1
S6	0	93 ± 3.7	187 ± 4.6	11 ± 2.0
S6S	163	93 ± 3.1	179 ± 5.1	8 ± 1.0
B6	0	58 ± 5.3	91 ± 8.1	3 ± 0.5
B6S	147	58 ± 2.6	91 ± 8.2	3 ± 0.5
5B6	0	64 ± 4.7	123 ± 6.0	6 ± 0.3
5B6S	162	65 ± 7.7	122 ± 8.6	6 ± 0.9
2B6	0	80 ± 7.3	159 ± 12.6	11 ± 1.2
2B6S	171	62 ± 3.2	129 ± 6.3	10 ± 1.4
1B6	0	79 ± 9.3	170 ± 6.1	12 ± 0.4

The tensile test results of test bars prepared from Al-0.6% Si-0.38% Fe-0.64% Mg alloy in the non-modified (6 alloy) and Sr-modified (6S alloy, 144 ppm Sr) conditions, and aged for different times, are shown in Figure 5.10. As can be seen, the tensile strengths in each case increase with aging time, reaching their maximum values at the optimum aging time of 24h (*i.e.*, 256 MPa & 282 MPa for 6 alloy, and 259 MPa & 276 MPa for 6S alloy,

respectively). Both the non-modified and modified alloys exhibit very similar trends. When one considers the ductility, however, the modified alloy (6S) displays a much larger drop in ductility with progress in aging time. With respect to the initial microstructures before aging is commenced (at T0), the lower ductility value exhibited by the 6S alloy may be accounted for by the presence of the α-Al_8Fe_2Si phase in the microstructure, rather than the β-Al_5FeSi phase (present in the non-modified 6 alloy).

With increase in the Si content of the alloy, *i.e.*, S6 alloy (Al-1.01% Si-0.35% Fe-0.68% Mg), the tensile properties obtained with aging time are as shown in Figure 5.11. In this case, modification with Sr (163 ppm Sr, S6S alloy) improves the YS and UTS to a certain extent *i.e.*, YS from 111 MPa at T0 to 229 MPa at T24 for S6 alloy, and 114 at T0 to 301 MPa at T24 for S6S alloy; UTS from 231 MPa at T0 to 323 MPa at T24 for S6 alloy, and 233 at T0 to 328 MPa at T24 for S6S alloy. The elongation, however, remains practically unaffected (compared to the non-modified case), over the range of aging times studied (*i.e.*, from 20% at T0 to about 3% at T24 for both S6 and S6S alloys). The very similar values of elongation in the non-modified and Sr-modified alloys may be attributed to the fact that the microstructures of both alloys after solution treatment (*i.e.*, in T0 condition) contain the β-Al_5FeSi intermetallic (unlike the case of 6 and 6S alloys shown in Figure 5.10).

The strength curves show two peaks at aging times of 1h and 24h. Increase in the strength properties is generally associated with the decrease in elongation, as is observed clearly in Figure 5.11 for the stronger peak at 24h aging time. Enhancement in strength properties obtained with aging treatment occurs mainly due to the precipitation of

metastable phases from the supersaturated solution [85] according to the following sequence, in Al- Si- Mg alloys.

SS ⟶ Needle-shaped GP zones (β") ⟶ rod-like β' precipitates (Mg_2Si)

⟶ platelets of Mg_2Si (β).

The decomposition of the supersaturated solution (SS) starts with the clustering of Si atoms. This leads to the formation of coherent spherical Guinier-Preston (GP) zones that elongate along the cube matrix direction to become needle-shaped (also referred to as β" precipitates). The initially spherical GP zones (GP-1) convert to needle-like forms (GP-2) near the maximum strength inflections of the aging curves [1]. As aging proceeds, the initially disordered zones become ordered and, with further aging, grow to form rods of an intermediate β' phase, whose particles are semi-coherent with the matrix, with the rod axes parallel to the cube matrix directions. The final equilibrium Mg_2Si phase (β-phase) forms as incoherent platelets on the aluminum matrix. Peak hardness is achieved before the platelets form.

Thus, the two peaks observed in Figure 5.11 for the YS and UTS curves are associated with the formation of the GP-1 and GP-2 zones, respectively.

These results are similar to those recently reported by Bryant [86] on the effect of preaging treatments on aging kinetics and mechanical properties in AA6111 aluminum autobody sheet.

The mechanical properties after aging treatment are dependent upon the artificial aging conditions *i.e.*, temperature and time. Misra and Oswalt [87] have reported that in Ti-refined A356 and A357 aluminum castings, the $TiAl_3$ precipitate (that results from grain refining) appears to affect the aging kinetics of the alloy in that it delays the complete precipitation of the equilibrium Mg_2Si phase, and could also be responsible for lower tensile ductility during the early stages of aging.

The tensile properties of M6 alloys (Al-0.62% Si-0.34% Fe-0.2% Mn-0.6% Mg) in the non-modified and Sr-modified (206 ppm Sr) conditions, and aged for various times are shown in Figure 5.12. In general, the curves appear similar to those exhibited by the 6 alloys. However, the improvement in yield strength due to Sr-modification is comparatively more pronounced (110 - 255 MPa YS for non-modified, and 277 MPa YS for Sr-modified alloys). The corresponding drop in elongation for the M6S alloy is also more severe (from 25.4% for M6 alloy to 12% for M6S alloy). The presence of both Mn and Sr in the M6S alloy indicate that the iron intermetallic in this case should precipitate as the α-$Al_{15}(Fe,Mn)_3Si_2$ phase, with a script morphology.

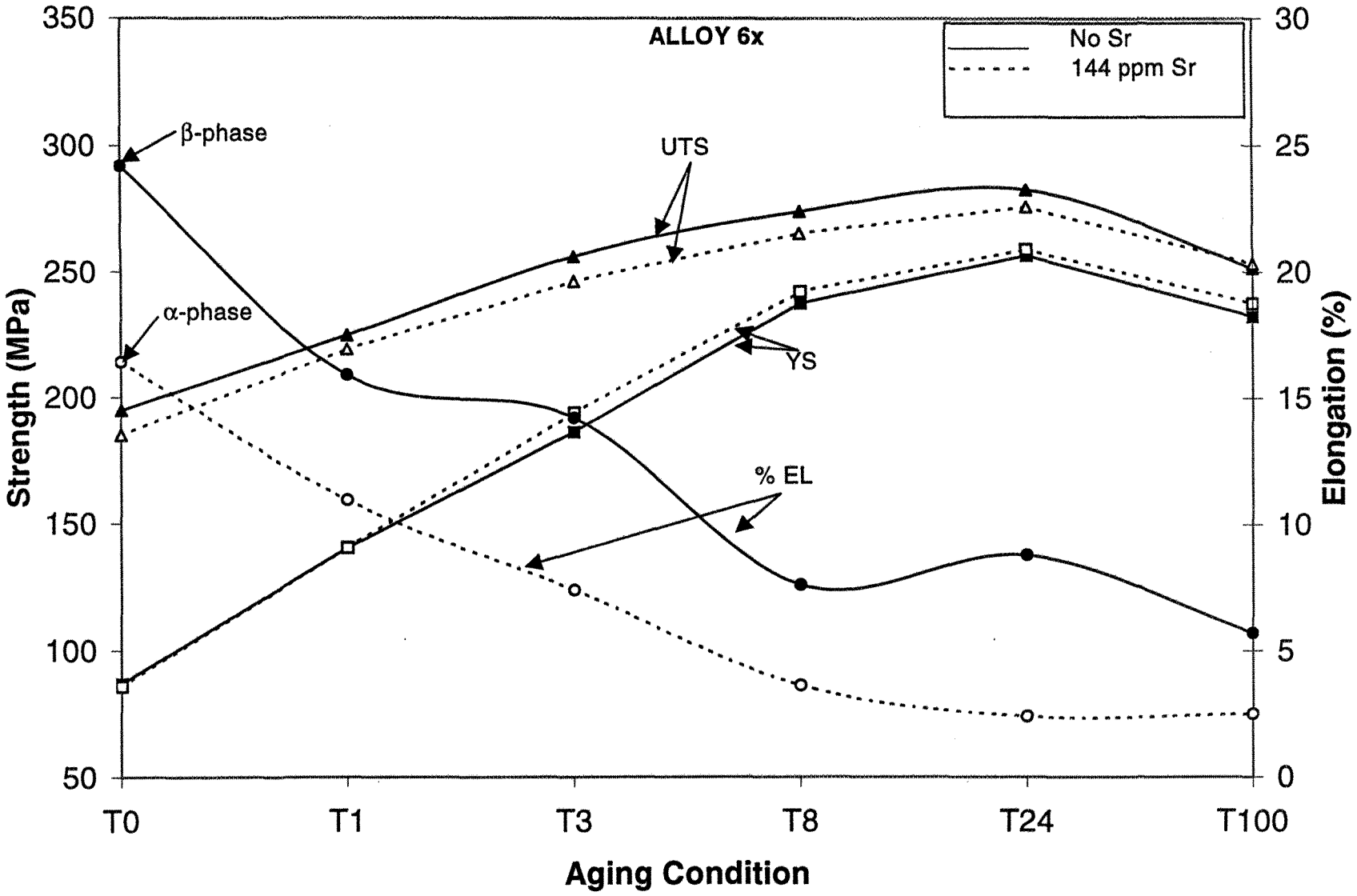

Figure 5.10. Effect of aging time on the tensile properties of non-modified and Sr-modified 6 alloys.

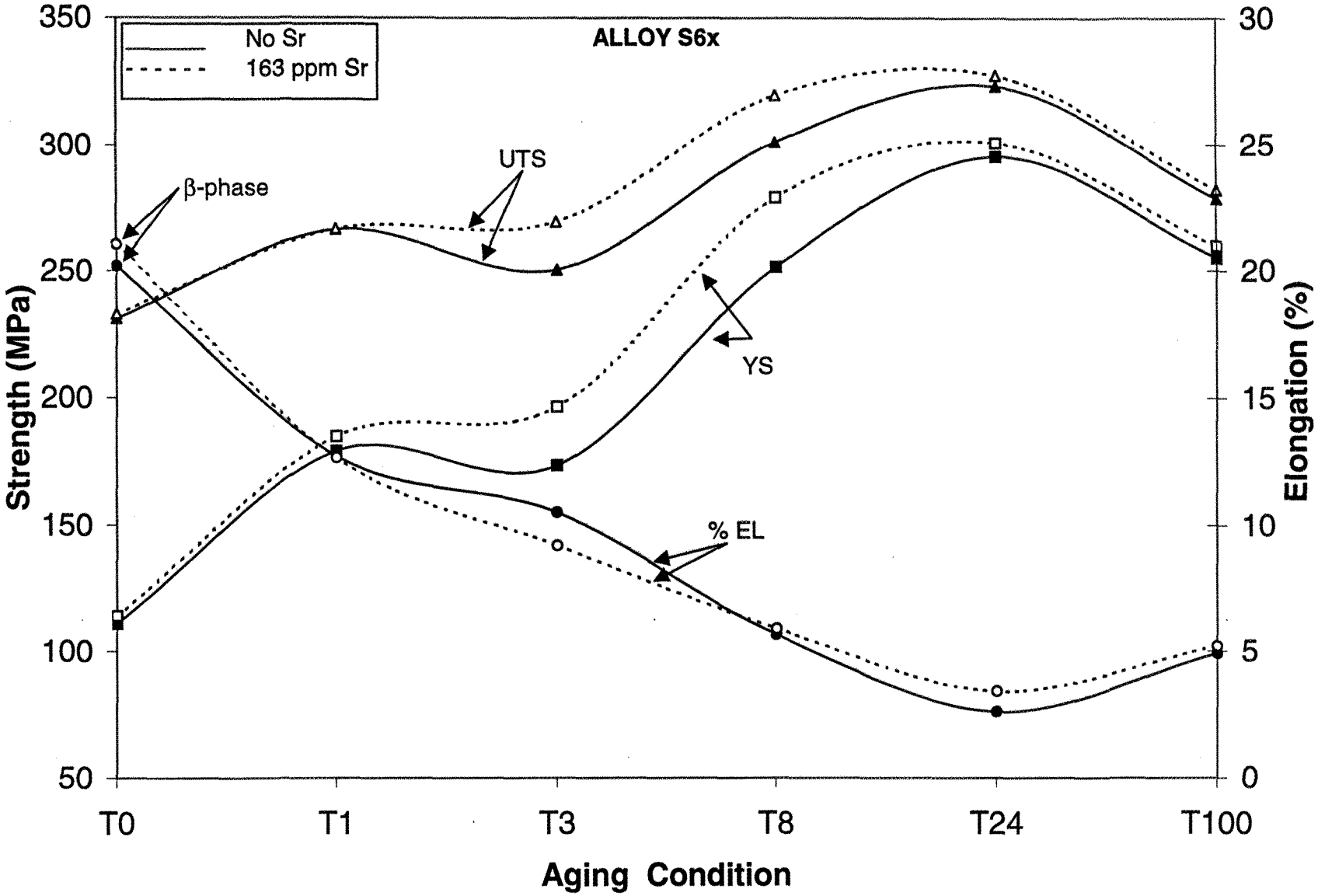

Figure 5.11. Effect of aging time on the tensile properties of non-modified and Sr-modified S6 alloys.

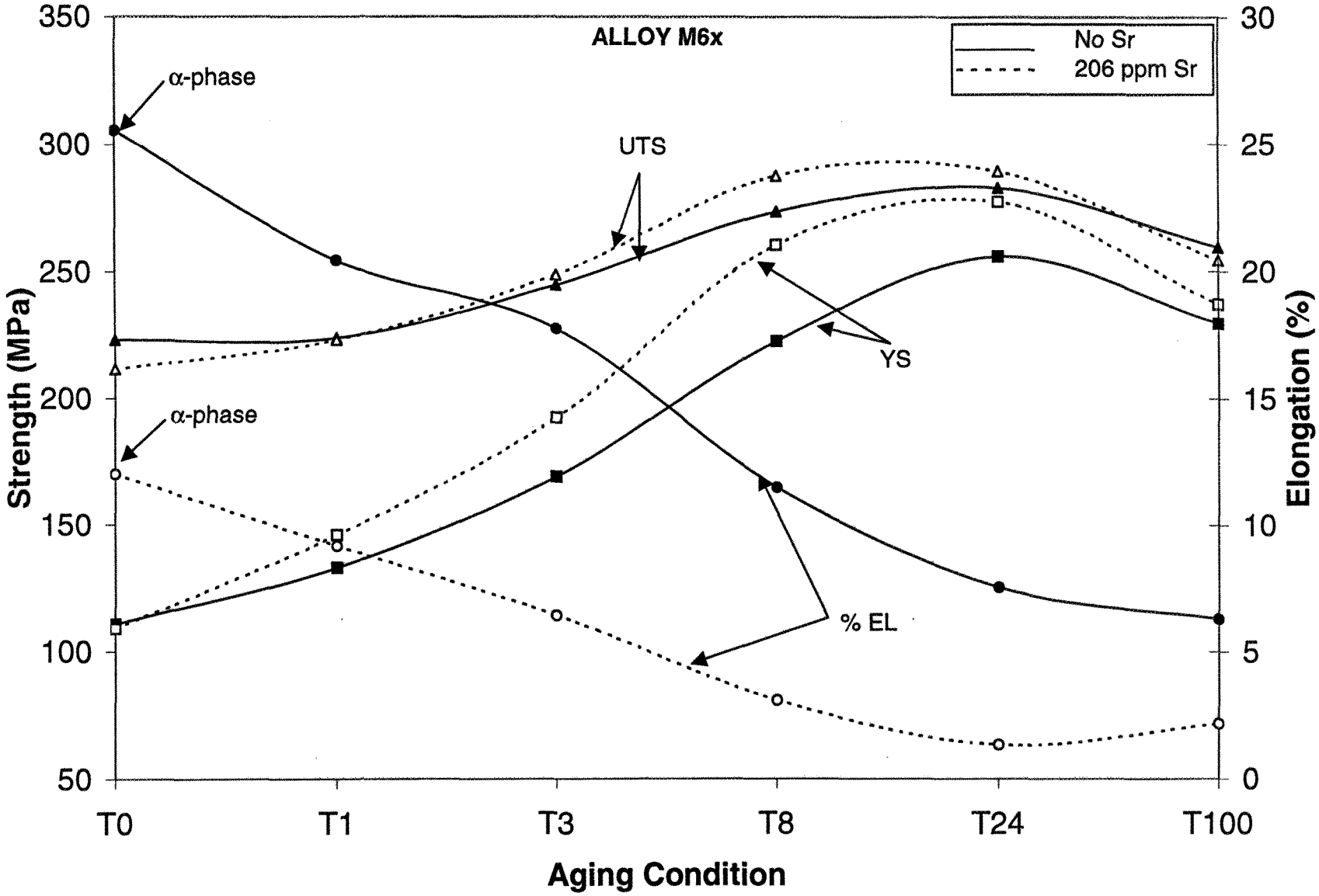

Figure 5.12. Effect of aging time on the tensile properties of non-modified and Sr-modified M6 alloys.

The effect of beryllium addition on the tensile properties of Al-0.61% Si-0.38% Fe-0.64% Mg alloy in the absence or presence of Sr is shown in Figures 5.13 through 5.15, as a function of aging time.

Figure 5.13 shows that addition of 0.02% Be (2B6 alloy) improves the mechanical properties with aging time. The modified alloy (2B6S alloy, 171 ppm Sr) exhibits somewhat lower properties (YS: 109 MPa at T0 to 287 MPa at T24 for 2B6 alloy, and 87 MPa at T0 to 263 MPa at T24 for 2B6S alloy and UTS: 221 MPa at T0 to 295 MPa at T24 for 2B6 alloy, and 180 MPa at T0 to 272 MPa at T24 for 2B6S alloy). As in the case of the 6 alloys (Figure 5.10), the modified alloy containing the α-iron phase exhibits a lower ductility after solution heat treatment (T0 condition) compared to the unmodified alloy (from 16% for 2B6 and 13% for 2B6S at T0, to about 2% at T24 for both alloys). Maximum strengths (and correspondingly, minimum ductilities) are observed at the peak aging time of 24h.

Increasing the Be addition to 0.04% (5B6 alloy) lowers the alloy strength, Figure 5.14. The UTS is decreased by about 70 MPa after solution treatment. With aging, the strength improves, although modification (162 ppm Sr, 5B6S alloy) does not produce any noticeable changes until after 8h of aging, when the strength improves somewhat, by about 12-15 MPa. The two peaks observed in the UTS curve correspond to the formation of the GP-1 and GP-2 zones. For both alloys, maximum ductility (~7 to 8%) is obtained after 1h aging, following which the ductility drops down to 1-2% for higher aging times.

At Be levels of 0.13% (B6 alloy), the alloy properties are considerably reduced, as shown in Figure 5.15. In both unmodified and Sr-modified (147 ppm Sr, B6S) alloys, the UTS and YS show almost identical responses to aging time, exhibiting a slow, gradual improvement until 24h aging time, after which the properties are stabilized. Due to the high volume fraction of iron-intermetallics present in the alloy, any effects due to Sr-modification are not apparent.

The severest effect of such a high Be addition is observed for the alloy ductility which is reduced from over 15% (in the 0.02% Be-containing alloy) to ~2.5% after solution treatment and deteriorates to almost zero with aging. The presence of a fairly large amount of Be (0.13%) results in the formation of significant shrinkage cavities, as revealed by the corresponding radiograph shown in Figure 5.4. Together with the increased amount of intermetallics, such cavities are expected to deteriorate the ductility significantly.

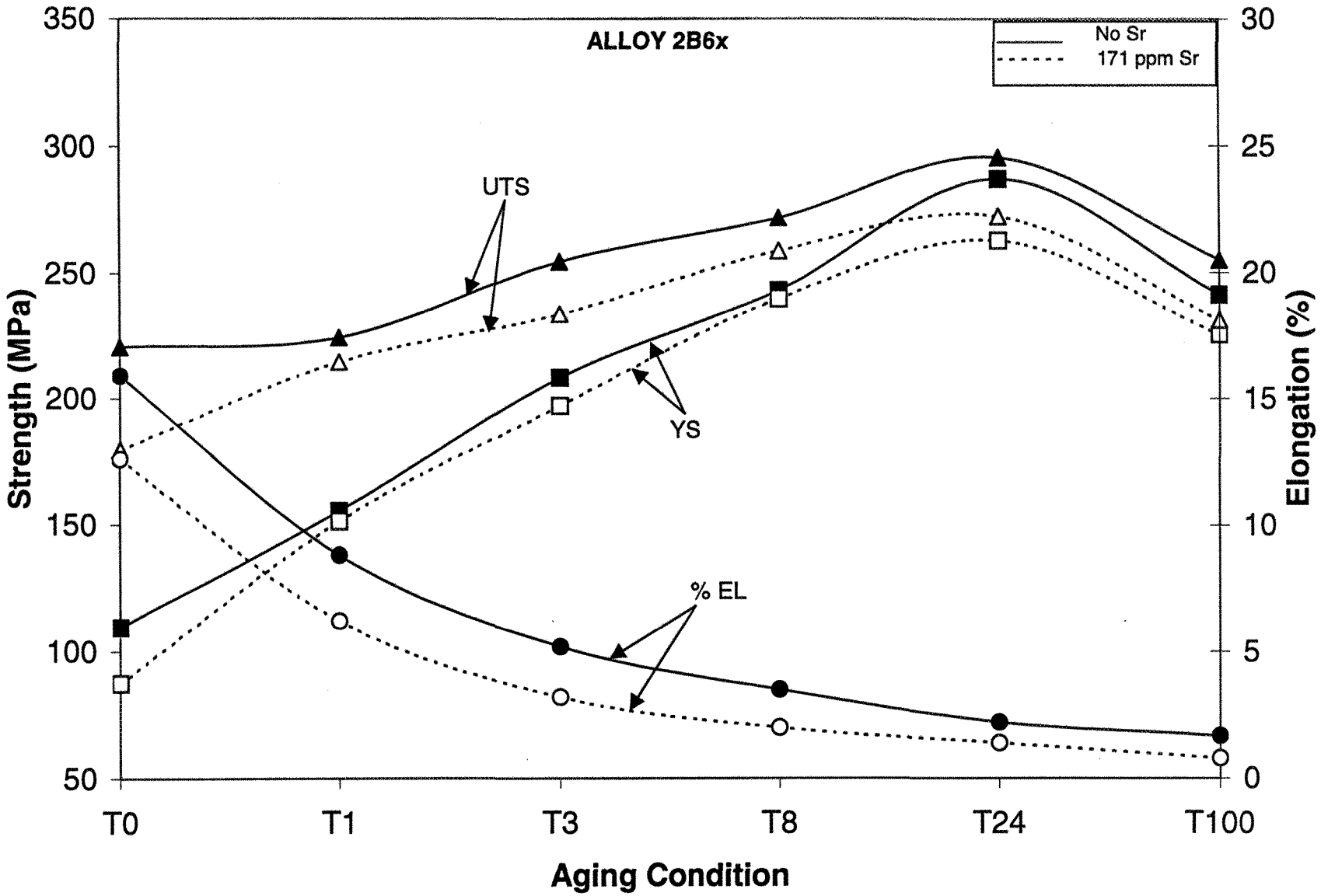

Figure 5.13. Effect of aging time on the tensile properties of non-modified and Sr-modified 2B6 alloys.

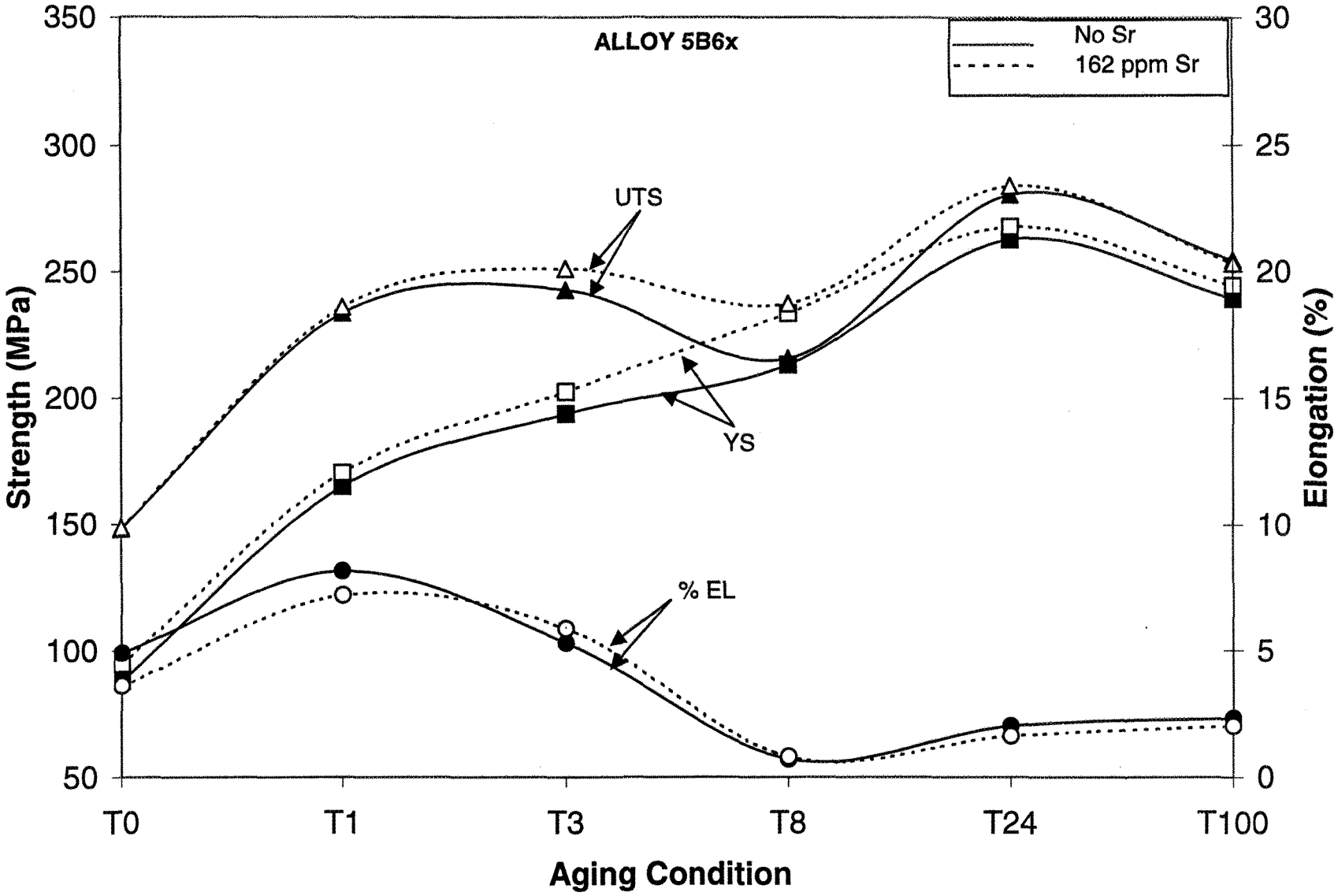

Figure 5.14. Effect of aging time on the tensile properties of non-modified and Sr-modified 5B6 alloys.

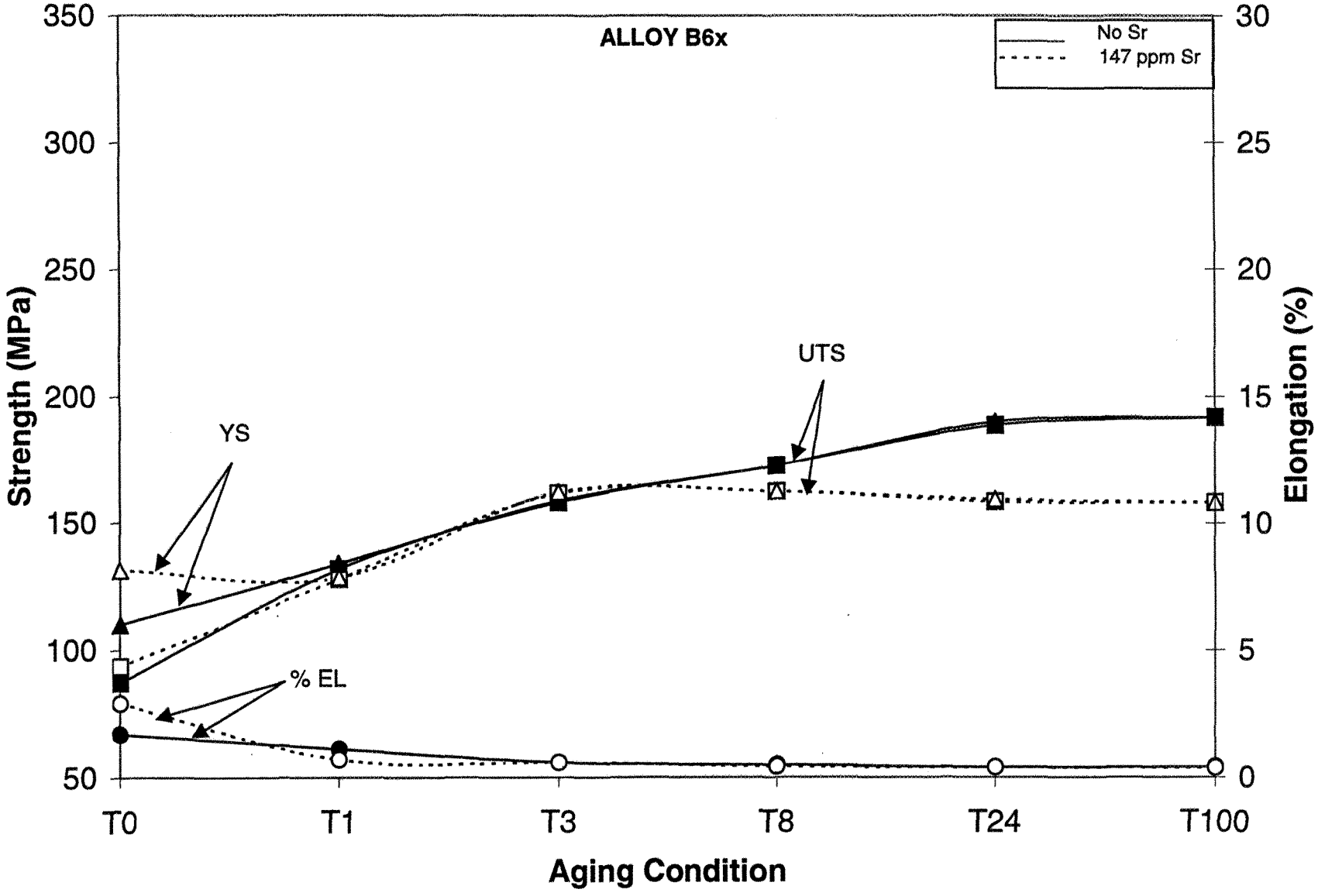

Figure 5.15. Effect of aging time on the tensile properties of non-modified and Sr-modified B6 alloys.

5.3.3.3. Prestraining Prior to Aging

The 2B6S (Al-0.68% Si-0.39% Fe-0.64% Mg-0.0171% Sr) and 6IS (Al-0.4% Si-0.19% Fe-0.55% Mg-0.0265% Sr) alloys were selected for studying the possible effect of prestraining before aging on the alloy tensile properties, due to their high formability (97% cold rolling reduction). The alloy test bars were solution treated (8h at 520 °C), quenched in hot water (60 °C- 80 °C), then pulled to 4% strain in the Instron testing machine. Prestrained and non-prestrained test bars corresponding to the two alloys were then aged at 175 °C for various times of 1h, 3h, 8h and 24h each. The tensile properties are shown in Figures 5.16(a) through 5.16(c).

Figure 5.16(a) shows the variation in the yield strength (YS) with aging time. As can be seen, prestraining has a more pronounced effect on the YS at shorter aging times: the properties obtained after 8h are comparable to those obtained from the non-prestrained alloy aged for 24h. Also, the 6IS alloy is more sensitive to prestraining than the 2B6S alloy. It should be mentioned that the tensile properties of the non-prestrained 2B6S alloy are always superior to those exhibited by the 6IS alloy, which may account for the difference in their response to prestraining. Similar observations were made for the variation in the UTS, Figure 5.16(b). Again, the 2B6S alloy shows practically no difference in the UTS after 8h aging at 175 °C for the two cases.

Figure 5.16(c) displays the variation in alloy ductility. As expected, the prestrained alloys had very low levels of elongation to rupture. In this case, the 6IS alloy in the non-prestrained condition was associated with the highest levels of ductility compared to the other three alloys. These results are in good agreement with those of Lloyd *et. al* [79].

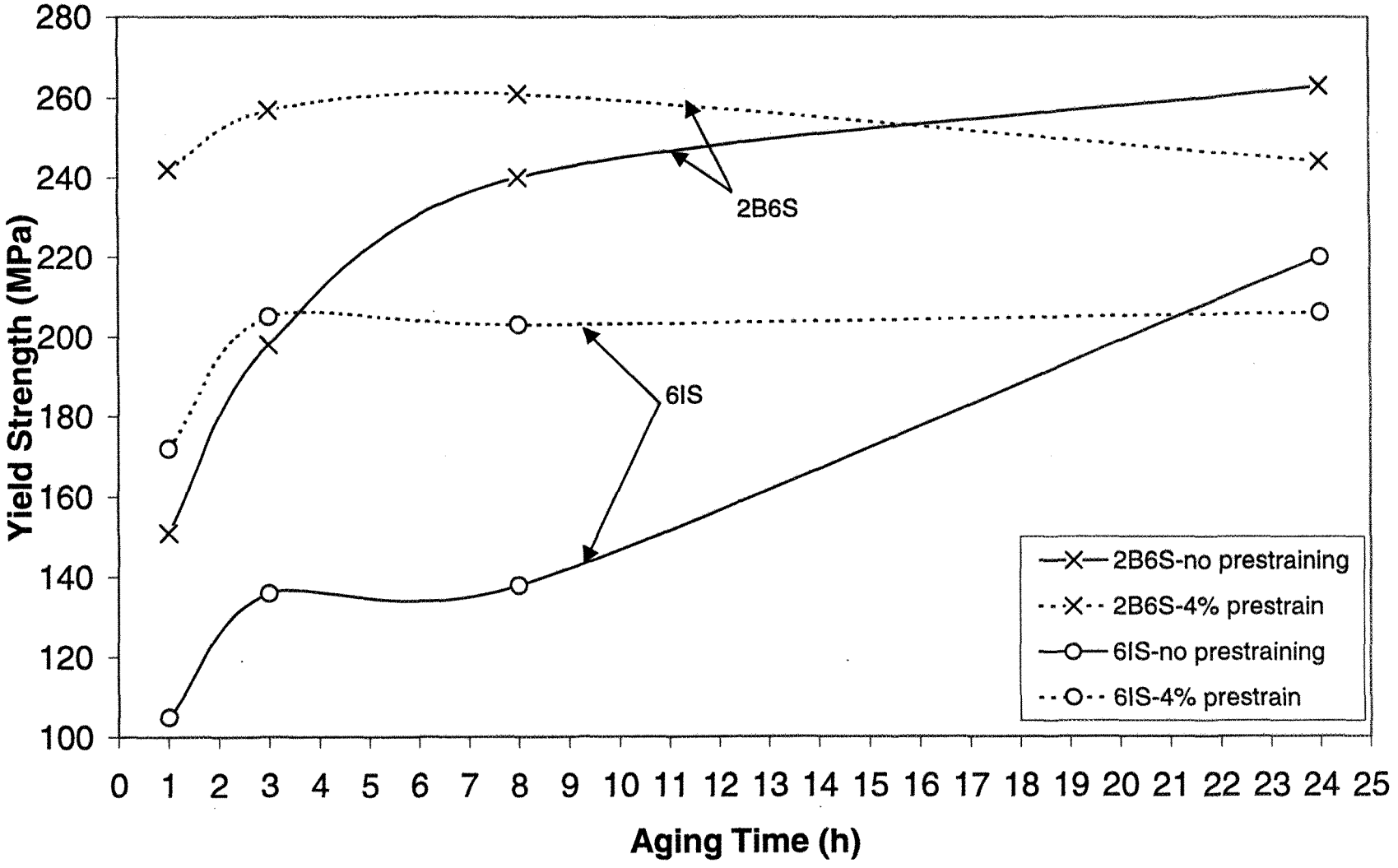
Yield Strength (MPa)
280
260
240
220
200
180
160
140
120
100
0 1 2 3 4 5 6 7 8 9 10 11 12 13 14 15 16 17 18 19 20 21 22 23 24 25
Aging Time (h)
2B6S
6IS
2B6S-no prestraining
2B6S-4% prestrain
6IS-no prestraining
6IS-4% prestrain

Figure 5.16(a)

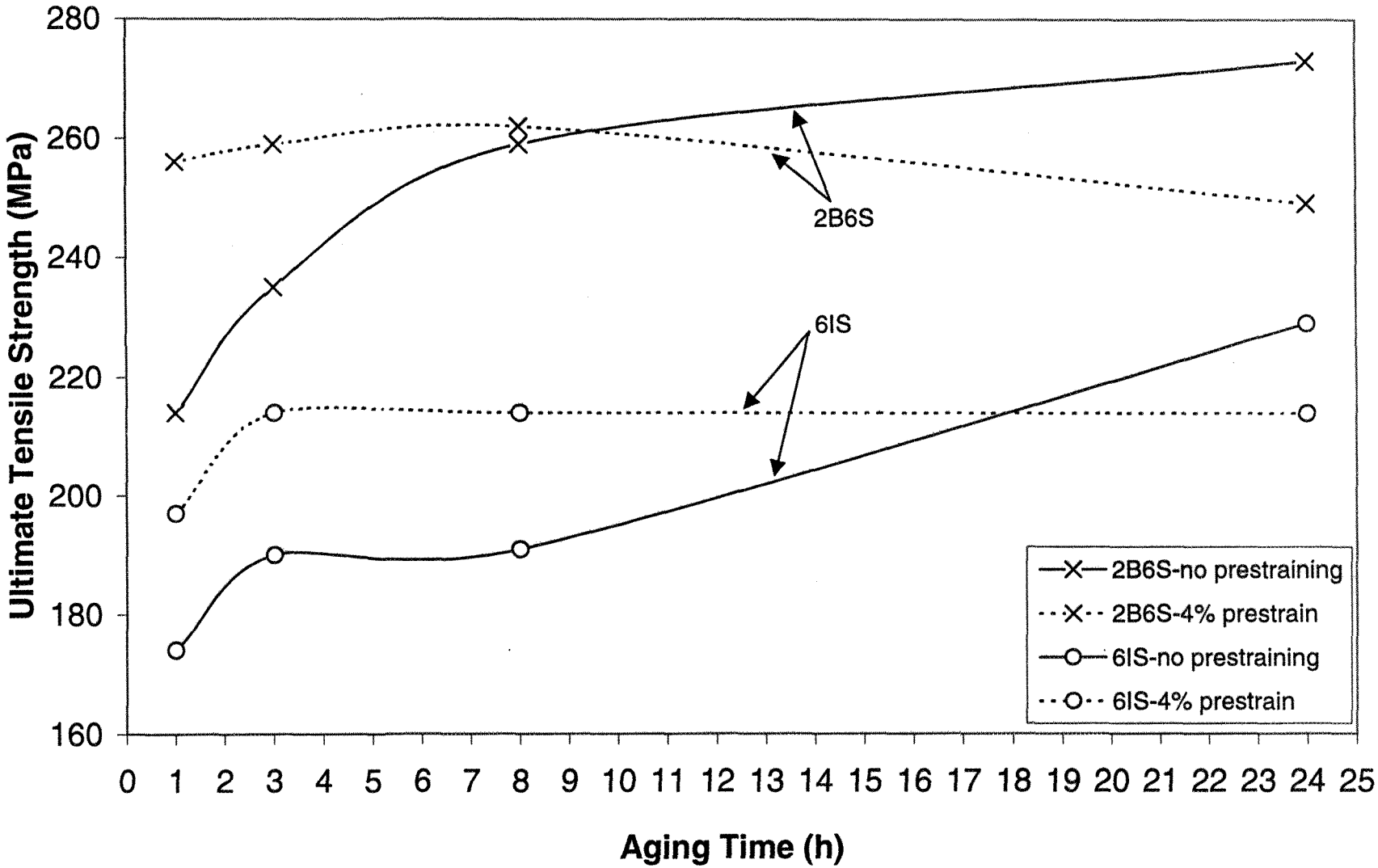
Ultimate Tensile Strength (MPa)
280
260
240
220
200
180
160
0 1 2 3 4 5 6 7 8 9 10 11 12 13 14 15 16 17 18 19 20 21 22 23 24 25
Aging Time (h)
2B6S
6IS
2B6S-no prestraining
2B6S-4% prestrain
6IS-no prestraining
6IS-4% prestrain

Figure 5.16(b)

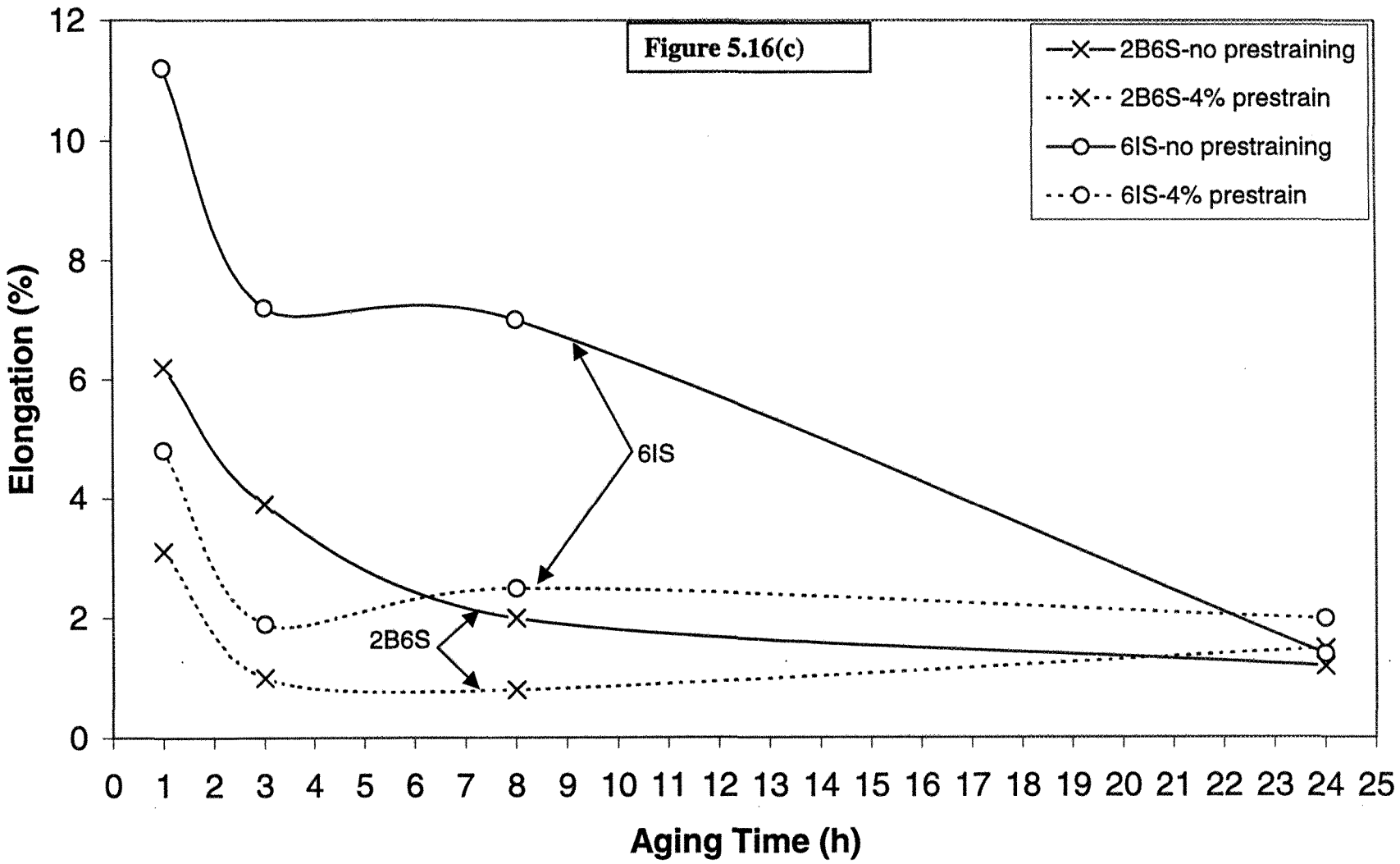

Figure 5.16. Tensile properties of 2B6S and 6IS alloys solution heat treated at 520 °C for times up to 24h: a) YS, b) UTS, c) %EL

5.3.4. Fractography

For fractographic examination, two alloys were selected, the experimental 2B6S alloy, and the industrial 6IS alloy, both alloys being characterized by their high formability, as mentioned previously. Fracture surfaces of the tensile-tested bars corresponding to these alloys were examined using a scanning electron microscope (SEM) operating at 10 kV.

Figure 5.17(a) represents the fractograph obtained from 2B6S alloy in the as-cast condition. In general, the microstructure is ductile, as evidenced by the large number of dimples present in the structure. Occasionally, cleavage fracture is also observed. Figure 5.17(b) is the high magnification micrograph of the same sample fracture surface, revealing the depth of the dimples and the presence of iron-intermetallics in the areas where cleavage is observed. The back scattered image, Figure 5.17(c), corresponding to Figure 5.17(b) reveals the presence of large, undissolved iron intermetallics. Due to the high atomic number of Fe, these intermetallics are clearly visible.

Figure 5.18(a) is the fractograph corresponding to a 2B6S test bar in the T-6 condition (solution heat treatment of 8h /520 °C, quenching in warm water, aging for 8h /175 °C - underaging condition). From this fractograph, and that taken at a higher magnification, Figure 5.18(b), it can be observed that the alloy is still maintaining its ductility, even though the dimple size is reduced, due to age-hardening.

The size and distribution of the undissolved iron intermetallics is shown in Figure 5.18(c), indicating that partial dissolution of the latter has taken place. However, the cleavage fracture at large iron intermetallic particle sites is also observed. Cleavage fracture

is always associated with such large particles, whereas the dimples are formed by the smaller, fragmented intermetallic particles observed within the interiors of the dimples.

The fractographs of Figures 5.19(a) to 5.19(c), also from the same alloy, show the fracture surface of a 2B6S alloy tensile test bar that was deformed 4% in tension (prestraining) immediately after solution heat treatment, followed by the same aging treatment (8h/175 °C). Compared to the previous fractographs, the dimple size in these fractographs is markedly reduced, while the back scattered image (Figure 5.19(c))shows a large number of ultra-fine particles (arrowed). However, some large particles are still visible in the microstructure.

Referring to Figure 5.16, the sensitivity of the 2B6S alloy properties to prestraining is much less after 8h/175 °C compared to that immediately after prestraining, and prior to aging. From the same figure, it can also be seen that the 6IS alloy exhibits a much stronger sensitivity to prestraining, even after aging for times up to 8h. Also, the industrial 6IS alloy is more ductile than the experimental 2B6S alloy.

This observation explains the features observed in Figures 5.20(a) to 5.20(c) (as-cast condition), *i.e.*, a larger dimple size, and the presence of slip lines on the surface of the dimples (Figure 5.20(c) arrowed).

In the T-6 condition, the alloy still maintains its ductility, as displayed by the large and deep dimples observed in Figure 5.21, with the strain lines covering the inner dimple surfaces. It is interesting to see the precipitation of very fine particles (<1 μm) homogeneously distributed within the microstructure.

Figure 5.22 represents the fracture surface of prestrained 6IS alloy. As seen from Figure 5.16, the tensile strengths of the prestrained alloy are relatively higher than those in the unstrained alloy. This is reflected mainly in the size of the dimples observed in the fractographs of Figure 5.22. However, in general, no changes in the nature of the fracture features are observed.

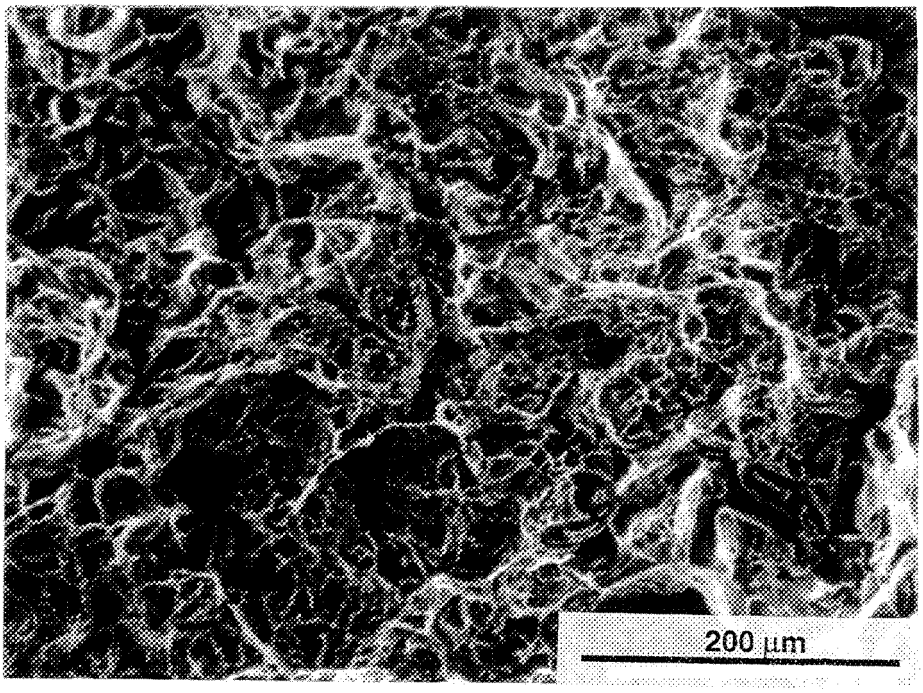

Figure 5.17(a)

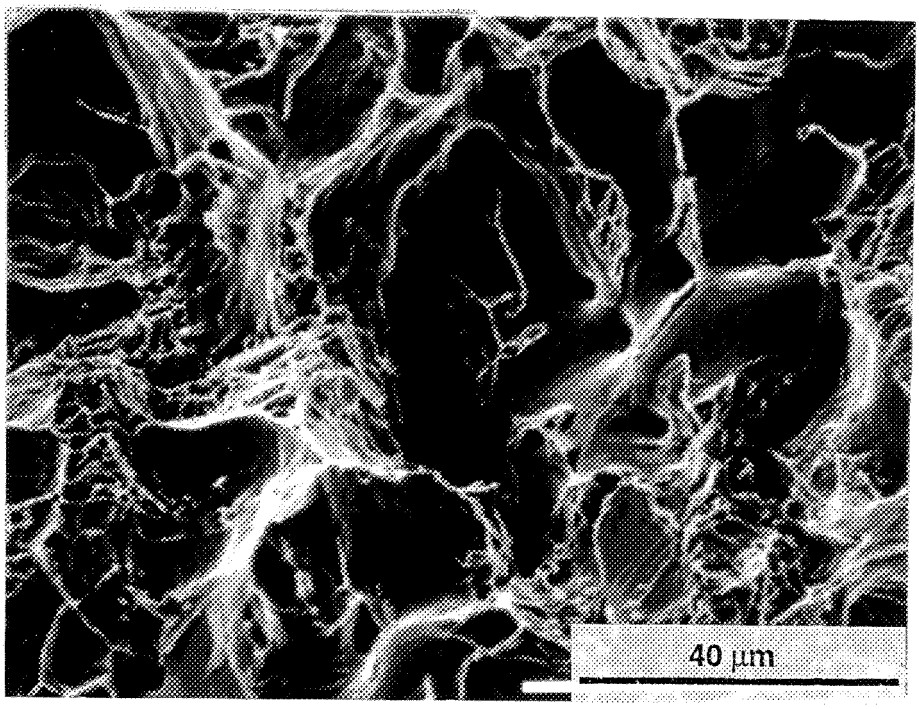

Figure 5.17(b)

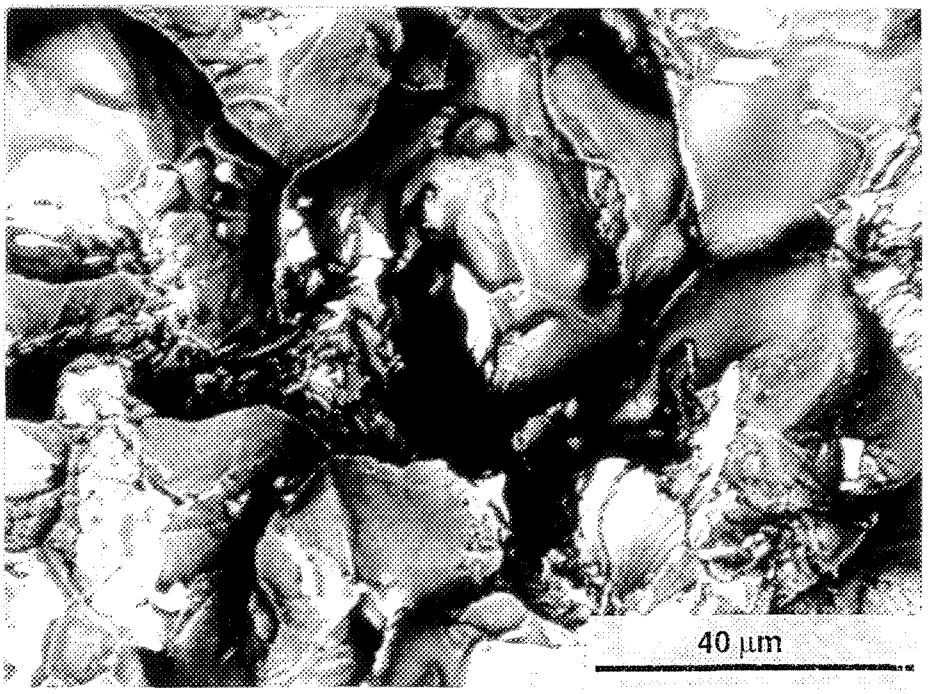

Figure 5.17(c)

Figure 5.17. Fractographs obtained from 2B6S alloy in the as-cast condition:

(a) SE, at low magnification
(b) SE, at high magnification
(c) BSE image of (b)

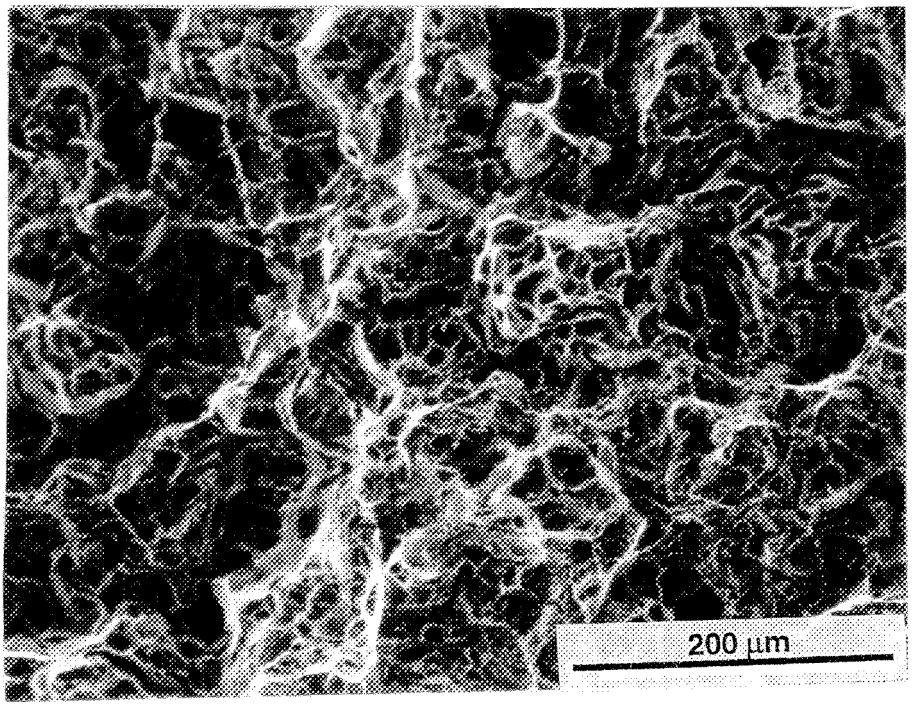

Figure 5.18(a)

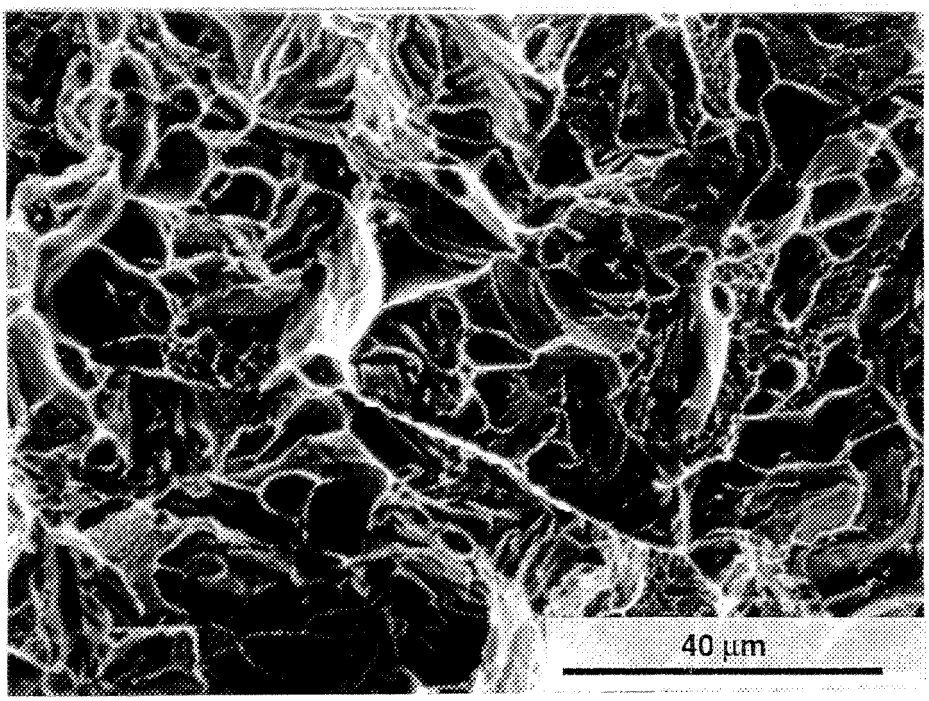

Figure 5.18(b)

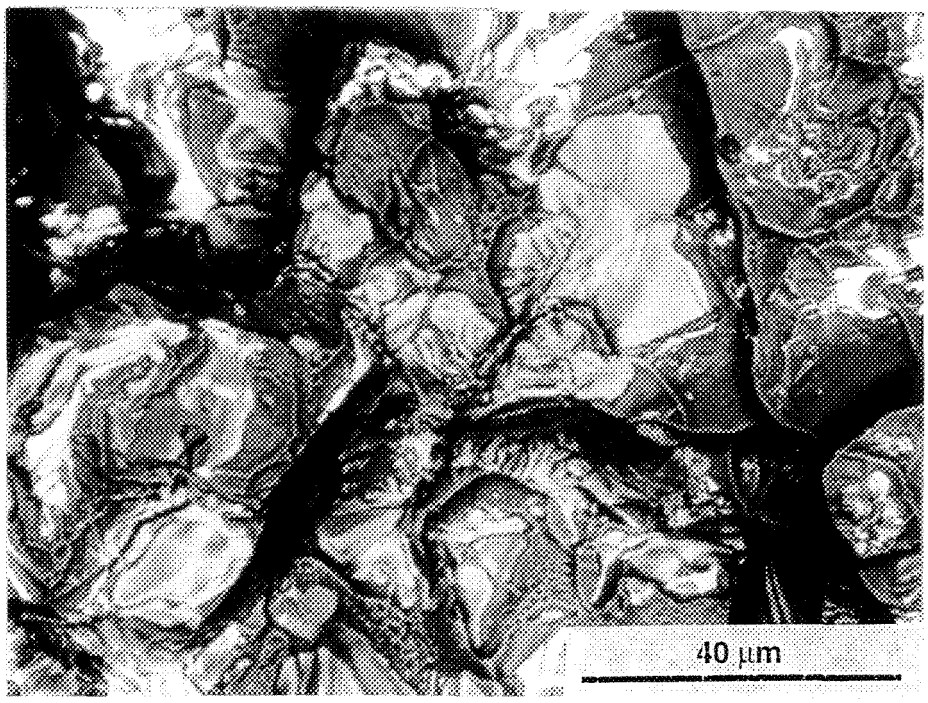

Figure 5.18(c)

Figure 5.18. Fractographs obtained from 2B6S alloy in the T6 condition:

(a) SE, at low magnification
(b) SE, at high magnification
(c) BSE image of (b)

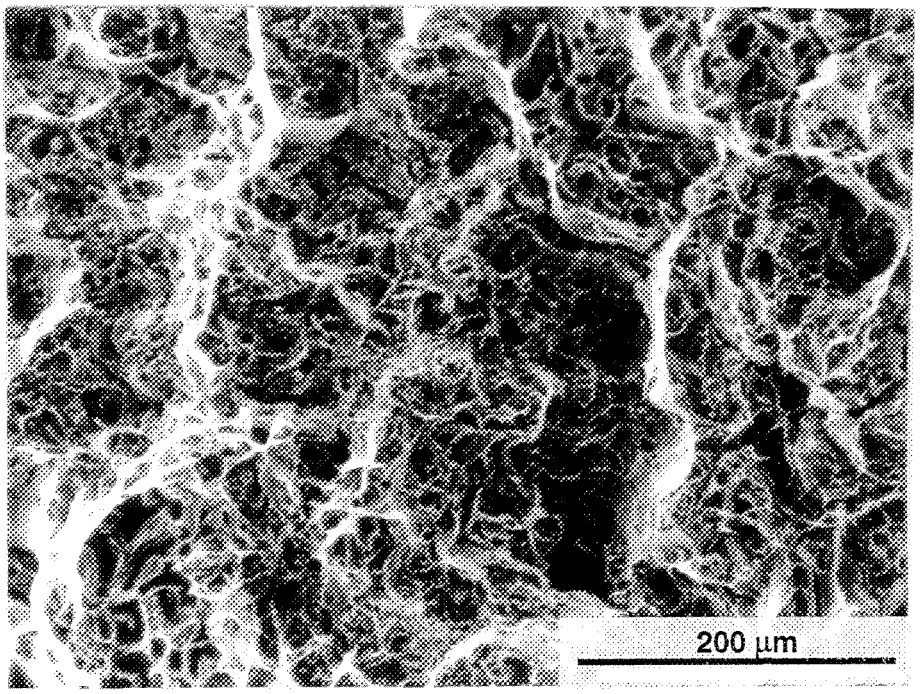

Figure 5.19(a)

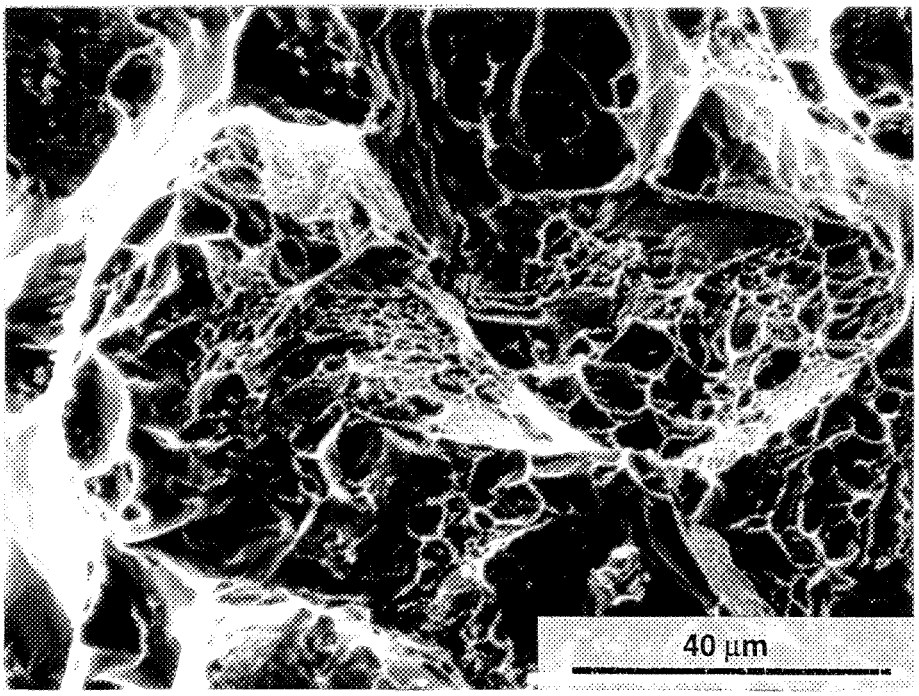

Figure 5.19(b)

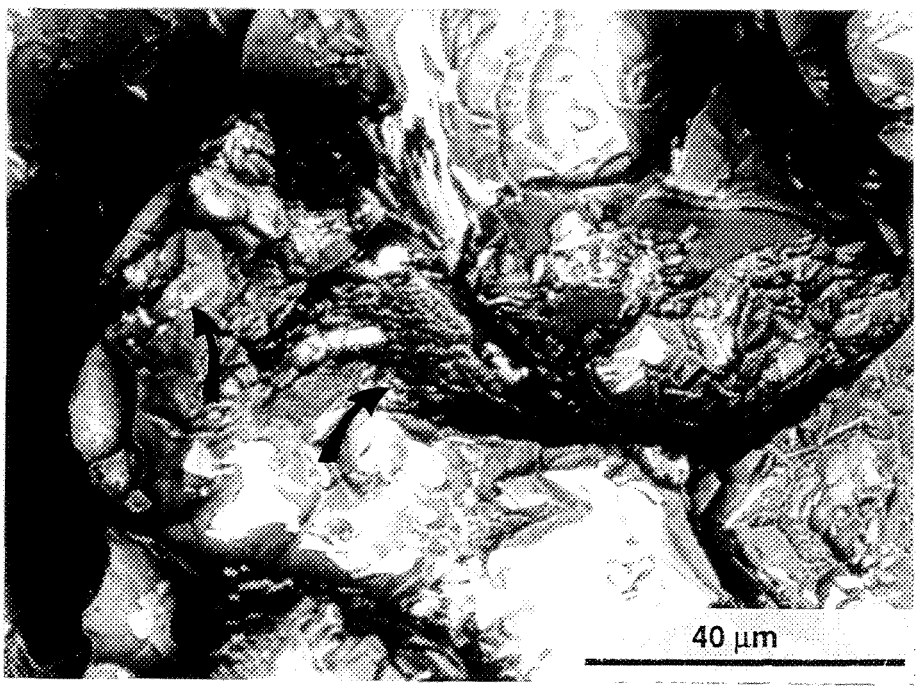

Figure 5.19(c)

Figure 5.19. Fractographs obtained from 2B6S alloy in the prestrained/aged condition:

(a) SE, at low magnification
(b) SE, at high magnification
(c) BSE image of (b)

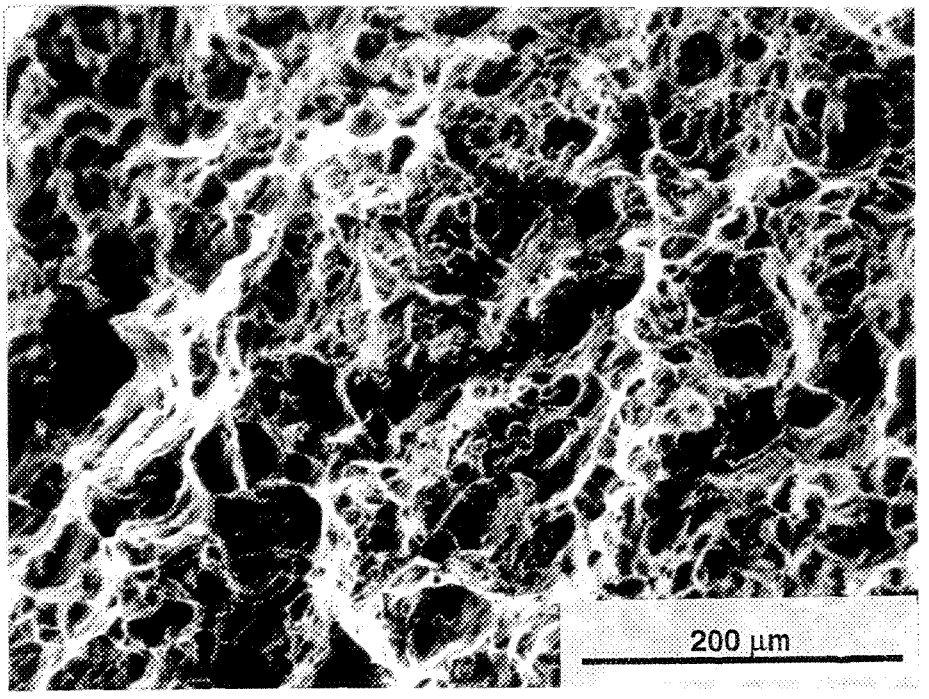

Figure 5.20(a)

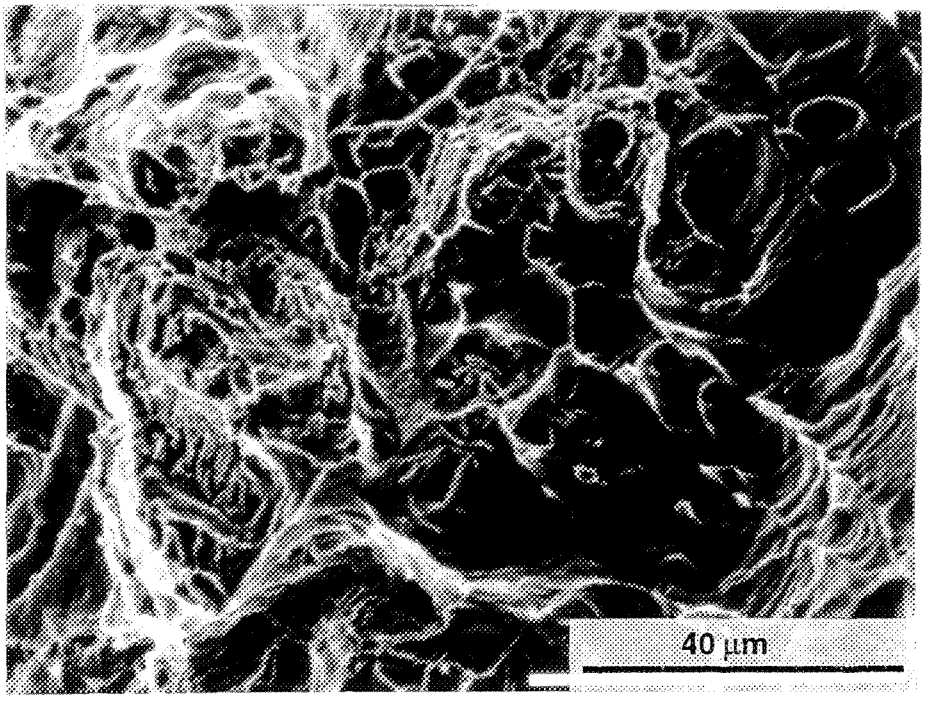

Figure 5.20(b)

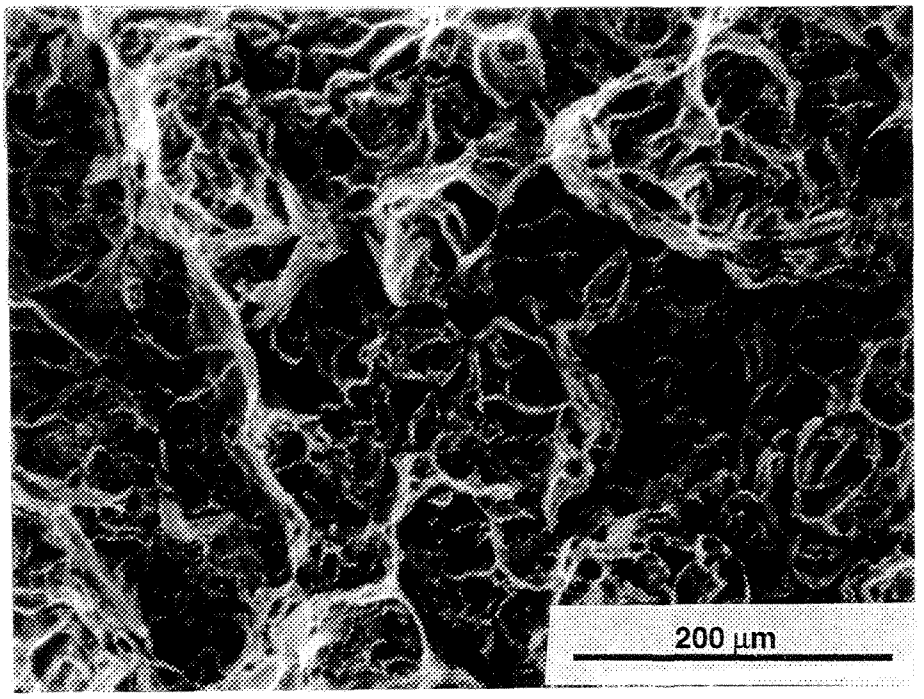

Figure 5.21(a)

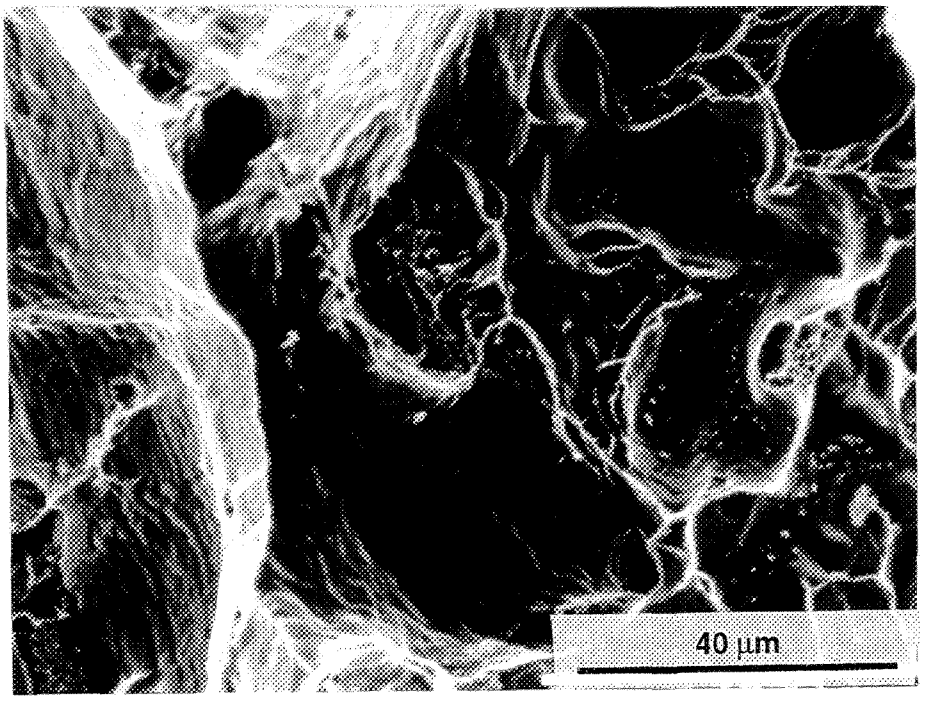

Figure 5.21(b)

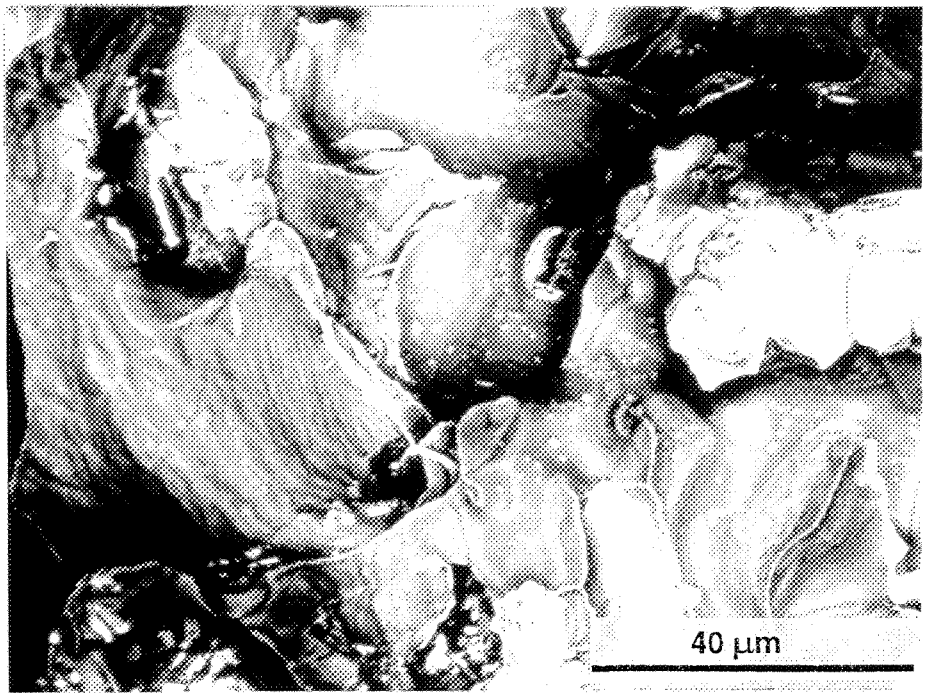

Figure 5.21(c)

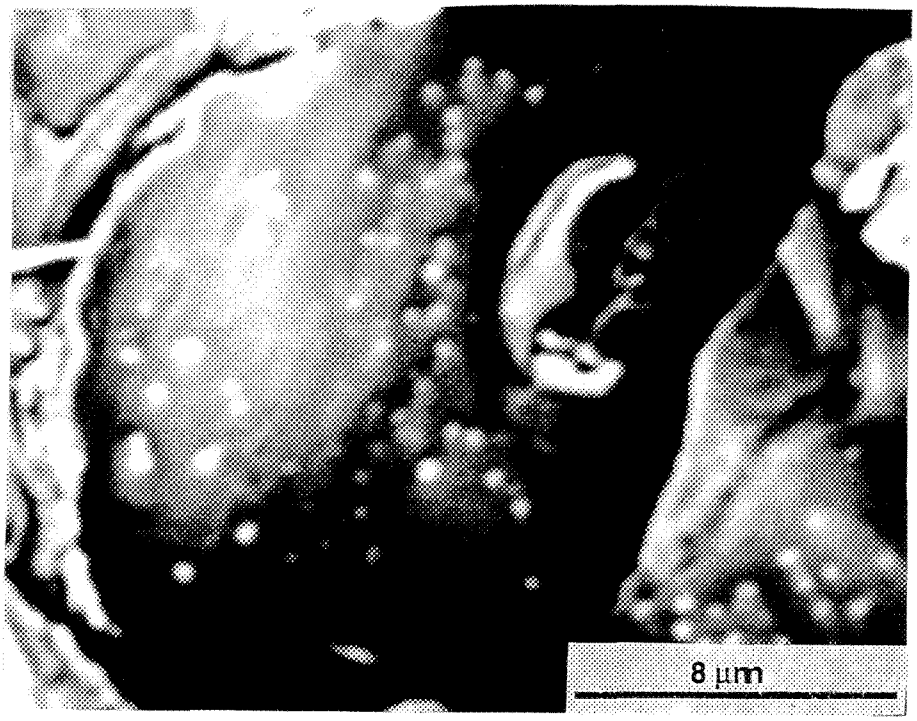

Figure 5.21(d)

Figure 5.21. Fractographs obtained from 6IS alloy in the T6 condition: (a) SE, at low magnification, (b) SE, at high magnification, (c) BSE image of (b), (d) a high magnification micrograph of (c) showing the size and distribution of the precipitated particles.

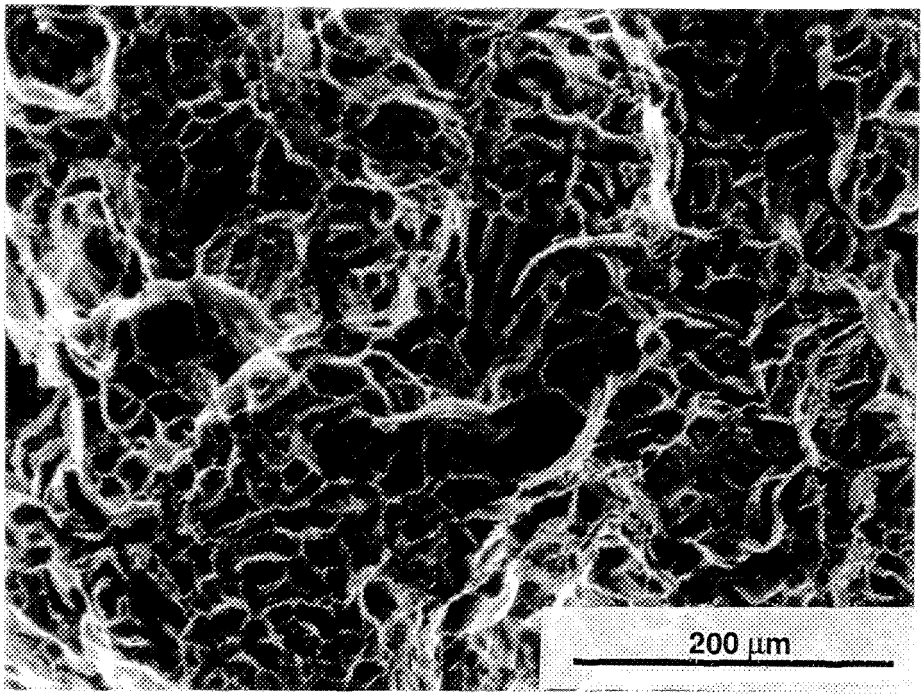

Figure 5.22(a)

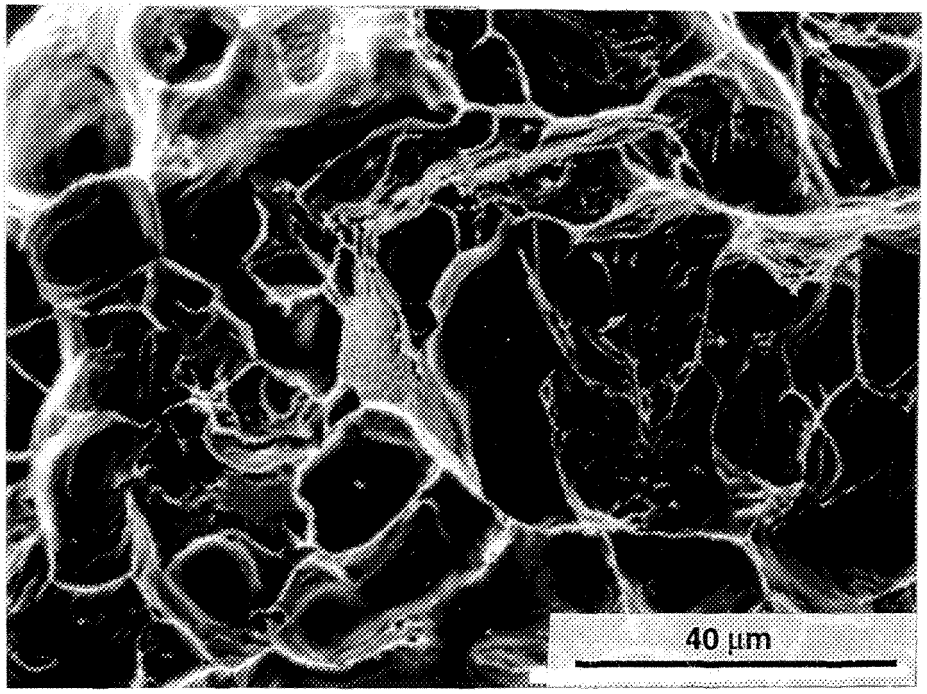

Figure 5.22(b)

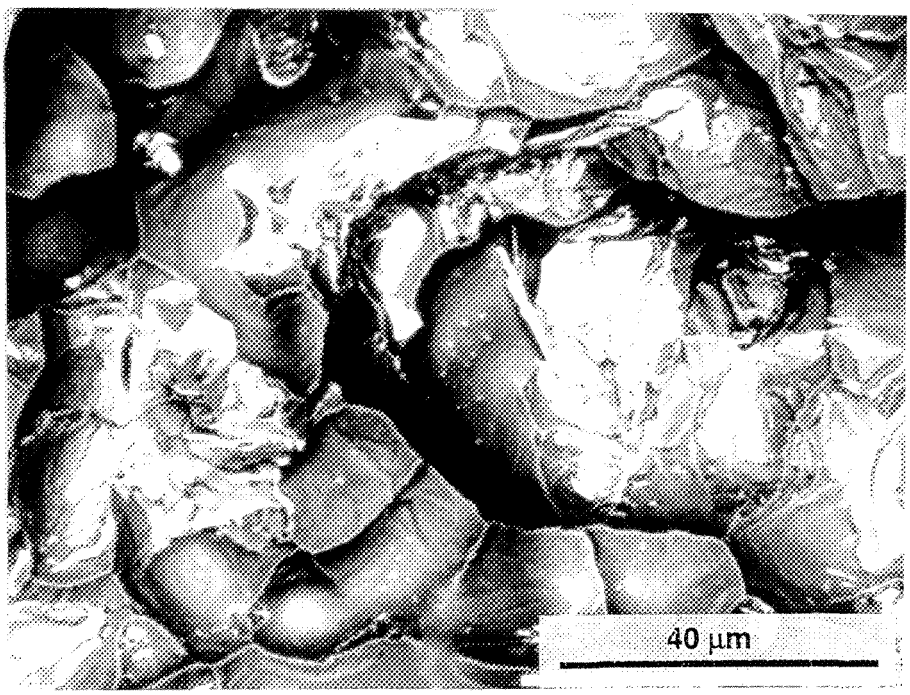

Figure 5.22(c)

Figure 5.22. Fractographs obtained from 6IS alloy in the prestrained/aged condition:

(a) SE, at low magnification
(b) SE, at high magnification
(c) BSE image of (b)

CHAPTER 6

CONCLUSIONS

The present study was carried out to investigate the role of trace elements such as Si, Fe, Mn, Be and Sr on the formation of intermetallics in 6XXX type experimental and industrial alloys, and their impact on the alloy formability and tensile properties. The types of intermetallics formed were identified using optical microscopy, scanning electron microscopy (equipped with EDX facilities) and image analysis. The hardness, tensile properties and cold working characteristics of these alloys were also evaluated to determine the relation between these properties and the intermetallics present.

From an analysis of the results obtained, as reported in Chapters 3, 4 and 5, the following conclusions are drawn.

Microstructure

1. Increasing the free silicon to iron ratio in the A base alloy (Al- 0.6% Si- 0.30% Fe- 0.64% Mg alloy) to ~1 results in the precipitation of the iron intermetallics in the form of long, thick needles/platelets of the β-Al_5FeSi phase.

2. Addition of a sufficiently high amount of strontium (~350 ppm) to the A alloy or increasing the cooling rate or both leads to precipitation of the iron intermetallics in the form of the α-Al_8Fe_2Si phase, instead.

3. When the free silicon to iron ratio is >1, addition of Sr (~350 ppm) leads to the breakdown of the β-Al_5FeSi needles/platelets into smaller fragments without change in the intermetallic type or morphology. A mechanism for the α-iron and β-iron intermetallic precipitation with respect to the Si/Fe ratio, Sr content and cooling rate has been proposed.

4. Addition of Mn or Be to the A alloy leads to the precipitation of the intermetallics in the form of α-$Al_{15}(Fe,Mn)_3Si_2$ and α-Al_8Fe_2BeSi script phases, respectively. In these cases, addition of Sr refines the size of the script particles.

Formability

5. The base alloy (6 alloy: Al-0.62% Si-0.38% Fe-0.65% Mg) containing mainly the β-Al_5FeSi intermetallic phase, displays low formability. The brittle, plate-like nature of the β-phase hinders deformation of the grains during cold rolling and leads to premature cracking (80.5% total reduction).

6. The high Si-containing alloy (S6 alloy: Al-1.01% Si-0.35% Fe-0.68% Mg), where both the amount and size of the β-phase platelets is large, exhibits 43% total reduction in thickness with cold rolling. Addition of strontium does not affect the microstructure and hence the alloy response to formability (*i.e.*, only 45% total reduction is obtained). The cold rolled structure contains elongated grains with broken β-Al_5FeSi platelet fragments.

7. In the Mn-containing alloy (M6 alloy: Al- 0.62% Si- 0.34% Fe- 0.6% Mg-0.2% Mn alloy with an Mn/Fe ratio of ~0.7), the iron intermetallics precipitate in the form of α-$Al_{15}(Fe,Mn)_3Si_2$ script particles. At high cooling rates the particles have much smaller sizes. The α-iron phase is more easily deformable, resulting in a 77% total reduction with cold rolling (*cf.* 43% for S6 alloy). Again, addition of Sr does not improve the alloy behavior, with only 67% reduction being obtained in the M6S alloy.

8. With beryllium additions of 0.02% (2B6 alloy), the iron intermetallics precipitate in the form of small, globular α-Al_8Fe_2SiBe script particles, in the interdendritic regions. Increasing the cooling rate or addition of Sr leads to the precipitation of the α-Al_8Fe_2SiBe phase as very fine, broken particles, which markedly enhance the alloy formability (*cf.* 97% total deformation for 2B6S alloy with 70% for the 2B6 alloy). The industrial alloys (6I, 6IS) show the same response to cold rolling (*i.e.*, 77% and 97% total deformation for 6I and 6IS alloys, respectively).

Tensile Properties

9. In general, the tensile strength curves of the solution heat treated and aged 6 base alloy display two precipitation hardening peaks related to the formation of the GP-1 and GP-2 zones, with the second peak much stronger than the first. Addition of strontium does not alter the hardening mechanism, but lowers the alloy ductility.

10. Addition of small amounts of beryllium (0.02%-0.05%) reduces the possibility of hot tearing during solidification and protects the outer surfaces of the cast test bars from oxidation during solution heat treatment or homogenization at temperatures as high as 520 °C.

11. Addition of a high amount of beryllium (0.13%) leads to the precipitation of a large amount of intermetallics associated with big shrinkage cavities in the central gauge portion of the test bars. Their combined effect deteriorates the alloy properties significantly.

Prestraining prior to aging

12. Prestraining the solution heat treated and quenched test bars (4% in tension) accelerates the precipitation hardening process during aging thereafter. This shortens the aging time required to reach peak hardening from 24h in the non-prestrained condition to 8h in the prestrained condition. The response varies from one alloy to the other.

SUGGESTIONS FOR FURTHER WORK

It is recommended that, for each alloying condition (alloy type and trace element additions), samples for transmission electron microscopy should be prepared from the tensile test bars corresponding to the two peaks observed in the aging curves, in order to confirm the nature and type of the precipitates responsible for the observed hardening.

REFERENCES

1 *Aluminum, Properties and Physical Metallurgy*, J.E. HATCH (ed.), American Society for Metals, Metals Park, OH, 1984, p. 144-148.

2 L.R. MORRIS and F.B. MINERS, *United States Patent,* No. 3,926,690, 1975.

3 J.E. GRUZLESKI and B.M. CLOSSET, "The Treatment of Liquid Al-Si Alloys", *American Foundrymen's Society*, Inc., Des Plaines, IL, USA, 1990.

4 *Aluminum and Aluminum Alloys*, J.R. DAVIS (ed.), ASM Speciality Handbook, ASM International, Materials Park, OH, 1993, 784 pp.

5 *Metals Handbook*, H.E. BOYER and T.L. GALL, American Society for Metals, Materials Park, OH, 1985, p. 6.1-6.64.

6 S. SHIVKUMAR, C. KELLER and D. APELIAN, "Aging Behaviour in Cast Al-Si-Mg Alloys", *AFS Transactions,* vol. 98, 1990, p. 905-911.

7 V. STEFANIAY, A. GRIGER and T. TURMEZEY, "Intermetallic Phases in the Aluminum-Side Corner of the AlFeSi-Alloy System", *Journal of Materials Science,* vol. 22, 1987, p. 539-546.

8 M.H. MULAZIMOGLU, A. ZALUSKA, J.E. GRUZLESKI, and F. PARAY, "Electron Microscope Study of Al-Fe-Si Intermetallics in 6201 Aluminum Alloy", *Metallurgical and Materials Transactions A,* vol. 27 A, 1996, p. 929-935.

9 L. BACKERUD, G. CHAI and J. TAMMINEN, "Solidification Characteristics of Aluminum Alloys, Vol. 2 : Foundry Alloys", *AFS/SKANALUMINIUM*, Des Plaines, IL, USA 1990, p.71-84.

10 S. MURALI, A. TRIVEDI, K.S. SHAMANNA and K.S.S. MURTHY, "Effect of Iron and Combined Iron and Beryllium Addition on the Fracture Toughness and Microstructures of Squeeze-Cast Al-7Si-0.3Mg Alloy", *Journal of Materials Engineering and Performance*, vol. 5(4), 1996, p. 462-468.

[11] J.E. GRUZLESKI, F. PARAY and S.G. SHABESTARI, "Applications of Strontium in Cast and Wrought Aluminum Alloys", *AL13, le magazine de l'aluminium*, vol. 3, 1997, p. 26-33.

[12] A.M. SAMUEL, F.H. SAMUEL and H.W. DOTY, "Observations on the Formation of β-Al5FeSi Phase in 319 Type Al-Si Alloys", *Journal of Materials Science*, vol. 31, 1996, p. 5529-5539.

[13] C. MASCRÉ, "Influence du Fer et du Manganèse sur les Alliages du Type de l'Al-S13 (Alpax)", *Fonderie*, vol. 108, 1955, p. 4330-4336.

[14] S. HAJAS, *Chemical Abstracts*, vol.73, 1970, no. 133571.

[15] W. BONSACK, *ASTM Bulletin*, vol. 117, 1942, p. 45.

[16] A. COUTURE, "Iron in Aluminum Casting Alloys - A Literature Survey", *AFS International Cast Metals Journal*, vol. 6, no. 4, December 1981, p. 9-17.

[17] S. YANEVA, N. STOICHEV, Z. KAMENOVA and S. BUDUROV, "Quaternary Iron-Containing Phases in Al-Si Cast Alloys", *Z. Metallkunde*, vol. 75, 1984, p. 395-398.

[18] L.A. NARAYANAN, F.H. SAMUEL and J.E. GRUZLESKI, "Dissolution of Iron Intermetallics in Al-Si Alloys Through Nonequilibrium Heat Treatment", *Metallurgical and Materials Transactions A*, vol. 26A, 1995, p. 2161-2174.

[19] L.A. NARAYANAN, "Crystallization and Dissolution Studies of Iron Intermetallics in Al-Si Alloys", Ph. D. Thesis, McGill University, Montréal, 1994, p. 80-145.

[20] S. MURALI, K.S. RAMAN and K.S.S. MURTHY, "Effect of Trace Additions on the Mechanical Properties and Fracture Toughness of Fe-Containing Al-7Si-0.3Mg Alloy", *Cast Metals*, vol. 6, no. 4, 1994, p. 189-198.

[21] C. VILLENEUVE, H.W. DOTY and F.H. SAMUEL, "Effect of Trace Elements on β-Al_5FeSi Characteristics and Tensile Properties of Al-Si-Cu (319) Foundry Alloys", *Int. J. Cast Metals Res.*, vol. 12, 1999, in Press.

22 S.C. FLOOD, P.V. EVANS, J.M. BROWN and J. WORTH, "The Influence of Extreme Variations in Casting Parameters and Iron & Silicon Composition on Can-End Stock (AA-5182)", *Light Metals,* 1995, p. 1127-1135.

23 G.J. MARSHALL, A.J. FLEMMING and R.A. RICKS, "The Effect of Fe and Si on the Microstructure, and Properties of AA5182 Alloy Sheet", *Light Metals,* 1996, p. 257-267.

24 I. TODD, and H. JONES, "The Effect of Cumulative Alloying Additions on Intermetallic Phase Selection in Alloys Based on Al-0.5 wt.%Fe", *Materials Science Forum,* vol. 217-222, 1996, p. 201-206.

25 D.J. LLOYD, "Ductility and Bendability in 6000 Series Automotive Alloys", 1999, to be published.

26 X.G. CHEN, "Growth Mechanisms of Intermetallic Phases in DC Cast AA1XXX Alloys", *Light Metals,* B. Welch (ed.), The Minerals, Metals & Materials Society, 1998, p. 1071-1076.

27 S.J. MAGGS, R.F. COCHRANE, S.C. FLOOD and P.V. EVANS, "The Effect of Trace Elements on Intermetallic Phase Selection in Simulated DC Castings," *Light Metals*, J. Evans (ed.), The Minerals, Metals & Materials Society, 1995, p. 1039-1047.

28 M.H. MULAZIMOGLU, F. PARAY, G. STEPHEN, B. KULUNK and J.E. GRUZLESKI, "Modification of Intermetallic Phases by Strontium in Aluminum Wrought Alloys", *Light Metals 1994*, U. Mannweiller (ed.), The Minerals, Metals & Materials Society, Warrendale, PA, 1994, p. 1047-1056.

29 J. IGLESSIS, C. FRANTZ et M. GANTOIS, "Conditions de Formation des Phases de Fer dans les Alliages Al-Si de Pureté Commerciale", *Mémoires Scientifiques de la Revue de Métallurgie,* vol. 73, no. 4, 1977, p. 237-242.

30 Y. AWANO and Y. SHIMIZU, "Non-Equilibrium Crystallisation of AlFeSi Compound in Melt-Superheat Al-Si Alloy Castings, *AFS Transactions*, Vol. 98, 1990, p. 889-895.

31 G. GUSTAFSSON, T. THORVALDSSON and G. L. DUNLOP, "The Influence of Fe and Cr on the Microstructure of Cast Al-Si-Mg Alloys", *Metallurgical Transactions A*, vol. 17A, 1986, p. 45-51.

[32] Y. KOMIYAMA, K. UCHIDA and M. GUNSH, "Effect of Fe, Mn, Zn and Ti on Mechanical Properties and Microstructure of Al-Si-Cu-Mg Casting Alloy", *J. Japan Inst. Light Metals*, vol. 26, 1976, p. 311-319.

[33] L.A. NARAYANAN, F.H. SAMUEL and J.E. GRUZLESKI, "Crystallization Behaviour of Iron-Containing Intermetallic Compounds in 319 Aluminum Alloy", *Metallurgical and Materials Transactions A*, vol. 25A, 1994, p. 1761-1773.

[34] I. MUSULIN, and O.C. CELLIERS, "Effect of Mn on the Quench Sensitivity of 6063"

[35] I. MUSULIN, and O.C. CELLIERS, "The Role of Manganese in 6XXX Alloys-Effect of Quench Sensitivity in 6063", *Light Metals*, C.M. Blckert (ed.), The Minerals, Metals & Materials Society, 1990, p. 951-954.

[36] D.A. GRANGER, "Investigation of a Star-Like Intermetallic Phase Occurring in Alloy 339", *AFS Transactions*, vol. 99, 1991, p. 379-383.

[37] J.L. JORSTAD, "Understanding 'Sludge'", *Die Casting Engineer*, Nov-Dec 1986, p. 30-36.

[38] K.G. WIKLE, "Improving Aluminum Castings with Beryllium", *AFS Transactions*, vol. 86, 1978, p. 513-518.

[39] W.A. BAILEY, "Beryllium Effect on Strength and Mechanical Properties of 356 Variant-T6 Aluminum Alloys", *Modern Casting*, August 1964, p. 443-454.

[40] S. MURALI, K.S. RAMAN and K.S.S. MURTHY, "Effect of Trace Additions on the Mechanical Properties and Fracture Toughness of Fe-Containing Al-7Si-0.3Mg Alloy", *Cast Metals*, vol. 6, no. 4, 1994, p. 189-198.

[41] S. MURALI, K.S. RAMAN and K.S.S. MURTHY, "The Formation of β-$FeSiAl_5$ and Be-Fe Phases in Al-7Si-0.3Mg Alloy Containing Be", *Materials Science and Engineering A*, vol. 190A, 1995, p. 165-172.

[42] A.M. SAMUEL, P. OUELLET, F.H. SAMUEL and H.W. DOTY, "Microstructural Interpretation of Thermal Analysis of Commercial 319 Aluminum Alloy with Magnesium and Strontium Additions", *AFS Transactions*, vol. 105, 1997, p. 951-962.

[43] H. de la SABLONNIÉRE and F.H. SAMUEL, "Solution Heat Treatment (of) 319 Aluminum Alloy Containing ~0.5wt% Mg: Part I- Solidification and Tensile Properties", *Int. J. Cast Metals Res.*, vol. 9 (4), 1996, p. 195-211.

[44] R. DASGUPTA, C.C. BROWN and S. MAREK, "Effect of Increased Magnesium Content on the Mechanical Properties of Sand-Cast 319 Aluminum Alloy", *AFS Transactions,* vol. 97, 1989, p. 245-254.

[45] K. SUKUMARAN, S.G.K. PILLAI, K.K. RAVIKUMAR and B.C. PAL, "Effect of Magnesium Addition on the Microstructure and Mechanical Properties of Al-7Si-0.3Mg", *Praktische Metallographie,* vol. 32(8), 1995, p. 414-423.

[46] A.T. JOENOES and J.E. GRUZLESKI, "Magnesium Effects on the Microstructure of Unmodified and Modified Al-Si Alloys", *Cast Metals*, vol. 4, no. 2, 1991, p. 62-71.

[47] R. KOWATSCHEWA, R. DAFINOWA, Z. KAMENOWA and E.MOMTSCHILOV, "Metallographic Determination of Intermetallic Compounds in Aluminium Alloys", *Praktische Metallographie,* vol. 10, 1973, p. 131-143.

[48] S. SHIVKUMAR, L. WANG and D. APELIAN, "Molten Metal Processing of Advanced Cast Aluminum Alloys", *JOM,* January 1991, p. 26-32.

[49] M.A. KEARNS and P.S. COOPER, "Effects of Solutes on Grain Refinement of Selected Wrought Aluminum Alloys", *Materials Science and Technology,* vol. 13, 1997, p. 650-654.

[50] G.W. BOONE, R.F. CARVER and R.G. SEESE, "Optimizing Grain Refiners and Modifiers in Al-Si Alloys", *Modern Casting,* 1998, p. 52-54.

[51] P. FISHER and G.T. CAMPELL, "Recycling-The Effect on Grain Refinement of Commercial Aluminum Alloys", *Light Metals 1993*, S.K. Das (ed.), The Minerals, Metals & Materials Society, 1992, p. 807-812.

[52] M.W. MEREDITH, A.L. GREER and P.V. EVANS, "The Effect of Grain-Refining Additions on Intermetallic Selection in Dilute Aluminum Alloys", *Light Metals 1998*, B. Welch (ed.), The Minerals, Metals & Materials Society, 1998, p. 977-982.

[53] P.N. ANYALEBECHI, T.N. ROUNS and R.E. SANDERS, Jr., "Effects of Cooling Rate and Grain Refining on Constituent Phase Particle Size in As-Cast 3004 Alloy", *Light Metals 1991,* E.L. Rooy (ed.), The Minerals, Metals & Materials Society, 1990, p. 821-850.

[54] S. SHIVKUMAR, S. RICCI, Jr. and D. APELIAN, "Influence of Solution Treatment on Tensile Properties of Sr-Modified Al-Si-Mg Alloys", *Proc. Intl. Sympos. on "Production and Electrolysis of Light Metals"*, 28th Annual Conf. of Metallurgists of CIM, Halifax, 1989, p. 173-182.

[55] F. PARAY and J.E. GRUZLESKI, "Effect of Modification on Aluminium Matrix of Al-Si-Mg Alloys", *Materials Science and Technology,* vol. 10, 1994, p. 757-761.

[56] J.E. GRUZLESKI, F. PARAY, S.G. SHABESTARI and M.H. MULAZIMOGLU, "Applications of Strontium in Cast and Wrought Aluminum Alloys", *Al13 le Magazine de l'Aluminium,* vol. 2, no. 1, 1996, p. 23-33.

[57] S. SHIVKUMAR, S. RICCI and D. APELIAN, "Influence of Solution Parameters and Simplified Supersaturation Treatments on Tensile Properties of A356 Alloy", *AFS Transactions,* vol. 98, 1990, p. 913-922.

[58] F. PARAY and J.E. GRUZLESKI, "Modification - A Parameter to Consider in the Heat Treatment of Al-Si Alloys", *Cast Metals*, vol. 5, no. 4, 1993, p. 187-198.

[59] B. KULUNK and D.J. ZULIANI, "Applications for the Strontium Treatment of Wrought and Die-Cast Al", *JOM,* 1996, p. 60-63.

[60] S.G. SHABESTARI, "Formation of Iron-bearing Intermetallics in Aluminum-Silicon Casting Alloys", Ph. D. Thesis, McGill University, Montréal, QC, 1994, p. 115-131.

[61] N. FAT-HALLA, "Structural Modification of Al-Si Eutectic Alloy by Sr and its Effect on Tensile and Fracture Characteristics", *Journal of Materials Science*, 1989, p. 2488-2490.

[62] W.D. VERNAM and B.W. LIFKA, *United States Patent,* No. 4,711,762, 1987.

[63] F.C. DIMAYUGA, H. MULAZIMOGLU, B. CLOSSET and J.E. GRUZLESKI, "Microstructural Effects of Strontium on Cast 6000 Series Aluminum Alloys"

[64] F.H. SAMUEL and A.M. SAMUEL, "Effect of Mg and Sr Addition on the Formation of iron Based Intermetallics in Al-Si-Fe DC Alloys", *Proc. Intl. Sympos. on Light Metals 1997,* 36th Annual Conf. of Metallurgists of CIM, Sudbury, Ontario, August 17-20, 1997, p. 425-437.

65 F. PARAY, J.E. GRUZESKI, B. KULUNK, M.H. MULAZIMOGLU, A. ZALUSKA and D.J. ZULIANI, "Metallurgical Effects of Strontium on Wrought 6061 Alloys", *Light Metals,* W. Hale (ed.), The Minerals, Metals & Materials Society, 1996, p. 707-711.

66 B. CLOSSET, F. PARAY, J. GRUZLESKI and H. MULAZIMOGLU, "Microstructures and Properties of Strontium Treated Aluminum Electrical Conductor Alloys", *Light Metals 1996,* W. Hale (ed.), The Minerals, Metals & Materials Society, 1996, p. 737-744.

67 M.H. MULAZIMOGLU, A. ZALUSKA, J.E. GRUZLESKI and F. PARAY, "Electron Microscope Study of Al-Fe-Si Intermetallics in 6201 Aluminum Alloy", *Metallurgical and Materials Transactions A,* vol. 27 A, 1996, p. 929-935.

68 H. FREDRIKSSON and T. NYLEN, *Metal Science,* vol. 16, 1982, p. 283-94.

69 B. XIUFANG, Z. GUOHUA, Z. SHENGXU and M. JIAJI, "The Spheroidisation of Needle-Form Iron Compounds in an Al-Si Alloy", *Cast Metals*, vol. 5, no. 4, 1992, p. 39-41.

70 A. GRIGER, V. STEFANIAY, A. LENDAL and T. TURMEZEY, *Aluminium,* vol. 10, 1989, p. 1049.

71 R. MORA, "Hardening During High Temperature Annealing of Al-Fe-Si Alloys", *Aluminium,* vol. 68, 1992, p. 1081-1082.

72 Z. LI, S.X. DING and J.G. MORRIS, "Influence of Precipitate Structure on Recrystallization and Formability Behaviour of Continuous Strip Cast AA3003 Aluminum Alloy", *Light Metals 1995,* J. Evans (ed.), The Minerals, Metals & Materials Society, Warrendale, PA, 1995, p. 1149-1154.

73 I.H. HOVE and B. ANDERSSON, "Formation of Edge Cracks During Hot Rolling of AA5182", *Proc. Int. Sympos. on Light Metals Processing and Applications,* Quebec City, Quebec, August 29-September 2, 1993, C. Bickert *et al.* (eds.), The Canadian Institute of Mining, Metallurgy and Petroleum, Montreal, p. 473-482.

74 D.J. LLOYD, "Aluminum Alloys Used in Automotive Skin Sheet", *Advances in Industrial Materials,* D.S. Wilkinson, W.J. Poole and A. Alpas (eds.), The Metallurgical Society of CIM, 1998, p. 3-17.

[75] J.D. BRYANT, "The Effects of Pre-Aging Treatments on Formability and Paint Bake Response in Aluminum Autobody Sheet Alloys", *Automotive Alloys,* Edited by S.K. Das and G.J. Kipouros, The Minerals, Metals & Materials Society, 1997, p. 19-36.

[76] H. UCHIDA and H. YOSHIDA, "Improvement in Paint Bake Response of an Al-Mg-Si Alloy by Reversion", *Aluminum and Magnesium for Automotive Applications,* J.D. Bryant (ed.), The Minerals, Metals & Materials Society, 1996, p. 97-104.

[77] E.S. PUCHI, M. STAIA, C. VILLALOBOS and A. PINEIRO, "Cold-Rolling and Annealing of a Commercial Twin Roll Cast Al-Fe-Si Alloy", *Light Metals 1995,* J. Evans (ed.), The Minerals, Metals & Materials Society, 1995, p. 1155-1159.

[78] E.S. PUCHI, M. STAIA, M. ESCORCHE and Y. PÉREZ, "Cold-Rolling and Annealing of a Commercial Twin Roll Cast 3003 Aluminum Alloy", *Light Metals,* J. Evans (ed.), The Minerals, Metals & Materials Society, 1995, p. 1183-1186.

[79] D.J. LLOYD and A.K. GUPTA, "Aluminum Alloy and the Thermal Processing Associated with Automotive Sheet", *Thermec 97,* International Conference on Thermomechanical Processing of Steels & Other Materials, T. Chandra and T. Sakai (eds.), The Minerals, Metals & Materials Society, 1997, p. 99-107.

[80] S. DING and J.G. MORRIS, "Processing of AA3004 Alloy Can Stock for Optimum Strength and Formability" , *Metallurgical and Materials Transactions A,* vol. 28A, 1997, p. 2715-2721.

[81] A.K. GUPTA and M.I. WHEELER, *United States Patent,* No. 5,728,241, 1998.

[82] A.M. SAMUEL and F.H. SAMUEL, "Influence of casting and heat treatment parameters in controlling the properties of an Al-10wt% Si-0.6wt% Mg/SiC/20p composite", *Journal of Materials Science,* vol. 29, 1994, p. 3591-3600.

[83] D. APELIAN, S. SHIVKUMAR and G. SIGWORTH, "Fundamental Aspects of Heat Treatment of Cast Al-Si-Mg Alloys", *AFS Transactions*, vol. 89, p. 727-742.

[84] F. PARAY, B. KULUNK and J. GRUZLESKI, "Effect of Strontium on Microstructure and Properties of Aluminum Based Extrusion Alloy 6061", *Materials Science and Technology,* vol. 12, 1996, p. 315-322.

[85] S. SHIVKUMAR, C. KELLER and D. APELIAN, "Aging Behavior in Cast Al-Si-Mg Alloys", *AFS Transactions*, vol. 98, 1990, p. 905-911.

[86] J.D. BRYANT, "The Effect of Preaging Treatments on Aging Kinetics and Mechanical Properties in AA6111 Aluminum Autobody Sheet", *Metallurgical and Materials Transactions A*, vol. 30A, 1999, p. 1999-2006.

[87] M.S. MISRA and K.J. OSWALT, "Aging Characteristics of Titanium-Refined A356 and A357 Aluminum Castings", *AFS Transactions*, vol. 90, 1982, p.1-10.

ANNEX

Table A.1. Quantitative metallographic measurements of iron intermetallics.

Table A.2. Tensile test data for experimental alloys.

Tensile test data for 2B6S and 6IS alloy in non-prestrained and 4% prestrained conditions.

Table A 1. Quantitative metallographic measurements of iron intermetallics (see **Chapter 3.2.2** for codes).

Alloy code	Condition	Strontium addition (ppm)	Si*/Fe	Average Max. β-length (μm)	Standard deviation	α-Script phas-caste present (%)
A	E	0	0.8	100	19	50
A1	E	231	0.8	65	39	24
A2	E	477	0.8	72	52	31
B	E	0	1,9	123	26	0
B2	E	410	2,0	103	27	1
B4	E	748	1,8	107	31	2.5
C	E	0	13.8	157	58	0
C2	E	354	13.2	139	43	0
C4	E	623	12.4	137	39	0
D	E	0	1,5	86	20	3
D2	E	415	1,8	76	19	5
A	M	0	0,8	43	9	2
A1	M	231	0,8	6	15	62
A2	M	477	0,9	-	-	86
B	M	0	1,9	64	8	2
B1	M	163	1,9	62	28	10
D	M	0	1,5	62	12	0
D2	M	415	1,8	57	13	4
B	G	0	1,9	40	8	0
B1	G	163	1,9	39	15	8
A	SHT	0	0,8	52	12	0
A1	SHT	231	0,8	6	16	81
A2	SHT	477	0,9	-	-	78
A3	SHT	746	1,0	-	-	94
A4	SHT	951	1,1	-	-	98
D	SHT	0	1,5	52	12	0
D2	SHT	415	1,8	44	9	2

Table A.2. Tensile test data for experimental alloys (see **Chapter 5.2.2** for codes).

Alloy code	Strontium addition (ppm)	Temper	YS (MPa)	UTS (MPa)	EL (%)
6	0	as-cast	83.7 ± 4.0	174.7 ± 7.7	13.8 ± 2.2
6S	144	as-cast	83.4 ± 4.6	172.5 ± 3.6	9.9 ± 1.3
S6	0	as-cast	93.1 ± 3.7	187.4 ± 4.6	10.5 ± 2.0
S6S	163	as-cast	93.4 ± 3.1	179.2 ± 5.1	8.4 ± 1.0
M6	0	as-cast	86 ± 2.6	183.4 ± 1.9	18.3 ± 2.4
M6S	206	as-cast	85.4 ± 4.5	170.7 ± 1.8	9.5 ± 1.1
B6	0	as-cast	57.7 ± 5.3	90.9 ± 8.1	3.4 ± 0.5
B6S	147	as-cast	57.9 ± 2.6	90.6 ± 8.2	2.5 ± 0.5
5B6	0	as-cast	64.1 ± 4.7	123.5 ± 6.0	6 ± 0.3
5B6S	162	as-cast	65.2 ± 7.7	121.6 ± 8.6	6.1 ± 0.9
2B6	0	as-cast	80.2 ± 7.3	158.8 ± 12.6	10.5 ± 1.2
2B6S	171	as-cast	62 ± 3.2	128.6 ± 6.3	10.2 ± 1.4
1B6	0	as-cast	79.1 ± 9.3	170.1 ± 6.1	11.8 ± 0.4
6	0	T0	86.9 ± 4.1	194.9 ± 7.9	24.2 ± 0.6
6S	144	T0	85.9 ± 3.6	185.2 ± 5.3	16.4 ± 4.5
S6	0	T0	110.9 ± 1.9	231.2 ± 1.9	20.2 ± 2.2
S6S	163	T0	114.1 ± 2.1	233.1 ± 2.1	21.1 ± 2.2
M6	0	T0	110.9 ± 6.5	223.4 ± 5.8	25.4 ± 0.4
M6S	206	T0	109.1 ± 1.4	211.7 ± 5.5	12 ± 1.2
B6	0	T0	87 ± 2.7	110 ± 3.0	1.7 ± 0.3
B6S	147	T0	93.5 ± 2.3	131.3 ± 7.4	2.9 ± 0.8
5B6	0	T0	87.8 ± 2.0	148.1 ± 7.7	4.9 ± 0.6
5B6S	162	T0	94.6 ± 0.2	148.5 ± 7.4	3.6 ± 1.0
2B6	0	T0	109.5 ± 6.6	220.6 ± 6.5	15.9 ± 3.0
2B6S	171	T0	87.4 ± 1.9	179.6 ± 0.9	12.6 ± 0.4
1B6	0	T0	97.9 ± 1.4	201.9 ± 4.9	13.7 ± 1.2

Table A.2. Continued...

Alloy code	Strontium addition (ppm)	Temper	YS (MPa)	UTS (MPa)	EL (%)
6	0	T1	140.5 ± 1.1	224.8 ± 3.0	16 ± 3.0
6S	144	T1	140.5 ± 1.9	219.2 ± 8.6	10.9 ± 2.3
S6	0	T1	179 ± 0.6	266.4 ± 1.0	12.7 ± 0.1
S6S	163	T1	184.8 ± 0.8	266.6 ± 1.5	12.6 ± 0.0
M6	0	T1	133.1 ± 3.4	224 ± 3.4	20.4 ± 0.3
M6S	206	T1	146 ± 0.5	223.3 ± 1.0	9.2 ± 0.1
B6	0	T1	131.8 ± 8.1	133 ± 6.9	1.1 ± 0.8
B6S	147	T1	128 ± 7.0	128.5 ± 7.0	0.7 ± 0.1
5B6	0	T1	164.9 ± 0.5	233.5 ± 1.2	8.1 ± 0.9
5B6S	162	T1	170.3 ± 7.1	235.9 ± 4.9	7.2 ± 0.2
2B6	0	T1	155.3 ± 3.3	224.4 ± 4.1	8.8 ± 1.6
2B6S	171	T1	151.4 ± 2.7	214.5 ± 4.2	6.2 ± 0.7
1B6	0	T1	159.2 ± 4.3	231 ± 2.6	9.3 ± 0.6
6	0	T3	186.5 ± 2.0	256 ± 6.6	14 ± 1.9
6S	144	T3	194 ± 2.9	246.3 ± 9.6	7.4 ± 1.5
S6	0	T3	173.5 ± 3.2	250.3 ± 5.6	10.5 ± 1.5
S6S	163	T3	196.4 ± 2.1	269.5 ± 4.8	9.2 ± 0.8
M6	0	T3	169.3 ± 4.5	244.8 ± 3.1	17.8 ± 2.0
M6S	206	T3	192.5 ± 7.5	248.8 ± 6.5	6.4 ± 0.8
B6	0	T3	158.1 ± 4.4	158.8 ± 4.5	0.6 ± 0.1
B6S	147	T3	161.7 ± 5.6	162.2 ± 5.0	0.6 ± 0.1
5B6	0	T3	193.7 ± 3.7	242.8 ± 5.5	5.3 ± 0.7
5B6S	162	T3	202.5 ± 2.9	251.1 ± 2.3	5.9 ± 0.5
2B6	0	T3	208.3 ± 2.4	254.4 ± 1.4	5.2 ± 0.3
2B6S	171	T3	197.3 ± 2.0	235.3 ± 2.9	3.6 ± 0.7
1B6	0	T3	201.8 ± 4.2	253.2 ± 8.3	6.6 ± 1.4

Table A.2. Continued...

Alloy code	Strontium addition (ppm)	Temper	YS (MPa)	UTS (MPa)	EL (%)
6	0	T8	238.3 ± 2.1	273.3 ± 2.3	7.6 ± 1.4
6S	144	T8	241.7 ± 5.4	263.5 ± 2.9	3.3 ± 0.2
S6	0	T8	251.4 ± 3.3	301.1 ± 5.1	5.7 ± 1.6
S6S	163	T8	279 ± 4.7	319.6 ± 1.2	5.9 ± 0.8
M6	0	T8	222.8 ± 8.2	273.5 ± 7.2	11.4 ± 0.6
M6S	206	T8	260.5 ± 9.9	287.6 ± 5.8	3.1 ± 0.5
B6	0	T8	172.8 ± 8.2	172.8 ± 8.2	0.5 ± 0.0
B6S	147	T8	162.6 ± 7.9	162.6 ± 7.9	0.4 ± 0.0
5B6	0	T8	213.1 ± 8.0	215.5 ± 11.7	0.7 ± 0.1
5B6S	162	T8	233.5 ± 9.2	237.3 ± 7.5	0.8 ± 0.1
2B6	0	T8	243 ± 6.6	271.6 ± 3.7	3.5 ± 0.4
2B6S	171	T8	239.8 ± 3.0	258.6 ± 3.0	2.0 ± 0.8
1B6	0	T8	242.7 ± 3.2	267.3 ± 4.9	2.9 ± 0.6
6	0	T24	256.5 ± 2.6	282.5 ± 1.3	8.8 ± 0.7
6S	144	T24	258.9 ± 2.7	275.8 ± 2.5	2.4 ± 0.7
S6	0	T24	295.3 ± 1.5	323.3 ± 0.4	2.6 ± 0.6
S6S	163	T24	300.9 ± 7.7	327.6 ± 9.0	3.4 ± 1.2
M6	0	T24	255.9 ± 6.7	282.9 ± 7.2	7.6 ± 1.1
M6S	206	T24	277.4 ± 8.3	289.4 ± 9.0	1.4 ± 0.2
B6	0	T24	188.8 ± 4.9	190.1 ± 7.2	0.4 ± 0.0
B6S	147	T24	158.5 ± 6.9	159.4 ± 8.5	0.4 ± 0.0
5B6	0	T24	262.6 ± 4.0	280.3 ± 1.8	2 ± 0.3
5B6S	162	T24	267.6 ± 2.3	283.8 ± 1.9	1.6 ± 0.2
2B6	0	T24	287.1 ± 6.0	295.5 ± 2.1	2.2 ± 0.3
2B6S	171	T24	262.7 ± 2.2	272.2 ± 1.9	1.4 ± 0.7
1B6	0	T24	270.6 ± 3.1	282.9 ± 4.2	1.3 ± 0.2

Table A.2. Continued...

Alloy code	Strontium addition (ppm)	Temper	YS (MPa)	UTS (MPa)	EL (%)
6	0	T100	232.4 ± 2.4	251.5 ± 1.2	5.3 ± 2.4
6S	144	T100	237.7 ± 1.8	253.2 ± 1.9	2 ± 1.0
S6	0	T100	254.9 ± 7.0	278.5 ± 6.4	4.9 ± 0.9
S6S	163	T100	259.7 ± 7.8	282.1 ± 5.1	5.1 ± 0.6
M6	0	T100	229.8 ± 4.9	259.6 ± 4.2	7 ± 0.5
M6S	206	T100	237.3 ± 6.4	254.5 ± 6.0	2.2 ± 0.4
B6	0	T100	191.8 ± 6.4	191.8 ± 6.4	0.4 ± 0.0
B6S	147	T100	158.2 ± 7.3	158.2 ± 7.3	0.4 ± 0.0
5B6	0	T100	239.2 ± 2.9	254.5 ± 4.0	2.3 ± 0.3
5B6S	162	T100	244.5 ± 6.9	253.1 ± 4.4	2 ± 0.2
2B6	0	T100	241.3 ± 5.1	254.9 ± 2.3	1.7 ± 0.3
2B6S	171	T100	232.2 ± 8.3	243.5 ± 14.3	1.3 ± 0.3
1B6	0	T100	242.7 ± 2.4	252.3 ± 7.6	1.9 ± 0.2
Tensile test data for 2B6S and 6IS alloys in non-prestrained (TX) and 4% prestrained (PX) conditions.					
2B6S	171	P1	241.8 ± 3.2	255.8 ± 2.7	3.1 ± 0.1
6IS	265	T1	105.0 ± 0.7	173.9 ± 5.0	11.2 ± 1.3
		P1	172.2 ± 0.5	196.6 ± 2.9	4.8 ± 0.6
2B6S	171	P3	256.5 ± 2.1	258.8 ± 2.4	1.0 ± 0.0
6IS	265	T3	136.4 ± 2.2	189.6 ± 4.8	7.2 ± 1.3
		P3	205.0 ± 0.9	214.2 ± 1.4	1.9 ± 0.2
2B6S	171	P8	260.5 ± 2.5	261.7 ± 2.2	0.8 ± 0.1
6IS	265	T8	138.4 ± 0.7	190.7 ± 3.8	7.0 ± 1.2
		P8	203.0 ± 1.9	213.8 ± 2.2	2.5 ± 0.4
2B6S	171	P24	244.4 ± 4.7	249.3 ± 4.0	1.5 ± 0.1
6IS	265	T24	219.7 ± 0.8	229.0 ± 0.8	1.4 ± 0.1
		P24	205.9 ± 2.1	213.6 ± 2.4	2.0 ± 0.4

Table A.2. Continued...

Alloy code	Strontium addition (ppm)	Temper	YS (MPa)	UTS (MPa)	EL (%)
A0	0	as-cast	88 ± 2.7	184 ± 5.4	14.3 ± 1.7
A1	231	as-cast	86.8 ± 5.8	177.8 ± 8.8	10.4 ± 1.6
A2	477	as-cast	92.9 ± 0.5	177.6 ± 3.1	9 ± 0.8
A3	746	as-cast	82.1 ± 7.8	161.2 ± 10.6	7.7 ± 0.8
A4	951	as-cast	89.3 ± 5.8	166.1 ± 9.8	6.7 ± 0.5
A0	0	T0	98.1 ± 2.0	209.1 ± 5.7	22 ± 2.7
A1	231	T0	97.3 ± 3.5	201 ± 1.9	16.4 ± 1.1
A2	477	T0	95 ± 2.1	196.9 ± 1.8	15.1 ± 0.6
A3	746	T0	91.9 ± 1.8	186.4 ± 4.8	14.6 ± 1.9
A4	951	T0	88.8 ± 1.5	182.8 ± 3.2	12.6 ± 0.9
A0	0	T3	208.3 ± 1.1	284.6 ± 6.8	11.4 ± 1.5
A1	231	T3	235.3 ± 2.5	281.9 ± 6.8	5.7 ± 0.6
A2	477	T3	223.5 ± 2.1	269.1 ± 11.5	4.9 ± 0.8
A3	746	T3	210.7 ± 7.9	249.2 ± 0.6	3.4 ± 0.5
A4	951	T3	213 ± 9.7	253.6 ± 3.9	3.7 ± 0.8
A0	0	T8	277.1 ± 0.7	313.1 ± 1.4	5.9 ± 1.2
A1	231	T8	282.5 ± 9.4	299.3 ± 5.2	1.4 ± 0.4
A2	477	T8	265.6 ± 1.7	290 ± 1.1	2.3 ± 0.2
A3	746	T8	245.1 ± 3.5	266.3 ± 8.2	2.3 ± 0.5
A4	951	T8	260.9 ± 0.7	273.2 ± 1.9	1.3 ± 0.2
A0	0	T24	293.5 ± 0.4	317.7 ± 0.6	4.3 ± 0.8
A1	231	T24	295.2 ± 9.1	302.9 ± 3.5	1.1 ± 0.1
A2	477	T24	294.3 ± 3.2	303.5 ± 8.0	1.1 ± 0.3
A3	746	T24	291.1 ± 4.5	300.9 ± 5.6	1.3 ± 0.9
A4	951	T24	290.8 ± 4.8	294.4 ± 3.2	0.9 ± 0.5
A0	0	T100	263 ± 1.2	283.7 ± 0.4	4.1 ± 0.7
A1	231	T100	263 ± 2.8	271 ± 1.7	1.2 ± 0.2
A2	477	T100	274.1 ± 4.4	278.7 ± 2.1	1 ± 0.3
A3	746	T100	248.8 ± 3.9	262.3 ± 4.2	1.2 ± 0.1
A4	951	T100	236.9 ± 9.8	249 ± 8.6	0.7 ± 0.1